Advances in the Development of the Discrete Element Method for Excavation Processes

C. A. Labra
E. Oñate
J. Rojek

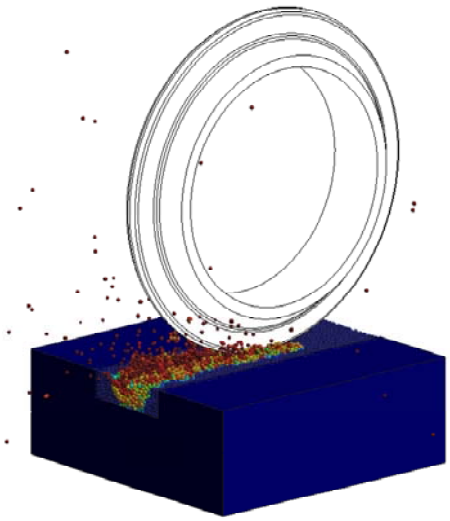

Monograph CIMNE Nº-132, September 2012

Advances in the Development of the Discrete Element Method for Excavation Processes

C. A. Labra
E. Oñate
J. Rojek

Monograph CIMNE Nº-132, September 2012

International Center for Numerical Methods in Engineering
Gran Capitán s/n, 08034 Barcelona, Spain

INTERNATIONAL CENTER FOR NUMERICAL METHODS IN ENGINEERING
Edificio C1, Campus Norte UPC
Gran Capitán s/n
08034 Barcelona, Spain
www.cimne.com

First edition: September 2012

ADVANCES IN THE DEVELOPMENT OF THE DISCRETE ELEMENT METHOD FOR EXCAVATION PROCESSES
Monograph CIMNE M132

ISBN: 978-84-940243-5-1

Depósito legal: B-27595-2012

To my parents...

Acknowledgements

This research was partially supported by project SAFECON of the European Research Council (ERC).

Abstract

Modelling of granular materials, soils and rocks has been a challenging topic of investigation for decades. Classical continuum mechanics has been used to idealize soils and rocks, and numerical solution techniques such as finite element method (FEM) has been used to model these materials. Considering the idealization of the material, continuum mechanics allows the analysis of phenomena with discontinuous nature such as fracture in rock or soil via damage models. However, in more complex processes like rock milling or crushing, this kind of models are usually not suitable. Discrete models are more appropriate for problems with multiple discontinuities and particulate materials. The discrete element method (DEM) has been gaining popularity in analysis of granular materials, soils and rocks. Many aspects of this method still require more profound investigation.

This work presents new developments of the discrete element method improving efficiency and accuracy of modelling of rock-like materials, especially in excavation processes. All the numerical algorithms has been implemented in an in-house software, which was then used to run numerical examples.

The basic formulation of DEM with linear elastic-perfectly brittle contact model is presented. The main difference with other models found in the literature is the consideration of global stiffness and strength parameters that are constants in the whole model.

The result of a simulations is strongly related with the configuration of the particle assembly used. Particle assemblies should be sufficiently compact and ensure the isotropy to reproduce the physical properties of the modelled material. This work presents a novel technique for the generation of highly dense particle assemblies in arbitrary geometries, satisfying all the requirements for accurate discrete element simulations.

One of the key issues in the use of the DEM is the estimation of the contact model parameters. A methodology is proposed for the estimation of the contact model parameters yielding required macroscopic properties of the material. The relationships between the contact model parameters and the mechanical properties of brittle materials, as well as the influence of the particles assembly configuration on the macroscopic

properties, are analysed.

A major difficulty in the application of the DEM to real engineering problems is the high computational cost in simulation involving a large number of particles. The most common way to solve this is the use of parallel computing techniques, where multiple processors are used. As an alternative, a coupling scheme between DEM and the finite element method (FEM) is proposed in the work. Within the hybrid DEM/FEM model, DEM is only used in the region of the domain where it provides an advantage over a continuum-based approach, as the FEM. The coupling is dynamically adapted, starting with the whole domain discretized with FEM. During the simulation, in the regions where a high stress level are found, a change of modelling method from continuum FEM to the discrete DEM is employed.

Finally, all the developments are applied to the simulation of a real excavation process. An analysis of the rock cutting process with TBM disc cutters is performed, where DEM and the DEM/FEM coupling technique presents an important advantage over other simulation techniques.

Table of Contents

List of Figures

List of Tables

Chapter 1

Introduction

1.1 Motivation and objectives

Modelling granular materials, solid and rocks has been a challenging topic of investigation for decades. The particulate nature of granular materials controls their engineering behaviour. According to a classical definition [37], granular materials are characterized by hard inelastic contacts of their elementary constituents, friction, and negligible thermodynamic effects.

Classical continuum mechanics has been used to idealize soils and rocks, and numerical solution techniques such as *finite element method* (FEM) have been successfully used to model these materials. The continuum mechanics models are phenomenological and are primarily concerned with the mathematical modelling of the observed phenomenon without giving detailed attention to the fundamental physical significance. This approach considers three completely independent assumptions: continuity, homogeneity and isotropy. This is an idealization of the materials for the representation of its mechanical behaviour.

Considering the idealization of the material, continuum mechanics allows the analysis of certain phenomenas such as fracture in rock or soil via damage models [20]. However, in more complex processes like rock milling or crushing these kind of models are not always suitable. This is because the discrete nature makes the constitutive relationship complex and needs an excessive number of parameters to be able to model the behaviour accurately.

Granular materials consist of grains in contact and surrounding voids. The mechanical behaviour of granular materials is, therefore, inherently discontinuous and heterogeneous, and typically anisotropic.

A different approach is the use of discontinuous or discrete models which treats the particles in a direct way. The particulate nature is automatically simulated as discrete

particles and forces are transferred through the contacts between particles. The material behaviour is modelled in a realistic way, considering the random distribution of particles size and shape. In the case of cohesive materials, like rocks, fracture can be obtained in a simple way through the breakage of bonds between particles with adhesive contacts.

The most common discrete techniques for the simulation of granular materials are the *discrete element method* (DEM) [33] and *molecular dynamics* (MD) [4, 90]. Both methods can handle a wide range of materials constitutive behaviours, contact laws, and arbitrary geometries. The DEM for modelling granular soils within the context of civil engineering was first introduced by Cundall and Strack [33]. The particles were modelled as a random assembly of discrete discs. Many research studies have since been conducted to improve the simulation of angular grain shapes. Nowadays, the DEM is used in a wide range of engineering problems like fracture, rock crushing, excavation processes, or even in the pharmaceutical or chemical industry, for the transport of particles.

The DEM allows the use of different contact laws, linear and non-linear, depending on the process that will be simulated. This permits the simulation of a problem in different scales, and even the modelling of the particles behaviour at its real size, involving the interaction of many particles in the system.

This technique is a very efficient tool for the analysis of different problems, but does come with some drawbacks. The calculation of each particle-particle interaction, in some cases with complex contact laws, requires a high computational effort. Sometimes, a DEM simulation can take days or week. This restricts its application to simple problems with a small number of elements or simple shape particles. Another requirement of the DEM is the estimation of the contact model parameters, that in some cases cannot be obtained in a direct way.

This work aims to advance in the use of the DEM technology, seeking to make contributions to enable a better understanding of it. In particular, its use in the simulation of brittle materials. Different aspects of the DEM will be developed, like the estimation of parameters or the particles packing techniques. These aspects are strongly related, because the behaviour of the particles system depends of the initial configurations. Other aspects, like the improvement of the computational efficiency associated with the simulations are developed. A coupling technique with continuum-based methods is introduced, and the algorithms used for the contact resolution are studied.

All the developments are applied to the simulation of rock cutting processes. In mining or tunnelling, rock cutting is one of the most important processes used, and the global performance of the process and its cost are strictly related.

1.2 Outline

This work is divided into seven chapters; their contents are summarized in the following section.

In chapter 2, the formulation of the discrete element is presented. In the literature, different approaches for the implementation of the DEM are found. The contact model presents the most important part of the DEM, where the contact can be defined as a linear elastic contact model, like the elastic perfectly brittle model, or non-linear elastic response like the Hertz contact model, where the elastic range of the contact is defined with a power function of the contact gap. This work presents the description of the elastic perfectly brittle model implemented, as well as the time integration scheme and other important numerical aspects involved. The main difference with other models found in the literature is the consideration of global stiffness and strength parameters that are constants, which are not scaled at the contact level.

In chapter 3, a novel technique for the generation of the particulate media is introduced, where the most important characteristic is the highly dense particles assembly in arbitrary geometries, satisfying all the requirements for accurate DEM simulations. In a DEM simulation the results obtained are strongly related with the configuration of the particle assembly used. This *mesh dependence* requires a good characterization of the generated package of particles in order to ensure the level of anisotropy or other physical properties of the material to be modelled.

In chapter 4, a methodology for the estimation of the contact model parameters based on the mechanical properties of the material is presented. In the simulation of solid material like rock, a contact model with cohesion is used. The parameters associated with the elastic deformation are related with the stiffness of the contact, but the strength should be reflected in a contact model as a limit force for the cohesion, breaking the bonds between particles. This micro-macro transition enables the collective behaviour of many particles to be understood as a function of their contact properties. The relationships between the contact model parameters and the mechanical properties of the brittle materials are analysed, as well as the influence of the particles assembly configuration.

In chapter 5, a coupling scheme between DEM and the finite element method (FEM) is presented. A major difficulty in the application of the DEM to real engineering problems is the high computational cost in simulations involving a large number of particles. The most common way to solve this is the use of parallel computing techniques, where multiple processors are used. As an alternative, a coupling scheme between DEM and FEM is proposed. In the simulation of processes which involve fragmentation or fracture, a discrete technique is very useful in order to model the discontinuity, but in the region far from the damage the behaviour can be perfectly solved with FEM. Within the hybrid

DEM/FEM model, DEM is only used in the region of the domain where it provides an advantage over a continuum-based approach. The multi-scale approach minimizes the extra computational cost of the DEM. An adaptive coupling process is introduced, allowing a dynamic change of modelling technique. The simulation process starts with the whole domain discretized with FEM. During the simulation, in the regions where high stress level are found, a change of model from continuum FEM to discrete DEM is employed.

In Chapter 6, the techniques developed in the previous chapters are applied to the analysis of excavation processes. Special emphasis has been put on the simulation of the rock cutting process, where both DEM and DEM/FEM coupling present an important advantage over other simulation techniques.

Finally, some remarks and conclusions are provided, and further developments are suggested.

Chapter 2

The discrete element method

The so-called discrete (or distinct) element method (DEM) was originally developed by Cundall [34, 35] for the analysis of rock mechanics problems. The basic formulation of the DEM using spherical or cylindrical particles was later proposed by Cundall and Strack [33] to investigate the constitutive laws for soil. Cundall and Hart [36] showed that DEM is better at modelling a discontinuous material than other numerical tools such as the finite element method.

The DEM assumes that the material can be represented by an assembly of rigid particles interacting among themselves. The overall behaviour of the system is determined by the cohesive/frictional contact laws. The contact law can be seen as the formulation of the material model on the microscopic level. Cohesive bonds can be broken, which allows to simulate fracture of material and its propagation.

This chapter presents the formulation used in the present work, based the formulation developed by Rojek et al. in [93].

2.1 Equations of motion

The translational and rotational motion of rigid spherical or cylindrical particles is described by means of Newton-Euler equations of rigid body dynamics. For the i-th element we have

$$\mathbf{m}_i \ddot{\mathbf{u}}_i = \mathbf{F}_i \tag{2.1}$$

$$\mathbf{I}_i \dot{\boldsymbol{\omega}}_i = \mathbf{T}_i \tag{2.2}$$

where $\mathbf{u}_i$ is the displacement of the particle center in a fixed (inertial) coordinate frame $\mathbf{X}$, $\boldsymbol{\omega}_i$ the angular velocity, $\mathbf{m}_i$ the element (particle) mass, $\mathbf{I}_i$ the moment of inertia, $\mathbf{F}_i$ the resultant force, and $\mathbf{T}_i$ the resultant moment about the central axes.

Vectors $\mathbf{F}_i$ and $\mathbf{T}_i$ are sums of all forces and moments applied to the i-th element

$$\mathbf{F}_i = \sum_{c=1}^{n_c} \mathbf{F}_i^c + \mathbf{F}_i^{ext} + \mathbf{F}_i^{damp} \tag{2.3}$$

$$\mathbf{T}_i = \sum_{c=1}^{n_c} (\mathbf{r}_i^c \times \mathbf{F}_i^c + \mathbf{q}_i^c) + \mathbf{T}_i^{ext} + \mathbf{T}_i^{damp} \tag{2.4}$$

where $\mathbf{F}_i^{ext}$ and $\mathbf{T}_i^{ext}$ are external load, $\mathbf{F}_i^c$ the contact force for the interaction with neighbouring spheres and other obstacles, $\mathbf{F}_i^{damp}$ and $\mathbf{T}_i^{damp}$ are the force and torque resulting from damping in the system (discussed in section 2.4), $\mathbf{r}_i^c$ is the vector connecting the center of the particles of the i-th element with the contact point c, n_c its number of particles being in contact and $\mathbf{q}_i^c$ are torques due to rolling or torsion (not related with the tangential forces).

The form of rotational equation (2.2) is valid for spheres and cylinders (in 2D) and is simplified with respect to a general form for an arbitrary rigid body with the rotational inertial properties represented by the second order tensor.

2.2 Contact forces

Once contact between a pair of elements has been detected, the forces occurring at the contact point are calculated. The interaction between the two interacting bodies can be represented by the contact forces $\mathbf{F}_i$ and $\mathbf{F}_j$, which by the Newton's third law satisfy the following relation:

$$\mathbf{F}_i = -\mathbf{F}_j \tag{2.5}$$

We take $\mathbf{F} = \mathbf{F}_i$ and decompose $\mathbf{F}$ into the normal and tangential components, $\mathbf{F}_n$ and $\mathbf{F}_t$, respectively (Figure 2.1)

$$\mathbf{F} = \mathbf{F}_n + \mathbf{F}_t = f_n \mathbf{n} + \mathbf{F}_t \tag{2.6}$$

where $\mathbf{n}$ is the unit vector normal to the particle surface at the contact point (this implies that it lies along the line connecting the centers of the two particles) and directed outwards from the particle i

$$\mathbf{n} = \frac{\mathbf{x}_j - \mathbf{x}_i}{\|\mathbf{x}_j - \mathbf{x}_i\|} \tag{2.7}$$

The contact forces f_n and $\mathbf{F}_t$ are obtained using a constitutive model formulated for the contact between two rigid spheres (or discs in 2D) (Figure 2.2). The contact

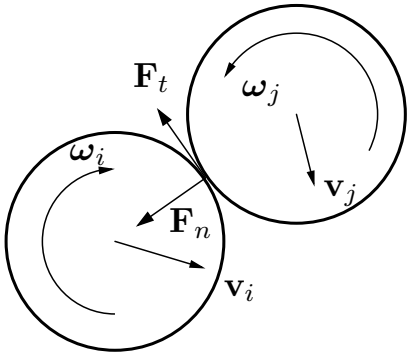

Figure 2.1. Decomposition of the contact force into the normal and tangential components.

interface in our formulation is characterized by the normal and tangential stiffness k_n and k_t, respectively, the Coulomb friction coefficient μ, and the contact damping coefficient c_n.

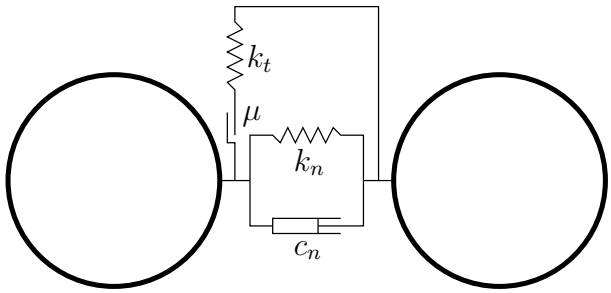

Figure 2.2. Rheological model of the contact.

2.2.1 Normal contact force

The normal contact force f_n is decomposed into the elastic part f_{ne} and the damping contact force f_{nd}

$$f_n = f_{ne} + f_{nd} \tag{2.8}$$

The damping part is used to decrease oscillations of the contact forces and to dissipate kinetic energy.

The elastic part of the normal contact force f_{ne} is proportional to the normal stiffness k_n and to the penetration of the two particle surfaces u_{rn}, i.e.

$$f_{ne} = k_n u_{rn} \tag{2.9}$$

The penetration is calculated as

$$u_{rn} = (\mathbf{x}_j - \mathbf{x}_i) \cdot \mathbf{n} - (r_j + r_i) \tag{2.10}$$

where $\mathbf{x}_i$, $\mathbf{x}_j$ are the center of the particles, $\mathbf{n}$ the normal unit vector between the particles (Eq. 2.7), and r_i, r_j their radii. If no cohesion is allowed, no tensile normal contact forces are allowed and hence

$$f_{ne} \leq 0 \tag{2.11}$$

If $u_{rn} < 0$, Eq. (2.9) holds, otherwise $f_{ne} = 0$. The contact with cohesion will be considered later on.

The contact damping force is assumed to be of viscous type and given by

$$f_{nd} = c_n v_{rn} \tag{2.12}$$

where v_{rn} is the normal relative velocity of the centres of the two particles in contact defined by

$$v_{rn} = (\dot{\mathbf{u}}_j - \dot{\mathbf{u}}_i) \cdot \mathbf{n} \tag{2.13}$$

The damping coefficient c_n can be taken as a fraction α of the critical damping C_{cr} for the system of two rigid bodies with masses m_i and m_j, connected with a spring of stiffness k_n ([107]) with

$$c_n = \alpha\, C_{cr} = 2\,\alpha\,\sqrt{m_{ij} k_n} \tag{2.14}$$

with $0 \leq \alpha \leq 1$, and where m_{ij} is the reduced mass of the contact

$$m_{ij} = \frac{m_i m_j}{m_i + m_j} \tag{2.15}$$

The fraction α it is related with the *coefficient of restitution* c_r, which is a fractional value representing the ratio of speeds after and before of an impact, through [65]

$$\alpha = \frac{-\ln c_r}{\sqrt{\pi^2 + \ln^2 c_r}} \tag{2.16}$$

In the present work, we have used for the fraction of critical damping α=0.9, assuming a quasi-static state for the simulated processes.

2.2.2 Tangential frictional contact

In the absence of cohesion (if the particles were not bonded at all or the initial cohesive bond has been broken) the tangential reaction $\mathbf{F}_t$ appears by friction opposing the relative motion at the contact point. The relative tangential velocity at the contact point $\mathbf{v}_{rt}$ is calculated from the following relationship

$$\mathbf{v}_{rt} = \mathbf{v}_r - (\mathbf{v}_r \cdot \mathbf{n})\mathbf{n} \tag{2.17}$$

with

$$\mathbf{v}_r = (\dot{\mathbf{u}}_j + \boldsymbol{\omega}_j \times \mathbf{r}_{cj}) - (\dot{\mathbf{u}}_i + \boldsymbol{\omega}_i \times \mathbf{r}_{ci}) \tag{2.18}$$

where $\dot{\mathbf{u}}_i$, $\dot{\mathbf{u}}_j$, and $\boldsymbol{\omega}_i$, $\boldsymbol{\omega}_j$ are the translational and rotational velocities of the particles, and $\mathbf{r}_{ci}$ and $\mathbf{r}_{cj}$ are the vectors connecting particle centres with contact points.

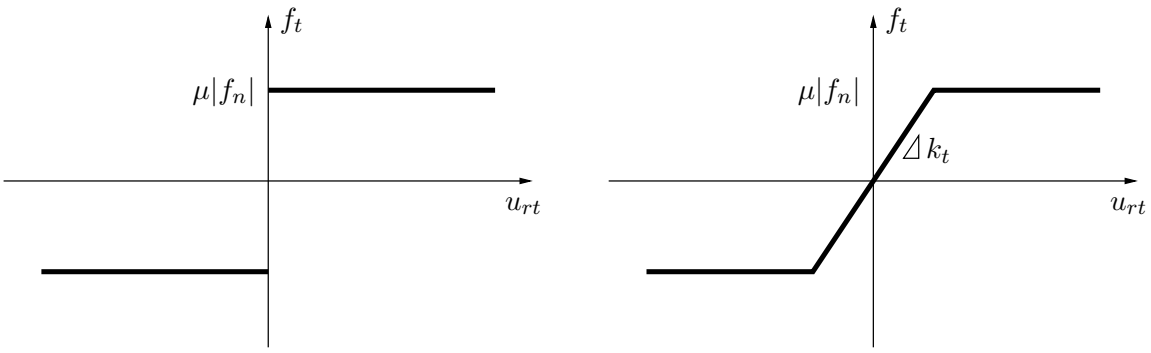

(a) Classical Coulomb law. (b) Regularized Coulomb law.

Figure 2.3. Friction force vs. relative tangential displacement.

The relationship between the friction force f_t and the relative tangential displacement u_{rt} for the classical Coulomb model (for a constant normal force f_n) is shown in Figure 2.3(a). This relationship would produce non physical oscillations of the friction force in the numerical solution due to possible changes of the direction of sliding velocity. To prevent this, the Coulomb friction model must be regularized. The regularization procedure chosen involves decomposition of the tangential relative velocity into reversible and irreversible parts, $\mathbf{v}_{rt}^{\mathrm{r}}$ and $\mathbf{v}_{rt}^{\mathrm{ir}}$, respectively as:

$$\mathbf{v}_{rt} = \mathbf{v}_{rt}^{\mathrm{r}} + \mathbf{v}_{rt}^{\mathrm{ir}} \tag{2.19}$$

This is equivalent to formulating the frictional contact as a problem analogous to that of elastoplasticity, which can be seen clearly from the friction force-tangential displacement

relationship in Figure 2.3(b). This analogy allows us to calculate the friction force employing the standard radial return algorithm. First a trial state is calculated

$$\mathbf{F}_t^{\text{trial}} = \mathbf{F}_t^{\text{n-1}} - k_t \mathbf{v}_{rt} \Delta t \tag{2.20}$$

and then the slip condition is checked

$$\phi^{\text{trial}} = \|\mathbf{F}_t^{\text{trial}}\| - \mu |f_n| \tag{2.21}$$

If $\phi^{\text{trial}} \leq 0$, we have stick contact and the friction force is assigned the trial value

$$\mathbf{F}_t^{\text{n}} = \mathbf{F}_t^{\text{trial}} \tag{2.22}$$

otherwise (slip contact) a return mapping is performed giving

$$\mathbf{F}_t^{\text{n}} = \mu |f_n| \frac{\mathbf{F}_t^{\text{trial}}}{\|\mathbf{F}_t^{\text{trial}}\|} \tag{2.23}$$

2.3 Constitutive models

In the literature it is possible found different constitutive models for the contact between particles.

The elastic response in the contact models can be separated into linear and nonlinear models. All of them can be represented by the normal and tangential stiffnesses, k_n and k_t respectively, defined in (2.9) and (2.20).

The Hertz contact model is the most classical nonlinear model used in particle collisions [60]. From the Hertz theory for an elastic sphere i the normal stiffness may be written as

$$k_n = \left(\frac{2}{3} \frac{G\sqrt{2r'}}{(1-\nu)} \right) \sqrt{u_{rn}} \tag{2.24}$$

where r' is called contact radius, defined as

$$r' = \frac{2\, r_i\, r_j}{r_i + r_j} \tag{2.25}$$

As a complement to the Hertz model, which considers just the normal collision, Mindlin and Deresiewicz [81] extended the theory for the stiffness in the tangential

direction as

$$k_t = \left(\frac{2(G^2 3(1-\nu)r')^{1/3}}{2-\nu} \right) |f_{ne}|^{1/3} \tag{2.26}$$

The called Hertz-Mindlin contact model has been extensively used for granular dynamic simulations [38, 65]. A more general version of this model considers a modified contact damping coefficient (2.12) in order to avoid the viscous force when $u_{rm} = 0$

$$f_{nd} = c_n u_{rn} v_{rn} \tag{2.27}$$

The Hertz theory does not work in the case of bonded particles, and it is just reserved for contacts under compression.

Cundall and Strack [33] defines a linear stiffness proportional to the particle size. This model has been implemented in the PFC2D and PFC3D codes [64].

This model assume that the elastic connection along the line passing through the centres of any two particles in contact is formed by two springs in series. Each spring which its own stiffness K_n^i

$$K_n^i = 4\, E_c\, r_i \tag{2.28}$$

where E_c is called *particle elastic modulus* and with the serial connection between particles we have

$$k_n = \frac{K_n^i\, K_n^j}{K_n^i + K_n^j} \tag{2.29}$$

Considering two particles of with the same mechanical properties, and radius r_i and r_j, the contact stiffness in normal and tangential direction are defined as

$$k_n = 2\, E_c\, r' \tag{2.30}$$

$$k_t = \frac{k_n}{\kappa} \tag{2.31}$$

where κ is the stiffness ratio k_n/k_t.

The most particular aspect of this linear model presents an scaled stiffness, directly related with the effective contact radius. This model allows bonded contacts for the simulation of cohesive materials.

In this work, the linear model introduced by Rojek [93] will be used. The linear contact

model considers a constant global stiffness in both, normal and tangential directions.

The simplest cohesive model is the elastic perfectly brittle model. This model is characterized by linear elastic behaviour when cohesive bonds are active. An instantaneous breakage of these bonds occurs when the interface strength is exceeded. When two particles are bonded the contact forces in both normal and tangential directions are calculated from the linear constitutive relationships:

$$f_n = k_n \, u_{rn} \tag{2.32}$$

$$f_t = k_t \, u_{rt} \tag{2.33}$$

where f_n and f_t are the normal and tangential contact force, respectively, k_n and k_t are the interface stiffness in the normal and tangential directions and u_{rn} and u_{rt} the normal and tangential relative displacements, respectively.

Cohesive bonds are broken instantaneously when the interface strength is exceeded in the tangential direction by the tangential contact force or in the normal direction by the tensile contact force. The failure (de-cohesion) criterion is written (for 2D) as:

$$f_n \leq R_n \tag{2.34}$$

$$f_t \leq R_t \tag{2.35}$$

where R_n and R_t are the interface strengths in the normal and tangential directions, respectively.

In the absence of cohesion the normal contact force can be compressive only, i.e.

$$f_n \leq 0 \tag{2.36}$$

and the (positive) tangential contact force is given by

$$f_t = \mu |f_n| \tag{2.37}$$

if $f_n < 0$ or zero otherwise. The friction force is given by Eq. (2.37) expressing the Coulomb friction law, with μ being the Coulomb friction coefficient. Contact laws for the normal and tangential directions for the elastic perfectly brittle model are shown in Figure 2.4.

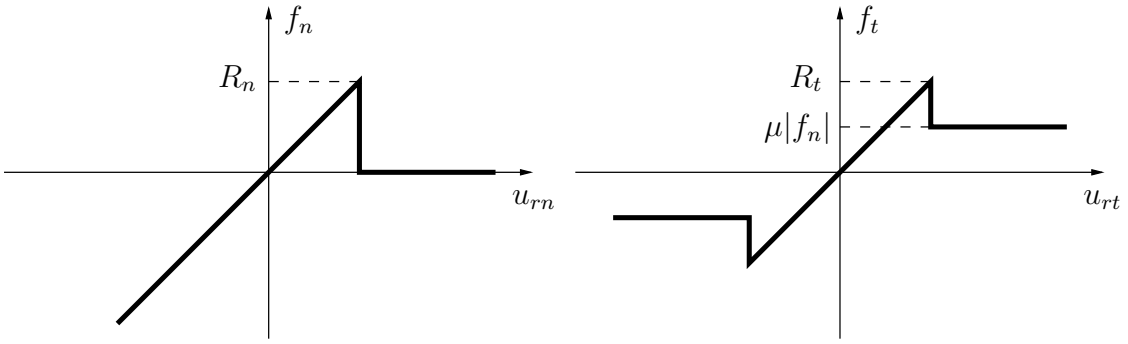

(a) Normal force. (b) Tangencial force.

Figure 2.4. Force-displacement behaviour in the linear elastic perfectly brittle model with bonded contacts.

2.4 Background damping

The contact damping previously described is a function of the relative velocity of the contacting bodies. It is sometimes necessary to apply damping for non-contacting particles to dissipate their energy. We have considered two types of such damping of viscous and non-viscous type, referred here as background damping. In both cases damping terms $\mathbf{F}_i^{\text{damp}}$ and $\mathbf{T}_i^{\text{damp}}$ are added to equations of motion (2.1) and (2.2).

In the case of the viscous damping, the value of the damping force is proportional to the magnitude of the velocity

$$\mathbf{F}_i^{\text{damp}} = -\alpha^t m_i \dot{\mathbf{u}}_i \tag{2.38}$$

$$\mathbf{T}_i^{\text{damp}} = -\alpha^r I_i \boldsymbol{\omega}_i \tag{2.39}$$

For the non-viscous damping, the damping force is proportional to the magnitude to the resultant force and resultant moment in the direction of the velocity

$$\mathbf{F}_i^{\text{damp}} = -\alpha^t \|\mathbf{F}_i'\| \frac{\dot{\mathbf{u}}_i}{\|\dot{\mathbf{u}}_i\|} \tag{2.40}$$

$$\mathbf{T}_i^{\text{damp}} = -\alpha^r \|\mathbf{T}_i'\| \frac{\boldsymbol{\omega}_i}{\|\boldsymbol{\omega}_i\|} \tag{2.41}$$

where α^t, α^r are damping constants, and $\mathbf{F}_i'$, $\mathbf{T}_i'$ are defined as

$$\mathbf{F}'_i = \sum_{c=1}^{n_c} \mathbf{F}_{ic} + \mathbf{F}_i^{ext} \tag{2.42}$$

$$\mathbf{T}'_i = \sum_{c=1}^{n_c} (\mathbf{l}_i^c \times \mathbf{F}_i^c + \mathbf{q}_i^c) + \mathbf{T}_i^{ext} \tag{2.43}$$

It can be seen from Eqs. (2.38)–(2.41) that both the non-viscous and viscous damping terms are opposite to the velocity and the difference lays in the evaluation of the damping force.

A quasi-static state of equilibrium for the assembly of particles can be achieved by application of adequate damping. The damping applied in such problems should be high enough to obtain a non-oscillatory overall response. This is necessary to dissipate kinetic energy of the assembly of particles.

In the present work, the non-viscous damping is used, as recommended in the literature.

2.5 Time integration scheme

In the context of large simulation problems, the implicit schemes are not suitable because of massive memory requirements. The discontinuous-based simulation methods like DEM of MD use explicit integration scheme. For this purpose a whole range of explicit schemes has been developed, where we can found the *Central Difference Scheme* [12] (also referred as the *Velocity Verlet* Algorithm), *Leap Frog Scheme* [108] (also referred as *Position Verlet* Algorithm), *Gear's Predictor-Corrector* [56], *Forest and Ruth* [52, 83], or *Runge-Kutta* [12]. Between these schemes, we can found second order, third order, or even fourth order. Higher order schemes are possible, but involve repeated force evaluations. Since intensive CPU-time is required, higher-order schemes may not be as efficient in terms of computational cost, in comparison with lower-order schemes. In the literature, we can found many comparisons between the different schemes where the stability, accuracy and computational cost are analysed. Some details of the comparisons can be found in [66, 99].

In this work, the *Central Difference Scheme* is used for the integration on the equation of motion (2.1) and (2.2). It is a second-order time integration scheme originally developed in the context of structural dynamics while in some applications it is also referred to as the *Velocity Verlet* algorithm. This scheme presents a good ratio between accuracy and computational cost.

Time integration operator for the translational motion at the n-th time step is as follows:

$$\ddot{\mathbf{u}}_i^n = \frac{\mathbf{F}_i^n}{m_i} \tag{2.44}$$

$$\dot{\mathbf{u}}_i^{n+1/2} = \dot{\mathbf{u}}_i^{n-1/2} + \ddot{\mathbf{u}}_i^n \Delta t \tag{2.45}$$

$$\mathbf{u}_i^{n+1} = \mathbf{u}_i^n + \dot{\mathbf{u}}_i^{n+1/2} \Delta t \tag{2.46}$$

The first two steps in the integration scheme for rotational motion are identical to those givens by Equations (2.44) and (2.45):

$$\dot{\boldsymbol{\omega}}_i^n = \frac{\mathbf{T}_i^n}{I_i} \tag{2.47}$$

$$\boldsymbol{\omega}_i^{n+1/2} = \boldsymbol{\omega}_i^{n-1/2} + \dot{\boldsymbol{\omega}}_i^n \Delta t \tag{2.48}$$

For the rotational plane (2D) motion the rotation angle θ_i can be obtained similarly as the displacement vector $\mathbf{u}_i$:

$$\boldsymbol{\theta}_i^{n+1} = \boldsymbol{\theta}_i^n + \boldsymbol{\omega}_i^{n+1/2} \Delta t \tag{2.49}$$

In three-dimensional motion, rotational position cannot be defined by any vector. The rotational velocity $\boldsymbol{\omega}$ cannot be integrated [5, 15]. The vector of incremental rotation is obtained as

$$\Delta \boldsymbol{\theta}_i = \boldsymbol{\omega}_i^{n+1/2} \Delta t \tag{2.50}$$

It must be remarked that knowledge of the rotational configuration is not always necessary. If tangential forces are calculated incrementally, then knowledge of the vector of incremental rotation $\Delta \boldsymbol{\theta}$ is sufficient. This saves considerable computational cost of the time integration scheme.

2.6 Numerical stability

Explicit integration in time yields high computational efficiency and it enables the solution of large models. The known disadvantage of the explicit integration scheme is its conditional numerical stability imposing the limitation on the time step Δt, i.e.

$$\Delta t \leq \Delta t_{cr} \tag{2.51}$$

where Δt_{cr} is a critical time step determined by the highest natural frequency of the

system ω_{max}

$$\Delta t_{cr} = \frac{2}{\omega_{max}} \tag{2.52}$$

If damping exists, the critical time increment is given by

$$\Delta t_{cr} = \frac{2}{\omega_{max}} \left(\sqrt{1+\xi^2} - \xi \right) \tag{2.53}$$

where ξ is the fraction of the critical damping corresponding to the highest frequency ω_{max}. Exact calculation of the highest frequency ω_{max} would require solution of the eigenvalue problem defined for the whole system of connected rigid particles.

In the algorithm implemented an approximate solution procedure is employed. An eigenvalue problem can be defined separately for every rigid particle [14]. The maximum frequency is estimated as the maximum of natural frequencies of mass–spring systems defined for all the particles with one translational and one rotational degree of freedom.

$$\omega_{max} = \max_i \ \omega_i \tag{2.54}$$

and the natural frequency for each mass-spring system (contact) is defined as

$$\omega_i = \sqrt{\frac{k}{m_i}} \tag{2.55}$$

with k the spring stiffness and m_i the mass of particle i. Now it is possible to rewrite the critical time step as

$$\Delta t_{cr} = \min \ 2\sqrt{\frac{m_i}{k}} \tag{2.56}$$

The effective time step is considered as a fraction of the critical time step

$$\Delta t = \beta \Delta t_{cr} \tag{2.57}$$

with

$$0 \leq \beta \leq 1 \tag{2.58}$$

The value of β has been studied by different authors. A good review can be found in [86], where the author recommend values close to β=0.17 for 3D simulation, and β=0.3 for the 2D case. Less conservative values are presented by different authors, as the recommended by Itasca [64].

Chapter 3

Discretization of the media

One of the most important phases in a simulation with DEM is the discretization of the media, because it has a strong influence in the results obtained in the simulations. For modelling granular materials without cohesion, a DEM particle represents a material particle, allowing the use of the mechanical properties. In the case of the simulation of solid materials (with bonded contacts), the DEM particle does not have a physical meaning, and its just the discretization of the media. In this last case, the characterization of the set of particles its strongly related with the results obtained, and should be considered in the process of calibration or estimation of the model parameters.

The package of particles used in the simulation should allow the representation of the mechanical properties in the material, as isotropy or the Poisson's ratio. For some applications, such as wear analysis of mechanical parts or impact analysis, a good compaction rate is crucial [62, 72, 84]. In these cases the generation of a sufficiently dense distribution of particles presents a major challenge.

This chapter introduces a new packing method, considering extremely dense granular packages for cylindrical (2D) and spherical (3D) particles. The algorithm is analyzed and compared to other existent methods.

3.1 Overview of available approaches

A number of approaches have been developed for the generation of cylindrical (2D) and spherical (3D) particles. The algorithms can be classified in three different groups, considering how it works: *constructive algorithms*, *dynamic algorithms* and *collective rearrangement algorithms*. All of them generate random packages. A fourth group can be considered for the *regular structure packages*, but the behaviour of materials with irregular micro-structure cannot be reproduced, and are not considered in this work.

3.1.1 Constructive algorithms

This kind of algorithms face the problem using purely geometrical considerations. An example is the algorithm used in the PFC2D code [64], where the particle position and size are obtained by a random number. If overlapping occurs, a new random location is achieved, with the same fixed radius. Similar schemes are proposed by Lin and Ng [76] and Evans [45]. In [64] it is proposed an alternative modification of the algorithm, where the radii of all particles are expanded by the same factor. The generation stops when contacts are found. These schemes are called *lily-pond models* [55]. The *Stienen Model* [105] uses a random location to calculate the radius of particles by half of the mean distance to neighbouring particles. The algorithm used by Cui and O'Sullivan [32] is an example of this technique where the circumcenter (2D), or circumsphere (3D), and the vertex are used for locating the particles, and their radii are calculated by the distance between the neighbouring particles. More examples of this and other techniques can be found in [105]. All these methods use a random location and some of them can prescribe a radius distribution. Nevertheless, the resultant packages present a low number of contacts and cannot control the porosity.

Recently, more sophisticated generation algorithms were proposed, based in *advancing front techniques*, where the radius distribution can be prescribed and the particle positions are calculated. The *sedimentation techniques*, like the *open front method* proposed by Feng [49] or the *dropping method* by Bagi [6], where the domain is filled up starting from the bottom, always adding one particle at the time to the already existing set of particles. The geometrical position of the actual new particle, with radii predefined by a prescribed radius distribution, is defined such a way that would exactly touch to previous particles beneath, or any of the walls of the domain, selecting a stable position upon application of a downwards force. One advantage of the sedimentation techniques if the possibility of prescribing the radius distribution. This can produce more dense arrangements, but the resultant micro-structure present a slight anisotropy, reflected in a behaviour slightly stiffer in the vertical direction than in the horizontal direction. Other disadvantage is the top wall of the domain, which cannot be filled up perfectly. A different approach is the *closed front method*, also proposed by Feng et al. [49], where the particle locations are calculated on the basis of previous particle inclusions, along an outwards spiral, starting with a triangle of three touching particles in the middle of the domain. The method present a very high generation velocity, and produce isotropic arrangements, but large gaps may remain in the walls of the domain. A similar behaviour is found in method presented by Löhner and Oñate in [77], which is extended to 3D.

A variation of these methods is the *inwards packing method* presented by Bagi [8], where first the wall of the domain are filled up in such a way that a closed chain of particles is formed. The subsequent particles are placed along the interior of the front. When a new grain is generated, it is attached to two existing particles in the front. The front is then updated, and a next particle can be generated. This method solves the problem of the gaps remaining in the walls of the *closed front method*, but results very difficult to implement in 3D.

3.1.2 Dynamic algorithms

Another category of techniques is based on the so called *dynamic algorithms*, where external helps are used, like body forces or DEM simulations, in order to find better values of densities. One possibility is start with the domain expanded, and progressively the walls are moving to the original positions. The particles are compressed to reduce any gaps produced by the initial random positions pushing the boundaries toward the particles in one or several directions. Normally, the same DEM code is used in order to obtain a good final packing of rigid particles with predefined radius. Other approach involves using a hopper on the top of the domain to mix different sizes of particles together. The particles are positioned in the top of the hopper, and the domain is filled using gravity forces. Some examples of this can be found in [50] and [49]. These techniques can result in dense distributions, with significantly high computational costs.

Other schemes, that do not require the use of a DEM simulation, like the one proposed by Han et al. [57], use an iterative compression algorithm for the density modifications.

The use of this set of techniques requires an initial generation, and some of the low porosity *constructive algorithms* are typically used.

3.1.3 Collective rearrangement techniques

In these methods the domain is filled by a defined number of particles. The particles are placed randomly into the domain and overlaps are allowed. These overlaps are attempted to be reduced during the process by moving the particles in a stepwise manner. Similarly to the *dynamic algorithms*, the displacements of the particles are calculated from the overlaps with the neighbour particles, but using in this case just geometrical or mathematical tools. Without taken into account any kind of physical consideration, as friction [78]. These methods allow predefine both, radius distribution and the desired porosity, and are faster than dynamic algorithms but slower than constructive algorithm [11].

In the present chapter an alternative collective rearrangement algorithm is proposed for the generation of high density packages of particle. As an alternative to obtain a dense package, the algorithm allow the modification of positions and radius. Initially it uses a fast constructive algorithm for an initial generation, like some of the ones presented previously, and densify the package by an optimization algorithm. In particular, a finite element mesh based scheme is used, similar to the *Stenien Model* [105].

3.2 The proposed algorithm

The main idea of the method is to *improve* a given particle assembly in order to obtain a lower porosity configuration.

Given an initial particle distribution, a high porosity exists when the neighbouring particles are not in contact (see Figure 3.1). The reduction of porosity can be written as a non-linear minimum least square problem where the function to be minimized is given by the distance between neighbouring particles in the original configuration. This allows the inclusion of boundary constraints to ensure a good reproduction of the boundaries, a feature which constitutes a major advantage in all the cases where the friction between surfaces is important. Some examples of these conditions are shown by Huang [62] and Zárate *et al.* [94].

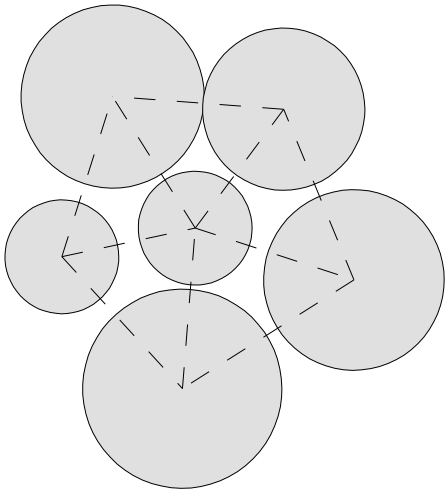

Figure 3.1. Local neighbourhood of a particle in the interior of the domain.

3.2.1 Internal contacts

A low density initial assembly is assumed in order to define the existence of neighbouring particles without contact. The low density is produced by the void areas where the contacts are not achieved. A modified distance function is defined between all neighbouring particles, where the existence of the contact pair is introduced by a triangulation. In a local neighbourhood for one particle, like the one shown in Figure 3.1, a distance function d_c between the connected particles i and j can be defined as

$$d_c = \|\mathbf{x}_i - \mathbf{x}_j\|^2 - (r_i + r_j)^2 \tag{3.1}$$

where $\mathbf{x}_i$ is the coordinate center of the particles i, and r_i its radius. The square of the values is used for the sake of simplicity, because a derivative function is required and the minimum of this modified distance is equivalent to the standard function.

For the particle i, the sum of the distance to its n_c^i neighbours is defined as

$$d_c^i = \sum_{j=1}^{n_c^i} \left(\|\mathbf{x}_i - \mathbf{x}_j\|^2 - (r_i + r_j)^2 \right) \tag{3.2}$$

In order to find the minimum of void areas or interstitial spaces, the function d_c needs to be minimized for all the particles in the assembly. For that purpose, a global distance function is defined using a minimum least square scheme, where the global distance function is written as

$$\min \psi = \sum_{c=1}^{N_c} d_c^2 = \mathbf{D}^T \mathbf{D} \tag{3.3}$$

The connectivities are achieved by the edges of the triangulation over the initial assembly. The square of d_c is used because the minimum of any contact pair is required, and the use of a linear system may cause some negative values in the radii of the particles. This solution does not consider contact constraints; then overlapping between particles is allowed. The treatment of this defect will be presented in the next section.

The solution of a small example is shown in Figure 3.2, where the modification of the radii and the center of the particles can be seen.

To solve the minimization problems, a Levemberg-Marquardt scheme is used [74, 80], where the final size and radius of the particles is achieved by the progressive modification of their values. The iterative scheme is

$$\mathbf{X}_{k+1} = \mathbf{X}_k + \mathbf{h}_k \tag{3.4}$$

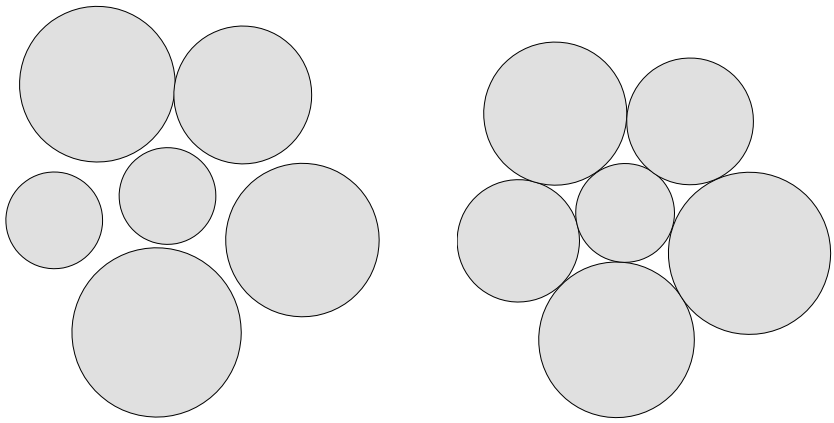

(a) Initial configuration (b) Final configuration

Figure 3.2. Minimization of the distance in a small assembly of cylindrical particles.

where $\mathbf{X}_k$ is the vector of degrees of freedom in the iteration k, for a particles package of length n.

$$\begin{array}{ll} \mathbf{X}_k = [x_1, y_1, r_1, ..., x_n, y_n, r_n]^T & \text{cylindrical particles, 2D} \\ \mathbf{X}_k = [x_1, y_1, z_1, r_1, ..., x_n, y_n, z_n, r_n]^T & \text{spherical particles, 3D} \end{array} \tag{3.5}$$

The increment vector $\mathbf{h}_k$ is calculated by

$$\left[\mathbf{J}^T\mathbf{J} + \mu\mathbf{I}\right] \mathbf{h}_k = -\mathbf{B} \tag{3.6}$$

where $\mathbf{J}$ is the Jacobian of Ψ ($\mathbf{J} = \nabla\Psi$), $\mathbf{B}$ is defined by $\mathbf{B} = \mathbf{J}^T\Psi(\mathbf{X}_k)$ and μ is a damping parameter.

Eq. (3.6) can be now solved for an initial assembly, where the final compaction degree allows a very low porosity level. The convergence rate of the scheme depends on the initial configuration. A good result is however obtained in few iterations.

3.2.2 Treatment of boundaries

One of the problems in the generation of the cylindrical or spherical package is the complexity of the geometry. The definition of the boundary is not good for most constructive algorithms. A good definition of the boundary is useful for the simulation of some geomechanics processes where the friction between surfaces is important. An example of this is shown in [94]. The triangulation based algorithm allows the generation over complex geometries, but not always a good boundary definition is obtained.

A boundary constraint is proposed with the same argument as in the previous section. A function of the distance between the contour of the geometry and the external particles is used in order to obtain a homogeneous boundary in the assembly. Figure 3.3(a) shows an external zone of the domain, where the distance function b_s for particle i and the surface k is defined as

$$b_s = \|\mathbf{l}_{ik}\|^2 - r_i^2 \tag{3.7}$$

where $\mathbf{l}_{ik}$ is the vector joining the center of particle i with the closest boundary point.

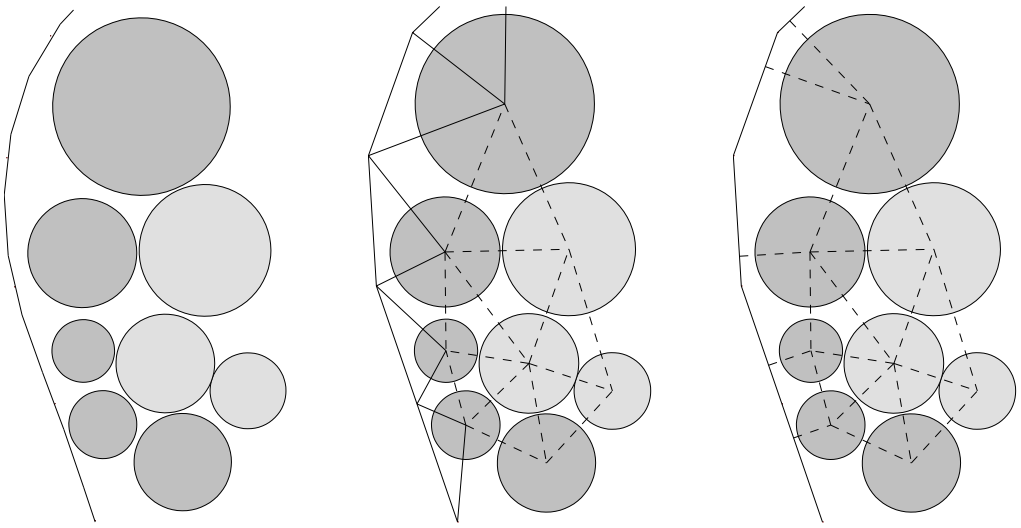

(a) Initial configuration (b) Support mesh (c) Boundary treatment

Figure 3.3. Boundary treatment in the exterior zone of the domain.

We will assume in the following that the algorithm is finite element mesh based. Hence only the inner nodes of the mesh are particles, while the outer nodes define the boundary mesh. With that consideration, it is possible to find a simple way to calculate $\|\mathbf{l}_{ik}\|$, where its value is defined as the projection of the vector defined by the center of particle $\mathbf{x}_i$ and some of the outer nodes $\mathbf{w}_k$ along the normal of that boundary element $\mathbf{n}_k$. This is shown in Figures 3.3(b) and 3.3(c).

The boundary condition (3.7) is rewritten as

$$b_s = \left([\mathbf{w}_k - \mathbf{x}_i] \cdot \mathbf{n}_k\right)^2 - r_i^2 \tag{3.8}$$

This allows for each element of the boundary mesh to have a single particle associated to it. Note that in complex zones of the geometry, as acute edges, one particle can have two or more boundary contacts. With the introduction of this new condition, a modified

version of Eq.(3.3) is written. Now, the minimization function is defined as

$$\min \psi \;=\; \sum_{c=1}^{N_c} d_c^2 + \sum_{s=1}^{N_s} b_s^2 \;=\; \mathbf{D'}^T\mathbf{D'} \tag{3.9}$$

where N_s is the number of particles connected to the surface, and **D'** is the new equation system with the boundary functions.

$$\mathbf{D}' = \left\{ \begin{array}{c} \mathbf{D} \\ \mathbf{B} \end{array} \right\} \tag{3.10}$$

The resolution of this new minimization problems for a set of particles solved the density problem and yields a good boundary definition for the final configuration of the assembly. Figure 3.4 shown a sample of dense packing with and without the boundary treatment, while in Figure 3.5 a 3D sample is depicted.

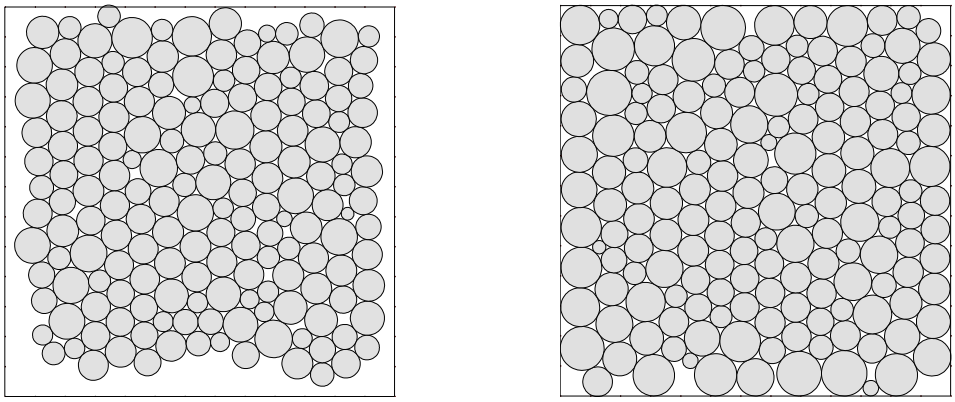

(a) (b)

Figure 3.4. Dense assembly of discs with and without the boundary treatment for a square domain. a) Generation without boundary treatment. b) Generation with boundary treatment.

One of the advantages of this boundary treatment is that no additional memory is required, because the new term in Eq. (3.6) is included in the diagonal blocks of the global matrix, which are always non-zeros. However, some additional iteration steps are required.

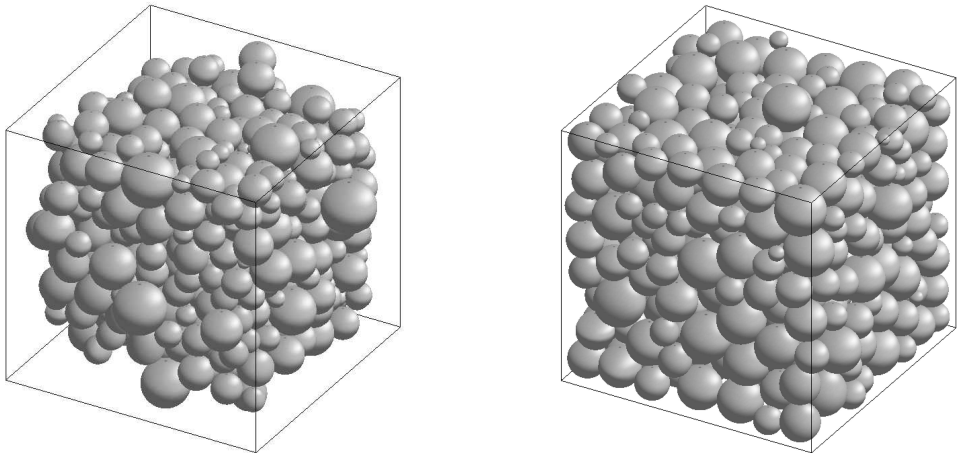

(a) (b)

Figure 3.5. Dense assembly of spheres with and without boundary treatment in cubic domain. a) Generation without boundary treatment. b) Generation with boundary treatment.

3.2.3 Treatment of particle overlapping

Particle overlapping can arise due to the definition of the distance function adopted. This function is defined so that the total distance between particle pairs is minimum. When the distance between certain pair is large, the minimization process would decrease the value of the global distance function by assigning negative distances to neighbouring particles, in order to compensate for positive values, as shown in Figure 3.6(a).

The standard method to avoid this behaviour is to add contact constraints in the minimization problem. However, this method has two drawbacks, the first being its computational cost, and the second that it does not avoid the appearance of overlapping between particles for which contact was not defined in the initial configuration. This phenomenon is depicted in Figure 3.6(b).

The solution for this problem, is to update the contact list and to solve a new distance minimization problem.

The algorithm that updates the contact list can be used to delete those contacts for which the distance is larger than a certain tolerance, which avoids the first type of contact overlapping. Also the same algorithm finds the new contact pairs, corresponding to the second type of overlapping described above (Figure 3.6(b)), which appear in the final configuration after the update process.

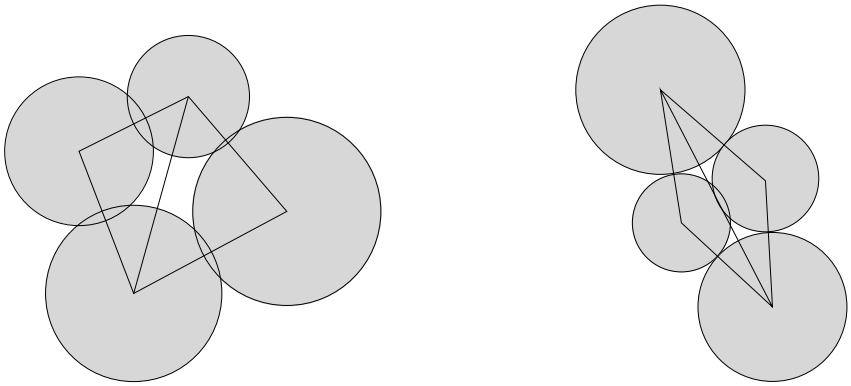

(a) (b)

Figure 3.6. Overlapping over spheres without contact pair definition.

Different techniques for updating the contact list can be used. In this work two different approaches have been adopted. The first one is to use of an spatial search algorithm, which requires setting a tolerance for the detecting the contact. The second one consists in the regeneration of the FEM mesh using *weighted Delaunay triangulation* [50, 51], which considers the dynamic movement of the mesh.

Considering the triangular mesh of the Figure 3.7, the swapping of the edge $\bar{AC}$ is evaluated considering the weighted Delaunay criteria, which consider the radius of the particles.

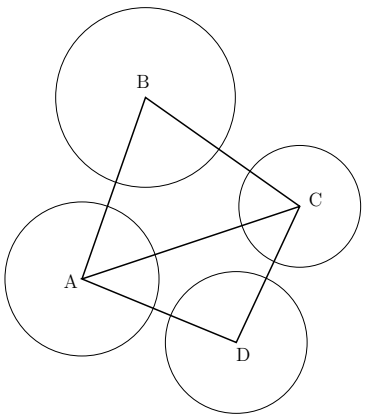

Figure 3.7. Scheme of element to verify the swapping.

The swapping criteria for the edge $\bar{AC}$ can be written as

$$\text{SwapElement}(A,B,C,D) = \quad sign \begin{vmatrix} A_x & A_y & (A_x^2+A_y^2)-A_r^2 & 1 \\ B_x & B_y & (B_x^2+B_y^2)-B_r^2 & 1 \\ C_x & C_y & (C_x^2+C_y^2)-C_r^2 & 1 \\ D_x & D_y & (D_x^2+D_y^2)-D_r^2 & 1 \end{vmatrix} \tag{3.11}$$

These modifications require the solution of the distance minimization problem after each update of the connectivities. However, in most cases an acceptable solution is reached after very few steps.

3.2.4 Initial generation of the media

For the generation of the initial configuration, it is possible to use any algorithm proposed in the literature. However finite element mesh based techniques offer better conditions for the algorithm proposed in this work. This is because many well established algorithms already exist and the generation of complex geometries is achieved easily. A modification of the *Stienen model* is used in our work, where the particles are located in the inner vertex of the mesh and the radii are calculated with a random number over the mean distance between the neighbouring nodes. In addition, the average radius is related to the element size used in the generation of the mesh.

One of the necessary considerations for the initial mesh is the structuration of the elements. A regular elements distribution produces a regular number of contacts for the different particles and a homogeneous package of particles is found. In the simulation of geomechanical processes that deal with particle cohesion, a structured lattice of particles can be problematic because small forces can lead to material fracture. In order to solve this problem, an initial preprocessing is performed over the mesh, where random local displacements over the node position are used to generate a random configuration. After this perturbation, a new triangulation is used for defining the contact pairs. An example of the initial mesh and its modification are shown in Figures 3.8 and 3.9.

In order to define the size of the particles, the average distance between nodes is calculated and a random number generator modifies these values with a user defined range. Overlapping is allowed, because the optimization of the distance between particles eliminates these defects.

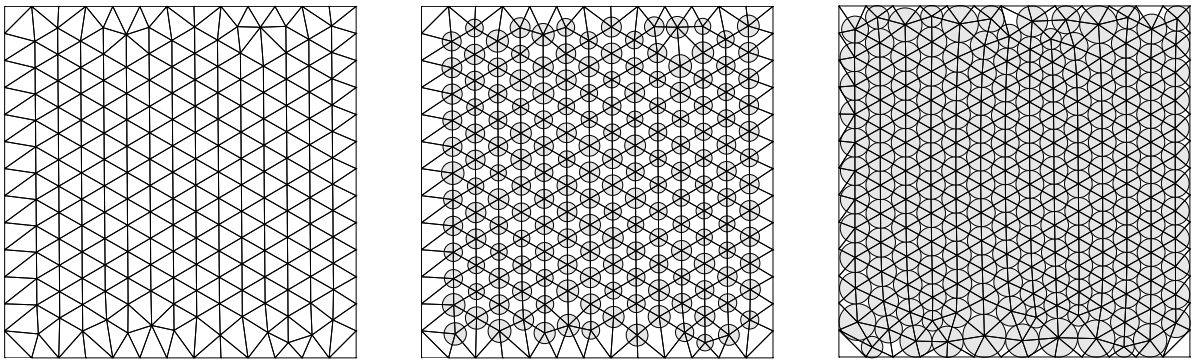

(a) Structured mesh (b) Initial configuration (c) Final configuration

Figure 3.8. Generation with structured mesh for the initial configuration.

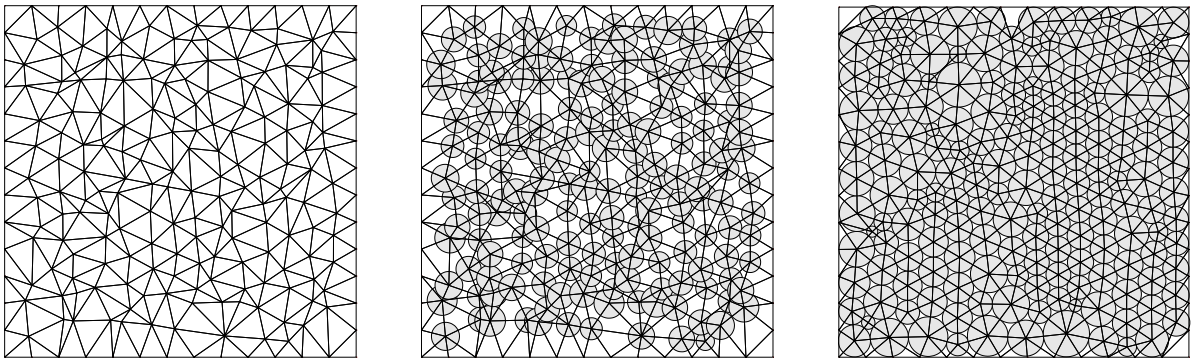

(a) Non-structured mesh (b) Initial configuration (c) Final configuration

Figure 3.9. Generation with non-structured mesh for the initial configuration.

3.3 Characterization of the generated package

In order to compare different packing algorithms, it is necessary to use some parameters which indicate the quality of the generated media. In the literature, several parameters can be found in order to analyse the quality of the results.

In dense particle assemblies, parameters like *average radius*, *void ratio* or *coordination number* are used. Other useful parameters exist, but none of them were used for the following comparisons. An introduction to some of these parameters can be found in [17, 79].

3.3.1 Average radius

Different possibilities can be used to the estimation of the average radius. In order to obtain a more representative value for the average radius, a volume-based average radius

is considered.

$$\bar{r} = \sqrt[d]{\bar{r^d}} = \sqrt[d]{\frac{\sum_{i=1}^{N_p} r_i^d}{N_p}} \tag{3.12}$$

where d is the dimension (d=2 in 2D, and d=3 in 3D). The volume-based value is considered because have a most direct relationship with the analysis of the porosity in the generated package.

3.3.2 Porosity

The porosity indicates the relationship between the volume achieved by the generation process V_p and the real volume of the geometry V_{real}. This value can be represented in different forms. The most used form is the porosity (e) written as

$$e \;=\; 1 - \frac{V_p}{V_{real}} \tag{3.13}$$

An alternative form founded in the literature is the called *void ratio* (ν), which is written as

$$\nu \;=\; \frac{V_{real}}{V_p} - 1 \;=\; \frac{e}{1-e} \tag{3.14}$$

Both cases are equivalents, and allows to determine the relative density of the packaging. Using the previous definition of the volume-based average radius, the porosity can be estimated in a average form.

$$e \;=\; 1 - \frac{N_p \bar{V}_p}{V_{real}} \tag{3.15}$$

In the same way, it is defined the *particles density* as

$$\rho_p = 1 - e = \frac{\sum_{i=1}^{N_p} V_p^i}{V_{real}} \tag{3.16}$$

This value will be use in the next chapter in the parameter estimation procesure.

3.3.3 Coordination number

The coordination number is an alternative parameter to the contact density, and is directly related to the structural stability of the assembly concerned. The apparent coordination number n_c is defined as the average number of contacts per particle and expressed as

$$n_c = \frac{2N_c}{N_p} \tag{3.17}$$

with N_c being the total number of contacts between the N_p particles of the generated packaging.

3.3.4 Fabric tensor

The Fabric tensor describes the local configuration of the grains as a second order tensor, reflecting the level of the isotropy of the assembly. This tensor it is written for a particle i as

$$\boldsymbol{\phi}_i = \sum_{c=1}^{n_c^i} \mathbf{n}^c \otimes \mathbf{n}^c \tag{3.18}$$

where $\mathbf{n}^c$ is the unit normal vector at contact c of the particle i. For the full particle assembly, the structural anisotropy can be characterized by the fabric tensor, defined by all the distribution of contact normals in the domain [102]

$$\boldsymbol{\phi} = \sum_{c=1}^{N_c} \mathbf{n}^c \otimes \mathbf{n}^c \tag{3.19}$$

The fabric tensor is a symmetrical second order tensor, which has three principal values (3D) as a stress tensor or strain tensor does. These values have an interesting properties related with its trace:

$$tr(\boldsymbol{\phi}) = N_c \tag{3.20}$$

This means that the principal values of fabric are not independent of each others. So, re-writting the fabric tensor as

$$\boldsymbol{\phi}' = \frac{1}{N_c} \sum_{c=1}^{N_c} \mathbf{n}^c \otimes \mathbf{n}^c \tag{3.21}$$

For isotropic structures of particles, all the principal values are equals

$$\phi'_1 = \phi'_2 = \frac{1}{2} \qquad \text{2D} \tag{3.22}$$

$$\phi'_1 = \phi'_2 = \phi'_3 = \frac{1}{3} \qquad \text{3D} \tag{3.23}$$

Using these properties, it is possible to obtain a measurement of the degree of

anisotropy in the system. A fourth-order fabric tensor can also be defined, and more information can be obtained, as shown Ghang and Gao in [26].

3.4 Analysis of the packing algorithm

A set of results is obtained by considering different sizes of particles in a square domain in 2D and in a cubic domain in 3D (similar to the examples shown in Figures 3.4 and 3.5).

The typical distribution of radii in 2D is shown in Figure 3.10, where a square sample with 30000 discs is used. A multimodal Gaussian distribution can be observed in most of the cases.

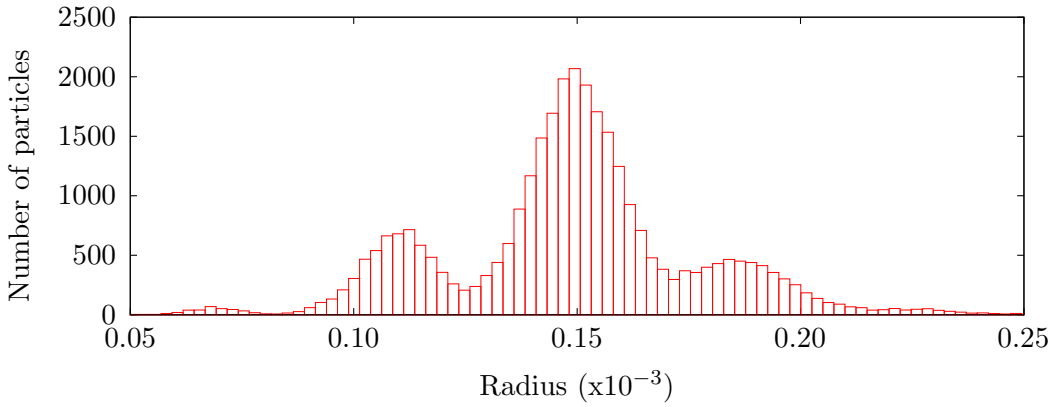

Figure 3.10. Radius distribution of assembly with 30.000 discs.

In order con analyse the anisotropy of the system, the polar distribution of contact directions is presented in Figure 3.11, using two samples with different particle sizes.

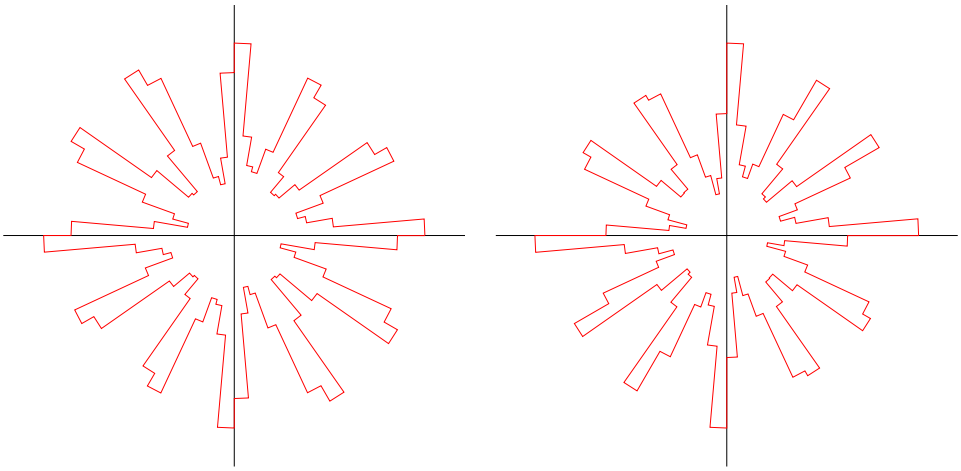

(a) 10000 discs (b) 30000 discs

Figure 3.11. Polar distribution of contacts with 10.000 and 30.000 discs.

The distribution shows the isotropy of the system, where in the most cases the

principal values of the fabric tensor are 0.5, with errors around $2\% - 4\%$.

The values of the coordination number and porosity for different number of 2D particles is shown in Figure 3.12. Note the fast decrease of the porosity as the number of particles increases.

A high dense assembly is obtained, where the porosity is around 10%, and slower when the number of particles increases, as shown in Figure 3.12. In the same figure, the evolution of the coordination number with the number of particles shows a value around 6, which is high in comparison with other packing algorithms.

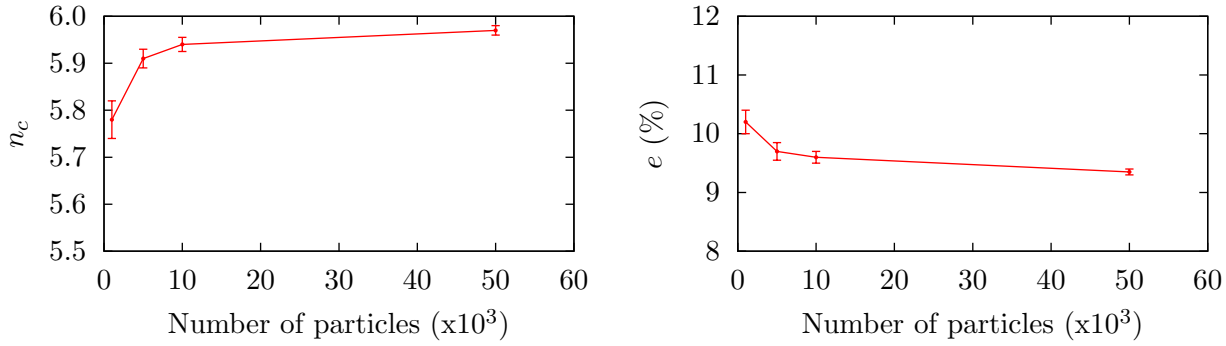

Figure 3.12. Coordination number and porosity for different number of cylindrical particles.

For a structured mesh, the mean number of neighbours is 6. The initial random displacement in the mesh modifies that number, but a similar number of neighbours is achieved. This produces a high coordination number while the minimization of the distance between neighbour particles decreases the porosity values.

Figure 3.13 shows the evolution of the average distance function for two different two-dimensional samples. The distance function is averaged over all the contact pairs, and normalized with the average radius.

The distance function decrease initially with a hight rate. In the successive iteration the distance function decrease slowly. As the same way, the coordination number increase faster in the initial steps. After that, its value is stabilized close to the final one, as shown Figure 3.14.

The above dimensionless parameters are used in order to determine the quality of the generation. Comparisons with the results obtained by Bagi [8] are also made. The values reported for the PFC2D code can be found in the same paper. Table 3.1 shows

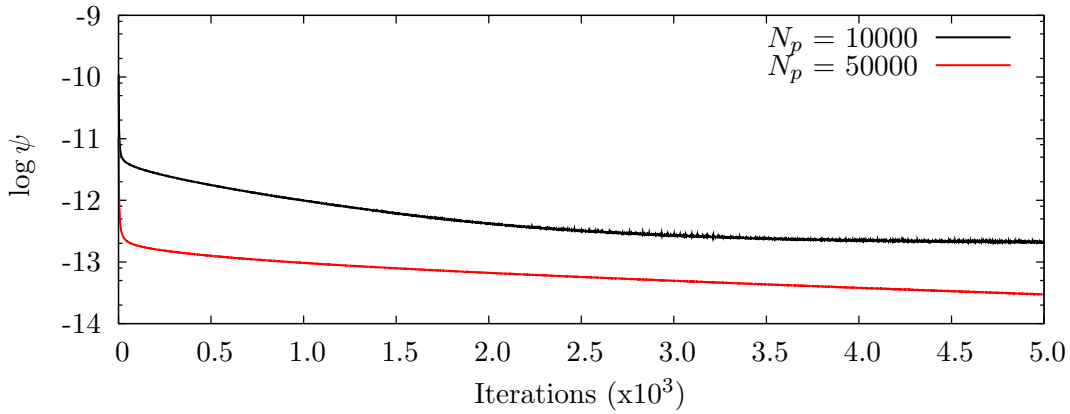

Figure 3.13. Evolution of average distance function in two square samples with different particle size (2D).

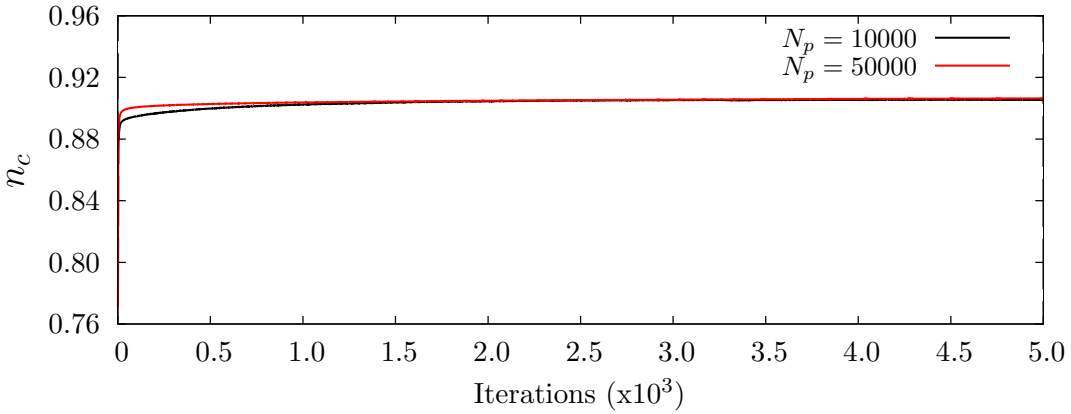

Figure 3.14. Evolution of coordination number in two square samples with different particle size (2D).

that the proposed algorithm achieves an interesting result. The porosity is significantly lower than for the other algorithms, while the coordination number is higher than both algorithms. The comparison of time should be treated carefully. Bagi mentions that the implementation of the algorithm can be optimized, and should be noted that in the case of in present algorithm just 1000 steps are used, allowing small overlapping.

In [49], Feng et al, reports 1 000 000 disks in 3.77 seconds with the *open form advancing front algorithm*, but the porosity should be higher than the presented by Bagi, because the gap founded in the top of the geometry. Another significant issue is the extension of the advancing front algorithm to 3D, which is not reported.

Algorithm	N_p	$\bar{r}$	e (%)	n_c	time
PFC^{2D}	–	0.259	13.1	4.34	64 hours
Bagi[8]	56213	0.221	14.2	3.98	388 seconds
Present algorithm	56084	0.223	9.03	5.97	118 seconds

Table 3.1. Comparison of cylindrical particles generation.

For 3D generation, the coordination number and porosity for different numbers of particles are shown in Figure 3.15 for the present algorithm. The decrease of the porosity for a high number of particles can be observed. A good number of neighbours is achieved in a similar way as for the 2D case.

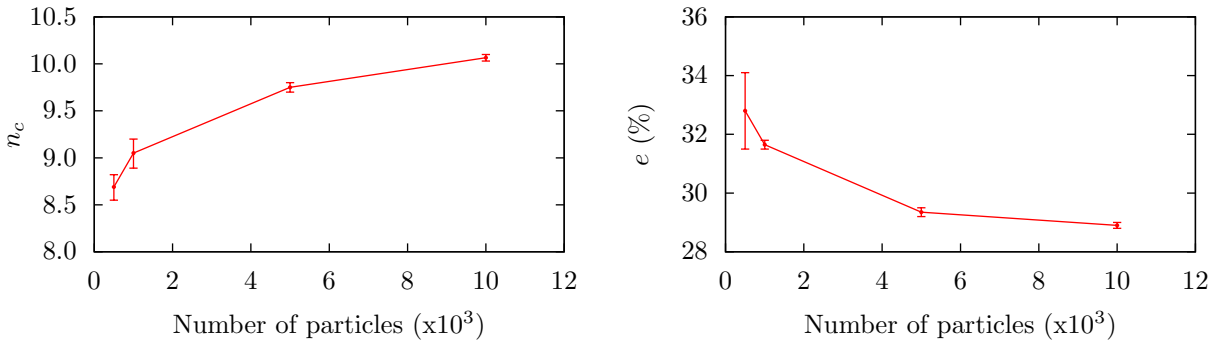

Figure 3.15. Coordination number and porosity for different number of spherical particles.

The radii distribution for an example with 50000 spheres is shown in Figure 3.16, where a mono-modal Gauss distribution is observed.

The good level of isotropy is observed, where the distribution of contacts in smooth in comparison with the two-dimensional case. In Figure 3.17, the polar distribution of the contact directions is shown in different planes.

Finally, the discretization of a cylinder of unitary length and diameter is presented in Table 3.2. The results are compared with the one obtained by the advancing front algorithm reported by Löhner and Oñate in [77]. Considering an equivalent number of particles, the present algorithm results in higher average radius and a lower porosity. Both discretizations shown a good level of isotropy.

An interesting characteristic of the present algorithm is the possibility of refinement

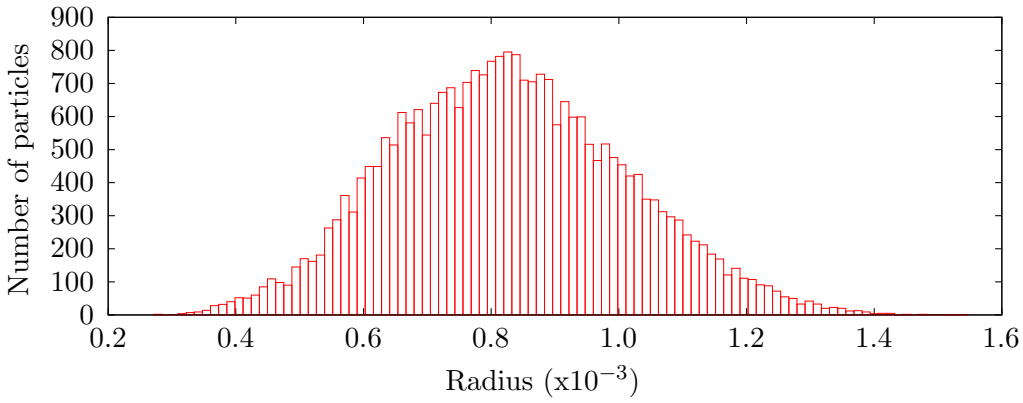

Figure 3.16. Radius distribution in 3D sample with 27.500 spheres.

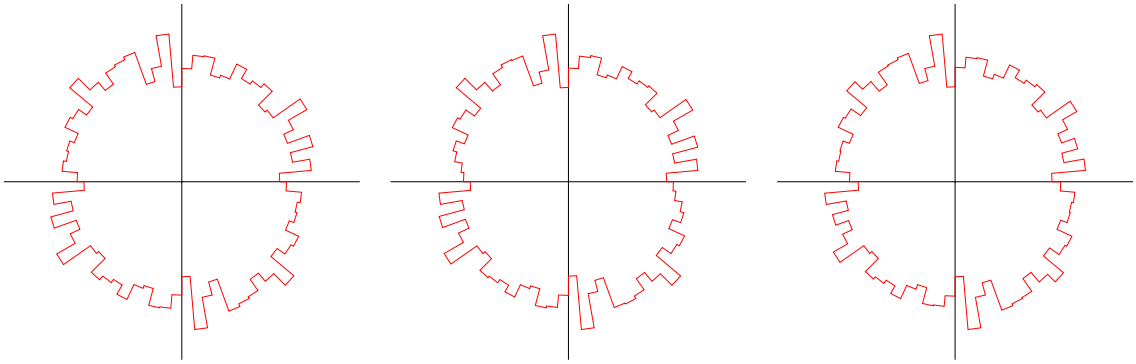

(a) Plane X-Y (b) Plane X-Z (c) Plane Y-Z

Figure 3.17. Polar distribution of contacts in 3D sample with 27.500 spheres.

Algorithm	N_p	$\bar{r}$	r_{max}/r_{min}	e (%)	n_c	Fabric
Lohner et al.[77]	30198	0.01520	3.5631	43.395	4.003	{0.33275,0.33285,0.33440}
Present algorithm	30130	0.01623	9.0526	31.297	8.236	{0.33317,0.33327,0.33356}

Table 3.2. Comparison of spherical particles generation.

in the generation. With an initial generation based in a FEM mesh, the refinement of this mesh can be exploited in the DEM assembly.

This characteristic results useful when a DEM contact model with local scaled parameters is used, as the model developed by Cundall and Strack [33, 64] or the Hertz-Mindlin model [38, 65].

This refinement is particularly useful to decrease the computational cost, using small

particles just in a certain the region of interest, where can be interaction fracture or interaction with other objects, as plates or cutter tools [106]. Other interesting application is the discretization of mechanical devices which interact with granular material, as presented in [94], where a special DEM model is used in excavation tool for the analysis of wear. Wear produces a change of shape in the tool via the elimination of particles with a defined accumulated wear.

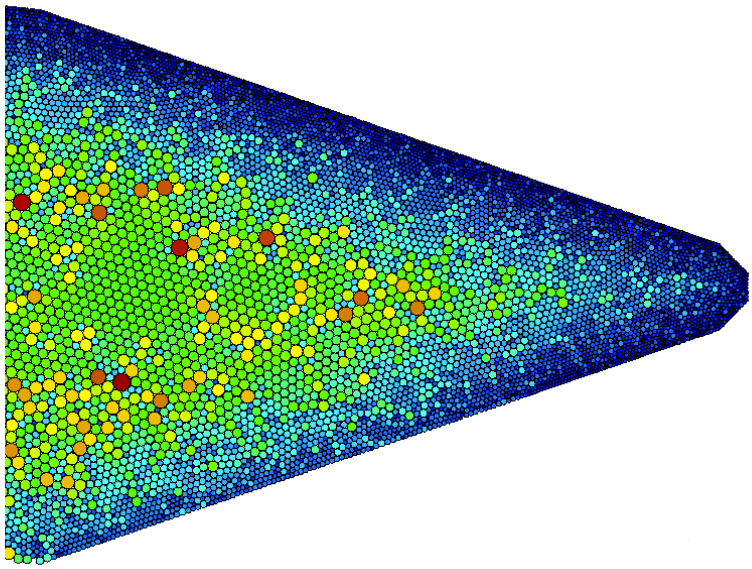

Figure 3.18. Tooth of excavation machine discretized with disks and refinement in the external surface.

A sample of the refinement with a dense particle assembly is presented in Figure 3.18, where a triangular domain representing the pick of a rock cutter tool. The domain, discretized with 10000 particles, presents the refinement in the right corner. The same domain discretized with a standard distribution of particles, considering the minimum radius in the assembly, take over 6 times more particles.

Chapter 4

Estimation of the discrete element parameters

The most challenging step in the use of the DEM for the simulation of solid materials is the estimation of model parameters. Since the DEM represents the behaviour of a collection of particles, the constitutive relations thats describe their behaviour can be obtained from the granular materials theory. Usually these constitutive relations are developed from the continuum-mechanical viewpoint and do not recognize the discrete nature of granular materials. The resulting relations are frequently phenomenological in nature.

In the literature, two possible lines in the analysis of these parameters are found. The first approach is related to micromechanical analysis, in which the granular material is modelled as an assembly of particles that interact at contacts, analyzing the constitutive relations in a *micromechanics-based* approach, and considering an averaging procedure over the particles assembly. An objective of this approach is to derive macroscopic relationships from the microscopic characteristics, such as contact constitutive relations and the characterization of the particle assembly. The second approach is based in statistical studies of virtual specimen, considering dimensionless numbers relating the contact model parameters (*micro-parameters*) with the mechanical properties (*macro-properties*) of the simulated material.

In the present chapter an analysis of the different approaches is performed and developed a methodology for the estimation of the DEM parameters based in the elastic perfectly brittle contact model is developed.

4.1 Micro-macro relationship

The relationship between local parameters and mechanical properties can be defined using different quantities that describes the local configuration of the granular assembly. In order to obtain the macroscopic behaviour, it is necessary the use of this quantities that permit the mechanical analysis of the system considering the behaviour at the micromechanical level and the characterization of the particle assembly, as shown in Figure 4.1.

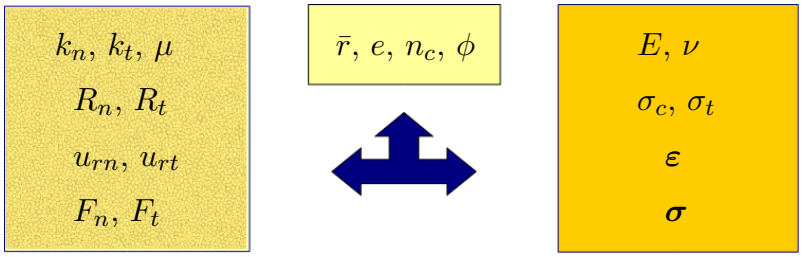

Figure 4.1. Scheme of the micro-macro relationship.

Many authors investigated the effective Young modulus and Poisson ratio for specific contact models. In [16], Brandt considered the Hertz-Mindlin contact law with a random packing of spherical particles of different radii. He demonstrated that the effective bulk modulus of an elastically isotropic, homogeneous porous rock is related to the confining pressure, porosity and liquid saturation. Digby [39] calculated the effective bulk and shear moduli of a porous granular rock modeled by a random packing of identical spherical particles with the Hertz-Mindlin contact law. The results showed that the elastic moduli depend on the contact stiffness between particles, the coordination number, particle radius, and contact radius.

Different authors, as Walton [109], Bathurst and Rothenburg [13], Chang and Misra [23, 24]) showed that the stress-strain relationship can be derived based on a microstructural continuum approach for random packing. In [24], Chang and Misra demonstrated that the elasticity tensor relating the stress and strain could take various forms depending on the symmetry of the mechanical properties of the granular material, which is closely related with the packing structure. The study analyzes the relationship between the symmetry of mechanical properties and the packing structure for random granular packing using a micromechanics-based approach. The packing structure was characterized by the distribution density functions that were represented by spherical harmonics expansion. For random packing of equal spheres with a linear contact law, the Young modulus and Poisson ratio were derived.

Most of the theoretical analysis found in the literature shows that the parameters related to the effective Young modulus and Poisson's ratio are the contact stiffness (k_n, k_t), the ratio of normal and tangential contact stiffness (k_t/k_n), particle size $(\bar{r})$, porosity (e), coordination number (c) and particle size distribution.

The strength properties do not appear to have been studied intensively. Most works do not consider cohesion, internal friction angle, or rotation of the particles. The behavior of bonded particles under biaxial compression was studied by Donzé et al. [40] for a hexagonal packing, Potyondy et al. [89] for an irregular packing using PFC^{2D} [64] or Hentz et al.[58, 59] for irregular packing, considering nonlinear deformation and damage.

The objective here is to establish scaling laws that relate the phenomenological parameters of a material at the macro-scale (e.g., the elastic modulus, the compressive strength) to the micro-scale parameters (e.g., the parameters that characterize the contact between particles), and to establish the dependence of the macro-scale response (e.g., how the material fails in tension) upon the micro-scale factors.

4.2 Micromechanical analysis

The micromechanics of granular materials deals with the study of relations between microscopic quantities and macroscopic quantities. A mayor objective of micromechanics is to formulate micromechanical constitutive relations. For assembly of rigid or semi-rigid particles, the microscopic level is that of contacts. The relevant microscopic static quantities are contact force and contact couple, and the associated kinematic quantities are relative displacement and relative rotation at contacts (see Figure 4.2).

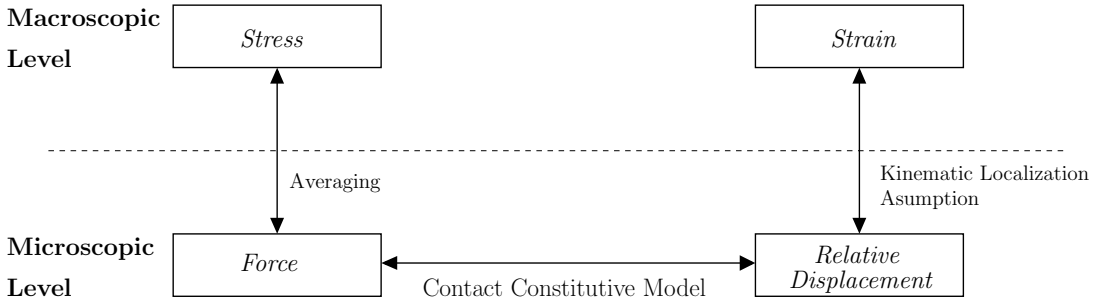

Figure 4.2. Relationships between micro and macro levels.

In the micromechanical analysis expressions for macroscopic tensor, like stress and strain tensor, are required in terms of contact quantities.

In this section the micromechanical analysis is considered to derivate relationships between the contact model parameters and the mechanical properties of the material, considering averaging procedures and kinematic localization assumptions.

4.2.1 Inter-particle contact law

Considering the contact c between particles p and q, a general expression for the constitutive relations (2.9) between the inter-particle force f_i^c and the relative displacement δ_j can be given by

$$f_i^c = K_{ij}^c \delta_j^c \tag{4.1}$$

where K_{ij}^c is the inter-particle contact stiffness tensor, and δ_j^c defined for a general case as

$$\delta_j^c = (u_j^p + e_{jkl}\,\theta_k^p\,r_l^{pc}) - (u_j^q + e_{jkl}\,\theta_k^q\,r_l^{qc}) \tag{4.2}$$

where θ_k is the rotation of the particle, r_l the vector which join the center with the contact point, and e_{jkl} the permutation tensor.

The rotation of the particles (θ_k^p and θ_k^q) in cohesive materials are considered negligible and are not included on the present formulation. This means that the relative displacement between particles is based in the particle displacements only, and (4.2) can be re-written as

$$\delta_j^c = u_j^p - u_j^q \tag{4.3}$$

The stiffness tensor K_{ij}^c can be expressed in terms of the inter-particle contact stiffness in the normal and tangential directions as

$$K_{ij}^c = k_n n_i n_j + k_t(s_i s_j + t_i t_j) \tag{4.4}$$

where the unit vector n_i is the contact normal direction. Vectors s_i and t_i are unit vectors defining the plane normal to the vector n_i, as shown in Figure 4.3.

4.2.2 Average stress and average strain tensors

The average stress tensor is introduced in order to analyze the field of inter-particle contacts in the macroscopic level. The definition of the average stress tensor is widely discussed in literature (see [33, 68]). Normally its defined in terms of the force acting in the contact between particles and the geometry of the assembly. The derivation of the micromechanical stress tensor and the averaging procedure are presented in Appendix A.

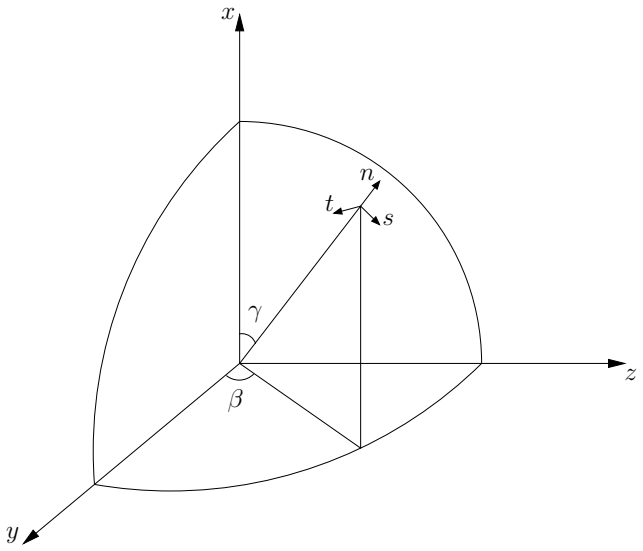

Figure 4.3. Local coordinates at inter-particle contact.

The average stress tensor in a domain defined by the volume V is written as

$$\bar{\sigma}_{ij} = \frac{1}{V} \sum_{c \in V} f_i^c l_j^c \tag{4.5}$$

where l_j^c is the called *branch vector*, which joins the center of the particles in contact $(x_q - x_p)$.

In the case of the strain tensor, different formulations can be found in the literature. As a general formulation, we can be define the average strain tensor as

$$\bar{\varepsilon}_{ij} = \frac{1}{V} \sum_{e} \delta_i^e d_j^e \tag{4.6}$$

where d_i^e is a characteristic vector related to the relative displacement, and complementary to the brach vector. Kruyt and Rodenburg [68, 69] propose a formulation in which d_i^e is the called *polygon vector*. The polygon vector is obtained by counter-clockwise rotation over 90° from the rotated polygon vector g_j^{pq}. The rotated polygon vector is defined as the vector that connects the centres of adjacent polygons. These polygons arise as a way of partitioning the plane network of particle centres and contacts (see Figure 4.4).

Bagi [7] proposes a version based in the Delaunay tessellation of the assembly, considering the center of the particles, where d_i^e is called *complementary area vector*. Both formulations are equivalent, and are similar to alternative versions proposed by Kuhn [70]

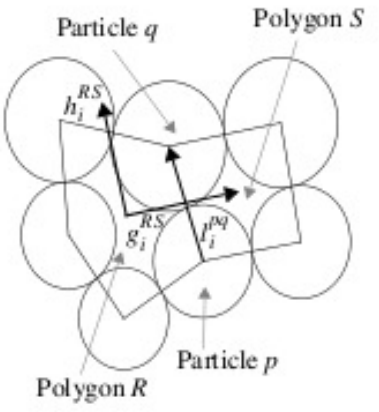

Figure 4.4. Polygon vector and rotated polygon vector defined by Kruyt and Rothenburg [69].

and Cambou et al. [18]. Bagi [9] has been shown that these different approaches based on partitioning domain into polygons are consistent with the macroscopic strain, and most of them are equivalents. Nevertheless, the average strain tensor version of Bagi is considered in this work as it can be extended to the 3D case with a small effort, as shown Durán et al. [41]. The derivation of the average strain tensor of Bagi can be found in Appendix B.

It is interesting to note that both characteristic vectors l_j^c and d_j^c are related. The vectors satisfy the geometrical relation

$$I_{ij} = \frac{1}{V} \sum_{c \in V} l_i^c d_j^c \tag{4.7}$$

where I_{ij} is the Kronecker delta symbol.

4.2.3 Kinematic localization assumption

The kinematic localization assumption is required in order to analyze the relation between the local relative displacement between particles as a function of the strain (Figure 4.2).

Different hypothesis can be found in the literature, based in the continuum elasticity theory. The most relevant are the based in the *uniform strain* and *uniform stress* assumptions.

The uniform strain hypothesis considering the relative displacement becomes

$$\delta_i^{pq} = \varepsilon_{ij} l_j^{pq} \tag{4.8}$$

while the uniform stress hypothesis can be written as

$$f_i^{pq} = \sigma_{ij} d_j^{pq} \tag{4.9}$$

In [69], Kruyt and Rothenburg showed that both hypothesis works as upper and lower bounds for the elastic behaviour of the assembly, depending on the coordination number, as depicted in Figure 4.5. Similar conclusion can be found in [75].

In Figure 4.5, the micro stiffness ratio (k_t/k_n) is represented by λ, Γ is the coordination number, K the bulk modulus, G the shear moduli. $K^{\varepsilon,\sigma}$ and $G^{\varepsilon,\sigma}$ the Bulk modulus and shear moduli by the uniform strain and uniform stress assumptions, respectively.

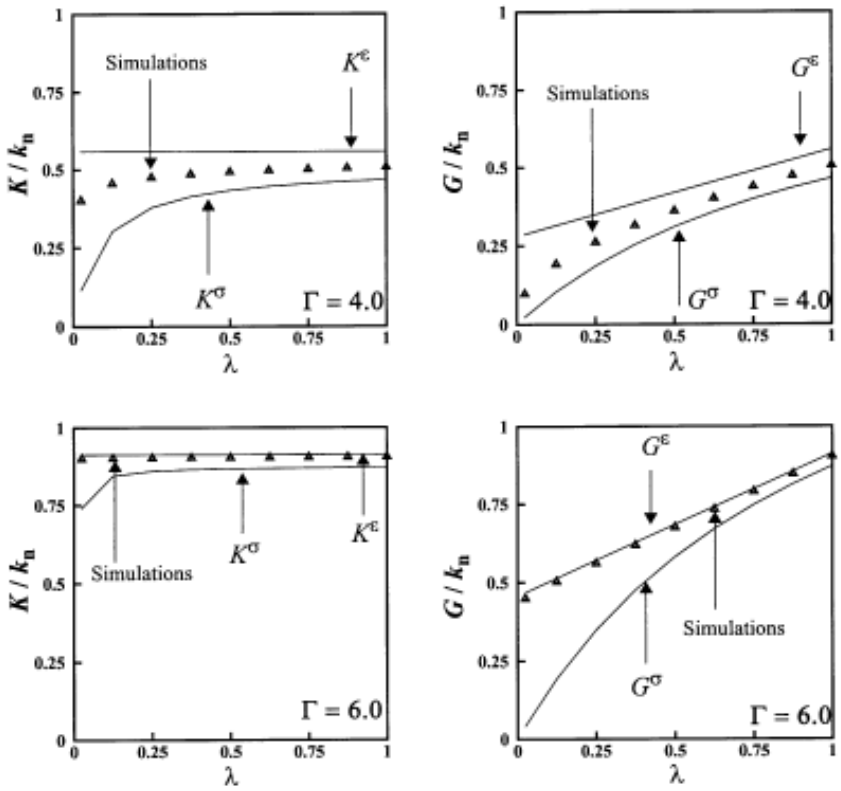

Figure 4.5. Upper and lower bounds for the elastic behaviour presented by Kruyt and Rothenburg in [67].

More complex assumptions are developed based on the Cosserat continuum, where the particle rotations are considered, and different fluctuations in the relative displacement and rotations are evaluated [2, 3, 25].

Considering the properties of the packing algorithm presented in the previous chapter, can be assumed that the elastic behaviour of the assembly is very close to the upper bound, and that the uniform strain assumption is appropriated for the estimation of the micro

parameters.

Taking into account the definition of the average stress tensor in (4.5) and the contact forces in (4.1), the stress tensor can be re-written as

$$\sigma_{ij} = \frac{1}{V}\sum_{c=1}^{Nc} K_{ik}^{c}\delta_{k}^{c}l_{j}^{c} \tag{4.10}$$

and with the assumption of uniform strain

$$\sigma_{ij} = \frac{1}{V}\sum_{c=1}^{Nc} K_{ik}^{c}\varepsilon_{kl}l_{l}^{c}l_{j}^{c} = \frac{1}{V}\varepsilon_{kl}\sum_{c=1}^{Nc} K_{ik}^{c}l_{l}^{c}l_{j}^{c} \tag{4.11}$$

With the matrix form of the constitutive stiffness tensor, based in Hooke's law

$$\sigma_{ij} = C_{ijkl}\,\varepsilon_{kl} \tag{4.12}$$

it is possible to define the constitutive stiffness tensor as

$$C_{ijkl} = \frac{1}{V}\sum_{c=1}^{Nc} l_{i}^{c}K_{jk}^{c}l_{l}^{c} \tag{4.13}$$

Replacing the local stiffness tensor K_{ik} defined in (4.4), the constitutive stiffness tensor is re-written as

$$C_{ijkl} = \frac{1}{V}\sum_{c=1}^{Nc} l_{i}^{c}(k_{n}n_{j}n_{k} + k_{t}(s_{j}s_{k} + t_{j}t_{k}))l_{l}^{c} \tag{4.14}$$

Note that the contact model used on this formulation considers the stiffness as global constants, so the constitutive stiffness tensor can be split into two terms. The first term considers the normal stiffness (C_{ijkl}^{n}), while the second one considers the tangential stiffness (C_{ijkl}^{t})

$$C_{ijkl} = k_{n}C_{ijkl}^{n} + k_{t}C_{ijkl}^{t} \tag{4.15}$$

where

$$C_{ijkl}^{n} = \frac{1}{V}\sum_{c=1}^{N} l_{i}^{c}n_{j}n_{k}l_{l}^{c} \tag{4.16}$$

$$C_{ijkl}^{t} = \frac{1}{V}\sum_{c=1}^{N} l_{i}^{c}(s_{j}s_{k} + t_{j}t_{k})l_{l}^{c} \tag{4.17}$$

Finally, considering the isotropy of the material, the association of the independent components of the constitutive stiffness tensor based in the contact model and the material properties, the relationship between local contact stiffness and the elastic constants of the material can be written as

$$C_{1111} = k_n C^n_{1111} + k_t C^t_{1111} = \frac{E(1-\nu)}{(1+\nu)(1-2\nu)} \tag{4.18}$$

$$C_{1122} = k_n C^n_{1122} + k_t C^t_{1122} = \frac{E\nu}{(1+\nu)(1-2\nu)} \tag{4.19}$$

For a defined assembly the high order fabric tensor can be obtained, and the contact stiffness evaluated.

4.2.4 Numerical analysis

Here, the foregoing equations are validated with two different specimens for a unconfined compression strength test, in both two-dimensional (2D) and three-dimensional (3D) cases. Both specimens with a size of 50x50 mm are simulated assuming the standard of compression test for natural stone [44]. The characterization of the specimens are presented in the Table 4.1.

Parameter	Description	specimen 2D	specimen 3D
N_p	Number of particles	11180	10395
e	Estimated porosity (%)	9.440	23.34
n_c	Coordination number	5.940	9.4871
$\bar{r}$	Average radius (mm)	0.2538	1.1653
$r_{\max}/r_{\min}$	Radius ratio	5.920	5.3674

Table 4.1. Mesh characterization parameters for uniaxial compressive strength test.

For the specimen 2D presented in the previous section, The Young modulus and Poisson's ratio for the specimen 2D obtained through micromechanics and the simulations are presented in Figure 4.6.

The curves shown a perfect agreement between the estimated values and the simulation. This can be explained because the high density of the assembly, as shown Kruyt and Rothenburg [69].

The same is presented in Figure 4.7 for the specimen 3D. Unlike the 2D case, in 3D the agreement between simulations and micromechanics is not completely satisfactory.

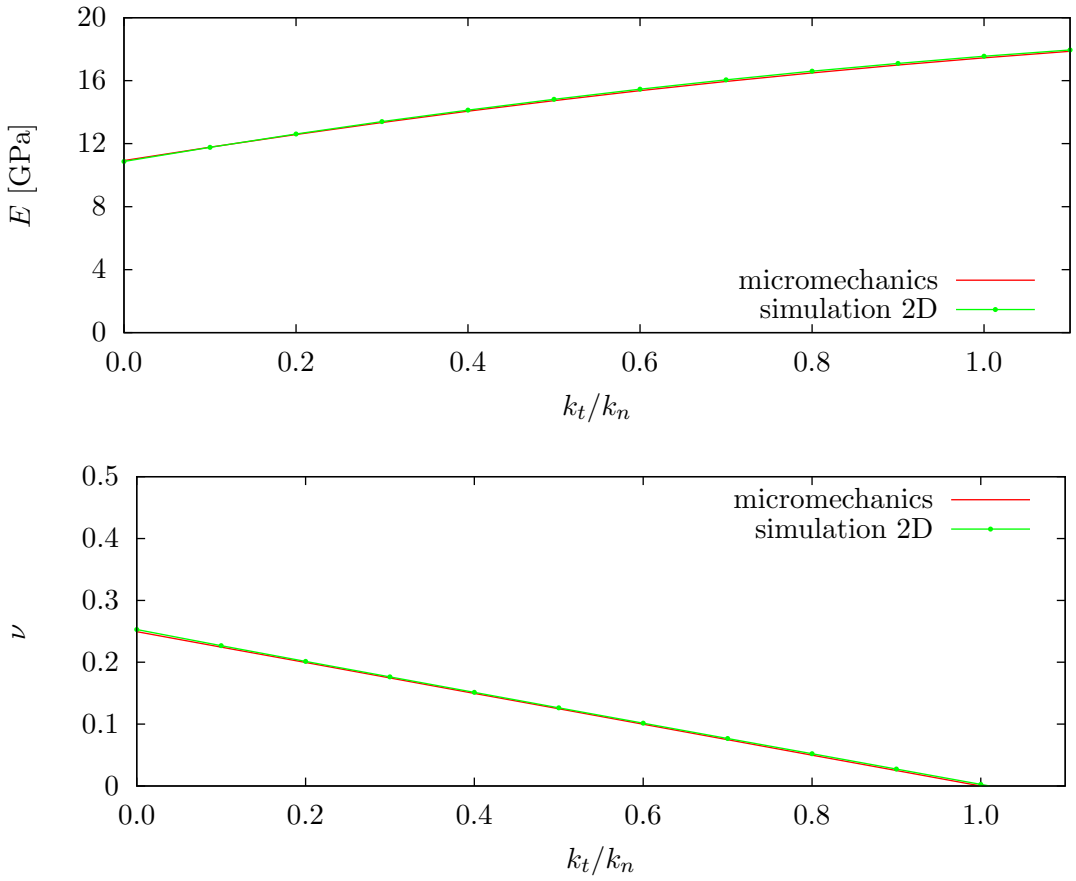

Figure 4.6. Comparison of Young modulus and Poisson's ratio estimated with micromechanics and simulations in specimen 2D.

This can be explained by different reasons. An important difference in the 3D case is the higher porosity compared with the case 2D. As shown in the previous chapter, the porosity and the coordination number are strongly related. According to the analysis of Kruyt and Rothenburg, it may be also possible that the assembly density, and the corresponding coordination number, are not sufficiently higher than required.

Even though the micromechanics results are a good way to estimate the elastic properties of the granular material, in case of cohesive material, it is also required to estimate the contact strength in the contact bonds.

The strength of cohesive granular materials using micromechanics has not been studied extensively. At this moment, it is not possible to extend in a simple way the micromechanics theory to the study the relationships between the material strength and the contact (micro) strengths.

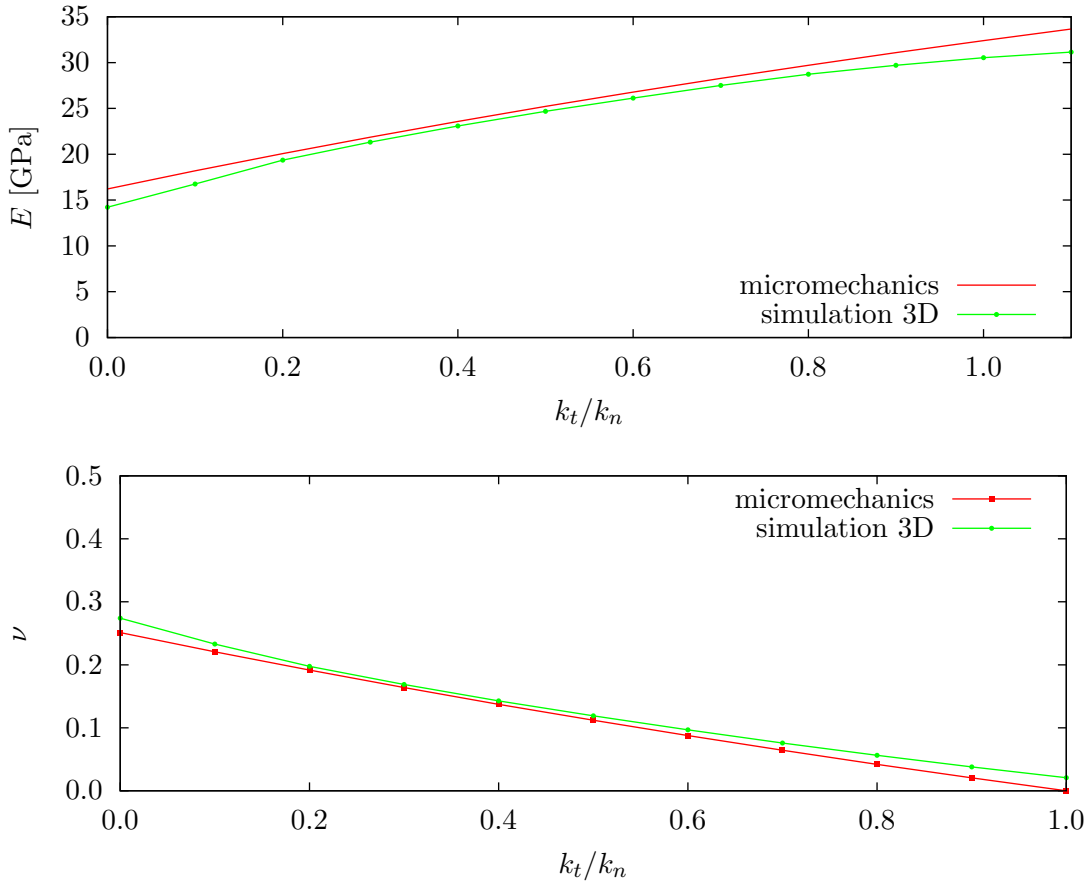

Figure 4.7. Comparison of Young modulus and Poisson's ratio estimated with micromechanics and simulations in specimen 3D.

4.3 Dimensional analysis

Huang [62] used dimensionless laws in order to estimate the mechanical behaviour of an assembly of particles governed by the following set of characteristics parameters: k_n, k_t, $\bar{r}$, e, ρ, L, V; where $\bar{r}$ is the average radius, ρ the density, L is the sample length, V is the load velocity and e the porosity of the assembly, as a indirect measure of the particle size distribution and contact density.

Dimensional analysis is based on the Buckingham π theorem, which states that any physically meaningful functional relationship of N variables $\Psi(Q_1, Q_2, ..., Q_N)$ can be expressed equivalently by a function of N-M dimensionless parameters $\Psi'(\pi_1, \pi_2, ..., \pi_{N-M})$, where M is the number of primary dimensions, and N-M is the maximum number of independent parameters [73].

Elastic constants

Since there are seven parameters and three independent dimensions, according to the Buckingham theorem four independent dimensionless parameters govern the elastic response of the assembly

$$\left\{ \frac{k_t}{k_n}\,,\, e\,,\, \frac{r}{L}\,,\, \frac{V}{\sqrt{k_n/\rho}} \right\} \tag{4.20}$$

It is assumed that an enough number of particles is considered, the ratio $(r/L << 1)$ can be ignored. The same can be assumed for the velocity, considering the condition of quasi-static loading ($V/\sqrt{k_n/\rho} << 1$).

The dependence of the elastic constants on the micro-scale parameters can thus be reduced to the following scaling laws

$$\frac{E\,l}{k_n} = \Psi_E\left(\frac{k_t}{k_n}, e\right) \tag{4.21}$$

$$\nu = \Psi_\nu\left(\frac{k_t}{k_n}, e\right) \tag{4.22}$$

where Ψ_E and Ψ_ν are dimensionless functions. Obviously E can be scaled by either k_n or k_t, plus a length parameter in order to obtain a dimensionless number. The characteristic length l will be defined in a different way for 2D and 3D problems. For 2D problems, where the plain strain condition is assumed, and cylindrical particles are used, l can be defined as the length (height) of the particles, with unitary value [47, 62, 112]. For 3D problems, the characteristic length can be defined by the average radius $\bar{r}$ of the particles, in equivalence with the 2D problem, but considering spherical particles.

Yang et al. [112], showed that the porosity e may not be a good index to represent the particle size distribution, or in a most general sense the influence of the particle assembly, and can be replaced by a different parameter representing the geometrical characterization of the assembly. The porosity is replaced with the particle size ratio $(r_{\max}/r_{\min})$ in order to considers the influence of the particle size distribution influence.

The geometrical characterization of the assembly, considering the different values involved like porosity, particle size distribution, coordination number, etc. can be represented by a function of these parameters Φ. Equations (4.21) and (4.22) can be rewritten as

$$\frac{E\,l}{k_n} = \Psi_E\left(\frac{k_t}{k_n}, \Phi\right) \tag{4.23}$$

$$\nu = \Psi_\nu\left(\frac{k_t}{k_n}, \Phi\right) \tag{4.24}$$

These relationships can be used to determine the shear and normal contact stiffnesses corresponding to E and ν.

Note that according to the scaling laws, the elastic constants are completely determined if the shear and normal stiffnesses k_t and k_n are known for a given size distribution of the particles. This means that the curves hold for a specific assembly of particles, with a given configurations, and can not be scaled to a different one. This is very important, because the geometric characterization of an assembly is strongly related with the mechanical behaviour of the specimen. This will be discussed further in Section 4.2.

Compressive and tensile strengths

Most of the work done in the study of the micro-parameters is related to both the effective Young modulus and Poisson's ratio. The effect of the micro-scale parameters on the strength properties has not been systematically studied.

Using the same analysis for the elastic constants, the compressive and tensile strengths can be defined considering the combination of the involved parameters

$$\frac{\sigma_c A}{R_t} = \Psi_c \left(\frac{k_n \bar{r}}{R_n}, \frac{R_t}{R_n}, \frac{k_t}{k_n}, \mu, \Phi \right) \tag{4.25}$$

$$\frac{\sigma_t A}{R_n} = \Psi_t \left(\frac{k_n \bar{r}}{R_n}, \frac{R_t}{R_n}, \frac{k_t}{k_n}, \mu, \Phi \right) \tag{4.26}$$

where A is a characteristic area related with the particles. For 2D problems, the characteristic area is considered over the cylindrical particle of unitary length, while for 3D problems the area can be directly considered as the square of the radius $\bar{r}^2$.

Different authors on [62, 63, 88] propose to neglect the influence of the Coulomb friction coefficient because is associated with the post-critical behaviour. Nevertheless, experience shows a non-negligible influence of the friction in particle packings with high density. In [62], Huang shows that the number $k_n \bar{r}/R_n$ has a weak influence on the micro strength ratio, so it can be avoided. Finally, the equations (4.25) and (4.26) can be rewritten as

$$\frac{\sigma_c A}{R_t} = \Psi_c \left(\frac{R_t}{R_n}, \frac{k_t}{k_n}, \mu, \Phi \right) \tag{4.27}$$

$$\frac{\sigma_t A}{R_n} = \Psi_t \left(\frac{R_t}{R_n}, \frac{k_t}{k_n}, \mu, \Phi \right) \tag{4.28}$$

4.3.1 Elastic constants for two-dimensional case

Based in equations (4.23) and (4.24), the dimensionless number defined for the two-dimensional case is defined as

$$\frac{E}{k_n} = \Psi_E^{2D}\left(\frac{k_t}{k_n}, \Phi\right) \tag{4.29}$$

$$\nu = \Psi_\nu^{2D}\left(\frac{k_t}{k_n}, \Phi\right) \tag{4.30}$$

The elastic constants of a particle assembly are obtained from the simulation of the uniaxial compressive strength test (UCS). Different specimens of size $50 \times 50\ mm$ are simulated considering standard compression tests for natural stones [44]. The particle assembly characterization parameters are presented in Table 4.2. The model is shown in Figure 4.8(a) and the contact model parameters are shown in Table 4.3.

Parameter	Description	specimen 1	specimen 2	specimen 3
N_p	Number of particles	11180	15436	20836
e	Estimated porosity (%)	9.440	9.2663	9.0848
n_c	Coordination number	5.940	5.9322	5.9559
$\bar{r}$	Average radius (mm)	0.2538	0.2095	0.1863
$r_{\max}/r_{\min}$	Radius ratio	5.920	6.3815	8.0400

Table 4.2. Mesh characterization parameters for UCS tests in 2D.

Parameter	Description	Value
μ	Coulomb friction coefficient	0.5
k_n	Stiffness in the normal direction (GN/m)	10.0
k_t	Stiffness in the tangential direction (GN/m)	4.0
R_n	Strength of cohesive bonds in the normal direction (kN)	1.0
R_t	Strength of cohesive bonds in the tangential direction (kN)	1.0

Table 4.3. Model parameters for UCS tests in 2D.

The failure model of the UCS test is shown in Figure 4.8(b). A realistic fracture is obtained.

The stress is evaluated considering the average stress tensor over all the specimen volume (see Appendix A for details). The axial strain can be estimated from the imposed axial strain rate. Nevertheless, the average strain tensor presents a more accurate estimation, showing a small difference with the axial strain rate [7, 41]. The definition

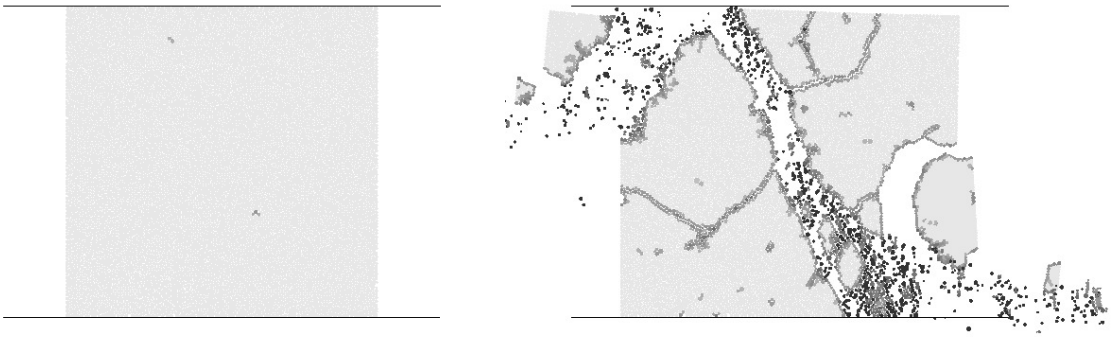

(a) Model of the UCS test. (b) Failure mode in the UCS test.

Figure 4.8. Model and failure mode for the UCS test in 2D, with $k_t/k_n = 0.4$.

can be found in appendix B.

A typical stress-strain curve is presented in Figure 4.9, where the linear elastic behaviour and the brittle failure can be appreciated.

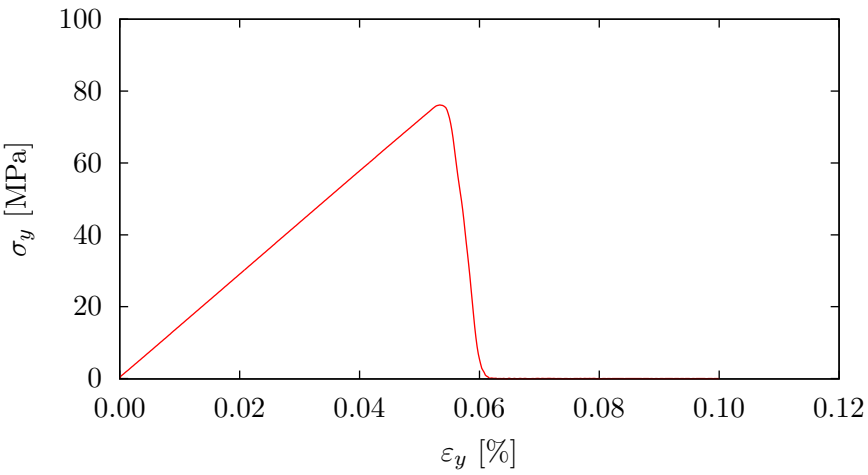

Figure 4.9. Curve stress vs strain for 2D UCS test in specimen 1, with k_t/k_n=0.4 and R_t/R_n=1.

The apparent Young modulus can be obtained directly from the stress-strain curve, considering an average value between 1%–50% of the maximum stress, as

$$E' = \frac{\Delta\sigma_{yy}}{\Delta\varepsilon_{yy}} \tag{4.31}$$

Equation (4.31) take into account that a small degree of anisotropy is produced during the deformation process [79]. The isotropy of the particle assembly is evaluated considering the initial state. During the compression process, the strain introduces changes in the contact directions resulting in a loss of isotropy.

It should be noted that in the 2D case plane strain condition are assumed in the simulations, so the true Young modulus and Poisson's ratio are obtained from the following equation

$$\nu = \frac{\nu'}{1+\nu'} \tag{4.32}$$

$$E = \frac{E'}{1-\nu^2} \tag{4.33}$$

Considering different values of the stiffness ratio k_t/k_n, the dimensionless scale function is generated. This is shown in Figure 4.10.

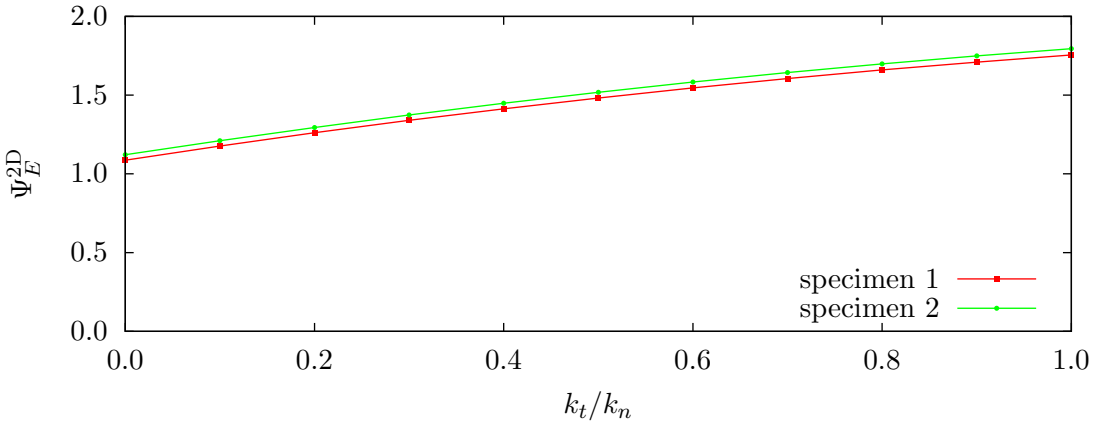

Figure 4.10. Dimensionless scale function of Young modulus Ψ_E^{2D} for different values of k_t/k_n in 2D UCS test.

The apparent Poisson's ratio is estimated considering the axial and lateral direction in the average strain tensor

$$\nu' = \frac{-\Delta\varepsilon_{xx}}{\Delta\varepsilon_{yy}} \tag{4.34}$$

where the axial strain ε_{yy} and the horizontal strain ε_{xx} are calculated from the average strain tensor over all the specimen.

Figure 4.11 shows the horizontal displacement of the specimen. It can be noted that the displacement field is uniform, which is a requirement for a good estimation of the Poisson's ratio. This uniform displacement field depends on the isotropy of the assembly, which is strongly related to the particle packing methodology.

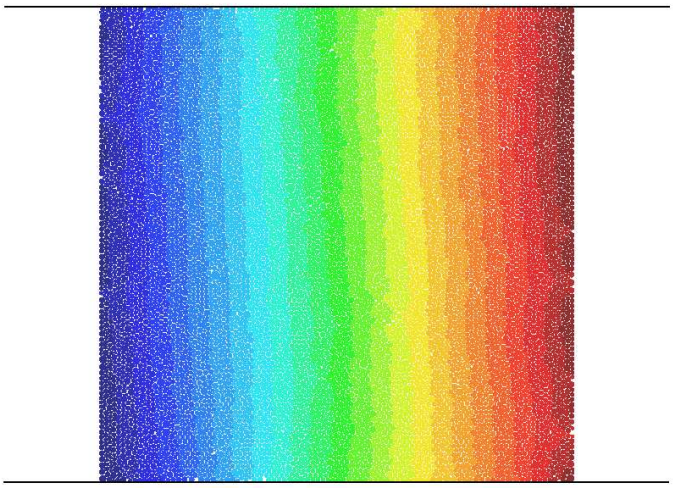

Figure 4.11. Horizontal displacement in the UCS test 2D, with $k_t/k_n = 0.4$ at $t = 0.025s$.

The variation of the Poisson's ratio versus the micro stiffness ratio is shown in Figure 4.12. The curve is in agreement with the results obtained by different authors [24, 62, 75].

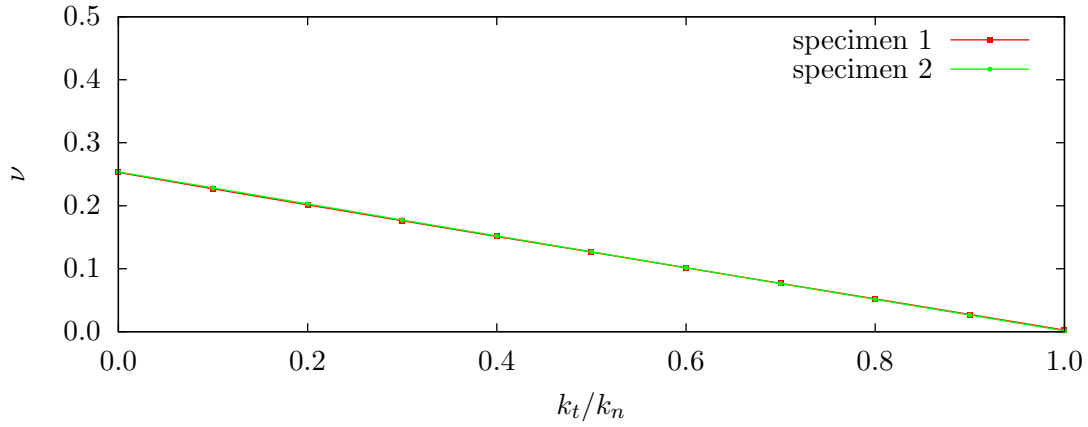

Figure 4.12. Poisson's ratio versus different values of k_t/k_n in 2D UCS test.

A linear behaviour is observed. The maximum value of the Poisson's ratio obtained is 0.25, and it is achieved with zero shear stiffness. With an equal value of the contact stiffnesses the Poisson's ratio is zero.

4.3.2 Elastic constants for three-dimensional case

Similarly to the 2D case, a cylindrical specimen of diameter 50 mm and length 50 mm is considered for the 3D problem. The specimen is discretized with a randomly assembly of 10395 spheres of radii between $0.4039 - 2.1679$ mm, and an average radius ($\bar{r}$) of 1.1653 mm. The assembly is characterized by a porosity of 23.34% and a coordination number of 9.48. In Figure 4.13, the discretized assembly is shown.

Parameter	Description	specimen 1	specimen 2	specimen 3	specimen 4
N_p	Number of particles	10395	17870	19563	24970
e	Estimated porosity (%)	23.34	21.27	21.612	24.143
n_c	Coordination number	9.4800	9.40325	9.51756	9.76580
$\bar{r}$	Average radius (mm)	1.1653	0.97525	0.93034	0.84619
$r_{\max}/r_{\min}$	Radius ratio	5.3674	4.95739	6.32802	8.85376

Table 4.4. Assembly characterization parameters for 3D UCS test.

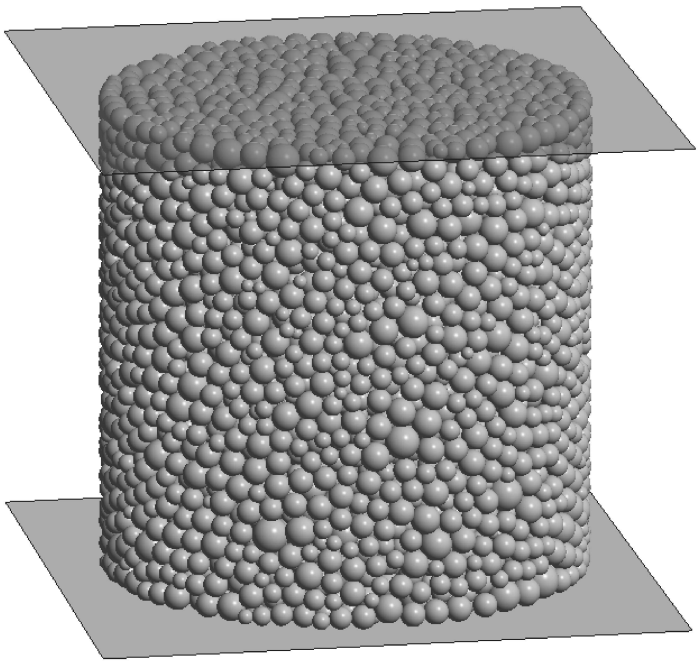

Figure 4.13. Assembly for UCS test in 3D specimen 1.

The contact model parameters used are presented in Table 4.5. An equal value of the normal and tangential strengths is used.

A stress-strain curve for the 3D UCS test is shown in Figure 4.14. Note that in this case, the behaviour of the specimen changes during the process, showing some non-

Parameter	Description	Value
μ	Coulomb friction coefficient	0.5
k_n	Stiffness in the normal direction (MN)	35
k_t	Stiffness in the tangential direction (MN)	10.5
R_n	Strength of cohesive bonds in the normal direction (N)	100
R_t	Strength of cohesive bonds in the tangential direction (N)	100

Table 4.5. Model parameters for UCS test of 3D specimens.

linearity at the end of the elastic range. This is because the broken bonds (micro-cracks) appear gradually before achieving the elastic limit, as shown in Figure 4.15. The figure shown the evolution of the broken bonds due to shear and tension. This will be discussed further, when the limit strengths are analyzed. At this moment, just the elastic range is considered, and the equivalent Young modulus and Poisson's ratio are evaluated at the arise of the curve. This avoids the influence of non-linear phenomena derived from the loss of isotropy or damage. For the estimation of the elastic constants a range of the curve between 1% and 50% of the maximum stress is considered, as recommended in laboratory tests.

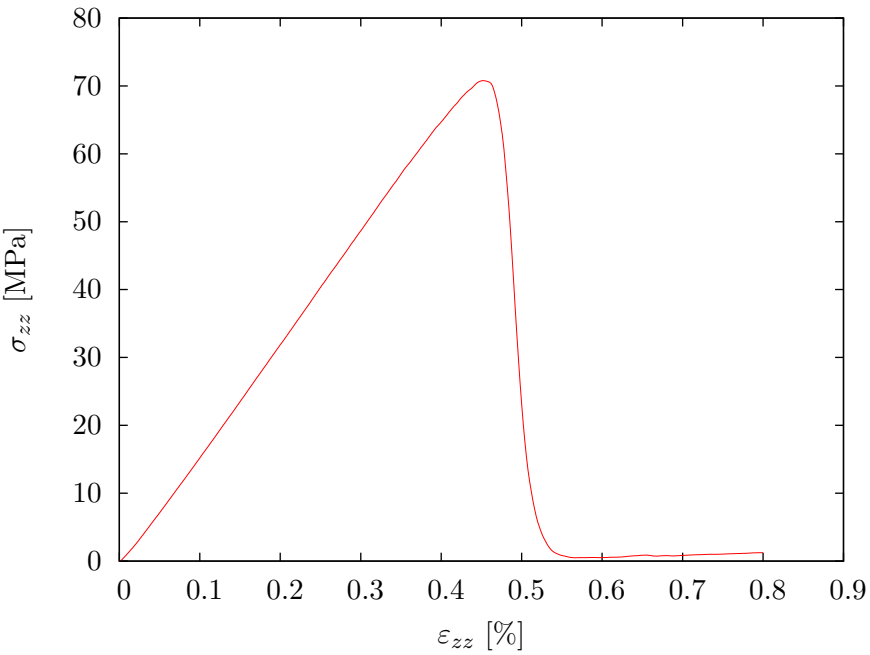

Figure 4.14. Curve stress vs strain for 3D UCS test of specimen 1, with k_t/k_n=0.3 and R_t/R_n=1.

The dimensionless scale function for the Young modulus is presented in Figure 4.16.

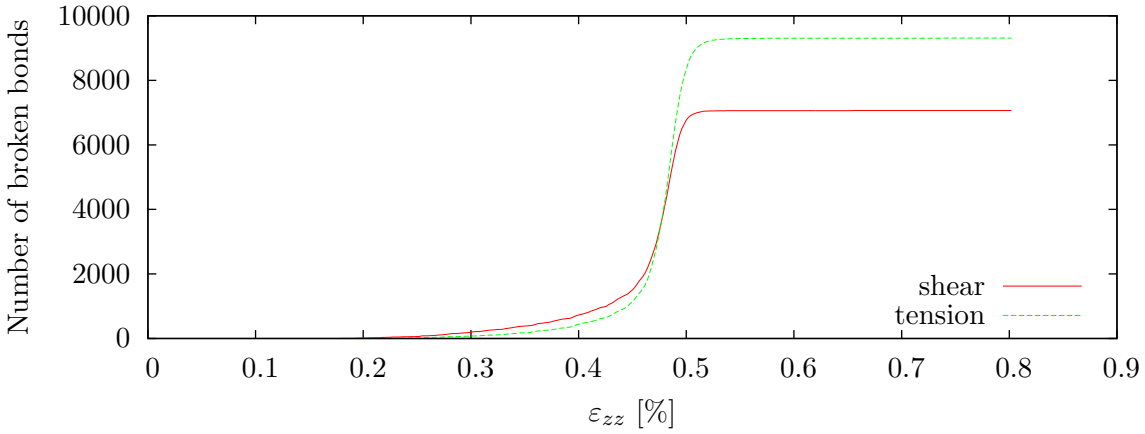

Figure 4.15. Evolution of the broken bonds during the 3D UCS test of specimen 1, with $k_t/k_n = 0.30$ and R_t/R_n=1.

As mentioned earlier, the dimensionless number used in the 3D case considers the characteristic length l as the average radius $\bar{r}$. The main difference with the 2D case is the spherical shape of the particles [62, 75].

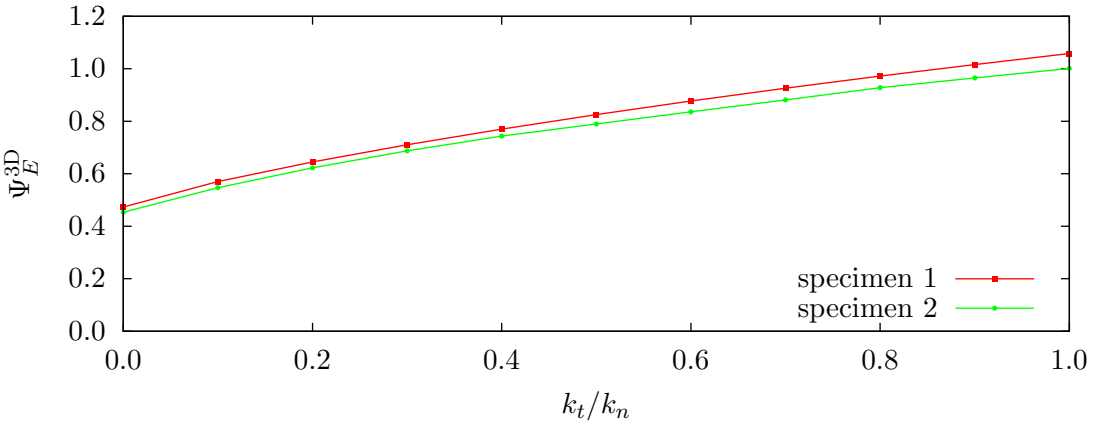

Figure 4.16. Dimensionless scale function for Young modulus Ψ_E^{3D} for different values of k_t/k_n in 3D UCS test specimens.

The dimensionless scale function for the Poisson's ratio is presented in Figure 4.17. Similarly as for the Young modulus case, this function is not linear, and its shape is different in comparison with the one obtained in the 2D case. The value obtained when the tangential stiffness equals the normal stiffness is close to zero. This can be considered far from the ideal behaviour shown in the 2D case.

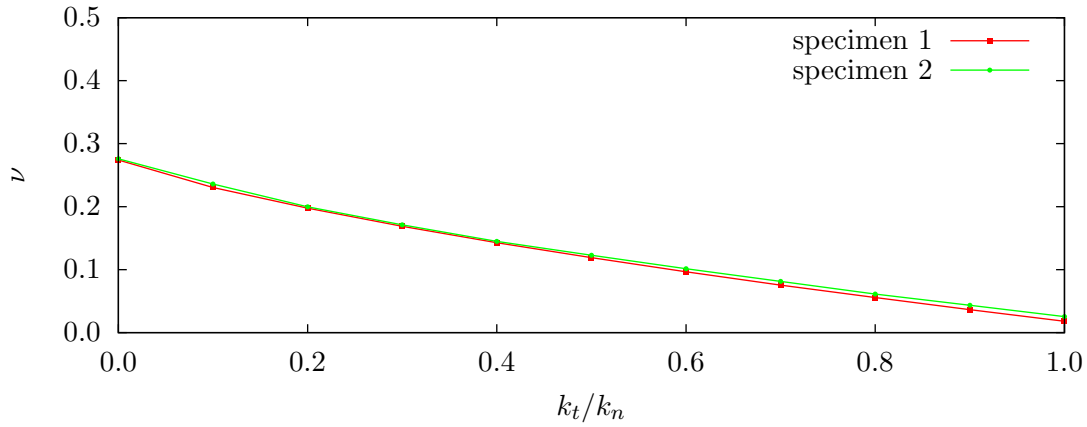

Figure 4.17. Poisson's Ratio for different values of k_t/k_n in 3D UCS test.

In 3D problems, the interaction mechanism is more complex than in the 2D case, making more difficult to obtain a good estimation of the equivalent strain.

4.3.3 Compressive and tensile strengths for two-dimensional case

Assuming that Equations (4.25) and (4.26) hold for the 2D problem, and the characteristic area defined for cylindrical particles with unit thickness, the equations can be re-written as

$$\frac{\sigma_c\,\bar{r}}{R_t} = \Psi_c^{\mathrm{2D}}\left(\frac{R_t}{R_n}, \frac{k_t}{k_n}, \mu, \Phi\right) \tag{4.35}$$

$$\frac{\sigma_t\,\bar{r}}{R_n} = \Psi_t^{\mathrm{2D}}\left(\frac{R_t}{R_n}, \frac{k_t}{k_n}, \mu, \Phi\right) \tag{4.36}$$

Several UCS and BTS tests has been performed varying the different parameters of the dimensionless scale functions, and considering all the specimens listed in Table 4.2.

4.3.3.1 Unconfined compressive strength test

The influence of the stiffness ratio in the behaviour of the specimen is depicted in Figure 4.18, where the failure mode in the UCS test for values of k_t/k_n between 0 and 1, and $R_t/R_n = 1.0$, are presented.

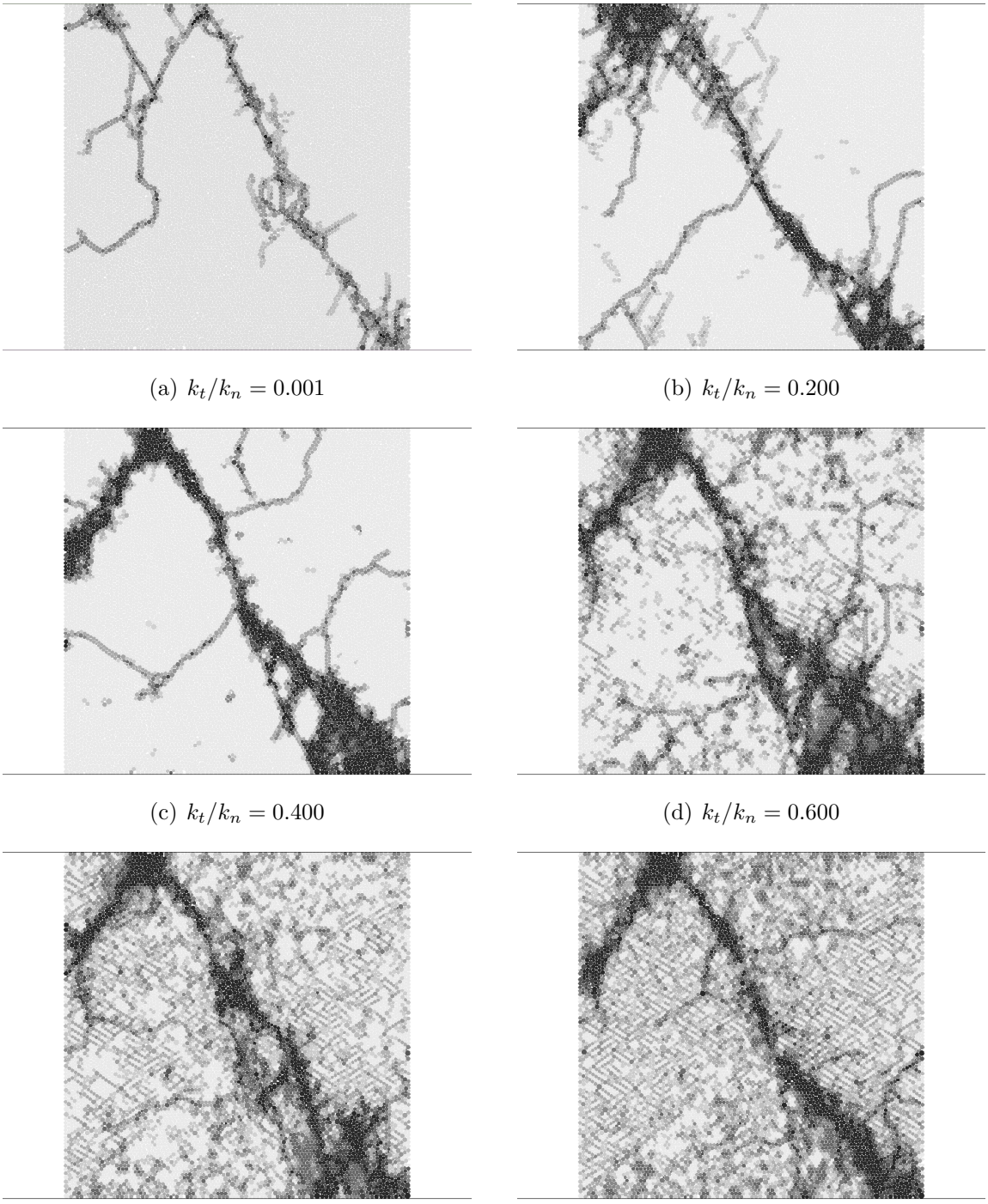

(a) $k_t/k_n = 0.001$

(b) $k_t/k_n = 0.200$

(c) $k_t/k_n = 0.400$

(d) $k_t/k_n = 0.600$

(e) $k_t/k_n = 0.800$

(f) $k_t/k_n = 1.000$

Figure 4.18. Failure mode of the 2D UCS test in specimen 1 for different values of k_t/k_n and $R_t/R_n = 1.0$.

Note that the fracture pattern in the specimen is equivalent for the different values

of k_t/k_n, and the differences are based in the resolution and the damage (micro-cracks) in the intact areas. This can be explained in the breakage mechanism involved in the process. With low values of shear stiffness, most of the bonds are broken by tension, while with equivalent values of contact stiffnesses ($k_t/k_n = 1.0$), the predominant mechanism is shear. In Figures 4.18(d)–4.18(f) the bonds broken by shear occurs during the elastic range, generating uniform damage in the specimens.

A typical curve obtained for the dimensionless scale function of the compressive strength is depicted in Figure 4.19, with $R_t/R_n = 1.0$. In Figure 4.19, the grey colour represents the range of values obtained in the different specimens, and the red line is the average curve. An important influence of the stiffness ratio over the compressive strength is appreciated.

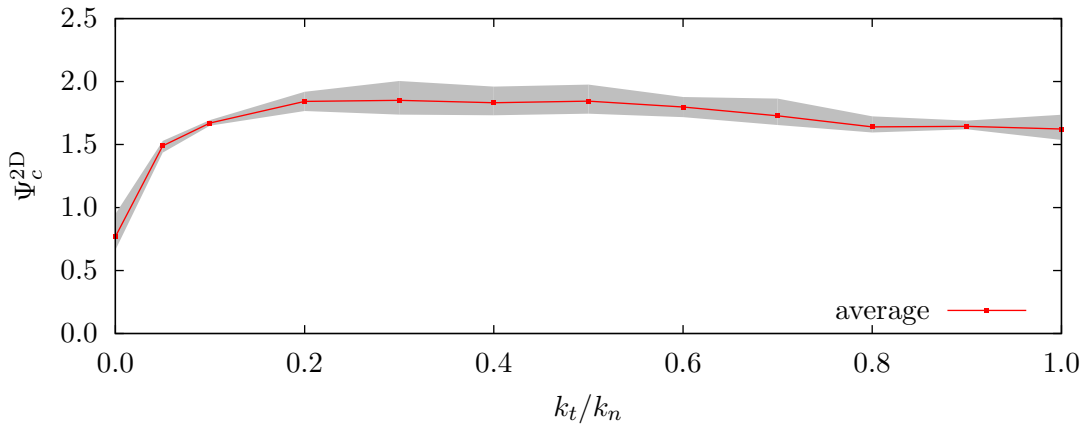

Figure 4.19. Dimensionless scale function of compressive strength Ψ_c^{2D} for different values of k_t/k_n and $R_t/R_n = 1.0$ in 2D UCS test.

The influence of the micro strength ratio in the dimensionless compressive strength function is investigated by varying the tangential contact strength R_t between 1 kN and 10 kN, while the normal contact strength is fixed in R_n=1 kN. The dimensionless scale function for the compressive strength for k_t/k_n= 0.5 is shown in Figure 4.20.

The compressive strength function shows a big influence for lower values of the micro strength ratio, while it influence decrease for higher values of R_t/R_n.

As the dimensionless scale function of compressive strength depends on the micro stiffness ratio k_t/k_n and the micro strength ratio R_t/R_n, a contour of the averaged values has been generated to represent the influence of both parameters. This is shown in Figure 4.21.

It can be seen that the scaling function increases when both k_t/k_n and R_t/R_n increase.

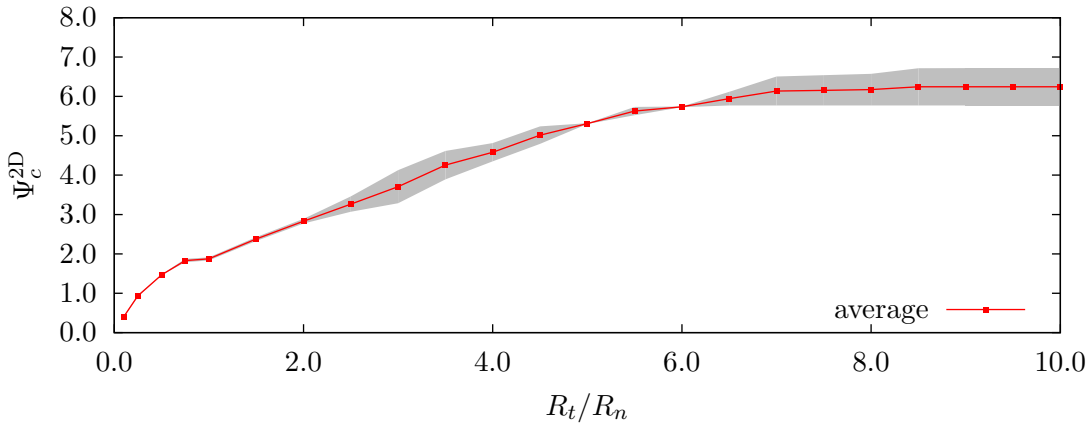

Figure 4.20. Dimensionless scale function of compressive strength for different values of R_t/R_n and $k_t/k_n = 0.5$ in 2D specimens.

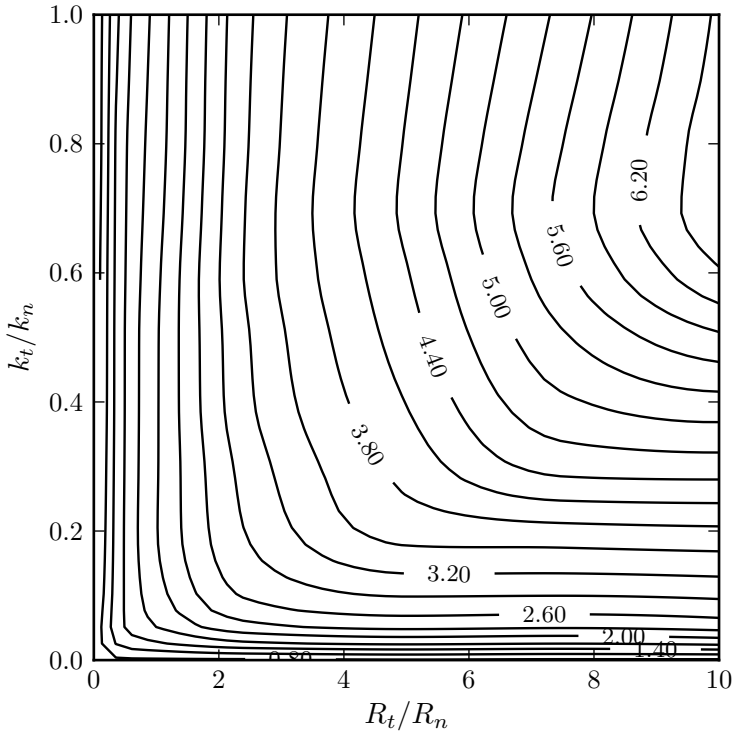

Figure 4.21. Dimensionless scale function of compressive strength Ψ_c^{2D} for different values of k_t/k_n and R_t/R_n, in 2D specimens.

For lower values of k_t/k_n, the function is constant for higher values of R_t/R_n. This behaviour can be explained by the bond-breakage mechanism. In Figure 4.22(a), it can be seen the fraction of broken bonds for each breakage mechanism (shear and tension)

for different values of the micro strength and micro stiffness ratios. The total number of broken bonds N_{bb} is defined as

$$N_{bb} = N_{bb}^{s} + N_{bb}^{t} \tag{4.37}$$

where N_{bb}^{s} and N_{bb}^{t} are the number of broken bonds due to shear and tension, respectively.

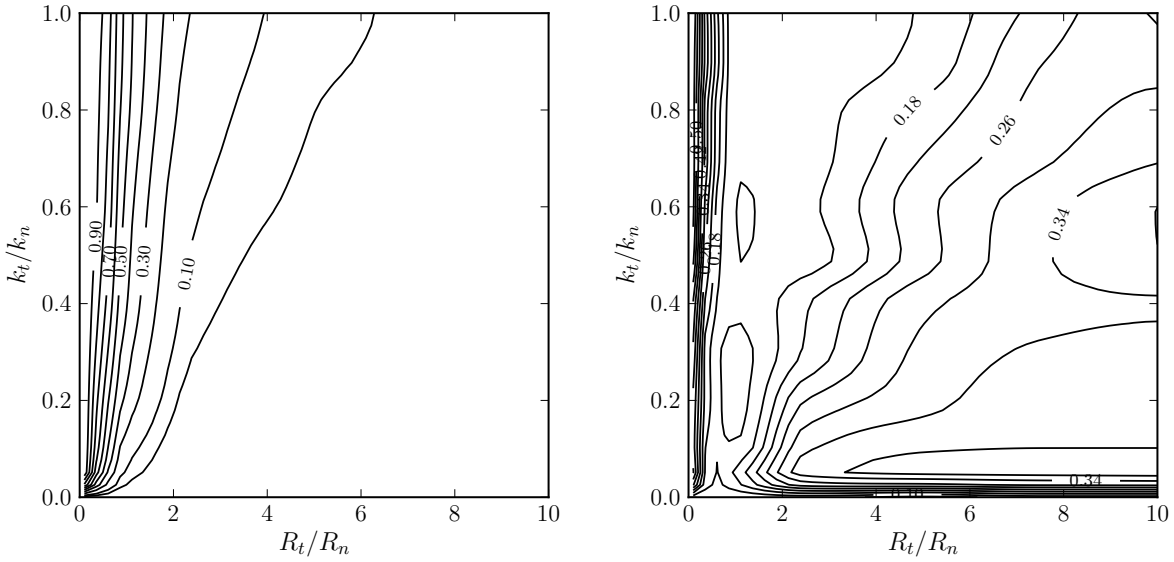

(a) Ratio of bonds broken due to shear over all broken bonds (N_{bb}^{s} / N_{bb})

(b) Ratio of broken bonds over initial bonds (N_{bb} / N_c)

Figure 4.22. Bonds broken for different values of k_t/k_n and R_t/R_n in 2D UCS test.

For a low value of k_t/k_n, the dominant breakage mechanism is tension and the value of R_t does not affect the scaling function Ψ_c^{2D}. For higher values of k_t/k_n, the dominant breakage mechanism is shear for lower values of R_t/R_n. While R_t/R_n increase, the influence of the shear in the breakage mechanism decrease (increasing Ψ_c). Finally the breakage is fully controlled by tension and again R_t does not affect Ψ_c^{2D}. Figure 4.20 shown this behaviour for k_t/k_n=0.5. For low values of the R_t/R_n, the dominant mechanism in the bond breakage is the shear. While the value of R_t increase (therefore increasing R_t/R_n), transitional region starts where σ_c increases faster, and most of the bonds are broken due to tension. When the dominant mechanism is tension, the scale function increases slowly. After a threshold value of R_t/R_n, the scaling function is independent of R_t and depends only of R_n.

In Figure 4.22(b), the fraction of all the bonds broken is depicted. It is interesting

that while R_t/R_n=1 the fraction of bonds broken due to shear increases (Figure 4.22(a)), the total number of broken bonds N_{bb} does not increase significantly. For a higher value of R_t/R_n, and seen that the breakage mechanism is completely based in tension, the number of bonds broken increases with R_t/R_n. This shows that even if the dominant breakage mechanism is shear, the total number of bonds broken due to shear is small in comparison with the number of bonds broken due to tension.

The influence of the Coulomb friction coefficient is shown in Figure 4.23. As mentioned earlier, some authors neglect the influence of friction in the limit strengths. Nevertheless the curve shows a change in the values that should be taken into account.

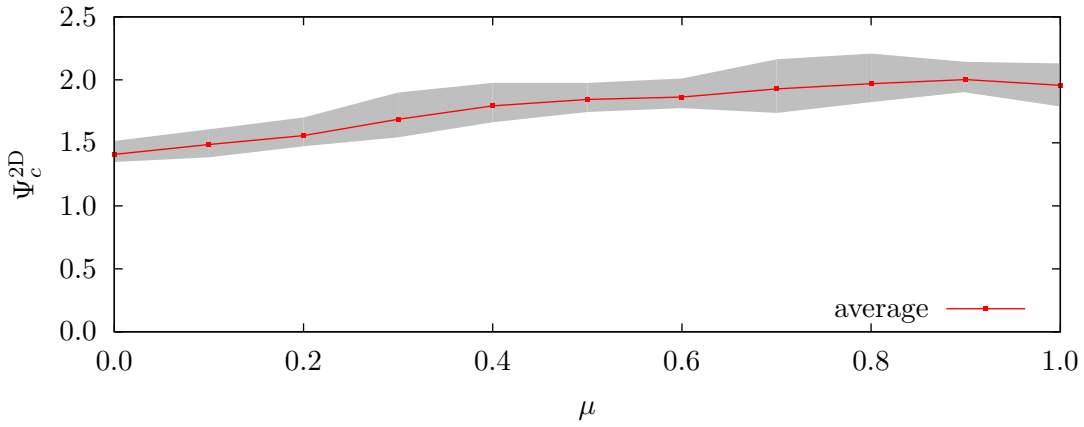

Figure 4.23. Dimensionless scale function of compressive strength Ψ_c^{2D} for different values of the friction coefficient in 2D UCS test, with k_t/k_n=0.5 and R_t/R_n=1.0.

Friction effects are activated when the bonds are broken, and hence are strongly related with the breakage mechanism. Taking into account the influence of the breakage due to shear in Figure 4.22, which is more than 40%, it is possible to understand why the scaling function increases.

In Figure 4.24, the influence of the Coulomb friction coefficient in the normalized compressive strength is depicted, where σ_c^o is the compressive strength for the frictionless case (μ=0). For R_t/R_n=1 friction has no influence on the compressive strength. The effect is more visible for R_t/R_n=4. This is because for R_t/R_n=4 the breakage mechanism is dominated by tension.

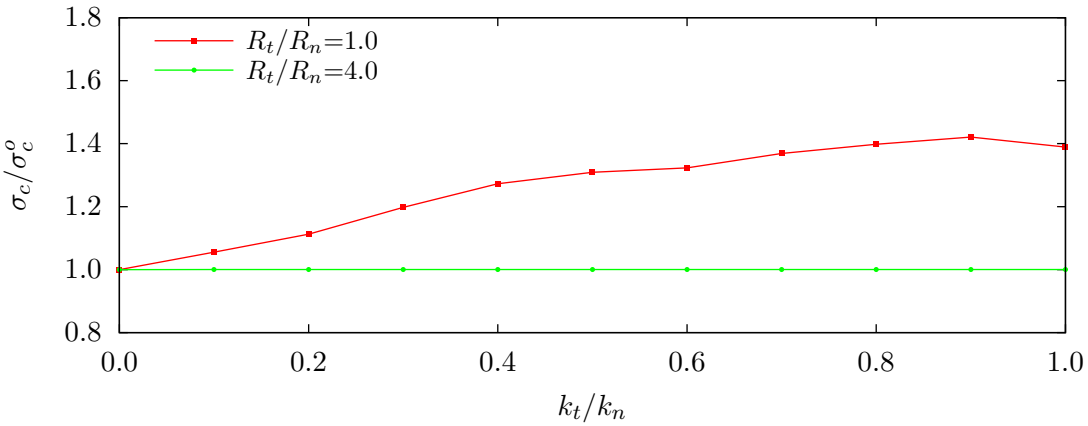

Figure 4.24. Average of normalized compressive strength for different values of the friction coefficient in 2D UCS test, with k_t/k_n=0.5.

4.3.3.2 Brazilian tensile strength test

The Brazilian tensile strength (BTS) test is used for the study of the tensile strength. For the BTS test, three new specimens are used reproducing the mesh characterization parameters of the specimens used in the UCS test. The characterization parameters for the BTS test specimens are presented in Table 4.6.

Parameter	Description	specimen 1	specimen 2	specimen 3
N_p	Number of particles	8396	12359	15231
e	Estimated porosity (%)	9.368	9.2720	9.1994
n_c	Coordination number	5.891	5.9317	5.9477
$\bar{r}$	Average radius (mm)	0.2556	0.2084	0.1871
$r_{\max}/r_{\min}$	Radius ratio	8.384	9.9024	8.0974

Table 4.6. Assembly characterization parameters for BTS test in 2D specimens.

Figure 4.25(a) shows a sample of the BTS test, for the specimen 1. The typical failure mode obtained it is depicted in Figure 4.25(b).

The Brazilian tensile strength σ_t is computed via [113]

$$\sigma_t = \frac{2\,F_t}{\pi\,D\,t} \tag{4.38}$$

where F_t is the peak force acting in the platens, D is the diameter of the disk, and t its longitudinal dimension. For the 2D case t=1.

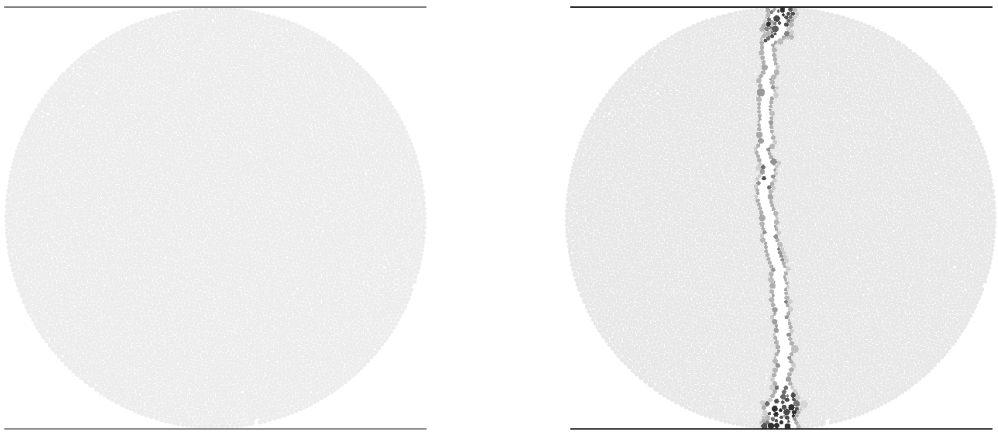

(a) BTS test model (b) Failure mode

Figure 4.25. Model and failure mode for 2D BTS test in specimen 1, with k_t/k_n=0.6 and R_t/R_n=1.

Following the same procedure than in the UCS test case, the influence of the micro stiffness ratio and micro strength ratio are analyzed. In Figure 4.26, a sample curve of the influence of k_t/k_n is presented for R_t/R_n=1. The curve shows a strong influence of dimensionless scale function of the tensile strength Ψ_t^{2D}.

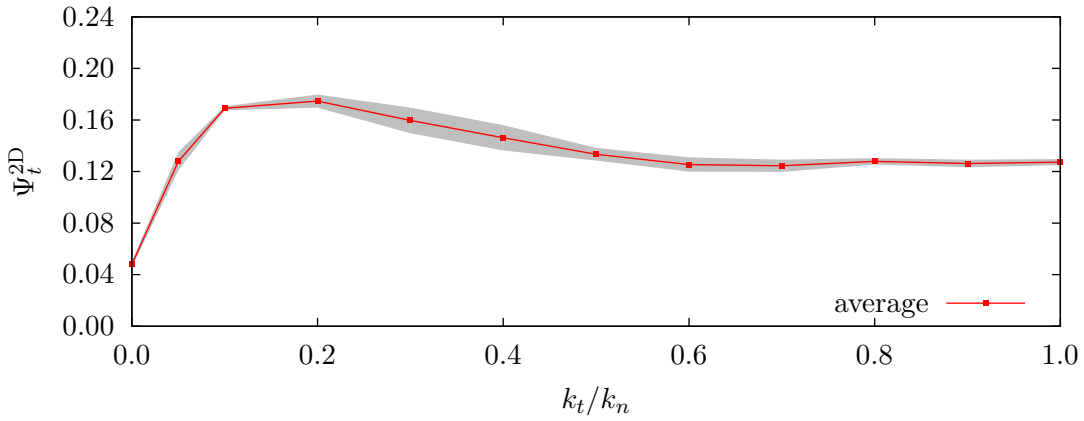

Figure 4.26. Dimensionless scale function of tensile strength Ψ_t^{2D} for different values of k_t/k_n in 2D BTS test, with R_t/R_n=1.

In Figure 4.27, the curve for the dimensionless tensile strength with k_t/k_n=0.4 is depicted. For lower values of R_t/R_n the curve increases fast. After a certain value of R_t/R_n the curve starts to be constant, being completely independent of R_t.

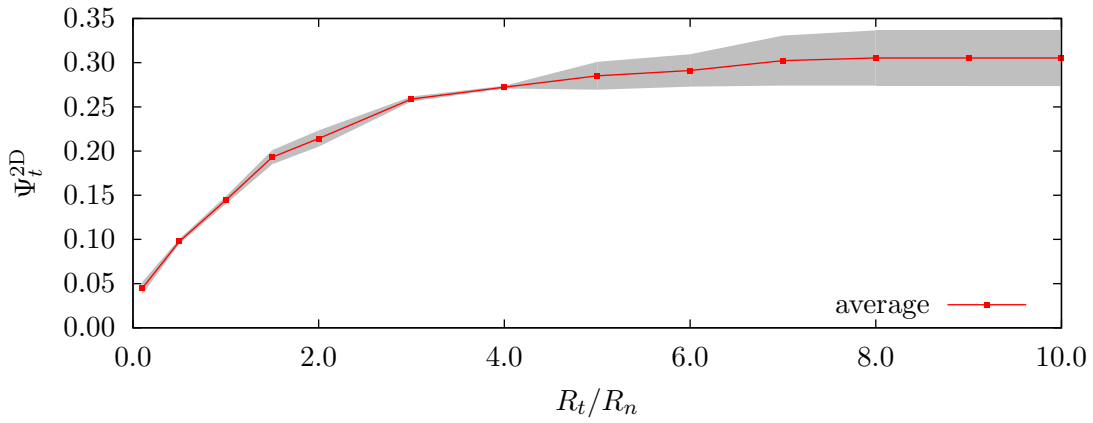

Figure 4.27. Dimensionless scale function of tensile strength Ψ_t^{2D} for different values of R_t/R_n in 2D BTS test, with k_t/k_n=0.4.

The same curves are obtained for different values of k_t/k_n and R_t/R_n, and a graph with the contour lines is created with the average values obtained for the different specimens. The contour lines are presented in Figure 4.28. A similar behaviour that in the UCS test can be appreciated, where the higher values of the tensile strength are obtained when both, k_t/k_n and R_t/R_n are higher.

This behaviour follows the same pattern than for the compressive strength case, which is dominated by the tensile breakage mechanism, as shown in Figure 4.29(a), where the shear breakage mechanism has an influence just for lower values of R_t/R_n. In Figure 4.29(b), the ratio of broken bonds over initial bonds (N_{bb}/N_c) is depicted.

It is interesting to note that in the BTS test the total number of broken bonds is lower than in the UCS test. This means that in the BTS test damage is more localized and the fracture should be clean, while in the UCS test damage is more distributed over the specimen.

Based in the UCS and BTS tests, the influence of the micro stiffness ratio k_t/k_n and the micro strength ratio R_t/R_n over the macro strength ratio σ_c/σ_t is analyzed. The contour lines are presented in Figure 4.30.

Different regions can be observed, based in the bond breakage mechanism. The graph shows a well defined diagonal band where the macro strength ratio increases fast with R_t/R_n. In the bottom region of the graph, the macro strength ratio decreases for small values of k_t/k_n. The maximum value of the macro strength ratio is around 10, for k_t/k_n=0.6 and R_t/R_n=10, which is close to the typical values obtained in natural stone,

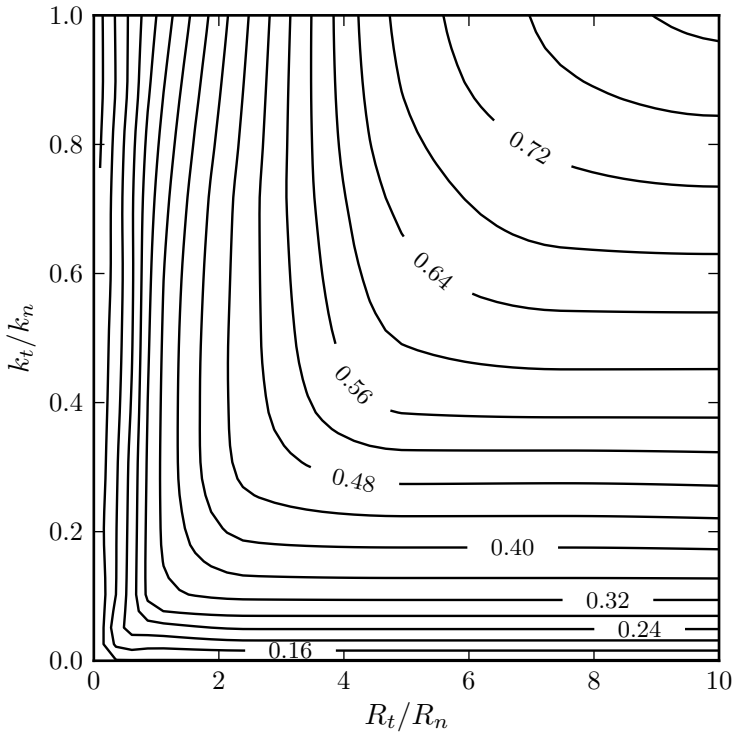

Figure 4.28. Dimensionless scale function of tensile strength Ψ_t^{2D} for different values of k_t/k_n and R_t/R_n in 2D BTS test.

but it is not possible to cover higher values of the macro strength ratio. Huang et. al. [62, 63] present a similar curve for different values of R_t/R_n and k_t/k_n=1, obtaining lower values of the macro strength ratio. Nevertheless, this can be related to the high density level of the assembly.

4.3.4 Compressive and tensile strengths for three-dimensional case

Considering the equations (4.27) and (4.28), and following the same idea that in the 2D case, the area A now is considered to be proportional to the square of the average radius $\bar{r}^2$. The dimensionless relationships can be re-written as

$$\frac{\sigma_c\,\bar{r}^2}{R_n} = \Psi_c^{3D}\left(\frac{R_t}{R_n}, \frac{k_t}{k_n}, \mu, \Phi\right) \tag{4.39}$$

$$\frac{\sigma_t\,\bar{r}^2}{R_n} = \Psi_t^{3D}\left(\frac{R_t}{R_n}, \frac{k_t}{k_n}, \mu, \Phi\right) \tag{4.40}$$

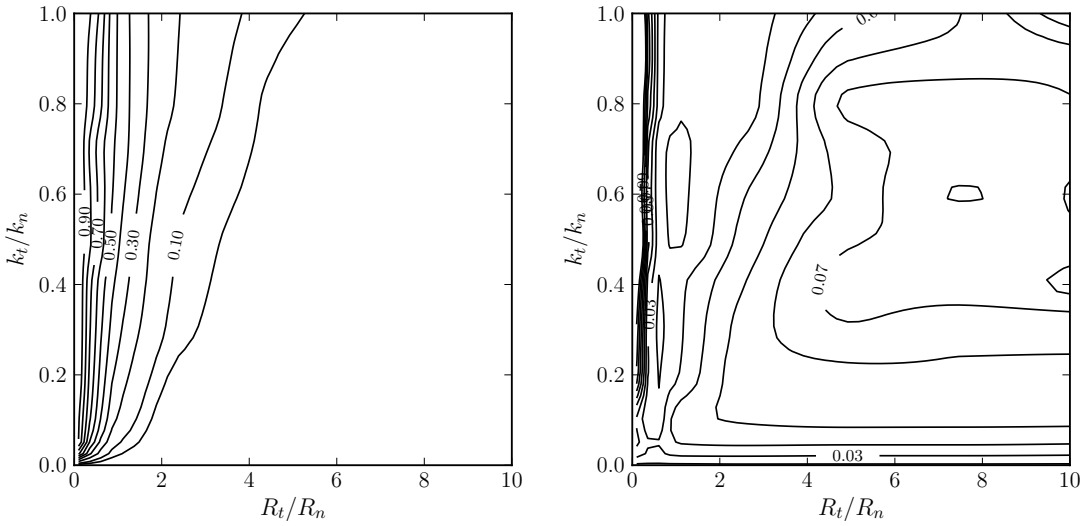

(a) Ratio of bonds broken due to shear over all broken bonds (N^s_{bb} / N_{bb})

(b) Ratio of total broken bonds over initial bonds (N_{bb} / N_c)

Figure 4.29. Bonds broken for different values of k_t/k_n and R_t/R_n in 2D BTS test.

4.3.4.1 Unconfined compressive strength test

The failure mode in the specimen 1, for k_t/k_n=0.3 and R_t/R_n=1, is shown in Figure 4.31. The fracture presents a pattern similar at the observed in laboratory tests, with a well defined fracture surface.

Using the same procedure as for 2D case, the influence of the micro stiffness ratio k_t/k_n and micro strength ratio R_t/R_n has been analyzed. In Figure 4.32, the dimensionless scale function of the compressive strength considering different values of stiffness ratio between 0 and 1, and R_t/R_n = 1.0, in all the specimens of Table 4.4, is presented. An important influence of the stiffness ratio over the compressive strength is appreciated. The grey line, presenting the variation of the curve between the different specimens, shows that all the specimens follow the same behaviour. The variation between the different specimens is attributed to the differences in the particle assemblies and the estimation of the characteristic area A.

A similar situation occurs when the influence of the micro strength ratio R_t/R_n is analyzed for a defined value of k_t/k_n. In Figure 4.33, the curve obtained for k_t/k_n=0.5 is depicted. The behaviour is similar to the obtained for the 2D case, but the curve now is more smoothed.

Performing the same analysis for different values of R_t/R_n and k_t/k_n a contour lines

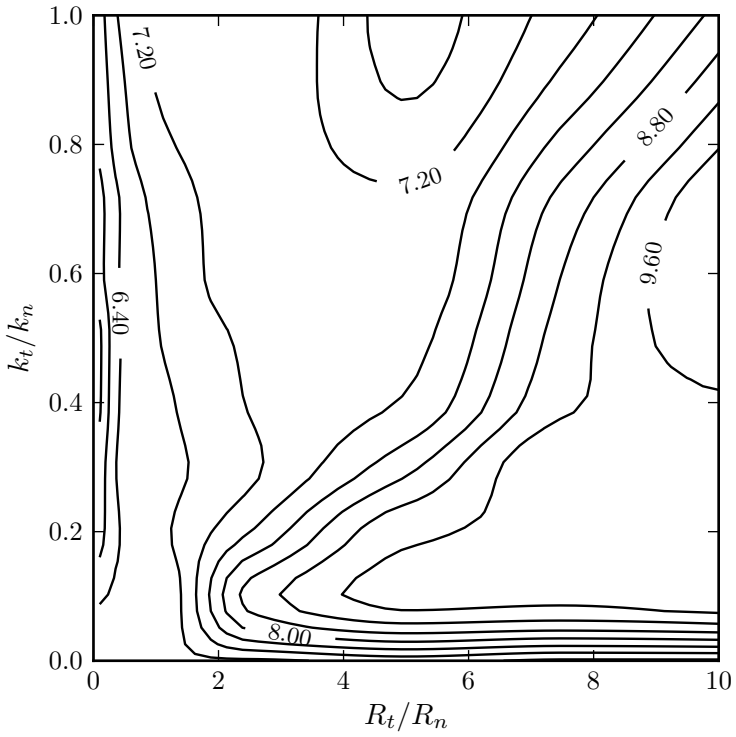

Figure 4.30. Strength ratio σ_c/σ_t for different values of k_t/k_n and R_t/R_n in 2D specimens.

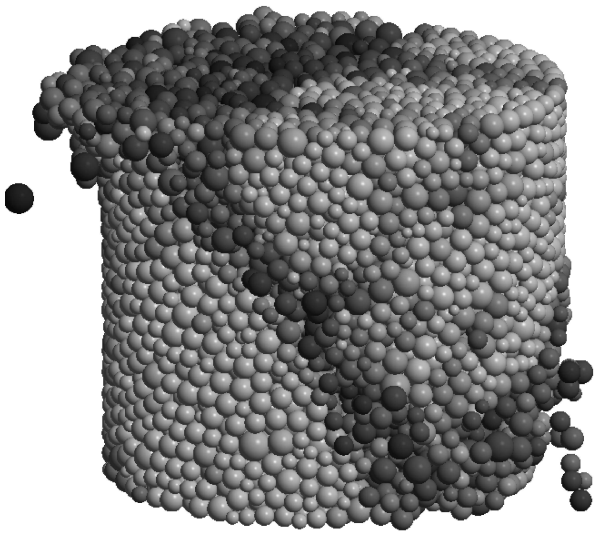

Figure 4.31. Failure mode of the 3D UCS test in specimen 1, with $k_t/k_n = 0.3$ and R_t/R_n=1.

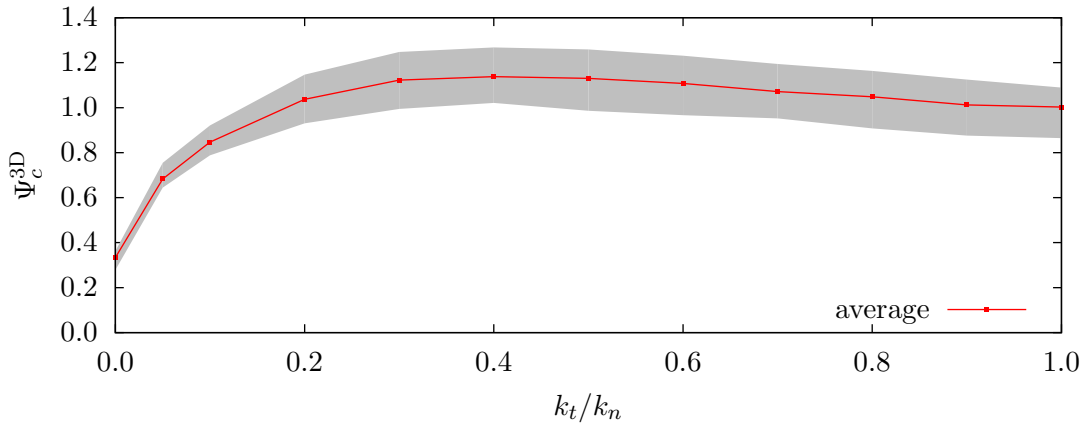

Figure 4.32. Dimensionless scale function of compressive strength Ψ_c^{3D} for different values of k_t/k_n in 3D UCS test, with R_t/R_n=1.

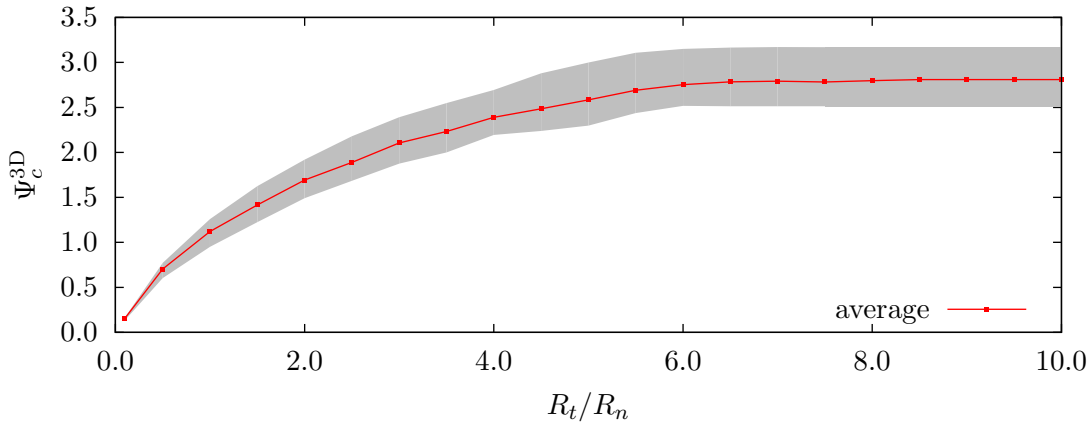

Figure 4.33. Dimensionless scale function of compressive strength Ψ_c^{3D} for different values of R_t/R_n in 3D UCS test, with k_t/k_n=0.5.

graph is generated, showing the influence of both parameters in the dimensionless scale function for the compressive strength. The generated graph is presented in Figure 4.34.

The Figure 4.34 shows an interesting relationship between k_t/k_n and R_t/R_n, with a diagonal band that mark a change of tendency. When the evolution of the compressive strength is considered for a fixed value of k_t/k_n, the band shows the threshold when the strength starts to be independent of R_t/R_n. Furthermore, it is possible see that when k_t/k_n is very small (a higher equivalent Poisson's ratio) the compressive strength is almost constant. The maximum values of the compressive strength are found exactly in the corner of the graph, where the maximum values of k_t/k_n and R_t/R_n are found. Nevertheless, this value can not be achieved in reality because it is equivalent to consider a null Poisson's ratio, as shown in Section 4.3.2.

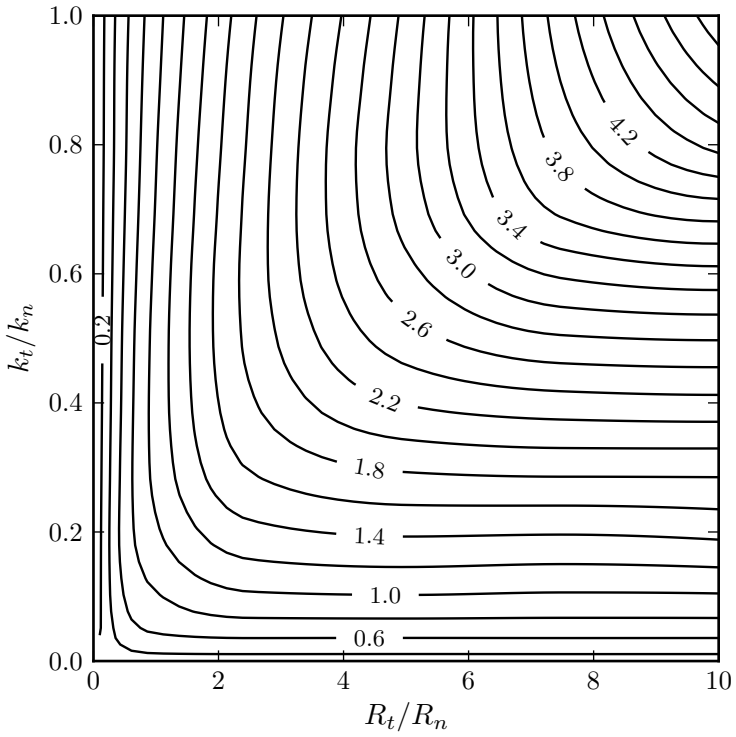

Figure 4.34. Dimensionless scale function of compressive strength Ψ_c^{3D} for different values of k_t/k_n and R_t/R_n in 3D UCS test.

The behaviour can be explained considering the breakage mechanism shown in Figure 4.35, where the band coincides with the change of tendency in the breakage mechanism.

The ratio of bonds broken due to shear over the broken bonds, shown in Figure 4.35(a), indicate that the shear mechanism does work just for lower values of R_t/R_n and increases with k_t/k_n. The diagonal presents the threshold when the breakage is completely controlled due to tension. In Figure 4.35(b) the ratio of broken bonds over the initial number of bonds is shown. This evidences that even in the area where the dominant breakage mechanism is tension, the number of broken bonds is still increasing with R_t/R_n, achieving values around 65% for k_t/k_n=0.6 and R_t/R_n=1. Similarly to the 2D case, the number of bonds broken decreases abruptly for low values of k_t/k_n.

Taking into account the graph obtained for the dimensionless scale function of compressive strength (Figure 4.34), the region where the value of compressive strength in completely independent of R_t is strongly related to the breakage mechanism dominated due to tension.

The influence of the Coulomb friction coefficient in the compressive strength is

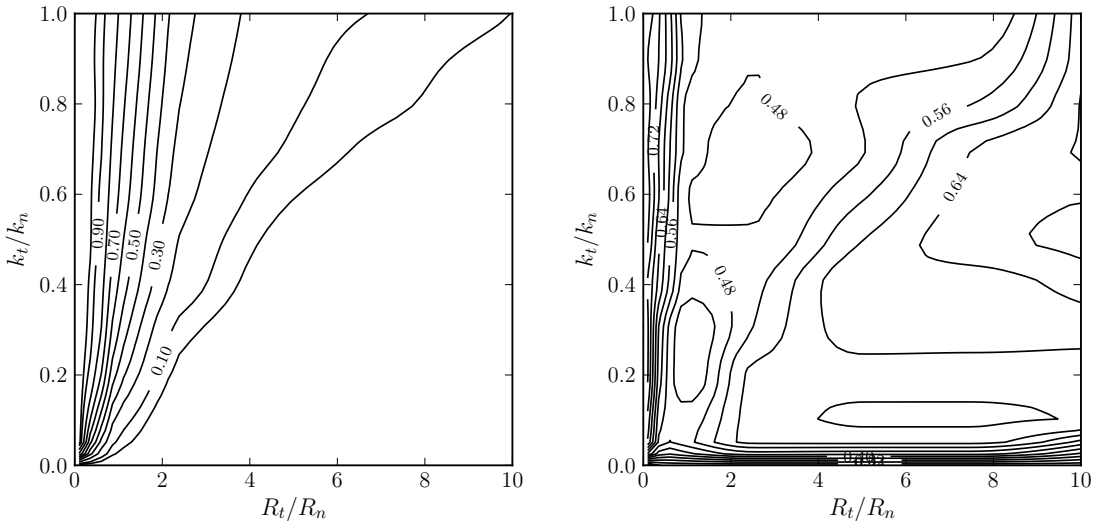

(a) Ratio of bonds broken due to shear over broken bonds ($N_{bb}^{s} \,/\, N_{bb}$)

(b) Ratio of broken bonds broken over initial bonds ($N_{bb} \,/\, N_{c}$)

Figure 4.35. Broken bonds for different values of k_t/k_n and R_t/R_n in 3D UCS test.

analyzed by relating the friction coefficient and the dimensionless scale function Ψ_c^{3D}, as shown in Figure 4.36. The curves shows a higher influence than on the 2D case. Note that the compressive strength increases around 60% with the friction coefficient. It is interesting to note that the curve shows a similar behaviour than in the 2D case, in which the compressive strength changes linearly for values lower than $\mu = 0.90$, after which the compressive strength is constant.

As in the 2D case, the influence of the friction in the compressive strength is related to the breakage mechanism, considering that friction will affect just after the bond breaks due to shear, and with compressive force between the contacting particles. In order to analyze the effect of friction, the UCS test is performed with different values of the friction coefficient and the micro strength ratio. The normalized compressive strength σ_c/σ_c^o, over the compressive strength for the frictionless case (σ_c^o), is depicted in Figure 4.37. The curves shows that for R_t/R_n=10 the compressive strength is almost constant. A higher variation is obtained for R_t/R_n=5, but considerably lower than for R_t/R_n=1. This behaviour can be directly related to the shear breakage mechanism.

4.3.4.2 Brazilian tensile strength test

The tensile strength is obtained through the BTS test, similarly as on the 2D case. On this case, the same specimens used in the compressive test are used. The specimen present a

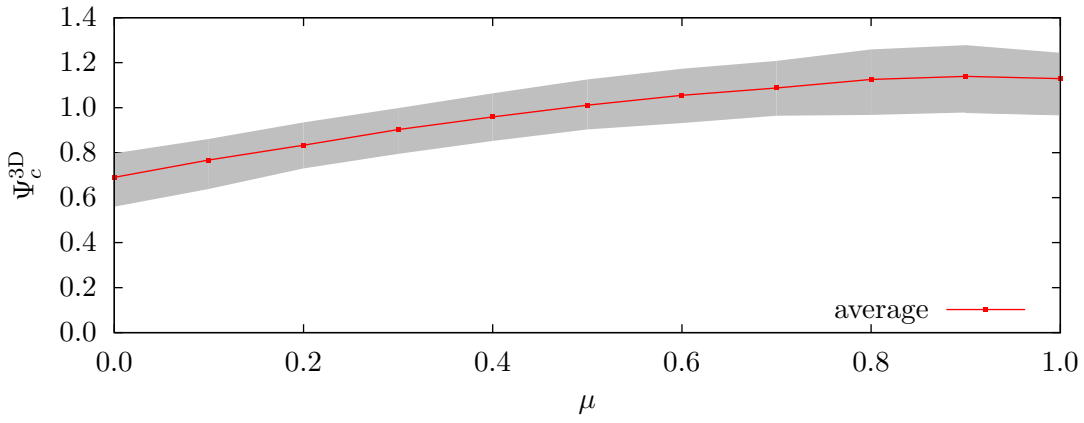

Figure 4.36. Dimensionless scale function of compressive strength Ψ_c^{3D} for different values of the friction coefficient in 3D UCS test, with k_t/k_n=0.5 and R_t/R_n=1.

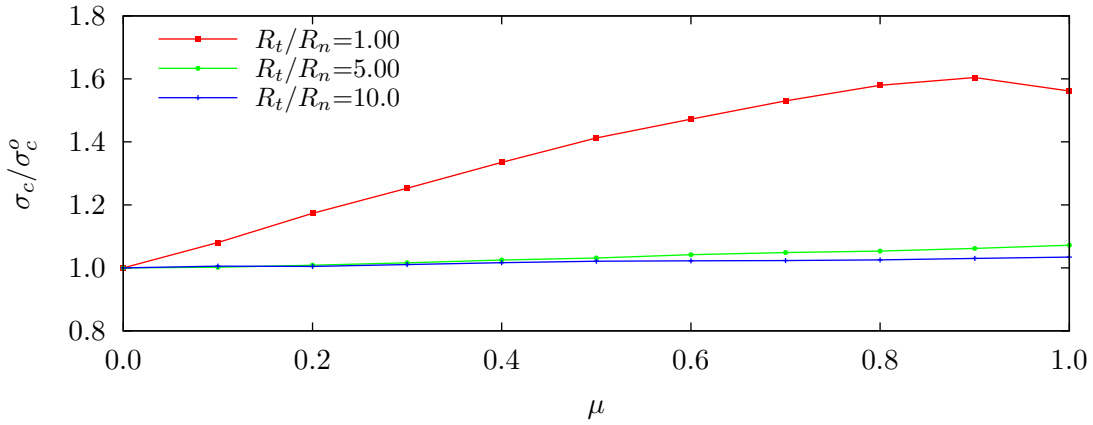

Figure 4.37. Average of normalized compressive strength for different values of the friction coefficient in 3D UCS test, with k_t/k_n=0.5.

length 2 times longer than the laboratory specimens. Nevertheless, a similar behaviour is assumed considering Equation (4.38). This allows to use the same specimens of Table 4.4.

A sample of the failure mode is shown in Figure 4.38, where it can be seen that the fracture presents a correct behaviour.

The BTS test is performed with all the specimens for different values of the micro stiffness and micro strength ratios. The influence of the micro stiffness ratio in the dimensionless scale function of tensile strength (for R_t/R_n=1) is presented in Figure 4.39. The curve presents a similar behaviour as the curve obtained for the UCS test and the

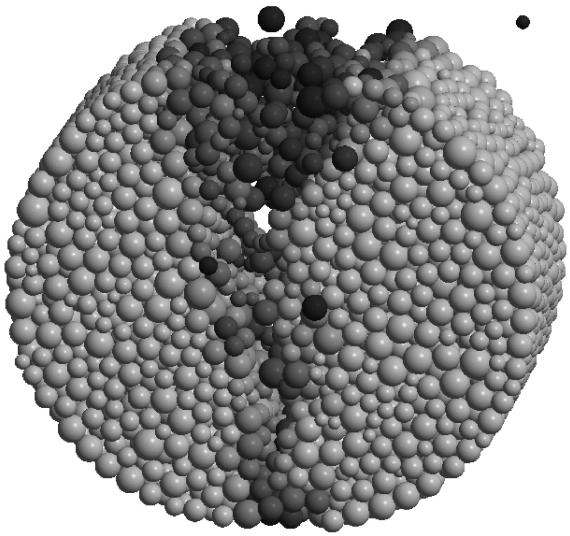

Figure 4.38. Failure mode for 3D BTS test in specimen 1, with k_t/k_n=0.5 and R_t/R_n=1.

BTS test in the 2D case, with a higher value for a stiffness ratio of $k_t/k_n = 0.3$.

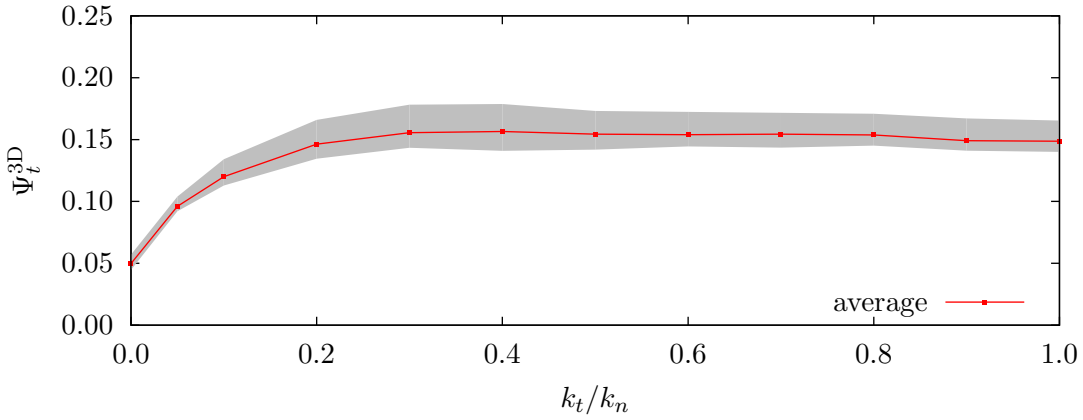

Figure 4.39. Dimensionless scale function of tensile strength Ψ_t^{3D} for different values of k_t/k_n in 3D BTS test, with R_t/R_n=1.

A sample of the curve obtained varying the micro strength ratio R_t/R_n with a fixed value of the micro stiffness ratio (k_t/k_n=0.5) is presented in Figure 4.40. The results for the different specimens present a similar result, and show the expected behaviour, considering the previous 2D and 3D tests.

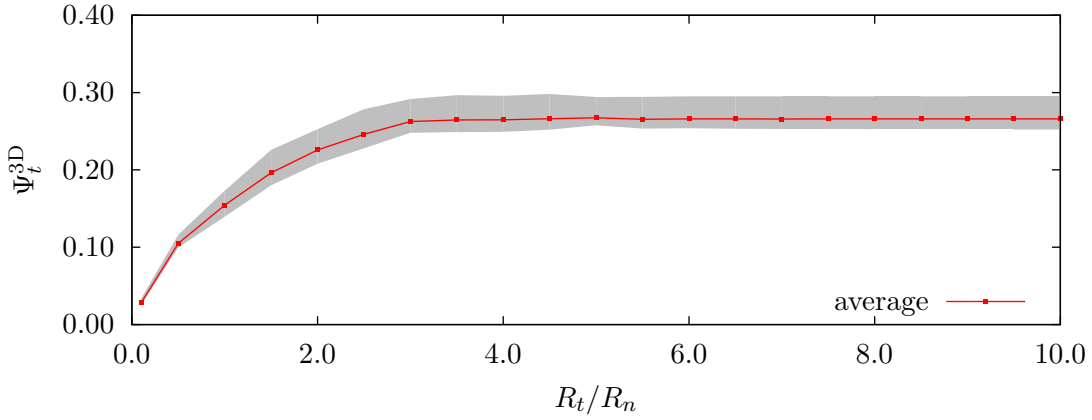

Figure 4.40. Dimensionless scale function of tensile strength Ψ_t^{3D} for different values of R_t/R_n in 3D BTS test, with k_t/k_n=0.5.

The results for the different values are used to generate a contour lines graph, showing the influence of both micro ratios. The graph is presented in Figure 4.41.

The figure shows that the diagonal band is shifted to the left. This means that for values of of micro stiffness ratio k_t/k_n lower than 0.1, the tensile strength does not depend of R_t even for lower values of R_t/R_n. For k_t/k_n=1, the value of the tensile strength is constant for values of R_t/R_n higher that 9.

Again, this behaviour is related to the bonds breakage mechanism. The influence of the micro strength ratio over the failure mechanism is shown in Figure 4.42. In Figure 4.42(a) the influence of shear in the breakage mechanism is shown. A similar behaviour to the previous cases is obtained. It is interesting to note that shear has a higher influence, achieving around 70% of the breakage with higher values of k_t/k_n. The ratio of all broken bonds over the initial number of bonds is presented in Figure 4.42(b). The graph shows a higher value of bonds broken and the same shift of the diagonal band.

Finally, the variation of the strength ratio as a function of the micro stiffness ratio and the micro strength ratio is shown in Figure 4.43. The curve presents a similar behaviour as for the 2D case with smoother isolines. The maximum value achieved for the strength ratio is close to 10.5, for k_t/k_n=0.2 and R_t/R_n=10.

As a conclusion, it is clear that the dimensional analysis can be a useful tool for the estimation of the local parameters. Nevertheless, it requires the use of similar assembly characteristic parameters. In equations (4.25) and (4.26), a parameter related to the

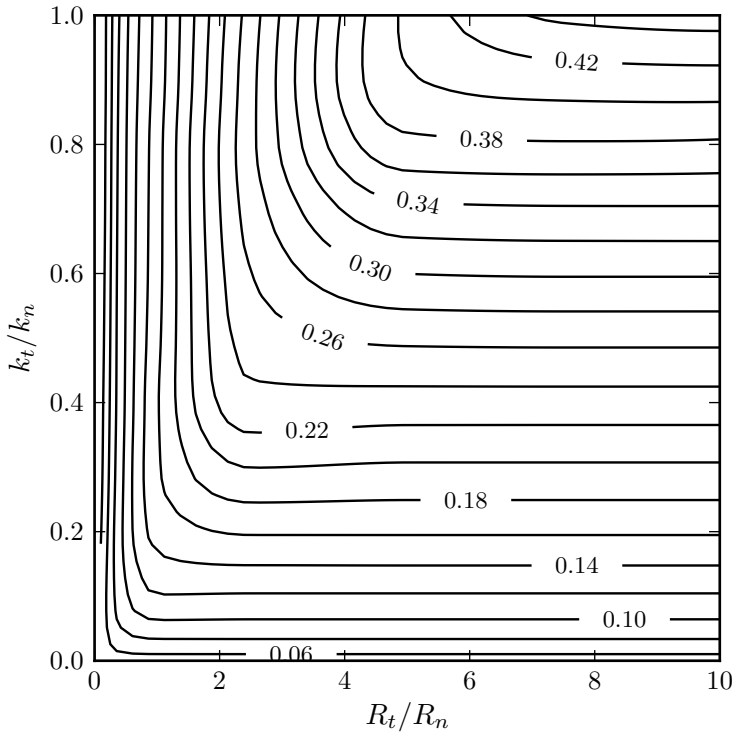

Figure 4.41. Dimensionless scale function of tensile strength Ψ_t^{3D} for different values of k_t/k_n and R_t/R_n in 3D BTS test.

assembly characterization has been included, but has not been completely analyzed. The consideration of the influence of the assembly will be considered in the next section, where micromechanics theory is used for the estimation of the local parameters.

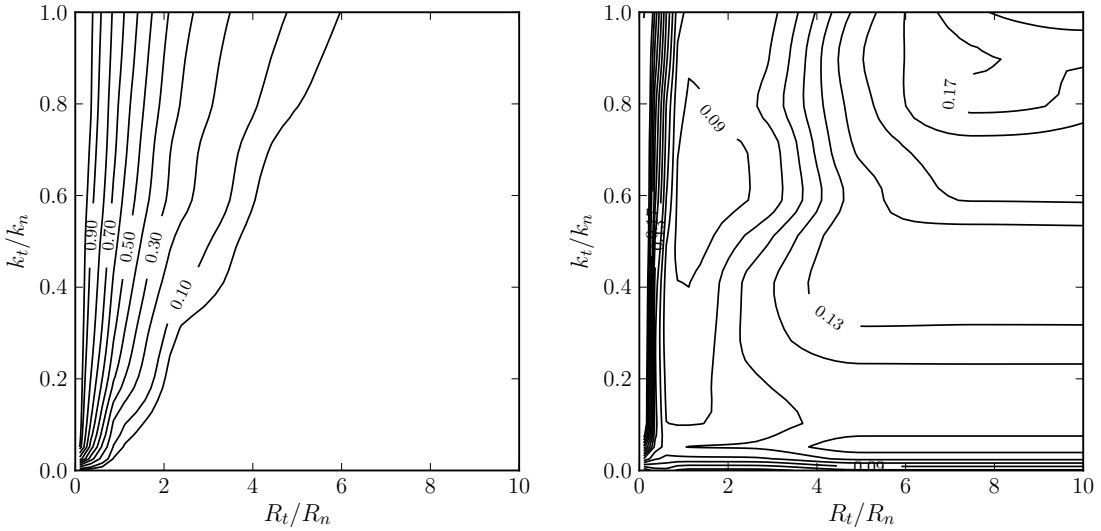

(a) Ratio of bonds broken due to shear over broken bonds ($N^s_{bb}\,/\,N_{bb}$)

(b) Ratio of broken bonds over initial number of bonds ($N_{bb}\,/\,N_c$)

Figure 4.42. Broken bonds for different values of k_t/k_n and R_t/R_n in 3D BTS test.

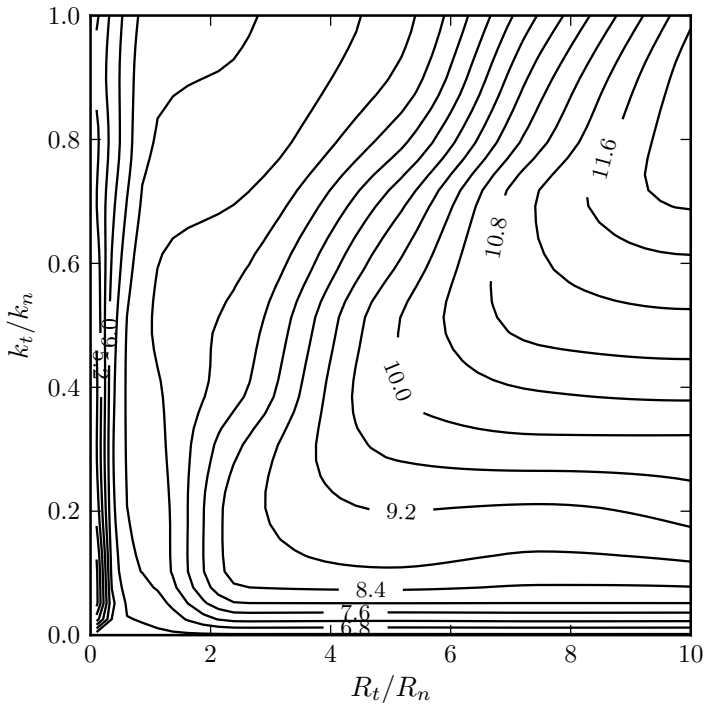

Figure 4.43. Strength ratio σ_c/σ_t for different values of k_t/k_n and R_t/R_n in 3D specimens.

4.3.5 Improving dimensionless number with micromechanics

Even if is not possible to recover completely the mechanical behaviour, it is clear that this formulation allows to redefine the dimensional analysis to improve the estimation, by accounting for the assembly influence.

For a suitably large representative volume with a large number of contacts, the summation of a quantity over all contacts can be expressed in an integral form. Let Q be a quantity dependent upon the orientation of the contact, the summation of such a function over all contacts can be written as

$$\sum_{i=c}^{N_c} Q^c = N_c \int_0^{2\pi} \int_0^{\pi} Q(\gamma,\beta)\xi(\gamma,\beta)\sin\gamma d\gamma d\beta \tag{4.41}$$

where $\xi(\gamma,\beta)$ is the directional distribution density function, which satisfies

$$\int_0^{2\pi} \int_0^{\pi} \xi(\gamma,\beta)\sin\gamma d\gamma d\beta = 1 \tag{4.42}$$

Therefore, recovering the stiffness tensor definition of the equation (4.13), can be re-written as follows

$$C_{ijkl} = \frac{N_c}{V} \int_0^{2\pi} \int_0^{\pi} l_i^c K_{jk}^c l_l^c \xi(\gamma,\beta)\sin\gamma d\gamma d\beta \tag{4.43}$$

If isotropic assemblies are considered, possible correlations between l_i^c and f_j^c are not accounted and the equation above can be simplified as

$$C_{ijkl} = \frac{N_c \overline{l^2}}{V} \int_0^{2\pi} \int_0^{\pi} n_i^c K_{jk}^c n_l^c \xi(\gamma,\beta)\sin\gamma d\gamma d\beta \tag{4.44}$$

where $\overline{l^2}$ is the average of the square branch length over all the contacts. Now, considering the definition of the local stiffness tensor K_{jk} in (4.4), we can rewrite equation (4.44) as

$$C_{ijkl} = \frac{N_c\, k_n\, \overline{l^2}}{V} \int_0^{2\pi} \int_0^{\pi} (n_i(n_j n_k + \frac{k_t}{k_n}(s_j s_k + t_j t_k))n_l)\xi(\gamma,\beta)\sin\gamma d\gamma d\beta \tag{4.45}$$

At this point, we can introduce the *contact density* (m_s). Different authors [67, 104] use

this value as a compaction measure of the assembly. The contact density is defined as

$$m_s = \frac{N_c}{V} \tag{4.46}$$

Nevertheless, at this moment the main interest is recovering the dimensionless relationships. For this purpose, we express the volume in terms of the average radius of the particles and number of particles.

The volume of the domain can be recovered in the 3D case as

$$V = \frac{4\pi N_p \overline{r^3}}{3(1-e)} \tag{4.47}$$

where $\bar{r^3}$ is the average of the cube of the radius. Substituting (4.47) into (4.45) we have

$$C_{ijkl} = \frac{3n_c(1-e)k_n\overline{l^2}}{8\pi\overline{r^3}} \int_0^{2\pi}\int_0^{\pi} (n_i(n_j n_k + \frac{k_t}{k_n}(s_j s_k + t_j t_k))n_l)\xi(\gamma,\beta)\sin\gamma d\gamma d\beta \tag{4.48}$$

Now in the definition of the stiffness tensor we can be see a clear contribution of the characteristic parameters of the assembly.

Many authors have developed different formulations for the definition of the Young's moduli and Poisson's ratio. Nevertheless, for the sake of simplicity, we will use the equation (4.48) in the definition of the dimensionless scale functions (4.23) and (4.24). Considering the influence of the assembly we can redefine, after some algebra, the dimensionless scale functions for the elastic constants as

$$\frac{E\,\tilde{r}}{k_n\,n_c\,(1-e)} = \hat{\Psi}_E^{3\mathrm{D}}\left(\frac{k_t}{k_n}\right) \tag{4.49}$$

$$\nu = \hat{\Psi}_\nu^{3\mathrm{D}}\left(\frac{k_t}{k_n}\right) \tag{4.50}$$

where $\tilde{r}$ is a characteristic radius reflecting the size of the particles and its distribution, defined as

$$\tilde{r} = \frac{4\,\overline{r^3}}{\overline{l^2}} \tag{4.51}$$

Note that the Poisson's ratio scale function does have not any correction factor. The same

is shown by Liao et al. [75] using the Voight hypothesis.

In the 2D case, the volume can be written in terms of the area in a cylindrical particles and its thickness as

$$V = A\,t = \frac{2\pi N_p \overline{r^2} t}{(1-e)} \tag{4.52}$$

Now, considering a unit thickness for the cylindrical particles, the characteristic length of the equation (4.21) can be re-written in a similar way as

$$\tilde{r} = \frac{4\,\overline{r^2}}{\overline{l^2}} \tag{4.53}$$

and the new dimensionless scale function for the Young modulus can be written as

$$\frac{E\,\tilde{r}}{k_n\,n_c\,(1-e)} = \hat{\Psi}_E^{\mathrm{2D}}\left(\frac{k_t}{k_n}\right) \tag{4.54}$$

$$\nu = \hat{\Psi}_\nu^{\mathrm{2D}}\left(\frac{k_t}{k_n}\right) \tag{4.55}$$

The dimensionless numbers defined for 2D in (4.54) and (4.55), and for 3D in (4.49) and (4.50), allow us to *normalize* the obtained values, taking into account the influence of the assembly. This yield a more accurate dimensionless scale curves.

The new dimensionless scale functions for the Young modulus in 2D and 3D specimens are shown in Figure 4.44 and 4.45, respectively. It can be seen that the dimensionless scale function presents a better agreement between both specimens.

The same idea can be applied for the strength parameters. Considering Hooke's law (4.12) and the uniform strain hypothesis (4.8), a similar derivation is performed. The new dimensionless scale function for strength parameters are re-defined as follows

$$\frac{\sigma_c\,\widetilde{A}}{R_n\,n_c\,(1-e)} = \hat{\Psi}_c\left(\frac{R_t}{R_n}, \frac{k_t}{k_n}, \mu\right) \tag{4.56}$$

$$\frac{\sigma_t\,\widetilde{A}}{R_n\,n_c\,(1-e)} = \hat{\Psi}_t\left(\frac{R_t}{R_n}, \frac{k_t}{k_n}, \mu\right) \tag{4.57}$$

where $\widetilde{A}$ is written for 2D and 3D cases as the square of the characteristic radius, i.e.

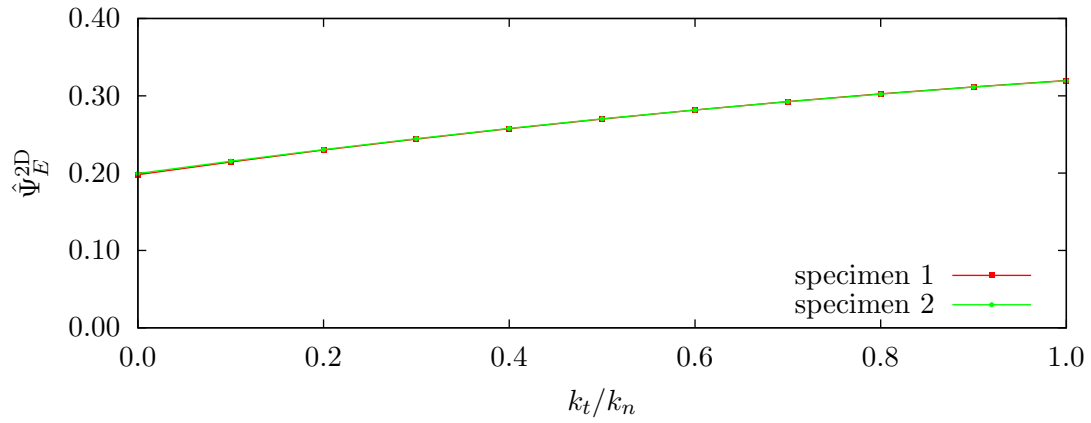

Figure 4.44. Modified dimensionless scale function of Young modulus $\hat{\Psi}_E^{2D}$ for different values of k_t/k_n in 2D specimens.

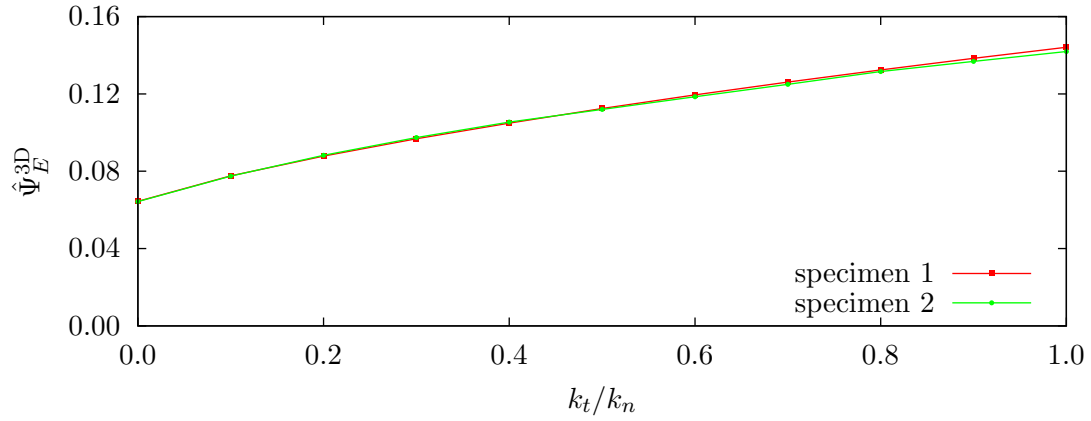

Figure 4.45. Modified dimensionless scale function of Young modulus $\hat{\Psi}_E^{3D}$ for different values of k_t/k_n in 3D specimens.

$$\widetilde{A}_{2D} = \widetilde{r^2}_{2D} = \frac{2\,\overline{r^2}\,t}{\bar{l}} \tag{4.58}$$

$$\widetilde{A}_{3D} = \widetilde{r^2}_{3D} = \frac{2\,\overline{r^3}}{\bar{l}} \tag{4.59}$$

With this change in the dimensionless scale function for the strength parameters, the new contour line graphs are presented in Figure 4.46 for the 2D case. The graphs do not presents a visible improvement in comparison with the standard curves (Figure 4.21 and 4.28). The range of values for the different specimens decreases 2% versus the standard curves.

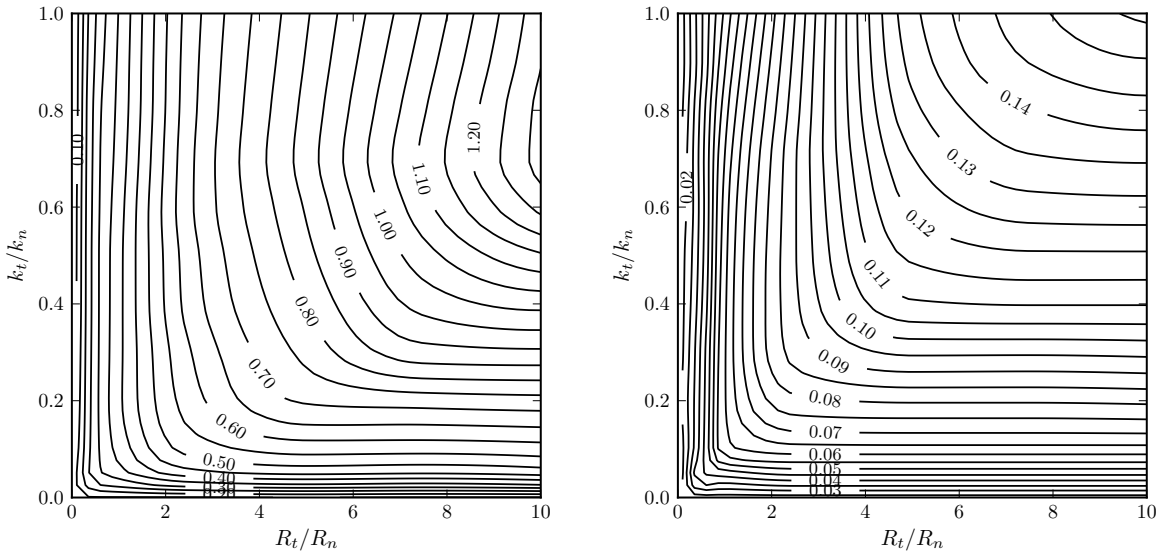

(a) Dimensionless scale function of compressive strength ($\hat{\Psi}_c^{2D}$)

(b) Dimensionless scale function of tensile strength ($\hat{\Psi}_t^{2D}$)

Figure 4.46. Modified dimensionless scale function of compressive and tensile strength for different values of k_t/k_n and R_t/R_n in 2D specimens.

The improved dimensionless scale functions for the compressive and tensile strength parameters in the 3D case are shown in Figure 4.47. Similar to the 2D case, the range of values does not presents a visible improvement versus the results of Figures 4.34 and 4.41. Nevertheless, are 4.6% lower than for the standard curves.

4.4 Parameter estimation

Based in the dimensional analysis and micromechanics, it is possible to predict the contact model parameters in order to reproduce a specific mechanical properties. In this section, the methodology for the estimation of the model parameters is presented for both, 2D and 3D cases.

In order to verify the parameter estimation procedure, the simulation of a predefined material for the UCS test is performed. The material properties considered are presented in Table 4.7.

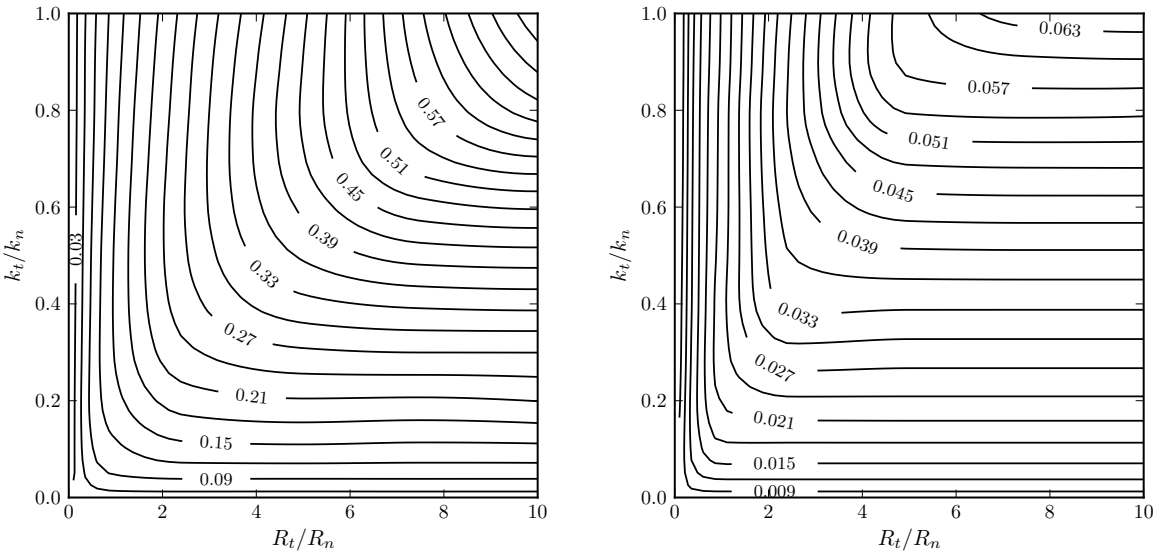

(a) Dimensionless scale function of compressive strength ($\hat{\Psi}_c^{3D}$)

(b) Dimensionless scale function of tensile strength ($\hat{\Psi}_t^{3D}$)

Figure 4.47. Modified dimensionless scale function of compressive and tensile strength for different values of k_t/k_n and R_t/R_n in 3D specimens.

Mechanical properties		Value
E	Young modulus (GPa)	18.691
ν	Poisson ratio	0.20
σ_c	Uniaxial compressive strength (MPa)	127.83
σ_t	Brazilian tensile strength (MPa)	12.30
ρ	Density (kg/m^2)	2580

Table 4.7. Mechanical properties for parameter estimation procedure verification.

The main idea of the parameter estimation procedure is to estimate the elastic constants based in micromechanics or the dimensionless scaling functions, depending if a 2D or a 3D case is considered. The micro strength parameters are estimated with the curves based in the micro strength and micro stiffness relationships presented in the dimensional analysis. The study of the micro strength relationships shows that friction affect the strengths just for certain values of micro strength ratio due to the breakage mechanisms. This friction effect can be considered as a correction factor for the dimensional scale function of strengths. Considering this, the dimensionless scaling

function for the micro strength is redefined as

$$\frac{\sigma_c \widetilde{A}}{R_n n_c (1-e)} = \hat{\Psi}_c \left(\frac{R_t}{R_n}, \frac{k_t}{k_n} \right) \psi(\mu) \tag{4.60}$$

where $\hat{\Psi}_c$ is now restricted to the influence of the micro strength and micro stiffness ratios, and the influence of Coulomb friction coefficient is considered as a correction factor, defined by ψ. The correction factor is defined by the curves relating its influence to the dimensionless number, as shown in Figure 4.24 for the 2D case and in Figure 4.37 for the 3D case.

4.4.1 Parameter estimation for two-dimensional case

In this case, elastic constants can be estimated directly from the micromechanics equation. For the strength parameters, the dimensionless scale function defined in the previous sections can be used. The methodology used for the estimation of the parameters it as follows.

Methodology:

1. Considering a defined particle assembly, with known characterization parameters, the micro stiffnesses (k_n and k_t) can be calculated using the micromechanics equations (4.18) and (4.19).

2. Assuming that the strength ratio is satisfied by the curve of Figure 4.30, the micro strength ratio R_t/R_n can be recovered directly from that curve.

3. If the strength ratio of the original material is higher than the maximum strength ratio, the maximum strength ratio of the curve is considered, and one of the dimensionless scaling function of compressive or tensile strength is used, depending of the dominant breakage mechanism we want to reproduce.

4. With the value of the micro strength ratio, the normal and tangential micro strengths can be estimated using the average value of the curves in Figure 4.46(a) and 4.46(b).

5. Taking into account Figure 4.24, if the micro strength ratio R_t/R_n is small, a correction of the dimensionless scale function for strengths is required taking into account the Coulomb friction coefficient. This correction can be estimated depending of the fraction of bonds broken due to shear, as shown in Figure 4.29(a).

Based on this methodology, a verification sample is defined considering a new specimen. A UCS test with the new specimen is performed, considering the material properties of Table 4.7.

For the verification sample, an assembly of 30480 cylindrical particles with a characteristic radius $\tilde{r}$= 0.15365 mm is used. The assembly has a porosity of 9.2121% and a coordination number of 5.9841.

The micro stiffnesses can be calculated directly from the assembly and the elastic constants, as k_n=14.392 GN/m and k_t=2.868 GN/m. Following the methodology presented before, the micro strength parameters are estimated with the respective curves. Taking the micro stiffness ratio k_t/k_n=0.1992774, from Figure 4.30 we can extract the curve of the macro strength ratio versus micro strength ratio, as shown in Figure 4.48.

As the strength ratio σ_c/σ_t=10.3927 (Table 4.7), is higher than the maximum value of the curve (σ_c/σ_t=9.3647), the compressive strength is taken as reference, with the micro strength ratio taken as R_t/R_n=10. Once the values of micro stiffness ratio and micro strength ratio are defined, the dimensionless scale function for the compressive strength is

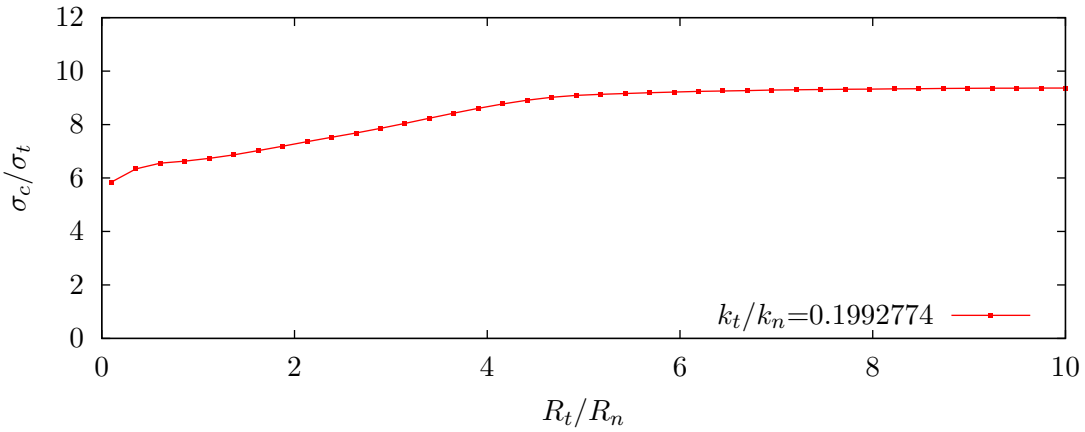

Figure 4.48. Macro strength ratio vs micro strength ratio for verification specimen in 2D, with k_t/k_n=0.079595.

calculated using Figure 4.46(a), as Ψ_c^{2D}=0.710. The micro strength in the normal direction is then calculated as R_n=4.9623 kN, and the micro strength in the tangential direction is R_t=49.623 kN. For values of R_t/R_n higher than 4.0, we know from Figure 4.24 that friction do not affect the strengths. The micro parameters obtained are summarized in Table 4.8.

Parameter	Description	Value
μ	Coulomb friction coefficient	0.8000
k_n	Normal stiffness (GN/m)	14.392
k_t	Tangential stiffness (GN/m)	2.8680
R_n	Normal bond strength (kN)	4.9623
R_t	Tangential bond strength (kN)	49.623
ρ'	Scaled density (kg/m^3)	2841.8

Table 4.8. Contact model parameters obtained for 2D UCS verification test specimen.

In Figure 4.49, the damage and failure mode in the 2D specimen is shown.

After the simulation of the UCS test, the mechanical properties of the virtual specimen are estimated and compared with the original properties of the material. In Figure 4.50, the strain vs stress curve is depicted. The curve presents a change in the elastic modulus due to homogeneous damage that starts with a stress close to σ=65 MPa. The resulting mechanical properties obtained are presented in Table 4.9.

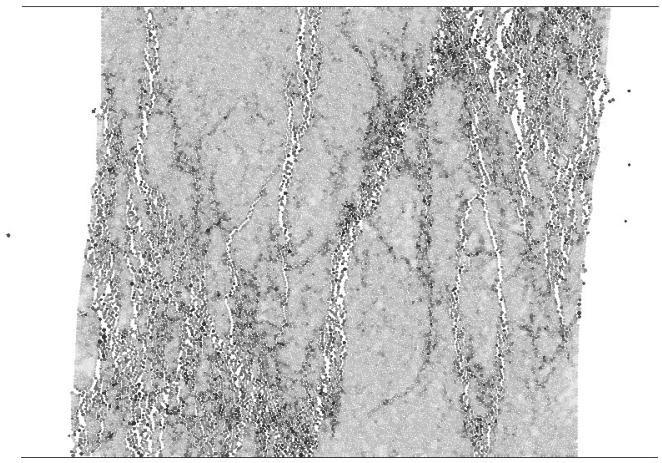

Figure 4.49. Failure mode in 2D UCS verification test.

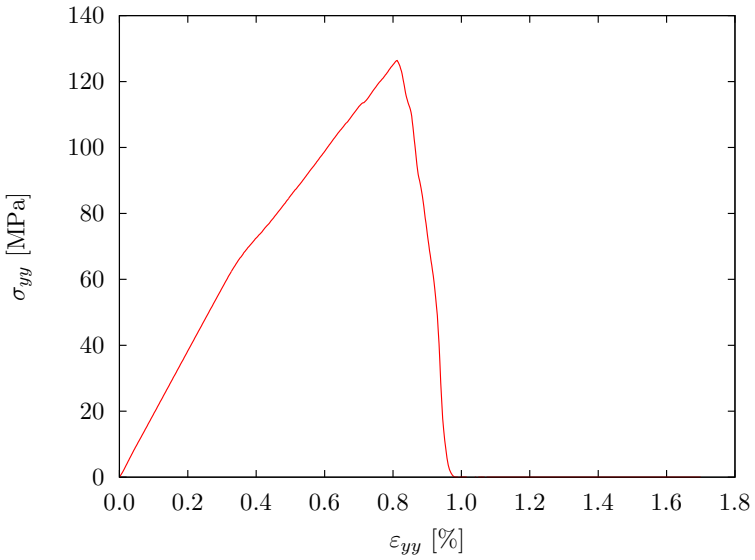

Figure 4.50. Curve stress vs strain for 2D UCS verification test.

Mechanical properties	Original	Simulation
Young modulus (GPa)	18.691	18.630
Poisson ratio	0.20	0.2009
Uniaxial compressive strength (MPa)	127.83	126.38

Table 4.9. Comparison of results in 2D UCS verification test.

A good agreement is obtained for the elastic constants is observed. For the compressive strength, an error around 2% for the values of Table 4.9 is found. The values can be

considered as a good approximation, and the parameter estimation methodology can be considered successful.

4.4.2 Parameters estimation for three-dimensional case

For the three-dimensional problem a similar strategy is used to identify the macro parameters. A similar strategy is used to identify the micro parameters for the 3D UCS test. The main difference with the methodology used in the 2D case is the estimation of the stiffnesses. Here, the stiffnesses are estimated using the dimensionless scaling function, not the micromechanics equations. The different steps considered for the estimation parameters are presented below.

Methodology:

1. Considering a defined particles assembly and the Poisson's ratio, the micro-stiffness ratio is estimated from the curve of Figure 4.17.

2. With the micro-strength ratio and the characterization parameters of the assembly, the normal contact stiffness (k_n) is estimated from the curve of Figure 4.45.

3. If the strength ratio satisfied the curve in Figure 4.43, the micro strength ratio R_t/R_n can be obtained considering the average value of the curve.

4. In case that the strength ratio of the original material is higher than the maximum strength ratio, the maximum strength ratio of the curve is considered, and one of the dimensionless scaling function for strength (compression or tension) should be used, depending of the dominant breakage mechanism to be reproduced.

5. Taking the values of micro strength and micro stiffness ratios, the normal and tangential micro strengths are estimated using the average value of the curves in Figure 4.47.

6. For a low value of the micro strength ratio, and depending of the influence of tangential breakage mechanism, the micro strength parameters should be corrected using the curves in Figure 4.37.

The verification of the parameters estimation procedure is performed in the same way that the 2D case. A 3D UCS test is performed considering the mechanical properties presented in Table 4.7. The characterization of the particle assembly considered for the simulation is presented in Table 4.10, with 28371 particles and an average radius

Parameter	Description	Value
N_p	Number of particles	28371
e	Estimated porosity (%)	27.450
n_c	Coordination number	9.3921
$\bar{r}$	Average radius (mm)	0.8431
$\widetilde{r}$	Characteristic radius (mm)	0.8431

Table 4.10. Characterization of the particle assembly in 3D UCS verification test.

of 0.8431 mm.

The estimation of the micro stiffness ratio is made in terms of the Poisson's ratio in Figure 4.17, obtaining k_t/k_n=0.19248. With the stiffness ratio, the normal stiffness is estimated considering the improved dimensionless scale function in Figure 4.45 as k_n=28.954 MN/m. Then, the tangential stiffness is recovered using the micro stiffness ratio, obtaining k_t=2.9397 MN/m.

For the estimation of the micro strength parameters, the curve of macro strength ratio vs micro strength ratio is obtained from Figure 4.43, for the micro stiffness ratio estimated before, as shown in Figure 4.51.

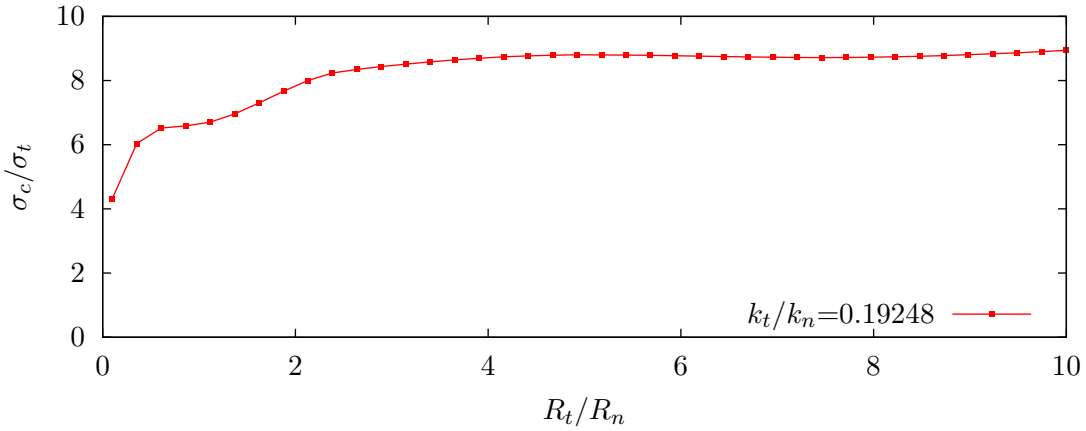

Figure 4.51. Macro strength ratio vs micro strength ratio for 3D UCS verification test, with k_t/k_n=0.19248.

The curve in Figure 4.51 presents a maximum value of σ_c/σ_t=8.938. This is lower than the value to be reproduced which is 10.392. As the exact value of the strength ratio can not be reproduced, the micro strength ratio for the simulation is selected as R_t/R_n=10, and the estimation of the strength parameters is made considering the dimensionless scale

function of compressive strength. Based in the improved dimensionless scale function of compressive strength in Figure 4.47, the curve obtained for the estimated value of the micro strength ratio is depicted in Figure 4.52.

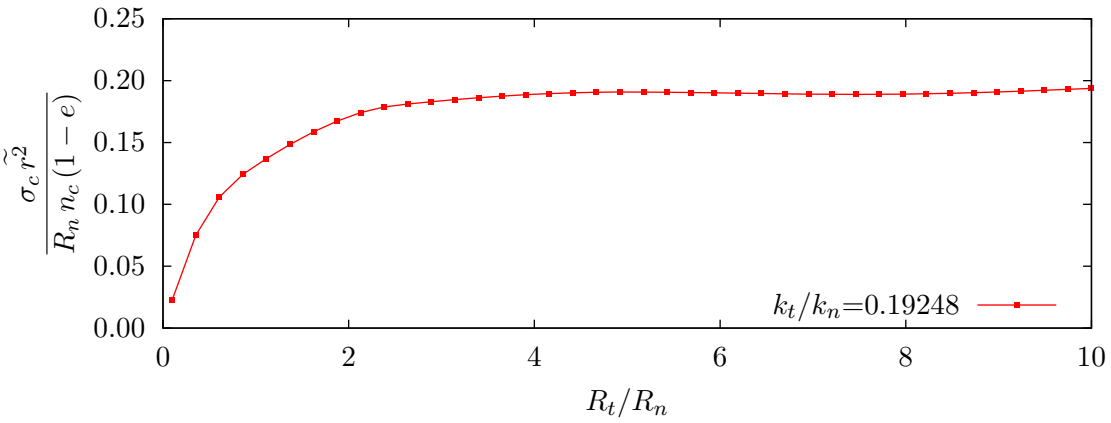

Figure 4.52. Dimensionless scale function of compressive strength vs micro strength ratio for 3D UCS verification test, with k_t/k_n=0.19248.

The micro strength in the normal direction is calculated considering R_t/R_n=10.0 in the dimensionless scale function, as R_n=91.971 N. The micro strength in the tangential direction is recovered using the micro strength ratio, as R_t=919.71 N.

In order to verify the influence of the proposed correction factors and the micromechanics considerations for the particle assembly characterization, the same simulation is performed using a standard estimation of the parameters, i.e. considering the dimensionless scaling function for normal stiffness of Figure 4.16, and the dimensionless scale function of micro strength in the normal direction of Figure 4.34, without any corrections. The model parameters estimated in both cases are summarized in Table 4.11.

The stress vs strain curve for the specimen with the contact model parameters with the improved dimensionless scale functions is presented in Figure 4.53, where it is compared with the curve obtained for the micro parameters obtained with the standard dimensionless scale functions.

The results of the simulation are shown in Table 4.12 for both cases, with and without correction factors. It is interesting to verify the improvement in the results for the elastic constants and compressive strength. The elastic constants in the simulation without the corrected parameters show lower values for the Young modulus and the Poisson's ratio.

Parameter	Description	Standard	Improved
μ	Coulomb friction coefficient	0.800	0.800
k_n	Normal stiffness (MN/m)	26.6181	27.889
k_t	Tangential stiffness (MN/m)	2.70248	5.3681
R_n	Normal bond strength (N)	84.550	91.971
R_t	Tangential bond strength (N)	591.85	643.80
ρ'	Scaled density (kg/m^3)	3556.2	3556.2

Table 4.11. Standard and improved model parameters for 3D UCS verification test.

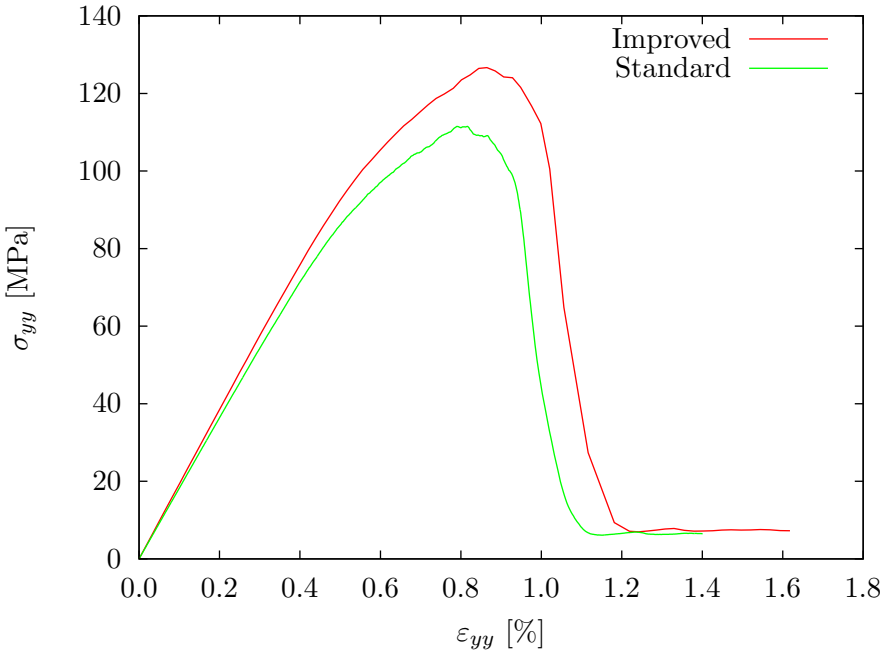

Figure 4.53. Comparison of strain vs stress curve in 3D UCS verification test, considering standard and improved dimensionless scale functions.

This can be explained with the lower value of the coordination number found in the assembly, which clearly decreases the global stiffness.

The compressive strength for the corrected parameters present a good agreement with the original value. The estimated micro strength parameters are increased for the consideration of the assembly characterization parameters, showing again an improved result.

Mechanical property		Original	Standard	Improved
E	Young modulus (MPa)	18691	17355	18652
ν	Poisson ratio	0.20	0.1913	0.2012
σ_c	Uniaxial compressive strength (MPa)	127.83	111.50	126.12

Table 4.12. Comparison of results in 3D UCS verification test, considering standard and improved dimensionless scale functions.

The parameter estimation procedure it is considered successful in both 2D and 3D cases, showing that the improvements made in the estimation procedure are correct.
$\hat{\Psi}$ Even if it is possible to reproduce the mechanical behaviour of rock materials, the contact model present a problem in the reproduction of materials with high strength ratio ratio. Different authors have been considered modified versions of the contact model in order to solve this problem. Nevertheless for the simulations made in the framework of this work, the model here proposed is considered to be sufficient.

Chapter 5

Coupling scheme with the finite element method

As shown in the previous chapters, the DEM is a good alternative to continuum based methods for the simulation of problems characterized by all kinds of discontinuities and material failure dominated by fracture. In most cases, the material failure is localized in a portion of the domain while the rest of the domain has a behaviour that can be represented as a continuum. This fact, and the consideration of the computational cost involved by the DEM, make interesting the possibility to simulate adjacent sub-domains employing the most suited simulation technique for each of them. This chapter presents the theoretical formulation and the numerical implementation of a procedure for coupling the DEM with the FEM. The idea considers the use of the DEM in the region, or sub-domain, where failure will be produced and the FEM in the rest of the domain. This allows taking advantage of the best functions of each method in each sub-domain and makes more efficient the numerical simulation.

In the next section, the formulation of the finite element method is summarized. Then, the basis of the coupling scheme of finite and discrete element methods is presented. Finally, the adaptivity algorithm for the coupling scheme is developed.

5.1 The finite element method

The finite element method implemented is developed within the so-called explicit dynamic formulation. The explicit finite element method is based in the solution of the discretized equations of motion written in the current configuration. The present formulation uses a mixed displacement-pressure formulation, stabilized by an orthogonal sub-scale approach in order to avoid the volumetric locking with linear triangles and tetrahedra.

5.1.1 Non-linear transient dynamic formulation

In the non-linear transient dynamic formulation the equation of motion for a solid material can be written in as

$$-\rho\frac{\partial^2 u_i}{\partial t^2} + \frac{\partial^2 \sigma_{ij}}{\partial {x_j}^2} + b_i = 0 \tag{5.1}$$

where ρ is density, t is time, σ_{ij} are the stress and b_i are the body forces. Equation (5.1) is completed with the boundary conditions in displacements u_i and the equilibrium in surface tractions

$$u_i - \bar{u_i} = 0 \qquad \text{on } \Gamma_u \tag{5.2}$$

$$\sigma_{ij} n_j - \bar{t_i} = 0 \qquad \text{on } \Gamma_t \tag{5.3}$$

In the above $\bar{u_i}$ and $\bar{t_i}$ are prescribed displacements and tractions over the boundaries Γ_u and Γ_t, respectively.

Employing a standard split of stresses into deviatoric and volumetric (pressure) parts, s_{ij} and p, respectively

$$\sigma_{ij} = s_{ij} + p\delta_{ij} \tag{5.4}$$

where δ_{ij} is the Kronecker delta function.

The linear elastic constitutive equations for the deviatoric stress s_{ij} are written as

$$s_{ij} = 2G(\varepsilon_{ij} - \frac{1}{3}\varepsilon_v \delta_{ij}) \tag{5.5}$$

where G is the shear modulus,

$$\varepsilon_{ij} = \frac{1}{2}\left(\frac{\partial u_i}{\partial x_j} + \frac{\partial u_j}{\partial x_i}\right) \quad \text{and} \quad \varepsilon_v = \varepsilon_{ii} \tag{5.6}$$

Note that the Einstein's summation convention is used.
The pressure equation is written as

$$\frac{p}{K} - \frac{\partial u_i}{\partial x_i} = 0 \tag{5.7}$$

where K is the bulk modulus.

The governing equations of the mixed displacement-pressure formulation can be

obtained then in the form

$$-\rho\frac{\Delta v_i}{\Delta t}+\frac{\partial s_{ij}}{\partial x_j}+\frac{\partial p}{\partial x_i}+b_i=0 \tag{5.8a}$$

$$\frac{\Delta u_i}{\Delta t}-v_i^{n+1/2}=0 \tag{5.8b}$$

$$\frac{\Delta p}{K}-\frac{\partial(\Delta u_i)}{\partial x_i}=0 \tag{5.8c}$$

where $\Delta v_i = v_i^{t+1/2} - v_i^{t-1/2}$, $\Delta u_i = u_i^{t+1} - u_i^t$ and $\Delta p = p^{t+1} - p^t$ are the increments of velocity, displacement and pressure, respectively.

Introducing the concept of orthogonal sub-scale approach developed by Codina in [30, 31] and later employed for elasticity and elasto-plasticity problems [21, 27, 28, 85], Equation (5.1) is split now as

$$\pi_i+\frac{\partial p}{\partial x_i}=0 \tag{5.9}$$

where

$$\pi_i=-\rho\frac{\partial v_i}{\partial t}+\frac{\partial s_{ij}}{\partial x_i}+b_i \tag{5.10}$$

The term π_i is the part of equation (5.1) not containing the pressure gradient and may be considered as the negative of a projection of the pressure gradient. In a discrete setting, the term π_i can be considered belonging to a *sub-scale* space orthogonal to that of the pressure gradient terms.

The weighted residual form of the governing equations can be written in the form

$$\int_\Omega \delta u_i\rho\frac{\Delta v_i}{\Delta t}\mathrm{d}\Omega+\int_\Omega \delta\epsilon_{ij}\sigma_{ij}\mathrm{d}\Omega-\int_\Omega \delta u_i b_i\mathrm{d}\Omega-\int_{\Gamma_t}\delta u_i\bar{t}_i\mathrm{d}\Gamma_t=0 \tag{5.11}$$

$$\int_\Omega \delta v_i\left[\frac{\Delta u_i}{\Delta t}-v_i\right]\mathrm{d}\Omega=0 \tag{5.12}$$

$$\int_\Omega q\left(\frac{\Delta p}{K}-\frac{\partial(\Delta u_i)}{\partial x_i}\right)\mathrm{d}\Omega+\int_\Omega\frac{\partial q}{\partial x_i}\left(\frac{\partial p}{\partial x_i}+\pi_i\right)=0 \tag{5.13}$$

$$\int_\Omega w\left(\pi_i+\frac{\partial p}{\partial x_i}\right)\mathrm{d}\Omega=0 \tag{5.14}$$

5.1.2 Finite element discretization

We choose C^0 continuous linear interpolations of the displacements, pressure and pressure gradient projection π_i over three-node triangles (2D) and four-node tetrahedra (3D). The linear interpolations are written as

$$u_i = \sum_{j=1}^{n} N_j \bar{u_i^j} \tag{5.15}$$

$$p = \sum_{j=1}^{n} N_j \bar{p^j} \tag{5.16}$$

$$\pi_i = \sum_{j=1}^{n} N_j \bar{\pi_i^j} \tag{5.17}$$

where $n = 3(4)$ for 2D (3D) problems and $\bar{(\cdot)}$ denotes nodal variables. N_j are the linear shape functions [114].

Substituting the approximations into Equations (5.11)–(5.14) gives the following system of discretized equations:

$$\mathbf{M}\frac{\Delta\bar{\mathbf{v}}}{\Delta t} - \mathbf{R}_v + \mathbf{f}_d = 0 \tag{5.18}$$

$$\frac{\Delta\bar{\mathbf{u}}}{\Delta t} - \bar{\mathbf{v}} = 0 \tag{5.19}$$

$$\mathbf{C}^T\Delta\bar{\mathbf{u}} - \mathbf{M}_p\Delta\bar{\mathbf{p}} - \mathbf{L}\bar{\mathbf{p}} - \mathbf{Q}\bar{\boldsymbol{\pi}} = 0 \tag{5.20}$$

$$\mathbf{Q}^T\bar{\mathbf{p}} + \bar{\mathbf{G}}\bar{\boldsymbol{\pi}} = 0 \tag{5.21}$$

where the element contributions are given by

$$\begin{aligned} \mathbf{L} &= \int_\Omega (\nabla\mathbf{N})^{\mathrm{T}}\boldsymbol{\tau}\nabla\mathbf{N}\mathrm{d}\Omega, \quad \bar{\mathbf{G}} = \int_\Omega \mathbf{N}^{\mathrm{T}}\boldsymbol{\tau}\mathbf{N}\mathrm{d}\Omega \\ \mathbf{f}_d &= \int_\Omega \mathbf{B}^{\mathrm{T}}\boldsymbol{\sigma}\mathrm{d}\Omega, \qquad\qquad \mathbf{Q} = \int_\Omega (\nabla\mathbf{N})^{\mathrm{T}}\boldsymbol{\tau}\mathbf{N}\mathrm{d}\Omega \end{aligned} \tag{5.22}$$

where $\mathbf{B}$ is the linear stress-strain operator matrix, and

$$\boldsymbol{\tau} = \begin{bmatrix} \tau_1 & 0 & 0 \\ 0 & \tau_2 & 0 \\ 0 & 0 & \tau_3 \end{bmatrix} \tag{5.23}$$

The matrices $\mathbf{M}$, $\mathbf{M}_p$, $\mathbf{C}$, $\mathbf{R}_v$ are defined as

$$\begin{aligned} \mathbf{M} &= \int_{\Omega} \rho \mathbf{N}_v^{\mathrm{T}} \mathbf{N}_v \mathrm{d}\Omega, & \mathbf{M}_p &= \int_{\Omega} \frac{1}{K} \mathbf{N}_p^{\mathrm{T}} \mathbf{N}_p \mathrm{d}\Omega \\ \mathbf{R}_v &= \int_{\Gamma} \mathbf{N}_p^{\mathrm{T}} \hat{\mathbf{t}} \mathrm{d}\Gamma + \int_{\Omega} \mathbf{N}_p^{\mathrm{T}} \mathbf{b} \mathrm{d}\Omega, & \mathbf{C} &= \int_{\Omega} \mathbf{N}_v^{\mathrm{T}} \nabla \mathbf{N}_p \mathrm{d}\Omega \end{aligned} \tag{5.24}$$

In the case of explicit solution, the two matrices $\mathbf{M}$ and $\mathbf{M}_p$ are usually diagonalized. In the discretization procedure the same interpolation has been assumed for all the discretized fields: $\mathbf{N}_v = \mathbf{N}_p = \mathbf{N}_\pi = \mathbf{N}$.

We can then define a four steps semi-implicit time integration algorithm as follows:

Step 1 Compute the nodal velocities $\bar{\mathbf{v}}^{n+1/2}$

$$\bar{\mathbf{v}}^{n+1/2} = \bar{\mathbf{v}}^{n-1/2} + \Delta t\, \mathbf{M}^{-1} \left(\mathbf{R}_v^n - \mathbf{f}_d^n \right) \tag{5.25}$$

Step 2 Compute the nodal displacements $\bar{\mathbf{u}}^{n+1}$

$$\bar{\mathbf{u}}^{n+1} = \bar{\mathbf{u}}^{n-1} + \Delta t\, \bar{\mathbf{v}}^{n+1/2} \tag{5.26}$$

Step 3 Compute the nodal pressures $\bar{\mathbf{p}}^{n+1}$

$$\bar{\mathbf{p}}^{n+1} = \left[\mathbf{M}_p - \mathbf{L} \right]^{-1} \left[\Delta t\, \mathbf{C}^{\mathrm{T}}\, \bar{\mathbf{v}}^{n+1/2} + \mathbf{M}_p\, \bar{\mathbf{p}}^n - \mathbf{Q}\, \bar{\boldsymbol{\pi}}^n \right] \tag{5.27}$$

Step 4 Compute the nodal projected pressure gradients $\bar{\boldsymbol{\pi}}^{n+1}$

$$\bar{\boldsymbol{\pi}}^{n+1} = -\bar{\mathbf{G}}^{-1}\, \mathbf{Q}^{\mathrm{T}}\, \bar{\mathbf{p}}^{n+1} \tag{5.28}$$

In above matrices, $\mathbf{M}$, $\mathbf{M}_p$, $\mathbf{L}$, $\mathbf{C}$, $\mathbf{Q}$, and $\mathbf{G}$ are evaluated at t^{n+1}.

Note that the steps (1), (2) and (4) are fully explicit. A fully explicit algorithm can be obtained by computing $\bar{\mathbf{p}}^{n+1}$ from step (3) in Equation (5.27) as follow:

$$\bar{\mathbf{p}}^{n+1} = \mathbf{M}_p^{-1} \left[\Delta t\, \mathbf{C}^{\mathrm{T}}\, \bar{\mathbf{v}}^{n+1/2} + \left(\mathbf{M}_p - \mathbf{L} \right) \bar{\mathbf{p}}^n - \mathbf{Q}\, \bar{\boldsymbol{\pi}}^n \right] \tag{5.29}$$

Obviously, the explicit solution is efficient if diagonal form of the matrices $\mathbf{M}_p$, $\mathbf{M}$ and $\bar{\mathbf{G}}$ are used. The explicit solution is possible if certain compressibility is assumed, i.e. $K \neq 0$. If $K \to \infty$ pressure must be obtained using the implicit scheme given by Equation (5.27).

5.1.3 General discrete/finite element dynamic formulation

The general algorithm for the transient dynamic problem involving discrete elements and finite elements includes the following steps [84]:

Step 1 Compute nodal velocities

Discrete elements

$$\dot{\mathbf{u}}_i^{n+1/2} = \dot{\mathbf{u}}_i^{n-1/2} + \ddot{\mathbf{u}}_i^n \Delta t \quad \text{with} \quad \ddot{\mathbf{u}}_i^n = \mathbf{F}_i^n / m_i \tag{5.30}$$

$$\boldsymbol{\omega}_i^{n+1/2} = \boldsymbol{\omega}_i^{n-1/2} + \dot{\boldsymbol{\omega}}_i^n \Delta t \quad \text{with} \quad \dot{\boldsymbol{\omega}}_i^n = \mathbf{T}_i^n / I_i \tag{5.31}$$

Finite elements

$$\dot{\mathbf{u}}_i^{n+1/2} = \dot{\mathbf{u}}_i^{n-1/2} + \Delta t \mathbf{M}_d^{-1} (\mathbf{f}^n - \mathbf{g}^n) \tag{5.32}$$

Step 2 Compute nodal displacements

Discrete elements

$$\mathbf{u}_i^{n+1} = \mathbf{u}_i^n + \dot{\mathbf{u}}_i^{n+1/2} \Delta t \tag{5.33}$$

$$\Delta\theta_i^{n+1} = \omega_i^{n+1/2} \Delta t \tag{5.34}$$

Finite elements

$$\mathbf{u}_i^{n+1} = \mathbf{u}_i^n + \dot{\mathbf{u}}_i^{n+1/2} \Delta t \tag{5.35}$$

Step 3 Compute the nodal pressure

Finite elements

$$\bar{\mathbf{p}}^{n+1} = [\mathbf{C} + \mathbf{L} - \mathbf{S}]^{-1} \left[\Delta t \mathbf{G}^T \dot{\bar{\mathbf{u}}}^{n+1/2} + \mathbf{C} \bar{\mathbf{p}}^n \right] \tag{5.36}$$

Step 4 Update the nodal coordinates

Discrete and finite elements

$$\mathbf{x}_i^{n+1} = \mathbf{x}_i^n + \Delta \bar{\mathbf{u}} = \mathbf{x}_i^n + (\bar{\mathbf{u}}^{n+1} - \bar{\mathbf{u}}^n) \tag{5.37}$$

Step 5 Update residual force vector

Go to the Step 1

5.2 Coupling scheme

A special coupling algorithm is used to impose constraints between the subdomains with different scale modelling. The idea of the coupling follows the concept presented by Xiao and Belytschko [110] for molecular dynamics coupling with a continuous model, and has been applied to DEM by Rojek and Oñate in [92]. The DEM and FEM subdomains can overlap each other. In this way a transitory zone between the DEM model and FEM model subdomains is introduced. In this zone contributions of each of the two methods to the overall stiffness vary gradually. This allows us to avoid or minimize unrealistic wave reflections at the interface between the DEM and FEM subdomains.

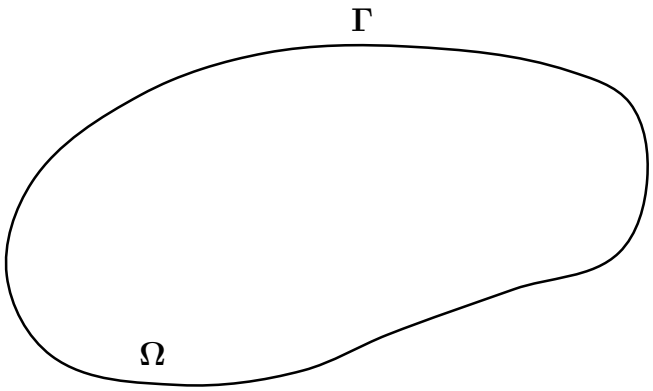

(a)

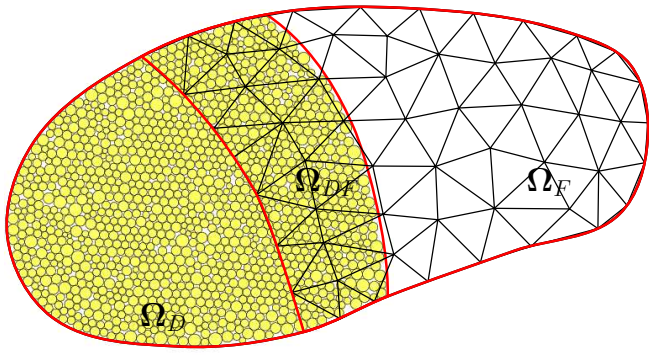

(b)

Figure 5.1. Overlap region between DEM and FEM subdomains.

We consider motion of a deformable body occupying the domain Ω with the boundary Γ (Figure 5.1) in the Euclidean space E^{n_d}, where $n_d = 2$ or 3. Two different subdomains will be distinguished in the domain Ω. Ω_F - discretized with finite elements and Ω_D -

modelled with discrete elements

$$\Omega = \Omega_F \cup \Omega_D \tag{5.38}$$

The subdomains Ω_F and Ω_D are not necessarily disjoint - they can overlap each other. The common part of the subdomains Ω_F and Ω_D is the part where both discretization types are used.

$$\Omega_{DF} = \Omega_F \cap \Omega_D \neq \emptyset \tag{5.39}$$

Following the idea used for molecular dynamics coupling with a continuum model in Xiao and Belytschko [110], the virtual work in the domain W is written as linear combination of the virtual work δW_F due to the finite element contribution and δW_D yielded by the discrete element part of the model, i.e.

$$\delta W = \alpha \delta W_F + (1 - \alpha)\delta W_D \tag{5.40}$$

where α is the contribution function, defined as

$$\alpha(\mathbf{x}) = \begin{cases} 0 & \text{when } \mathbf{x} \in \Omega_D \\ \dfrac{d(\mathbf{x})}{L(\mathbf{x})} & \text{when } \mathbf{x} \in \Omega_{DF} \\ 1 & \text{when } \mathbf{x} \in \Omega_F \end{cases} \tag{5.41}$$

with $d(\mathbf{x})$ and $L(\mathbf{x})$ being defined in the overlap region Ω_{DF}.

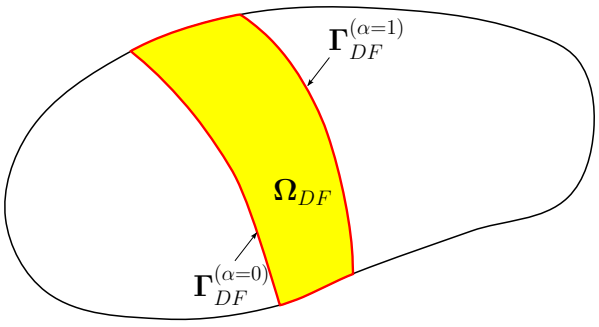

Figure 5.2. Overlap region Ω_{DF}. Definition of function $\alpha(\mathbf{x})$.

In the transition zone Ω_{DF} the value of function $\alpha(\mathbf{x})$ varies linearly from zero on the surface, to one on the surface (Figure 5.2). The surface $\Gamma_{DF}^{(\alpha=0)}$ separates the domain of

mixed discrete-continuous modelling from the domain where the DEM is used

$$\Gamma_{DF}^{(\alpha=0)} = \Gamma_F \cap \Omega_D \tag{5.42}$$

The surface $\Gamma_{DF}^{(\alpha=1)}$ separates the domain of mixed discrete-continuous modelling from the domain where the FEM is used

$$\Gamma_{DF}^{(\alpha=1)} = \Gamma_D \cap \Omega_F \tag{5.43}$$

Definition of the functions $d(\mathbf{x})$ and $L(\mathbf{x})$ is shown graphically in Figure 5.3. Function $d(\mathbf{x})$ is defined as the shortest distance from the point $\mathbf{x} \in \Omega_{DF}$ to the boundary of the overlap region $\Gamma_{DF}^{(\alpha=0)}$

$$d(\mathbf{x}) = \|\bar{\mathbf{x}}^0 - \mathbf{x}\| \tag{5.44}$$

where

$$\mathbf{x} \in \Omega_{DF}, \quad \bar{\mathbf{x}}^0 \in \Gamma_{DF}^{(\alpha=0)} : \quad \|\bar{\mathbf{x}}^0 - \mathbf{x}\| = \min_{\mathbf{x}^0 \in \Gamma_{DF}^{(\alpha=0)}} \|\mathbf{x}^0 - \mathbf{x}\| \tag{5.45}$$

Function $L(\mathbf{x})$ is the width of the overlap zone measured along the vector $\bar{\mathbf{x}}^0 - \mathbf{x}$.

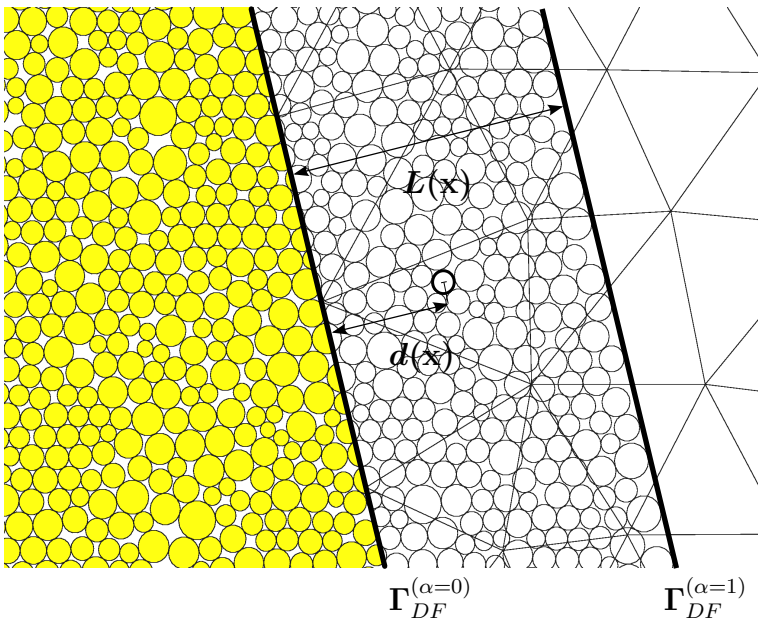

Figure 5.3. Detail of overlap region between DEM and FEM subdomains.

In the subdomain Ω_F, the finite element discretization allows to express the displacement $\mathbf{u}$, velocity $\dot{\mathbf{u}}$ and acceleration $\ddot{\mathbf{u}}$ fields in terms of the shape functions $\mathbf{N}$

and the nodal displacements $\mathbf{u}_F$, velocities $\dot{\mathbf{u}}_F$ and accelerations $\ddot{\mathbf{u}}_F$ in the form

$$\mathbf{u}(\mathbf{x},t) = \mathbf{N}(\mathbf{x})\,\mathbf{u}_F(\mathbf{x},t) \tag{5.46a}$$

$$\dot{\mathbf{u}}(\mathbf{x},t) = \mathbf{N}(\mathbf{x})\,\dot{\mathbf{u}}_F(\mathbf{x},t) \tag{5.46b}$$

$$\ddot{\mathbf{u}}(\mathbf{x},t) = \mathbf{N}(\mathbf{x})\,\ddot{\mathbf{u}}_F(\mathbf{x},t) \tag{5.46c}$$

The configuration and motion of the discrete elements are described by the vectors of translational displacements, $\mathbf{u}_D$, translational and rotational velocities, $\dot{\mathbf{u}}_D$ and $\boldsymbol{\omega}_D$, and translational and rotational accelerations, $\ddot{\mathbf{u}}_D$ and $\dot{\boldsymbol{\omega}}_D$, respectively.

5.2.1 Kinematic constraints

The coupling between subdomains Ω_D and Ω_F, in the transition zone Ω_{DF}, is provided by additional kinematic constraints resulting from the assumption that the discrete elements contained in the transition zone can be constrained kinematically by the finite element discretization as

$$\mathbf{x}_{d_i} = \mathbf{x}_F, \quad \forall\, d_i \in \Omega_{DF}, \quad \mathbf{x}_F \in \Omega_{DF} \tag{5.47}$$

The following relationships linking virtual displacements, velocities and accelerations of the i-th discrete element with respective nodal velocities of the overlapping finite element can be used to write the kinematic constrains, as

$$\delta\mathbf{u}_{d_i} - \mathbf{N}(\mathbf{x}_F)\,\delta\mathbf{u}_F = 0 \tag{5.48a}$$

$$\dot{\mathbf{u}}_{d_i} - \mathbf{N}(\mathbf{x}_F)\,\dot{\mathbf{u}}_F = 0 \tag{5.48b}$$

$$\ddot{\mathbf{u}}_{d_i} - \mathbf{N}(\mathbf{x}_F)\,\ddot{\mathbf{u}}_F = 0 \tag{5.48c}$$

where $\mathbf{x}_{d_i}$ is the center of the i-th discrete element and $\mathbf{x}_F$ is the equivalent point in the finite element discretization.

Defining the global vector of discrete elements in the transition zone Ω_{DF} as displacements $\mathbf{u}_{DF}$, velocities $\dot{\mathbf{u}}_{DF}$ and accelerations $\ddot{\mathbf{u}}_{DF}$, the kinematic constraints (5.48) can be written for all constrained discrete elements as

$$\delta\mathbf{u}_{DF} - \mathbf{N}\,\delta\mathbf{u}_F = 0 \tag{5.49a}$$

$$\dot{\mathbf{u}}_{DF} - \mathbf{N}\,\dot{\mathbf{u}}_F = 0 \tag{5.49b}$$

$$\ddot{\mathbf{u}}_{DF} - \mathbf{N}\,\ddot{\mathbf{u}}_F = 0 \tag{5.49c}$$

The additional kinematic constrains can be imposed using different schemes. In this work, the penalty function method and the Lagrange multipliers method are used.

In order to write the equations for the coupled system in a compact form, the kinematic constraints (5.48) are written in the general form

$$\chi\left(\delta\mathbf{u}_F, \delta\mathbf{u}_{DF}\right) = 0 \tag{5.50}$$

5.2.1.1 Penalty function method

The principle of virtual work for the coupled DEM/FEM system with coupling constraints (5.49) imposed by the penalty function method, and considering the contribution of both methods as shown in (5.40), can be expressed by the following equation

$$\begin{gathered}\delta\mathbf{u}_F^T(\bar{\mathbf{M}}_F\ddot{\mathbf{u}}_F + \bar{\mathbf{F}}_F^{int} - \bar{\mathbf{F}}_F^{ext}) + \delta\mathbf{u}_D^T(\bar{\mathbf{M}}_D\ddot{\mathbf{u}}_D - \bar{\mathbf{F}}_D) + \delta\mathbf{\Phi}_D^T(\bar{\mathbf{J}}_D\dot{\mathbf{\Omega}}_D - \bar{\mathbf{T}}_D) + \\ \delta\mathbf{u}_{DF}^T(\bar{\mathbf{M}}_{DF}\ddot{\mathbf{u}}_{DF} - \bar{\mathbf{F}}_{DF}) + \delta\mathbf{u}_F^T\left[\frac{\partial\chi}{\partial(\delta\mathbf{u}_F)}\right]^T\chi\mathbf{k}_{DF} + \delta\mathbf{u}_{DF}^T\left[\frac{\partial\chi}{\partial(\delta\mathbf{u}_{DF})}\right]^T\chi\mathbf{k}_{DF} = 0\end{gathered} \tag{5.51}$$

where $\mathbf{k}_{DF}$ is the vector of discrete penalty functions.

Taking into account the explicit form of the constraint (Equation (5.49)), Equation (5.51) can be written in the following form

$$\begin{Bmatrix}\delta\mathbf{u}_F\\ \delta\mathbf{u}_D\\ \delta\mathbf{u}_{DF}\\ \delta\mathbf{\Phi}_D\end{Bmatrix}^{\mathrm{T}}\left(\begin{bmatrix}\bar{\mathbf{M}}_F & 0 & 0 & 0\\ 0 & \bar{\mathbf{M}}_D & 0 & 0\\ 0 & 0 & \bar{\mathbf{M}}_{DF} & 0\\ 0 & 0 & 0 & \bar{\mathbf{J}}_D\end{bmatrix}\begin{Bmatrix}\ddot{\mathbf{u}}_F\\ \ddot{\mathbf{u}}_D\\ \ddot{\mathbf{u}}_{DF}\\ \dot{\mathbf{\Omega}}_D\end{Bmatrix} - \begin{Bmatrix}\bar{\mathbf{F}}_F^{ext} - \bar{\mathbf{F}}_F^{int} + \mathbf{N}^{\mathrm{T}}\chi\mathbf{k}_{DF}\\ \bar{\mathbf{F}}_D\\ \bar{\mathbf{F}}_{DF} - \chi\mathbf{k}_{DF}\\ \bar{\mathbf{T}}_D\end{Bmatrix}\right) = 0 \tag{5.52}$$

Since Eq. (5.52) must be satisfied for arbitrary admissible variations (excluding additional coupling constraints), the terms in parentheses should vanish. This yield the following equation

$$\begin{bmatrix}\bar{\mathbf{M}}_F & 0 & 0 & 0\\ 0 & \bar{\mathbf{M}}_D & 0 & 0\\ 0 & 0 & \bar{\mathbf{M}}_{DF} & 0\\ 0 & 0 & 0 & \bar{\mathbf{J}}_D\end{bmatrix}\begin{Bmatrix}\ddot{\mathbf{u}}_F\\ \ddot{\mathbf{u}}_D\\ \ddot{\mathbf{u}}_{DF}\\ \dot{\mathbf{\Omega}}_D\end{Bmatrix} = \begin{Bmatrix}\bar{\mathbf{F}}_F^{ext} - \bar{\mathbf{F}}_F^{int} + \mathbf{N}^{\mathrm{T}}\chi\mathbf{k}_{DF}\\ \bar{\mathbf{F}}_D\\ \bar{\mathbf{F}}_{DF} - \chi\mathbf{k}_{DF}\\ \bar{\mathbf{T}}_D\end{Bmatrix} \tag{5.53}$$

Equation (5.53) can be integrated in time using the standard explicit scheme used in finite and discrete element algorithms.

5.2.1.2 Lagrange multipliers method

Using the Lagrange multipliers technique, the principle of the virtual work of the coupled DEM/FEM system can be written as

$$\begin{aligned}&\delta\mathbf{u}_F^{\mathrm{T}}(\bar{\mathbf{M}}_F\ddot{\mathbf{u}}_F+\bar{\mathbf{F}}_F^{int}-\bar{\mathbf{F}}_F^{ext})+\delta\mathbf{u}_D^{\mathrm{T}}(\bar{\mathbf{M}}_D\ddot{\mathbf{u}}_D-\bar{\mathbf{F}}_D)+\delta\mathbf{\Phi}_D^{\mathrm{T}}(\bar{\mathbf{J}}_D\dot{\mathbf{\Omega}}_D-\bar{\mathbf{T}}_D)\\&+\delta\mathbf{u}_{DF}^{\mathrm{T}}(\bar{\mathbf{M}}_{DF}\ddot{\mathbf{u}}_{DF}-\bar{\mathbf{F}}_{DF})+\delta\mathbf{u}_F^{\mathrm{T}}\left[\frac{\partial\chi}{\partial(\delta\mathbf{u}_F)}\right]^{\mathrm{T}}\boldsymbol{\lambda}+\delta\mathbf{u}_{DF}^{\mathrm{T}}\left[\frac{\partial\chi}{\partial(\delta\mathbf{u}_{DF})}\right]^{\mathrm{T}}\boldsymbol{\lambda}=0\end{aligned}\tag{5.54}$$

where $\boldsymbol{\lambda}$ is the vector of unknown Lagrange multipliers.

Taking into account the explicit form of the constraint equation (5.49), Equation (5.54) can be written in the following form

$$\left\{\begin{array}{c}\delta\mathbf{u}_F\\\delta\mathbf{u}_D\\\delta\mathbf{u}_{DF}\\\delta\mathbf{\Phi}_D\end{array}\right\}^{\mathrm{T}}\left(\left[\begin{array}{ccccc}\bar{\mathbf{M}}_F&0&0&0&-\mathbf{N}^{\mathrm{T}}\\0&\bar{\mathbf{M}}_D&0&0&0\\0&0&\bar{\mathbf{M}}_{DF}&0&\mathbf{I}\\0&0&0&\bar{\mathbf{J}}_F&0\end{array}\right]\left\{\begin{array}{c}\ddot{\mathbf{u}}_F\\\ddot{\mathbf{u}}_D\\\ddot{\mathbf{u}}_{DF}\\\dot{\mathbf{\Omega}}_D\\\boldsymbol{\lambda}\end{array}\right\}-\left\{\begin{array}{c}\bar{\mathbf{F}}_F^{ext}-\bar{\mathbf{F}}_F^{int}\\\bar{\mathbf{F}}_D\\\bar{\mathbf{F}}_{DF}\\\bar{\mathbf{T}}_D\end{array}\right\}\right)=0\tag{5.55}$$

Since Equation (5.55) must be satisfied for arbitrary admissible variations, the terms in parenthesis should vanish. Adding the relationship for accelerations (5.49) the following equation set is obtained for the coupled system

$$\left[\begin{array}{ccccc}\bar{\mathbf{M}}_F&0&0&0&-\mathbf{N}^{\mathrm{T}}\\0&\bar{\mathbf{M}}_D&0&0&0\\0&0&\bar{\mathbf{M}}_{DF}&0&\mathbf{I}\\0&0&0&\bar{\mathbf{J}}_D&0\\-\mathbf{N}&0&\mathbf{I}&0&0\end{array}\right]\left\{\begin{array}{c}\ddot{\mathbf{u}}_F\\\ddot{\mathbf{u}}_D\\\ddot{\mathbf{u}}_{DF}\\\dot{\mathbf{\Omega}}_D\\\boldsymbol{\lambda}\end{array}\right\}=\left\{\begin{array}{c}\bar{\mathbf{F}}_F^{ext}-\bar{\mathbf{F}}_F^{int}\\\bar{\mathbf{F}}_D\\\bar{\mathbf{F}}_{DF}\\\bar{\mathbf{T}}_D\\0\end{array}\right\}\tag{5.56}$$

with kinematic-type and force-type unknowns. The above system can be solved directly for to the unknowns.

Another solution scheme has been implemented in this work. It is based on the elimination of Lagrange multipliers $\boldsymbol{\lambda}$ and the dependent variables $\mathbf{r}_{DC}$ before time integration. Performing some algebraic transformations, the reduced equation set is obtained as follows

$$\left(\bar{\mathbf{M}}_F+\mathbf{N}^{\mathrm{T}}\bar{\mathbf{M}}_{DF}\mathbf{N}\right)\ddot{\mathbf{u}}_F=\mathbf{F}_F^{ext}-\mathbf{F}_F^{int}+\mathbf{N}^{\mathrm{T}}\bar{\mathbf{F}}_{DF}\tag{5.57a}$$

$$\bar{\mathbf{M}}_D\ddot{\mathbf{u}}_D=\bar{\mathbf{F}}_D\tag{5.57b}$$

$$\bar{\mathbf{J}}_D\dot{\mathbf{\Omega}}_D=\bar{\mathbf{T}}_D\tag{5.57c}$$

These equations can be integrated in time using standard explicit integration schemes

used in the finite element and discrete element algorithms without constraints.

5.2.2 Example: Wave propagation

The propagation of a wave through the coupling interface has been studied in order to analyze the reflexion caused by the coupling scheme. A rectangular domain of 10 mm wide and 600 mm long with different overlapping region length are considered, as shown in Figure 5.4. The longer sides of the rectangle have restrained motion in the transverse direction.

(a) Overlap length = 40 mm.

(b) Overlap length = 80 mm.

Figure 5.4. Wave propagation sample in 2D.

The material properties are a Young modulus E = 20 GPa, Poisson's coefficient μ = 0.25 and mass density ρ = 7800 kg/m^3. In Figure 5.5 the detail of the contribution of each sub-domain in the overlap region is shown for a overlap length of 40 mm.

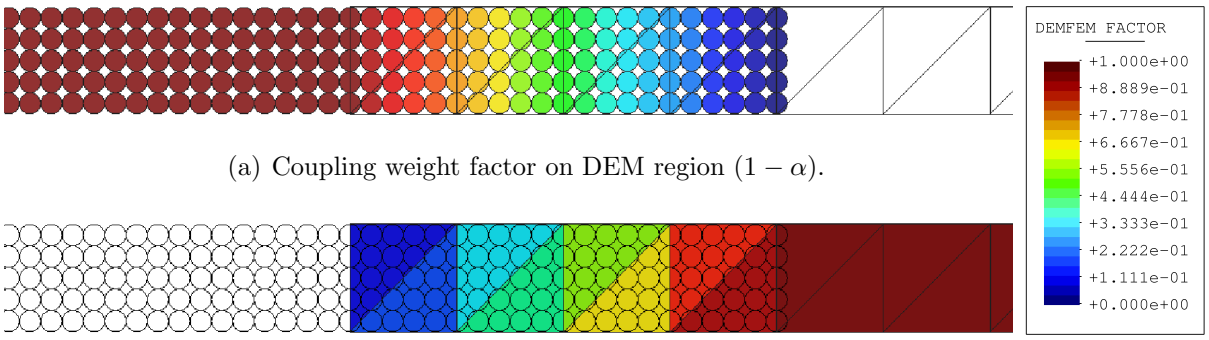

(a) Coupling weight factor on DEM region $(1 - \alpha)$.

(b) Coupling weight factor on FEM region (α).

Figure 5.5. Weight factor in coupling region. Overlap length of 40 mm.

The evolution of the wave through the domain is shown in Figure 5.6. The Lagrange multiplier method is used to model the coupling for a overlap length of 80 mm. The evolution shows a small reflection in the overlap region.

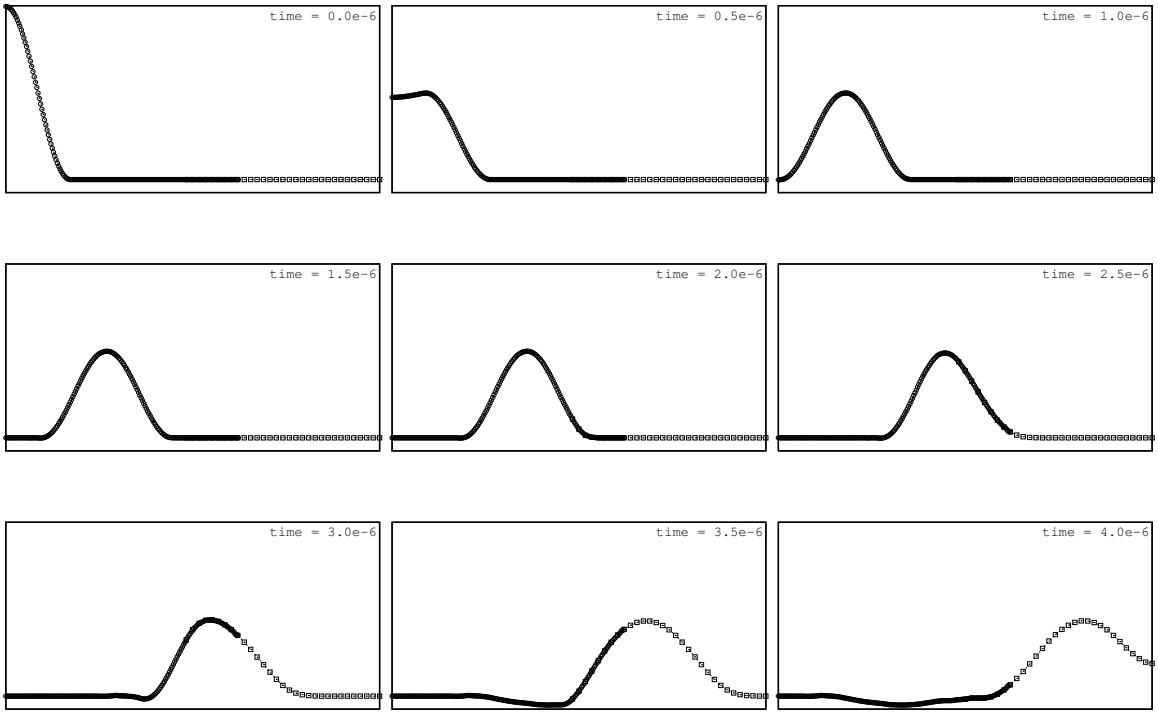

Figure 5.6. Wave evolution with the Lagrange multiplier method and an overlap length 80 mm.

In Figure 5.7, the energy in each region is depicted for different overlap lengths using the Lagrange multiplier method. The reflection of the wave can be appreciated, representing 0.57 % of the total energy.

In a similar way, Figure 5.8 shows the energy evolution in both regions using the penalty function method. In this case, the reflected energy is 0.61 % of the total energy.

5.2.3 Example: Mixed-mode bending beam with a notch

The case analyzed considers a mixed-mode bending beam with a notch. It is based in the geometry used by Galvez et al [53], where experimental results has been reported. The geometry and conditions are depicted in Figure 5.9.

The problem considers two cases; in the first case, called *type 1*, the stiffness K at the upper left is equal to zero ($K = 0$), representing a 3-point bending beam. The second case, called *type 2*, considers an infinite stiffness ($K = \infty$), representing a 4-point bending beam. The load is applied by a constant displacement rate.

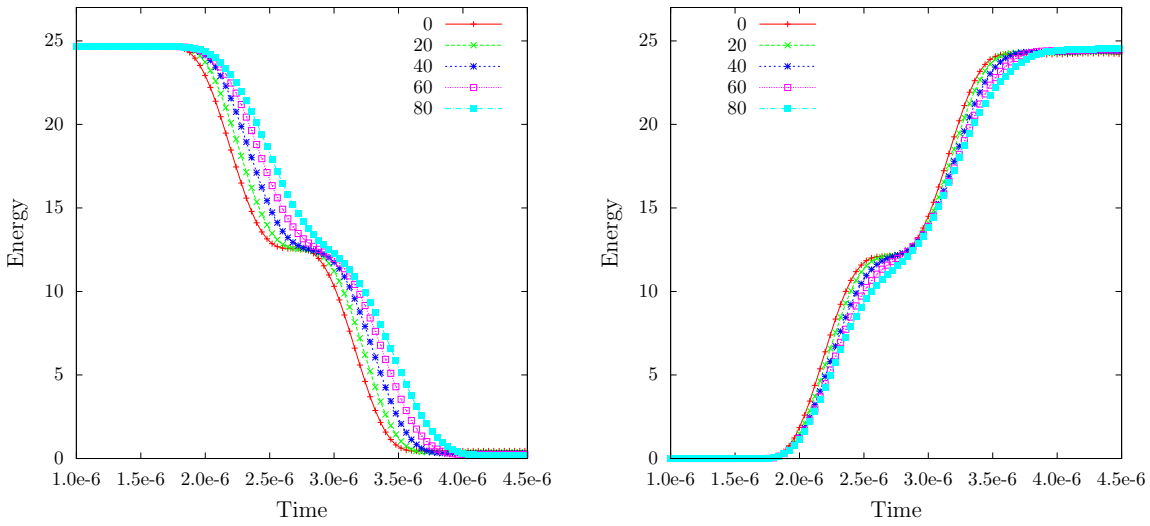

(a) DEM domain. (b) FEM domain.

Figure 5.7. Wave propagation sample in 2D. Energy in the coupling region with the Lagrange multipliers method.

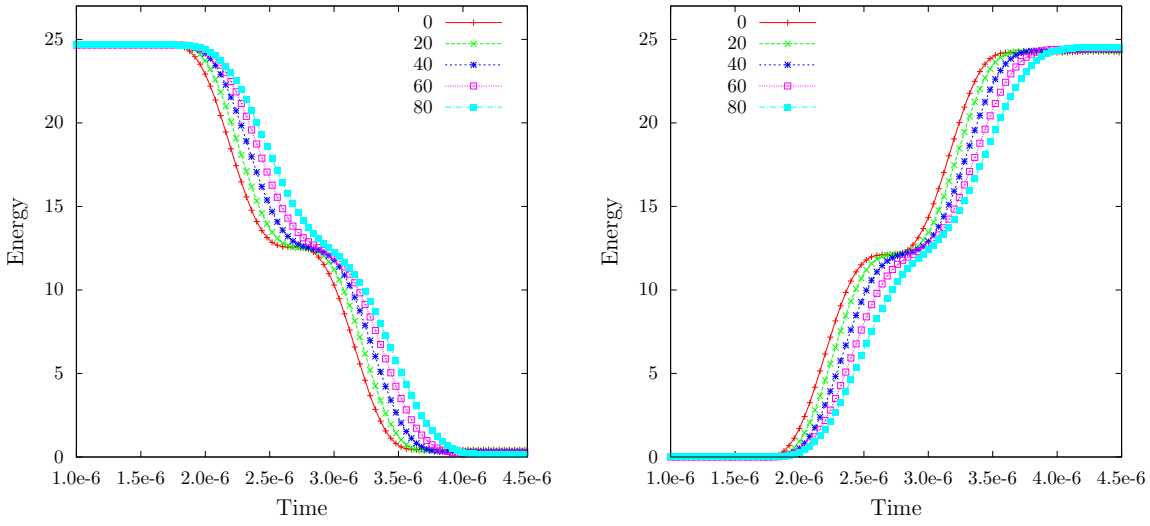

(a) DEM domain. (b) FEM domain.

Figure 5.8. Wave propagation sample in 2D. Energy in the coupling region with the penalty method.

The domain it is discretized by 392 triangular elements and 21955 cylindrical particles, as shown in Figure 5.10. The average mesh-size in the FEM region it is 20 mm, and the average particle size is 0.7 mm. The DEM/FEM overlap region has a length of 14 mm

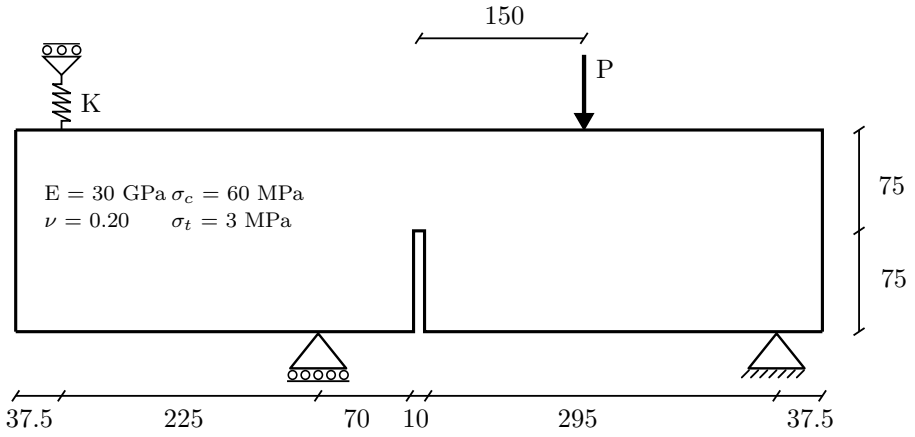

Figure 5.9. Mixed-mode bending beam with a notch. Geometry (mm) and conditions.

and the penalty method is considered.

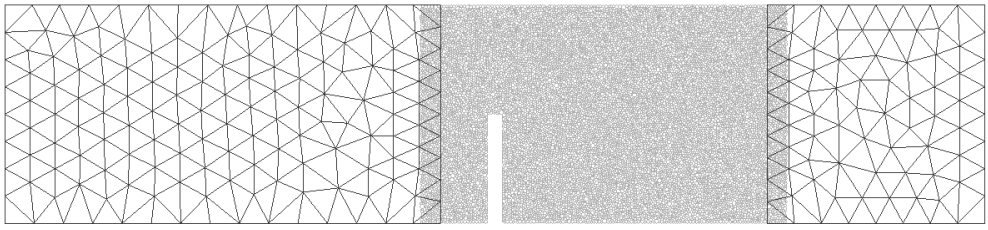

Figure 5.10. Mixed-mode bending beam with a notch. DEM/FEM coupled mesh.

The deformed mesh is shown in Figure 5.11. In Figure 5.12, the load vs. CMOD[1] is compared with the experimental envelope presented by Galvez et al. in [53], and the simulation results presented by Cervera et al. in [22], using the smeared damage approach, and the FEM.

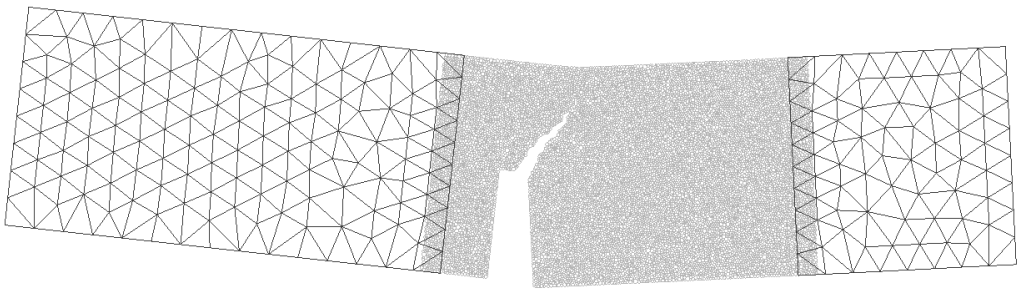

Figure 5.11. Mixed-mode bending beam with a notch. Deformed mesh (x100) with the fixed DEM/FEM coupling scheme in type 1 case.

The curve presents a good agreement with the reported results. The main difference in the post-critical behaviour is related to the perfectly brittle contact model used in the DEM, resulting in a higher decreasing rate of the maximum load.

The deformed mesh for the case type 2 it is shown in Figure 5.13. The crack presents a small curvature, similar to the type 1 case.

In Figure 5.14, the load vs. CMOD for the case type 2 is compared with the experimental envelope, and the simulation results using the smeared damage approach, and the FEM.

[1]CMOD: crack mouth opening displacement.

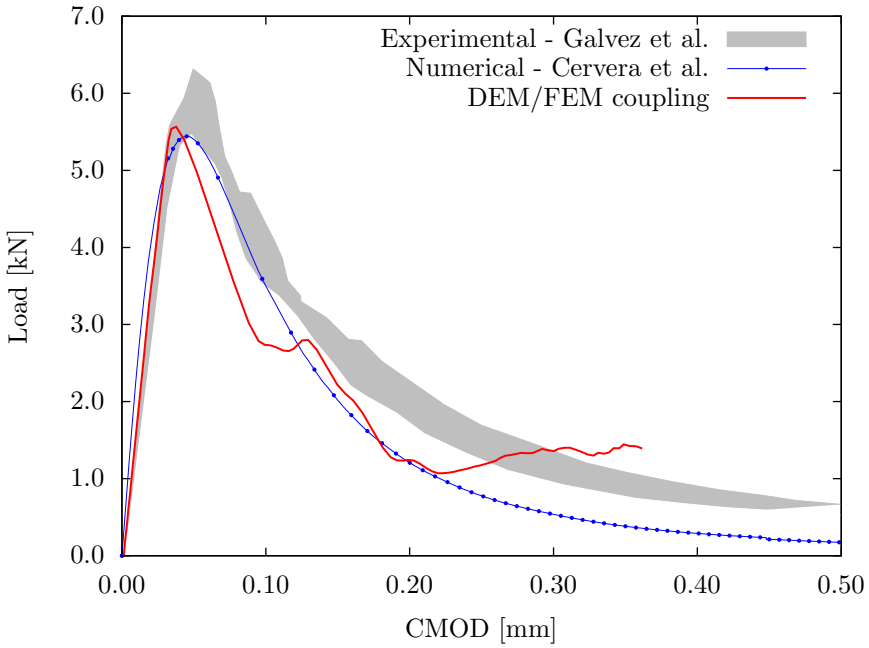

Figure 5.12. Mixed-mode bending beam with a notch. Load vs CMOD in type 1 case.

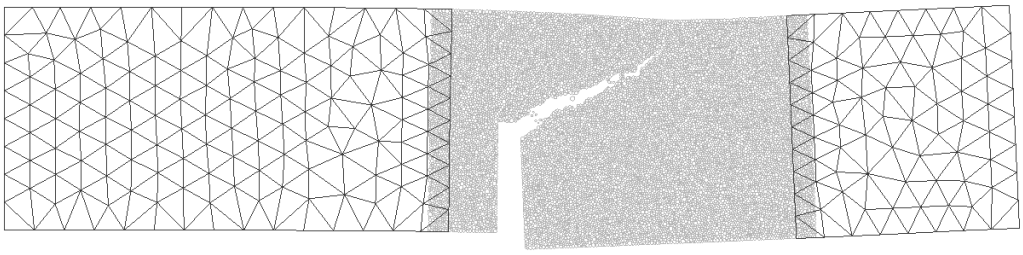

Figure 5.13. Mixed-mode bending beam with a notch. Deformed mesh (x100) with the fixed DEM/FEM coupling scheme in type 2 case.

5.3 Adaptivity of the coupling definition

In a real case, the zone which requires the use of DEM can change during the simulation. With the standard DEM/FEM coupling, both subdomains are predefined during the discretization process. This requires to know where fracture will appear, and the use of DEM even if the solid has a linear elastic behaviour. In order to make more efficient the use of the DEM during the simulation, an algorithm for the change of the subdomains is used. The idea is start the simulation using finite elements. When some area with a stress value higher than a predefined limit state is achieved, the FEM is replaced with

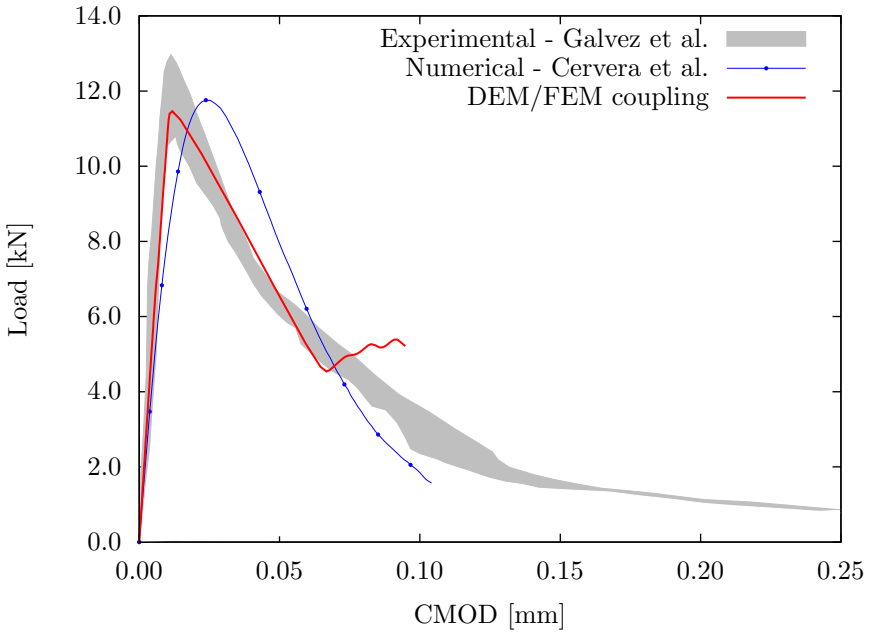

Figure 5.14. Mixed-mode bending beam with a notch. Load vs CMOD in type 2 case.

DEM and a new DEM/FEM interface is defined. The progressive change of the simulation method makes more efficient the use of both methods. The criteria for the change of the simulation method is defined by a predefined limit stress value (σ^*) in the center of the finite elements as

$$\sigma \geq \sigma^* \tag{5.58}$$

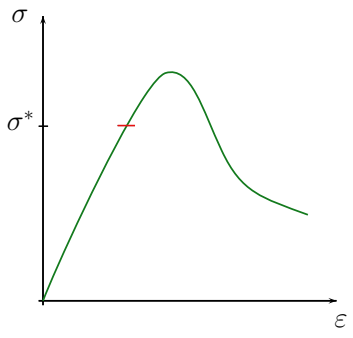

Figure 5.15. Scheme of stress criteria for change of simulation technique.

When a change of domain occur, the kinematic variables of the finite element are projected into the newly created discrete elements, so that the behaviour of both methods should be equivalent.

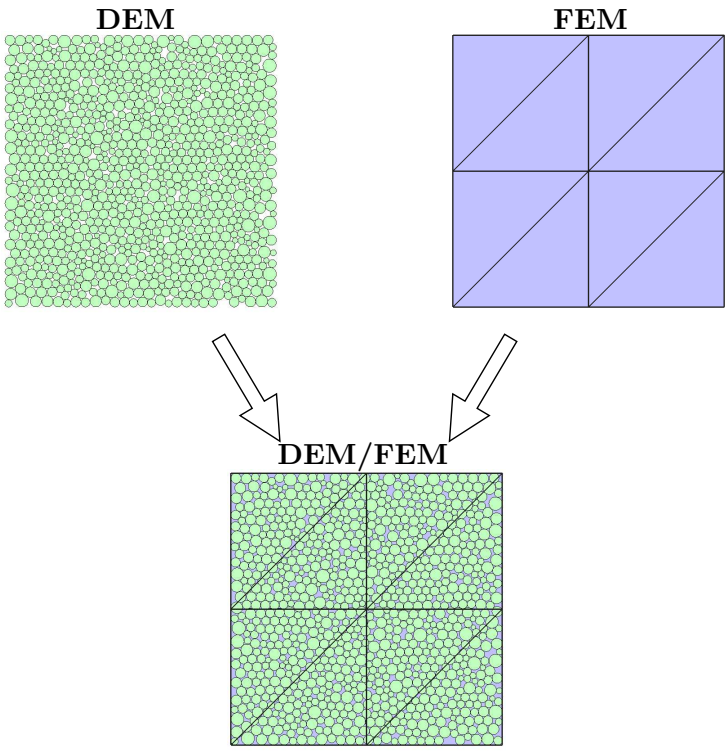

Figure 5.16. Geometry discretized with both methods.

In order to ensure the geometrical compatibility in the discrete elements used progressively during the simulation, a discretization of the full domain with cylindrical/spherical particles is generated and stored for its posterior use. The discrete elements are activated within the FEM mesh as required by the coupling scheme. The particles in the new overlap region are selected using a distance function [42] based in the new boundary elements generated in the FEM subdomain.

5.3.1 Transition from finite elements to discrete elements

The transition from the finite elements to the discrete elements it is shown in Figure 5.17. Initially, the finite elements that meet the criteria are selected. The particles associated to the selected elements are activated in all their degrees of freedom, and in counterpart the finite elements are deactivated. The distance function based in the modified finite element mesh is regenerated, in order to define the new interface subdomain. The particles in the new interface subdomain are identified and activated with the kinematic constraints.

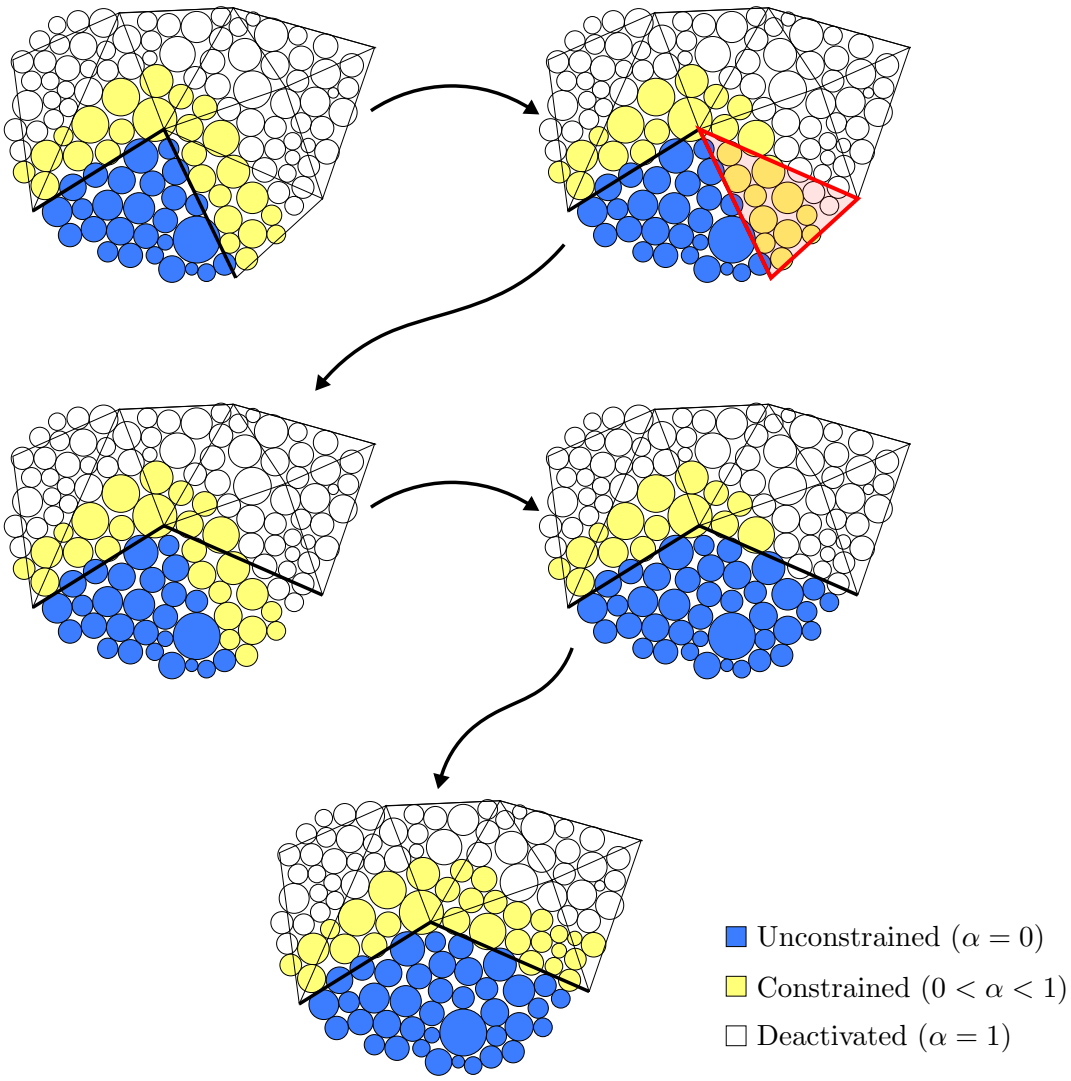

Figure 5.17. Scheme of update procedure of the coupling interface.

5.3.2 Projection of kinematic variables

Once a finite element is deactivated, and the new discrete elements are activated, the kinematic variables of the particles are recovered by the projection of the nodal values. The displacement and velocities are calculated by means of the projection using the finite element shape functions, considering the initial position, as

$$\mathbf{u}_{DF} = \mathbf{N}(\mathbf{x}^0_{DF})\,\mathbf{u}_F \tag{5.59}$$

$$\dot{\mathbf{u}}_{DF} = \mathbf{N}(\mathbf{x}^0_{DF})\,\dot{\mathbf{u}}_F \tag{5.60}$$

It should be noted that the rotational variables are not projected, nevertheless its

value is considered to be almost negligible and can be recovered after few iterations.

The contact force can be calculated using directly the contact model, or via a localization procedure considering the element stress. In Figure 5.18 a simple sample is shown considering a square domain of 1x1 with an horizontal displacement of 0.10 in the top wall, with a unit velocity.

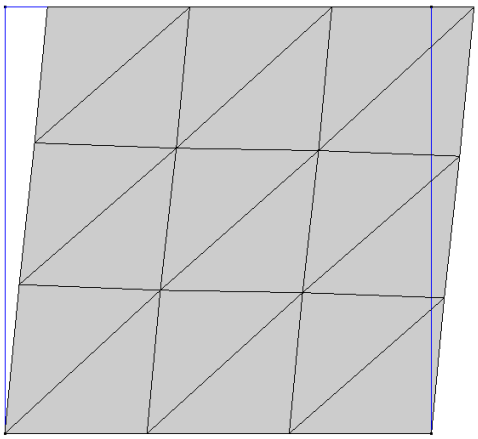

Figure 5.18. FEM mesh with imposed deformation.

The projected horizontal displacement and horizontal velocity are depicted in Figures 5.19 and 5.20, respectively.

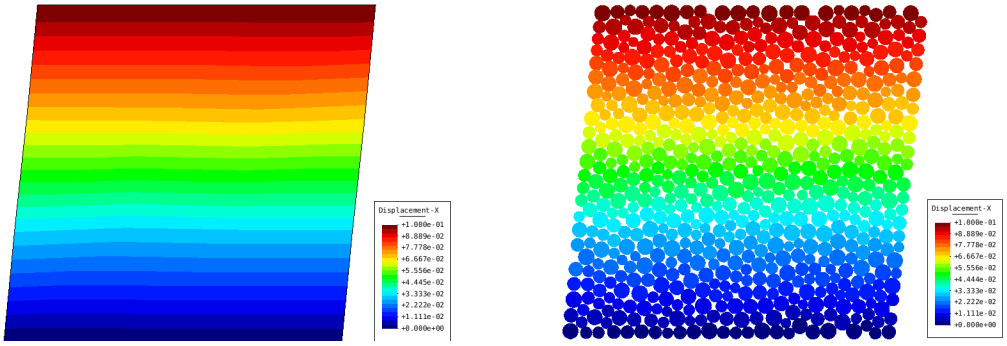

(a) FEM (b) DEM

Figure 5.19. Horizontal displacement projection from FEM to DEM.

After the projection procedure, the kinematic variables are estimated in the equivalent DEM mesh. The contact forces are calculated directly of the projected displacement, as shown in Figure 5.21.

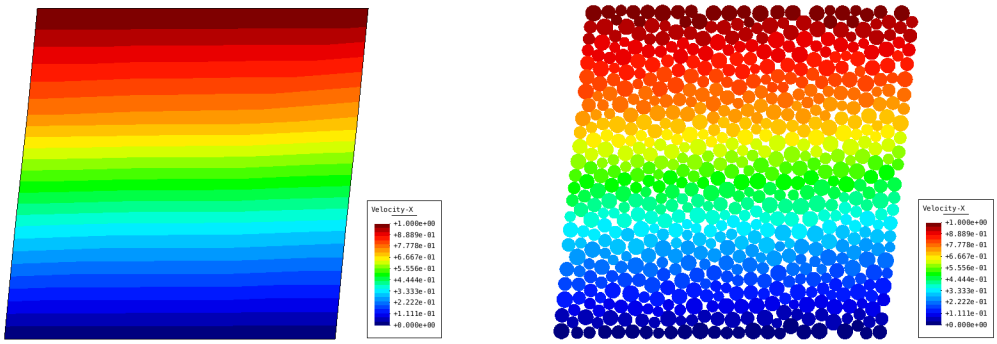

(a) FEM (b) DEM

Figure 5.20. Horizontal velocity projection from FEM to DEM.

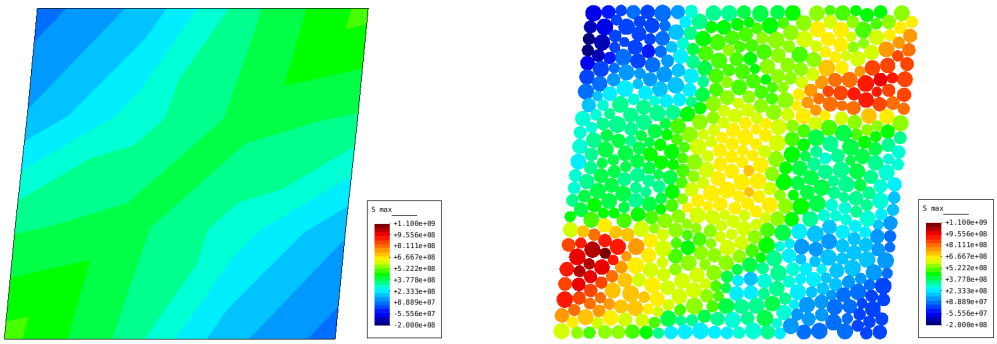

(a) FEM (b) DEM

Figure 5.21. Maximum principal stress calculated after projection.

The discrete system is not in equilibrium. Nevertheless the system can be relaxed after some iterations.

In Figure 5.22 the maximum principal stress is shown considering a different number of iterations for the relaxation of the system. It can be observed that after few iterations, the system presents a behaviour equivalent to the original FEM domain.

In Figure 5.23, the evolution of potential energy in the system is presented. The original model considers triangular elements (FEM-3). For the comparison, different number of iterations are considered in the projection. The same model is simulated using quadrilateral elements (FEM-4) in order to verify the potential energy obtained.

The projection is performed in a total time of 0.1 s. It is observed that with a small number of iterations the curve presents fluctuations and the resultant energy does not

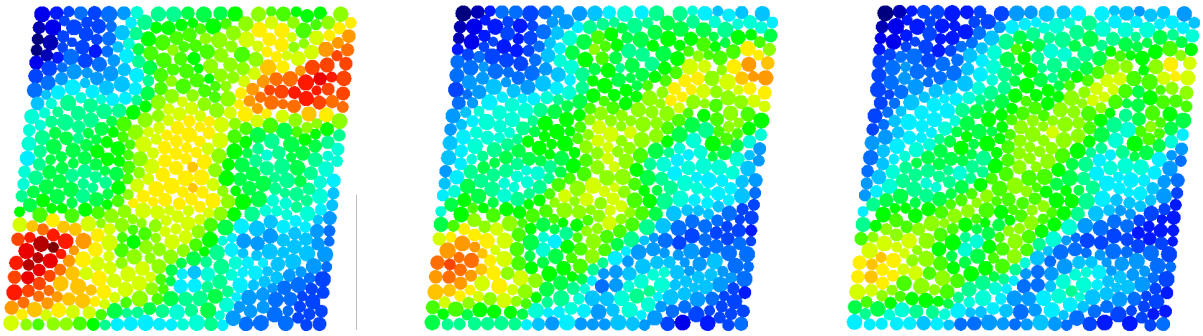

(a) Iteration 0 (b) Iteration 5 (c) Iteration 10

Figure 5.22. Maximum principal stress after different numbers of iterations over the contact forces.

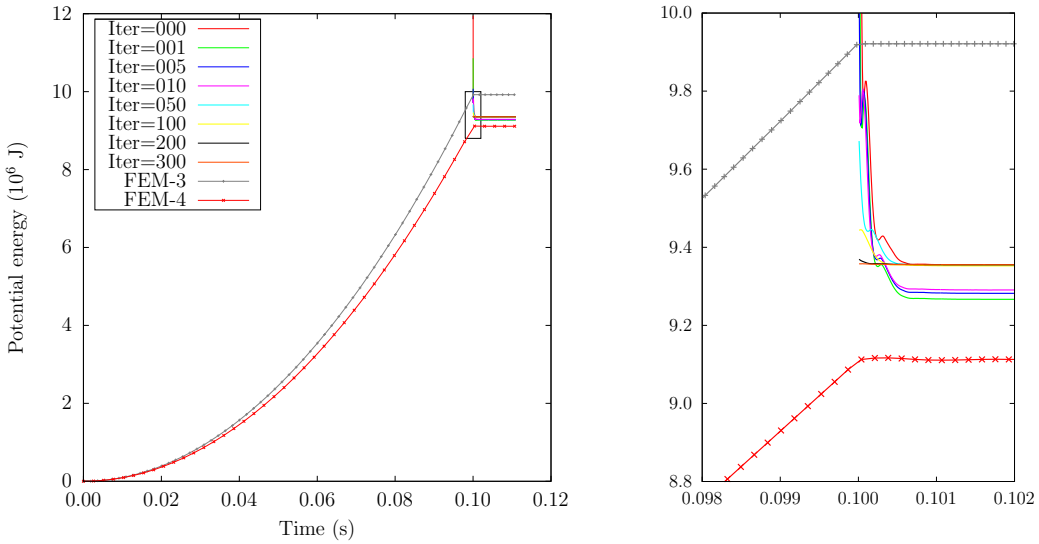

Figure 5.23. Evolution of potential energy.

converge. With a number of iterations larger than 50, the energy converges to a constant value without fluctuations. The difference between the potential energy of the FEM mesh and that obtained in the DEM mesh after the projection can be related with the differences in the mesh areas. While in the FEM mesh, all the domain is considered for the stress calculation. In the DEM the energy is calculated in term of the bonded particles, which represents a smaller equivalent domain.

5.3.3 Example: Mixed-mode bending beam with a notch solved with the adaptive DEM/FEM coupling scheme

The example is the same as previously presented in Section 5.2.3. Now, the mixed-mode bending beam is modelled using the adaptive DEM/FEM (ADF) coupling scheme. The finite element mesh considers 857 triangular elements, while the same discrete elements mesh of 26077 particles has been used. The threshold value for the change from finite to discrete elements is σ=2.8 MPa, in tension, with an overlap length of 7 mm. In Figure 5.24, the deformed mesh (x100) it is shown.

At the end of the simulation, the final mesh use 750 triangular elements and 5031 cylindrical elements. The computational cost decreases 82% compared to the fixed coupling scheme. The force vs. CMOD curve it is depicted in Figure 5.25. Results are compared with the curves obtained by Galvez et al. [53] and Cervera et al. [22].

The same results are presented for the case 1 in Figure 5.26. This time, two different threshold values are considered in order to analyze its influence in the results, that are compared those reported by the same authors.

Both curves presents small differences in the last part. This is due to the fact that the curve with the lower threshold value allows the change of more elements, avoiding possible concentration of the stresses close to the interface.

The evolution of the deformation process is shown in Figure 5.27. It is interesting note the change of elements in an area without fracture.

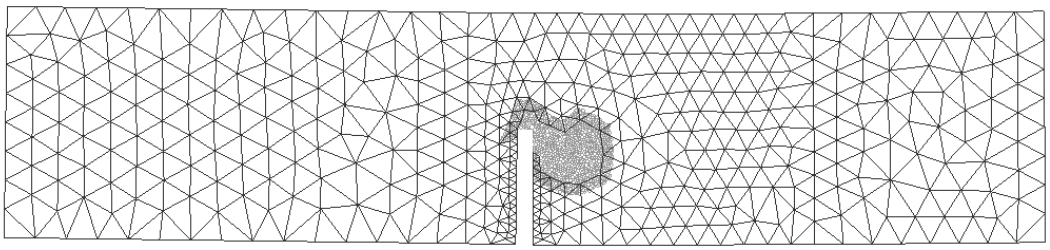

(a) CMOD=0.0140 mm

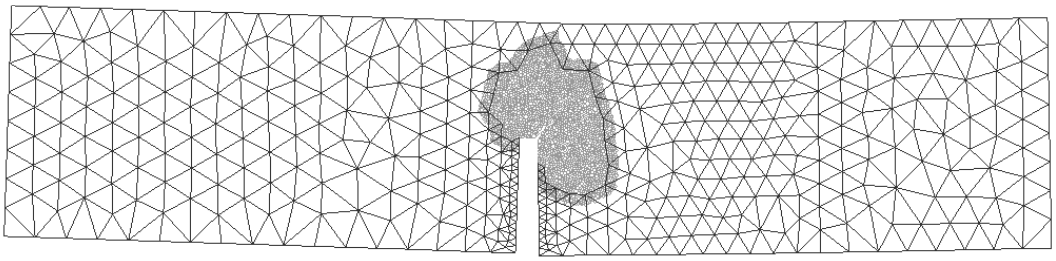

(b) CMOD=0.0546 mm

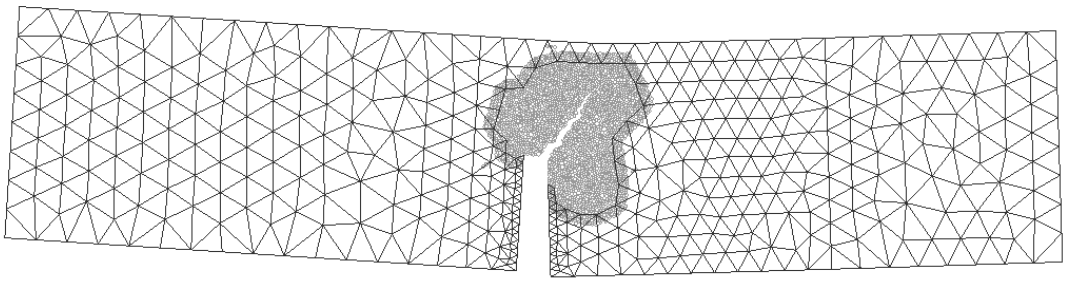

(c) CMOD=0.1245 mm

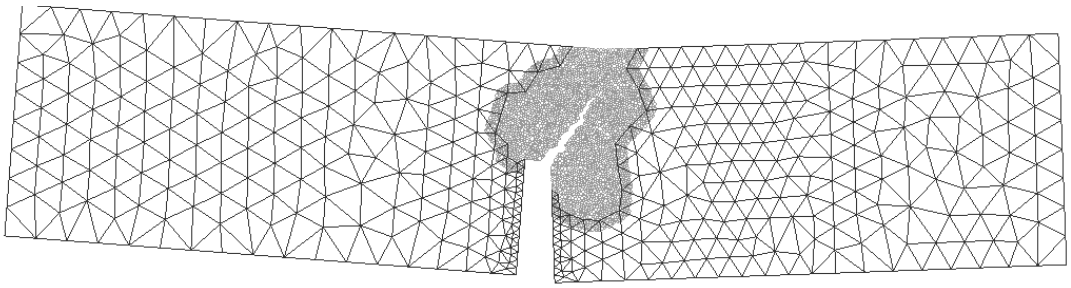

(d) CMOD=0.1518 mm

Figure 5.24. Mixed-mode bending 2D beam with notch, type 1 with ADF. Deformed mesh (x100) at different instants.

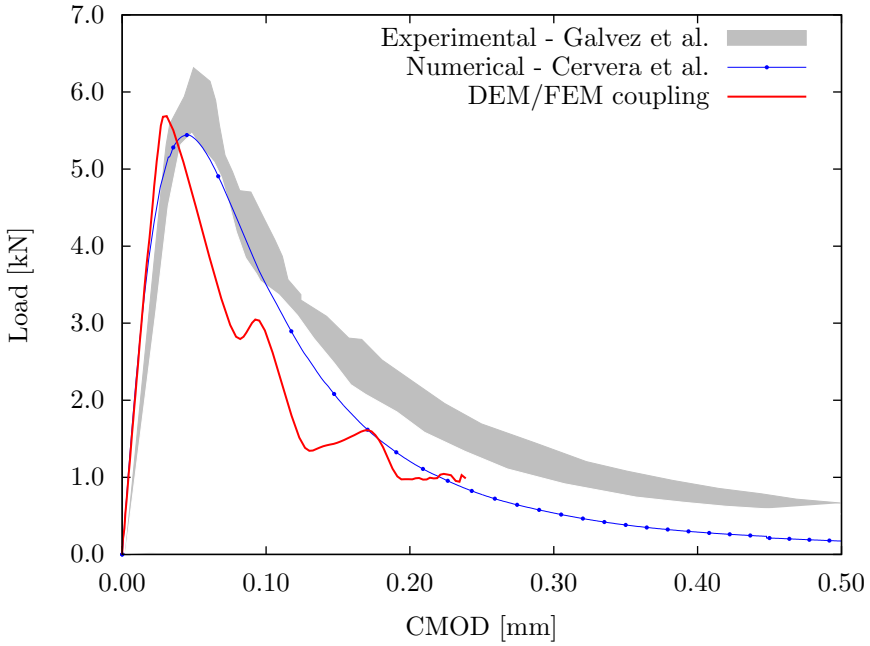

Figure 5.25. Mixed-mode bending 2D beam with notch, type 1 with ADF. Curve load vs CMOD.

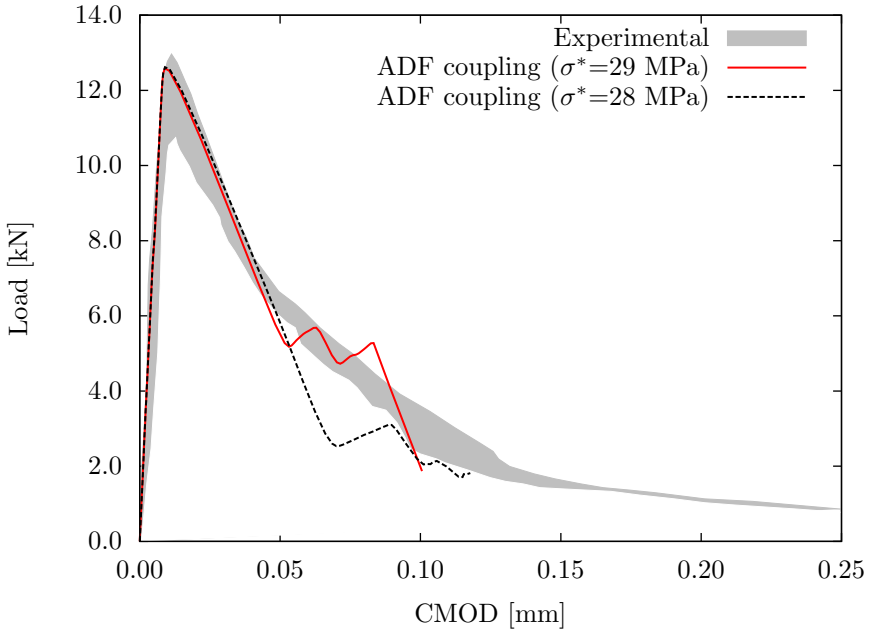

Figure 5.26. Mixed-mode bending 2D beam with notch, type 2 with ADF. Curve load vs CMOD.

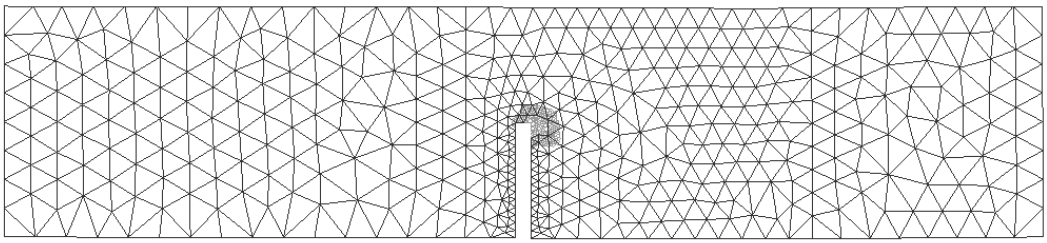

(a) CMOD=0.0140 mm

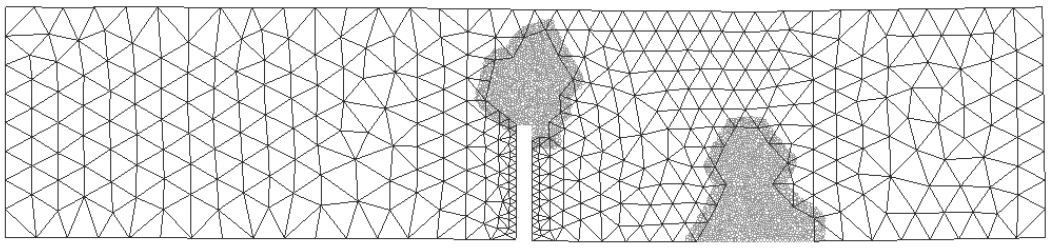

(b) CMOD=0.0546 mm

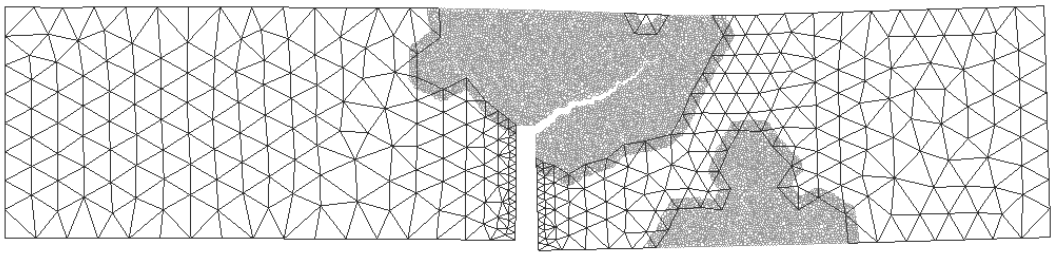

(c) CMOD=0.1245 mm

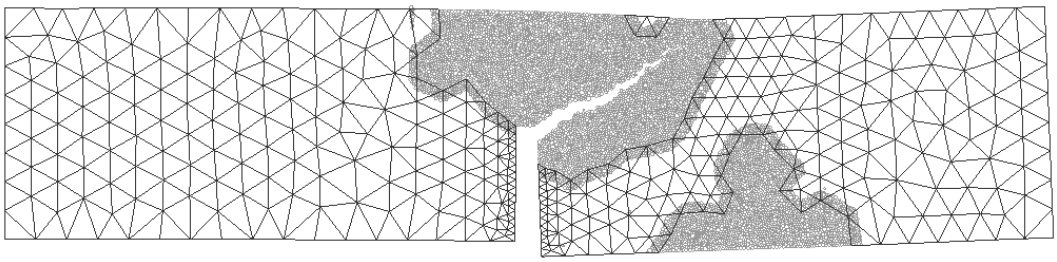

(d) CMOD=0.1518 mm

Figure 5.27. Mixed-mode bending beam with notch, type 2 with ADF. Failure mode.

5.3.4 Example: 3D three point bending beam

The next sample is the three point bending test on a notched beam [22] solved in 3D. The geometry and conditions are shown in Figure 5.28. The mechanical properties are: Young's modulus E = 20 GPa, Poisson's ratio $\nu = 0.2$, and tensile strength $\sigma_t = 2.4$ MPa.

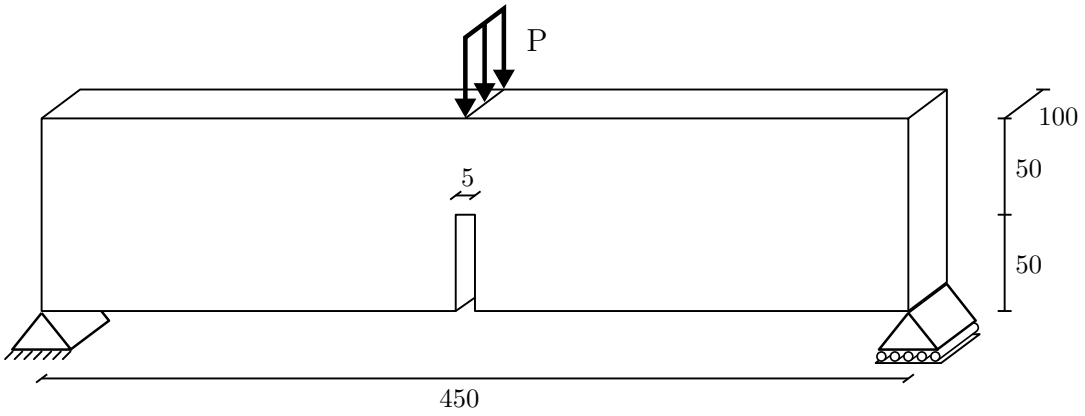

Figure 5.28. Three point bending 3D beam geometry.

The discrete element assembly is considered just in the area where fracture occurs, as depicted in Figure 5.29. The discretized model considers 49811 spherical elements and 23377 tetrahedra. A vertical velocity of 2 mm/s has been imposed in the middle top line.

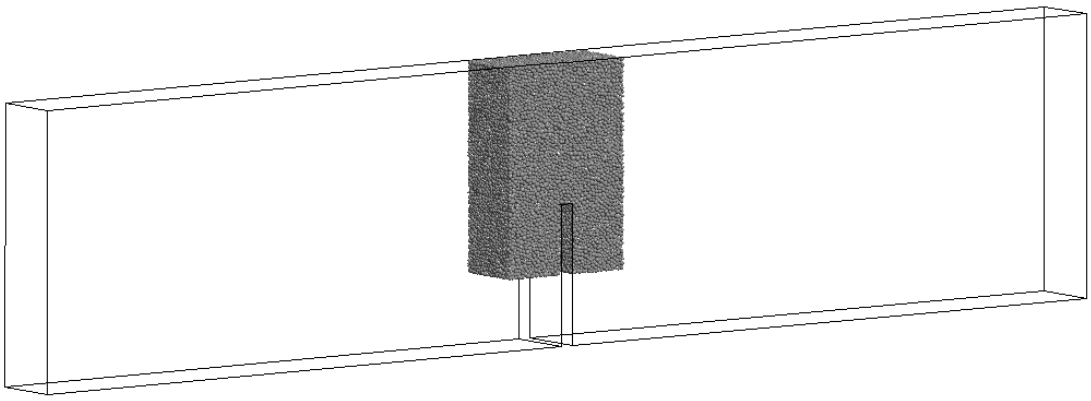

Figure 5.29. Three point bending 3D beam. Partial discretization of domain with discrete elements.

The evolution of the process is presented in Figure 5.30. The discrete elements activated at different times during the process can be appreciated.

The damage in the domain is depicted in Figure 5.31. A well localized fracture can be observed, as expected. Similar results are obtained in the literature [19, 22].

The curve load versus displacement is presented in Figure 5.32. Results agree well with other numerical and experimental values.

In the elastic part its behaviour is as expected. Nevertheless, after fracture starts the behaviour is perfectly brittle while the numerical and experimental behaviour present a more ductile damage. The DEM model implemented does not allow this kind of behaviour. Nevertheless, it can be observed a good agreement with the elastic properties and the limit strength estimated.

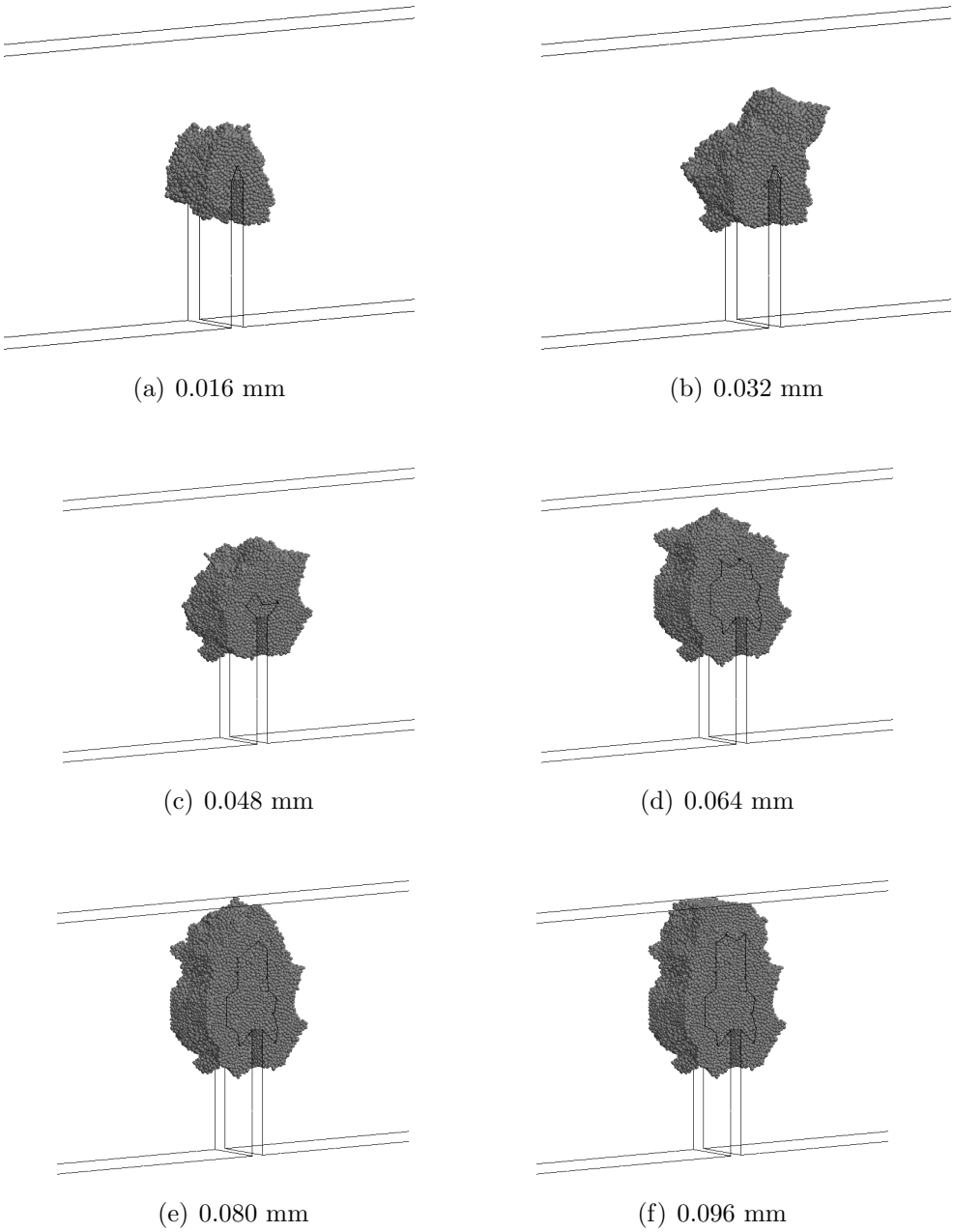

(a) 0.016 mm (b) 0.032 mm

(c) 0.048 mm (d) 0.064 mm

(e) 0.080 mm (f) 0.096 mm

Figure 5.30. Three point bending 3D beam. Evolution of DEM mesh.

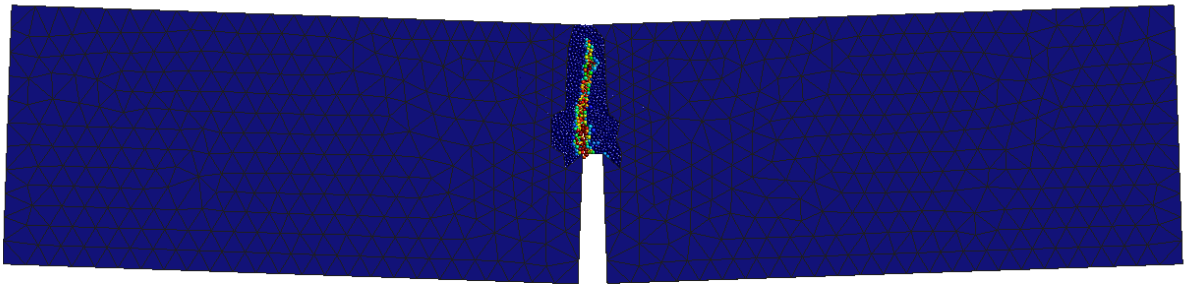

Figure 5.31. Three point bending 3D beam. Damage at the final point.

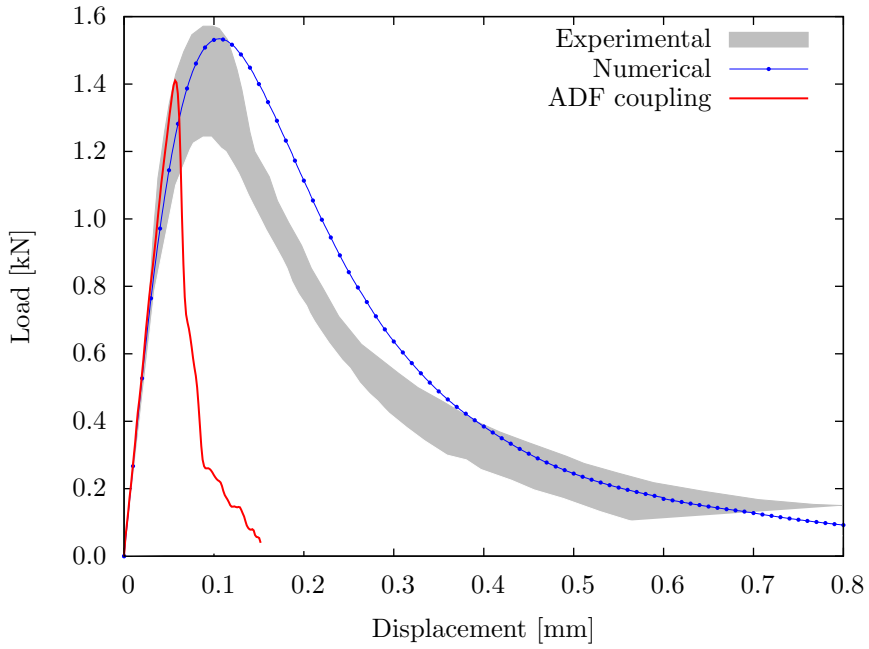

Figure 5.32. Three point bending 3D beam. Curve load vs displacement.

In Figure 5.33 a detail of the load vs displacement curve is shown. In the same figure, the evolution of the number of discrete elements is depicted.

As a conclusion of the chapter, the examples shows that both fixed and adaptive DEM/FEM coupling schemes decreases the computational time with a negligible influence in the accuracy of the results, and permits the consideration of higher domains.

The adaptive coupling scheme require to introduce equilibrium in the new particles

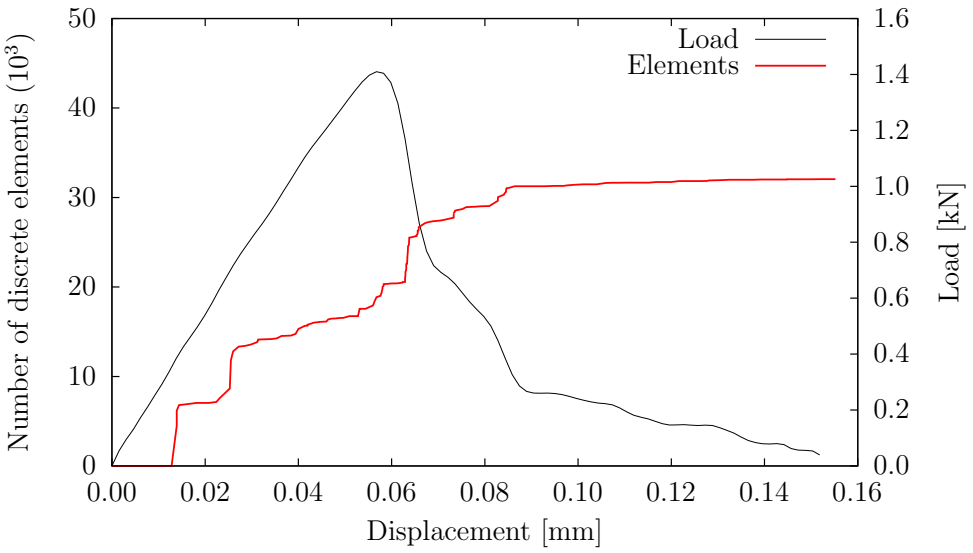

Figure 5.33. Three point bending 3D beam. Evolution of the number of discrete elements.

after the projection of the kinematic variables, as the rotation of the particles can not be projected. Even if this can be solved with few iterations, a more detailed study of different projection schemes for the kinematic variables could be performed, considering different stress localization techniques.

Chapter 6

Modelling of rock cutting process

This chapter presents the application of the DEM to a practical problem. All the aspect of the DEM and DEM/FEM coupling developed in the previous chapters are applied to the simulation of rock cutting processes.

The simulation of excavation processes in general, and the rock cutting process in particular, are an interesting case in which the continuum-based simulation techniques, like the FEM, present well known difficulties in its application. The fracture and fragmentation of the rock material with brittle failure, resulting typically in the excavation process, are difficult to reproduce with these techniques, while the discrete nature of the DEM offers a more realistic ways to simulate this kind of phenomena.

The design of rock cutting tools for the excavation machinery has been historically based in a combination of the experience of the workers and real size laboratory tests, resulting many times in an inefficient process, and involving high costs for the excavation companies. In the last decade, different empirical models have been developed for the estimation of the principal parameters involved. This models can be useful in certain cases; nevertheless its use is restricted to the availability of historical data and range of rock material properties [91].

The application of ad-hoc simulation techniques for this kind of processes can result in a faster design stage and lower costs, limiting the laboratory tests.

The simulation and analysis of a laboratory test used extensively in the design of rock cutting tool is performed. The cutting tools selected for this purpose are the disc cutters used in the tunneling with *tunnel boring machines* (TBM). The simulation results are compared with one of the empirical models more extended for this purpose [95], which presents accurate results under certain conditions, as homogeneity of the material, but has some problems dealing with fracturing or joints in the rock sample.

6.1 Linear cutting test with disc cutters

The *Tunnel Boring Machines* (TBM) is currently utilized in massive scale in underground construction and tunneling in civil construction and the mining industry (see Figure 6.1).

In the design and performance prediction of TBMs, the volume of rock cutted by TBM disc cutter are one of the most important parameters [111]. One of the most representative testing procedures for designing the cutterhead of TBMs and to predict its performance is the full-scale *linear cutting machine* (LCM) test [82, 97]. The LCM test provides a direct measure of rock cuttability under pre-defined field conditions. A simple approximation is to use the penetration depth considered in the LCM test to calculate the cutting volume after the test is run. However, the difference between the real cutting volume and the simply calculated volume varies depending upon the cutting performance of the disc cutter.

With the simulations of the LCM test for a single disc cutter is possible to perform an analysis of the effect of different parameters such as velocity, penetration rate, or geometry (width, radius, etc.), on the resultant forces, as well as their influence on the rock fracture.

(a) Herrenknecht AG, Gripper TBM.

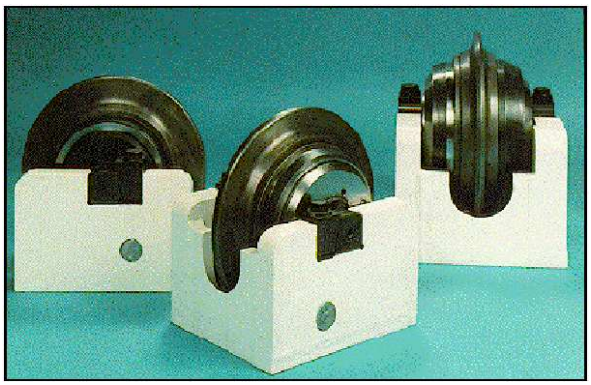

(b) Single disc cutter.

Figure 6.1. TBM and disc cutters.

The performance of the TBM depends basically on the disc cutters performance. Cutting tools serve for the transmission of energy generated by the machine to the rock in order to cause fragmentation. The cutting surface rolls across the rock surface during the cutting operation. Hence, different parts of the tool contact the rock thereby distributing the heat load and allowing time for each part of the cutting surface to cool during the machining operation, as shown in Figure 6.2.

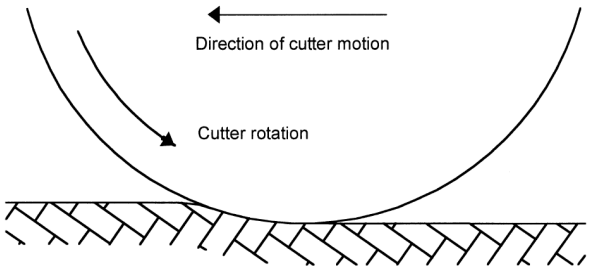

Figure 6.2. A rolling cutter machining a rock surface.

The prediction of the reaction forces over the disc cutter is necessary in order to estimate the real forces (thrust force and torque) over the TBM. One of the principal obstacles that arises during the excavation of rock tunnels without using explosives is the optimal design of the cutting tools that perform the fragmentation of the ground at an acceptable economical level.

The major overcost of this type of work is the wear and failure of the cutters which require continuous change of cutters. This is costly in itself and also shows the performance of the TBM. The cutter analysis allows to detect the reasons of cutter wear and failure, thus contributing to find solutions. Besides finding the causes and the reasons of the cutters reinstatement, looking for improvements in the performance of the change, maintenance and repair of the discs will reduce these overcosts.

In order to estimate the disc cutter behavior it is necessary to consider some factors, like the disc geometry (diameter and tip width), spacing between disc cutters, and penetration. The forces over a single disc cutter are the normal force, rolling force and side force, as depicted in Figure 6.3.

Efficient excavation by disc cutter correlates with the formation of large chips between disc cutter paths. A crushed zone develops beneath the cutter as it is forced into the rock. As stresses continue to build up in the crushed zone, radial cracks begin to form and propagate into the rock (see Figure 6.4). When one or more of these cracks meet those developed from adjacent cut, chips are released [10].

The LCM test was originally developed by the Colorado School of Mines (CSM), and has been actively used to design the TBM cutterheads. The biggest advantage of the linear cutting machine is that the design parameters such the cutter spacing, cutter penetration, cutter thrust and cutting speed can be controlled.

The LCM test is used for the analysis of forces over the disc cutter under different

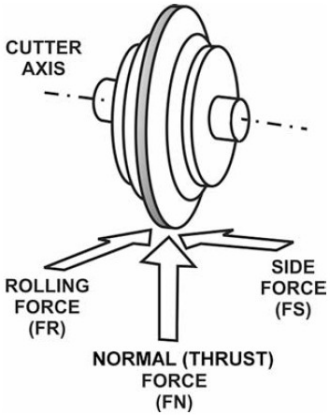

Figure 6.3. Individual force acting on a disc cutter.

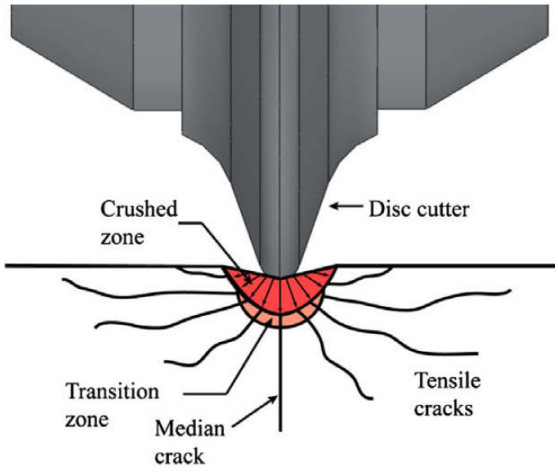

Figure 6.4. Stress field and resultant fractures beneath the penetrating edge of a disc cutter.

conditions of spacing between cuts and penetration into the rock, providing a direct measure of rock cuttability under simulated field conditions. The main parameters obtained in the test are the reaction forces, that are finally used for the estimation of the full TBM performance in operating conditions.

In Figure 6.5, the LCM setup of the CSM is depicted. The LCM features a large stiff reaction frame on which the cutter is mounted. A triaxial load cell, between the cutter and the frame, monitors forces and a linear variable displacement transducer monitors travel of the rock sample. A servo controlled hydraulic actuator forces the sample through the cutter at a preset depth of penetration, width of spacing and constant velocity. During the cut, the triaxial load cell measures the normal, rolling, and side forces acting on the cutter [43].

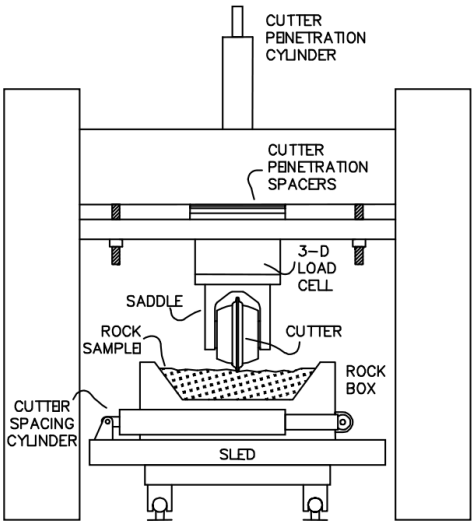

Figure 6.5. Linear cutting machine. Colorado School of mines.

6.2 Discretization of the linear cutting test model

The aim of this section is to analyze the capabilities of the DEM and DEM/FEM coupling presented in the previous chapter for the modelling of the rock cutting process with disc cutters, evaluating the influence of the different rock material properties, as strengths or Young modulus, and process parameters like penetration depth, spacing between cutter discs or advancing velocity. For this reason, a modelling of the full-scale LCM test is performed. Most of the results are compared with an empirical model commonly used in industry.

The numerical model considers the rock material sample discretized with DEM or coupled DEM/FEM. A more complex model of the rock cutting process should consider a thermo-mechanical coupled model, with the cutter disc discretized with FEM, in order to obtain the thermal-mechanical deformation and wear in the disc cutters. Nevertheless, the purpose of this analysis is to reproduce the interaction forces, and the cutter discs discretized as rigid bodies.

6.2.1 Disc cutters selection and discretization

For the geometry of the disc cutter samples, standard constant cross section (CCS) disc profiles of Herrenknecht AG are considered, with ring diameters of 17 and 19 inch. The detailed description of both disc profiles are depicted in Figure 6.6.

The CCS-shape disc cutters are used extensively since the late 1970s, in replace of the

V-shapes, because of their long-term durability and overall performance advantages [1].

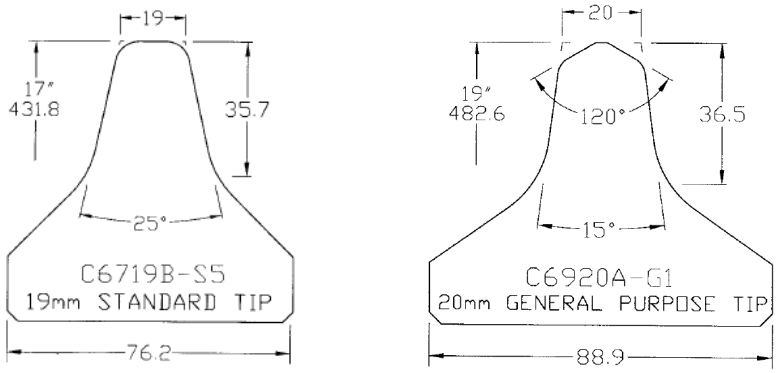

(a) 17" diameter disc. (b) 19" diameter disc.

Figure 6.6. CCS type disc cutter profiles.

Both cutter discs are discretized with a structured mesh of triangular elements. The 17" diameter disc is discretized with 9200 elements, considering a refinement in the cutter tip in order to reproduce its curvature. The 19" diameter disc is discretized with 8880 elements. In Figure 6.7, a sample of the model considered for the linear cutting test is shown.

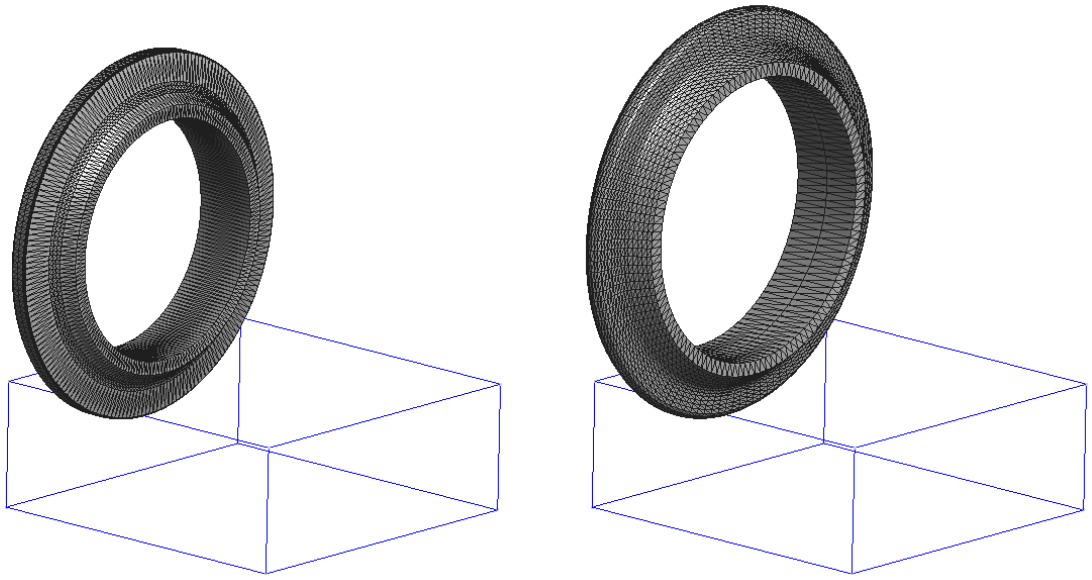

(a) 17" diameter disc. (b) 19" diameter disc.

Figure 6.7. Discretization of disc cutters.

Furthermore, we must consider the definition of the mass and moment of inertia in the disc cutter, because a virtual point is used to apply the movement and velocity conditions

in the axis of the cutter. These values have not a significant effect upon the normal forces, but can be relevant for the rotational forces. The mass considered in both discs is m = 10 kg, and moment of inertia I = 0.001 kg m^2. All the degrees of freedom in the disc axis are fixed, except the rolling axis.

6.2.2 Rock material sample

Initially, a unrelieved rock specimen is considered. A geometry for the rock material sample of 0.4 x 0.15 x 0.4 m is selected in order to obtain optimum results quality and the related computational cost. The full-scale LCM test considers a 1.0 x 0.7 x 0.7 m of block rock samples, in order to avoid any kind of boundary effect. Nevertheless, the simulation assumes that in the rock sample size selected boundary effects are negligible.

For the rock specimen, the mechanical properties are defined for a real *granitic gneiss* material, with values obtained from laboratory tests [71]. Two different material properties are considered for comparison purpose. For the cutting process, the most important material properties are UCS and BTS. Then it is possible to obtain a good result even with a less accurate in the estimation of the model parameters for the rest of mechanical properties. The mechanical properties considered for both rock material samples are presented in Table 6.1.

Parameter	Description	Material 1	Material 2
σ_c	Uniaxial compressive strength (MPa)	147.3	102.6
σ_t	Brazilian tensile strength (MPa)	10.2	11.5
E	Young modulus (GPa)	40.0	40.0
ν	Poisson's ratio	0.23	0.23
ρ	Density (kg/m^3)	2650	2650

Table 6.1. Mechanical properties for the linear cutting test.

Due to the high computational cost involved in the simulations, a good compromise between number of elements and model size should be selected. In order to maintain a rock specimen of sufficient size, a coupled DEM/FEM approach is considered. At the bottom of the rock sample, in the zone in interaction with the disc cutter, a DEM subdomain is defined of size 0.15 x 0.05 x 0.4 m, as shown in Figure 6.8. Both fixed and adaptive DEM/FEM coupling schemes are used, in order to compare the capabilities of both schemes. In both cases, the same DEM assembly is considered, and the domain

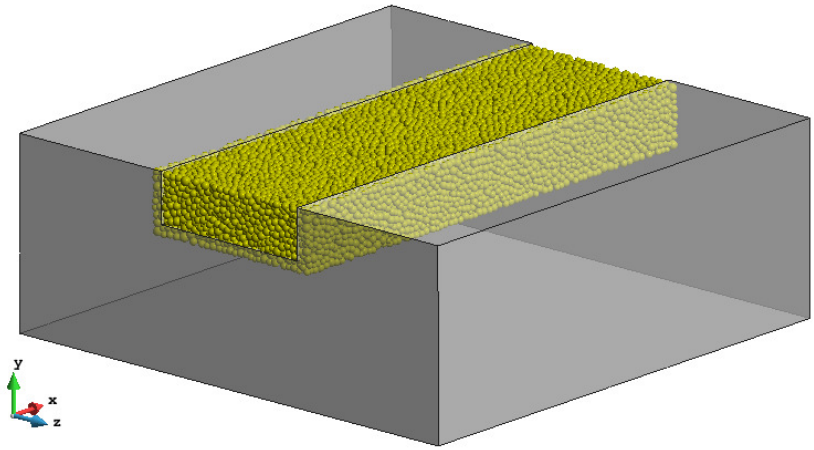

(a) Fixed DEM/FEM coupling

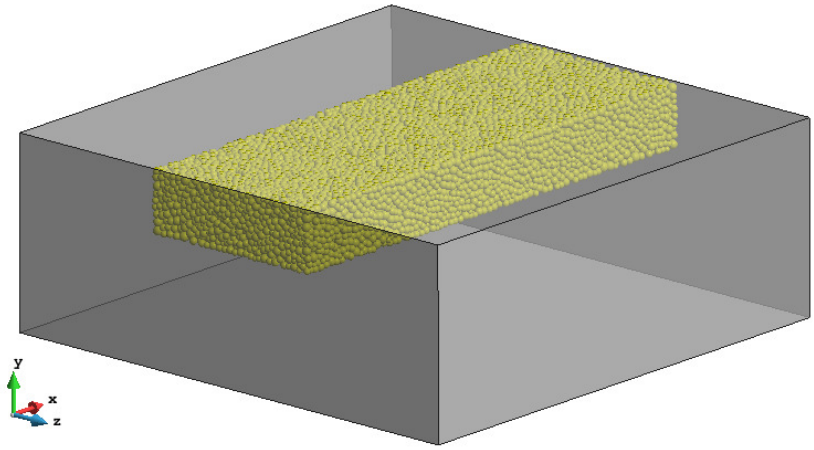

(b) Adaptive DEM/FEM coupling

Figure 6.8. Unrelieved rock specimen discretized with the fixed and adaptive coupled DEM/FEM scheme.

discretized with FEM changes. In the case of the adaptive DEM/FEM scheme, all the rock sample is discretized with FEM.

The domain discretized with FEM has 5040 tetrahedral elements for the case of adaptive DEM/FEM coupling. For the case of fixed coupling 4752 tetrahedral elements have been used.

The rock portion discretized with DEM has 35604 spherical particles. The range of radius is 1.4-3.9 mm, with a characteristic radius $\widetilde{r} = 2.55$ mm. The particle size distribution is presented in Figure 6.9. The detail of the particle assembly characterization

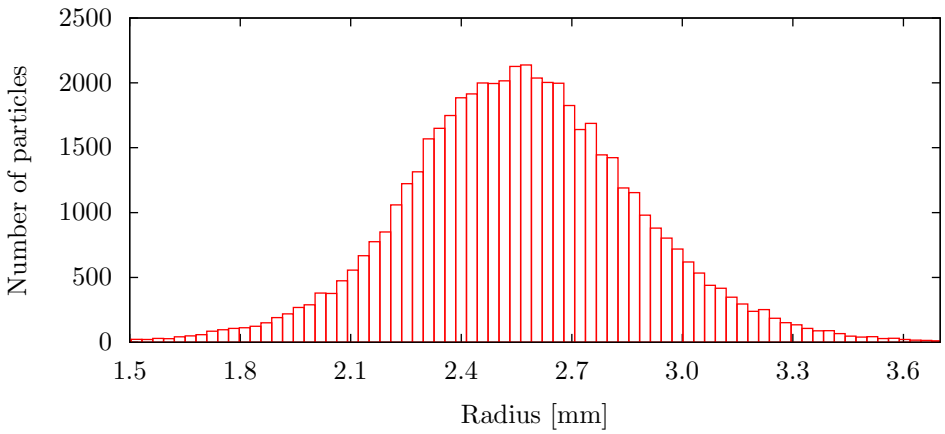

Figure 6.9. Radius size distribution of particle assembly for the LCM test.

is shown in Table 6.2.

Parameter	Description	Value
N_p	Number of particles	35604
$\bar{r}$	Average radius (mm)	2.5516
$\widetilde{r}$	Characteristic radius (mm)	2.7971
n_c	Coordination number	11.449
e	Porosity (%)	24.9122

Table 6.2. Characterization of the particle assembly for the LCM test.

Considering the particles assembly characterization and the mechanical properties of the rock, the DEM model parameters are estimated using the methodology presented in Section 4.4, and presented in Table 6.3 for both material samples.

Parameter	Description	Material 1	Material 2
K_n	Stiffness in normal direction (MN/m)	160.79	160.79
K_t	Stiffness in tangential direction (MN/m)	16.325	16.325
K_t/K_n	Stiffness ratio	0.1015	0.1015
R_n	Strength of cohesive bonds in the normal direction (kN)	0.8482	0.5908
R_t	Strength of cohesive bonds in the tangential direction (kN)	4.1759	2.9087
ρ	Density (kg/m^3)	3085	3085

Table 6.3. DEM model parameters for the LCM test.

The change of density is obtained assuming the void ratio of the generated mesh, in order to preserve the equivalent mass.

In the rock specimen, the lateral and bottom surfaces were restricted, as shown in Figure 6.10. The bottom surface have been completely restricted in its movement, while lateral surfaces has been restricted in direction of the side-force (z-direction). This allows the displacement in the normal and rolling forces in the rock specimen.

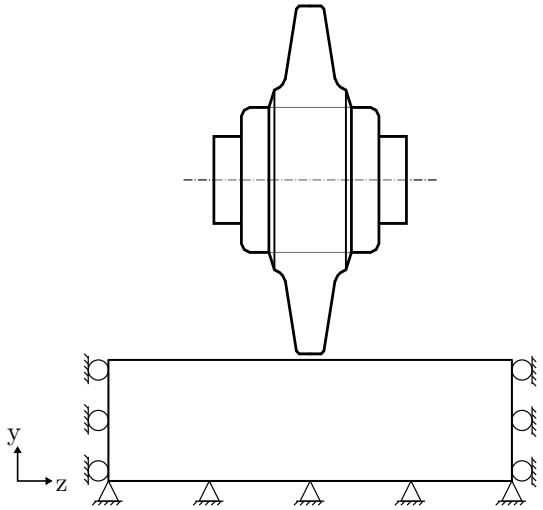

Figure 6.10. Boundary conditions employed in rock specimen sample for the LCM test.

6.2.3 Cutting process parameters

The cutting process parameter, such as velocity or penetration rates are taken from a real TBM drive [71]. The selected parameters consider different penetrations for each material specimen. For the advancing velocity, two different values are defined for each material sample. Nevertheless, most of simulations presented in this chapter have been carried out with the velocity of case 2 of material 1. This is because the velocity presents a low influence in the interaction forces, as will be shown bellow.

The cutting process parameters are shown in Table 6.4, for the two different rock material samples.

In the LCM test, one of the most important parameters is the spacing between the disc cutters [97]. As initially the simulation are performed in unrelieved rock samples, the spacing between disc cutters is not considered. Later on, the spacing is introduced in order to analyze its influence in a more realistic situation.

Parameter	Description	Material 1		Material 2	
		Case 1	Case 2	Case 1	Case 2
p	Penetration rate (mm)	3.9	3.9	3.2	3.2
v	Cutting velocity (m/s)	0.6519	2.3702	0.6190	2.3979

Table 6.4. Cutting process parameters for the LCM test.

6.3 Cutting forces prediction models

Since the middle of the 1950's, a wide variety of performance prediction methods have been developed for the estimation of the TBM performance. These methods can be classified in two categories: theoretical/experimental models, based on laboratory test and cutting forces, and empirical models, based on field performance of the TBM and rock properties. Within the category theoretical/experimental models, we will focus in methods based in the cutter load approach, which allow us to estimate the cutting forces in a single disc cutter. A detailed review of the different performance prediction methods can be found in [48, 91].

Considerable research has been performed on the estimation of the cutting forces, based on the correlation of different parameters, as the disc cutter geometry, spacing, penetration rate, disc rolling velocity and rock material properties.

Roxborough and Phillips [100] proposed a model based in basic principles and cutter geometry for the estimation of the normal and rolling forces on a single V-shape disc cutter. The normal force is calculated as a product of the area of the disc contact against the rock surface, and the compressive strength of the rock mass. This model does not include the spacing between the cutters, which is an important parameter that should be taken into account.

Sanio [101] presents a model based in the tensile failure for the chip formation, where is possible to estimate the cutting forces in V-shape disc cutters. The model allows to estimate the pressure in the crushed zone from the fracture toughness. This model can take into account the joint effects, by a correction factor based in the joint orientation.

Sato [103] follows the previous approach, but in a rotary cutting machine. The model shows the independence of the cutting coefficient (ratio of rolling and normal forces) with the spacing, and increasing with a square root of the penetration. Later studies introduce the effect of the tool orientation.

As V-shape disc cutters are no longer used on TBMs or other mechanical excavators, the Colorado School of Mines developed a model for the CCS-shape cutters [95, 97]. This model will be used for the comparison with the simulation of the LCM test.

6.3.1 Colorado school of mines model

The first version of this model was developed by Ozdemir in [87], and later was updated by Rostami [95, 97]. The CSM model estimates the cutting forces considering a given penetration, rock mass properties, cutter geometry and cutting conditions. The model is based in a large data base of full scale LCM tests, and does not consider the rock mass conditions, as fractures or joints.

The model proposes a pressure distribution P in the crushed zone as

$$P(\theta) = P_o \left(\frac{\theta}{\phi}\right)^{\psi} \tag{6.1}$$

where ψ a constant for the pressure distribution function (typically varies between 0.2 for V-shape and very sharp cutters to -0.2 for wider tip cutters), ϕ angle of contact between rock and cutter, defined as

$$\phi = \cos^{-1}\left(\frac{R-p}{R}\right) \tag{6.2}$$

and P_o is the base pressure in the crushed zone, established from regression analysis of several tests, and estimated from rock strength and cutting geometry:

$$P_o = C \sqrt[3]{\frac{\sigma_c^2\, \sigma_t\, s}{\phi \sqrt{R\,T}}} \tag{6.3}$$

where C is a dimensionless constant (usually C=2.12), and s the spacing between cutters.

The total resulting cutting force F_T can be obtained by integrating the pressure over the contact area (Figure 6.11), as

$$F_T = \int_0^{\phi} T\, R\, P(\theta)\, d\theta = \frac{T\, R\, P_o\, \phi}{1+\psi} \tag{6.4}$$

where T is the cutter tip width and R the cutter radius.

To recover the normal and rolling forces, the *cutting coefficient* CC (also called *rolling coefficient*) is used, which is the ratio of both forces defined by the angle β as

$$CC = \frac{F_r}{F_n} = \tan(\beta) \tag{6.5}$$

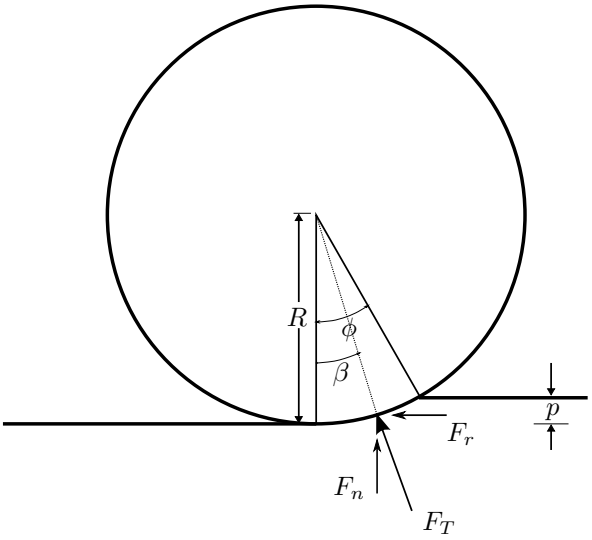

Figure 6.11. Scheme of forces acting on a disc cutter and incidence angles.

Assuming a uniform distribution of the pressure in the contact area, the model proposes a geometrical definition of β as the middle point of the contact area, i.e.

$$\beta = \frac{\phi}{2} \tag{6.6}$$

Finally, the normal and rolling forces are estimated projecting the total force in each direction as

$$F_n = F_T \cos(\beta) = \frac{T\,R\,\phi\,P_o}{1+\psi} \cos\left(\frac{\phi}{2}\right) \tag{6.7}$$

$$F_r = F_T \sin(\beta) = \frac{T\,R\,\phi\,P_o}{1+\psi} \sin\left(\frac{\phi}{2}\right) \tag{6.8}$$

This model have been used in many tunneling projects with a higher degree of success, for the estimation of the TBM cutterhead performance [46, 96, 98].

6.4 Numerical results and comparisons

Several simulations have been performed considering different materials, disc profiles and cutting conditions. Initially, the simulations have been performed in the unrelieved rock material presented before, where the potentiality of the simulation scheme is analyzed, and different parameters involved in the cutting process are studied.

Later on, simulations considering different penetrations and spacing between disc cutters were carried out for relieved rock specimens. A comparison of the reaction forces and the specific energy, with the CSM empirical model is performed.

6.4.1 Unrelieved rock specimen

The LCM test is performed considering the unrelieved rock specimen for both materials. The evolution of the simulation with disc diameter of 19" and the material 1, with a cutting velocity of 2.3702 m/s (case 1), is shown in Figure 6.12, where the movement of the disc cutter and the damage in the specimen can be appreciated.

In the full-scale LCM laboratory test, the results obtained are normally the volume of rock that has been cut and the reaction forces over the disc cutter. The advantage of the computer simulation is the capability of analysing more aspects of the process, as the stress field over both rock and disc, friction, interaction surface, etc. In Figure 6.13, an upper view of the evolution of the principal stress (σ_3) is shown. A stress concentration in the contact area can be appreciated during the evolution of the cutting process. Furthermore, the asymmetric distribution of stress due to the particle assembly presents a more realistic situation.

The distribution of stress in the rock around the contact point is shown in Figure 6.14, where the average stress in the particle assembly is projected over a longitudinal cut of the rock. A mesh of tetrahedral elements is generated from the center of the particles. This procedure allows the visualization of the different variables in the equivalent continuum.

It can be noted a small discontinuity between the stress in the DEM and the FEM regions. This is directly related to the average procedure for stress calculation, as the average stress calculation in the DEM region does not include the FEM nodes, which introduce this small difference.

This information can not be directly obtained in real laboratory tests and it is useful for analyzing the behaviour of the rock during the cutting process, and to verify the empirical/theoretical models, as it will be shown later.

The evolution of the normal and rolling cutting forces during the cutting process is depicted in Figure 6.15. The average value of the normal force is estimated considering the forces between 0.1 and 0.25 m, in order to avoid the boundary effect, resulting in a force of 191.08 kN. This value can not be compared with the CSM model, because the model considers a spacing between disc cutters. This require a relieved rock sample,

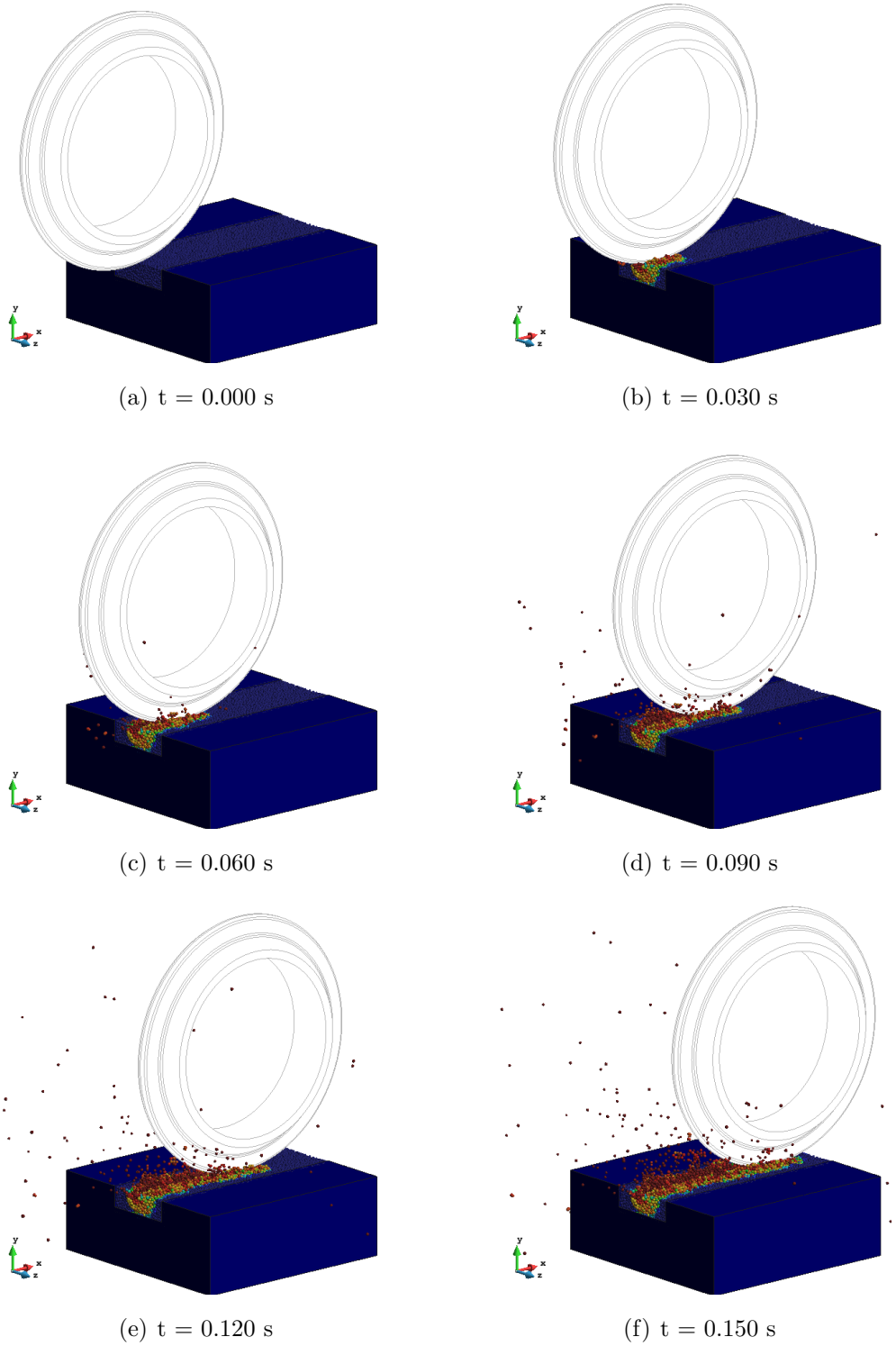

(a) t = 0.000 s (b) t = 0.030 s

(c) t = 0.060 s (d) t = 0.090 s

(e) t = 0.120 s (f) t = 0.150 s

Figure 6.12. Evolution of damage in the LCM test with unrelieved material 1 and ring of 19".

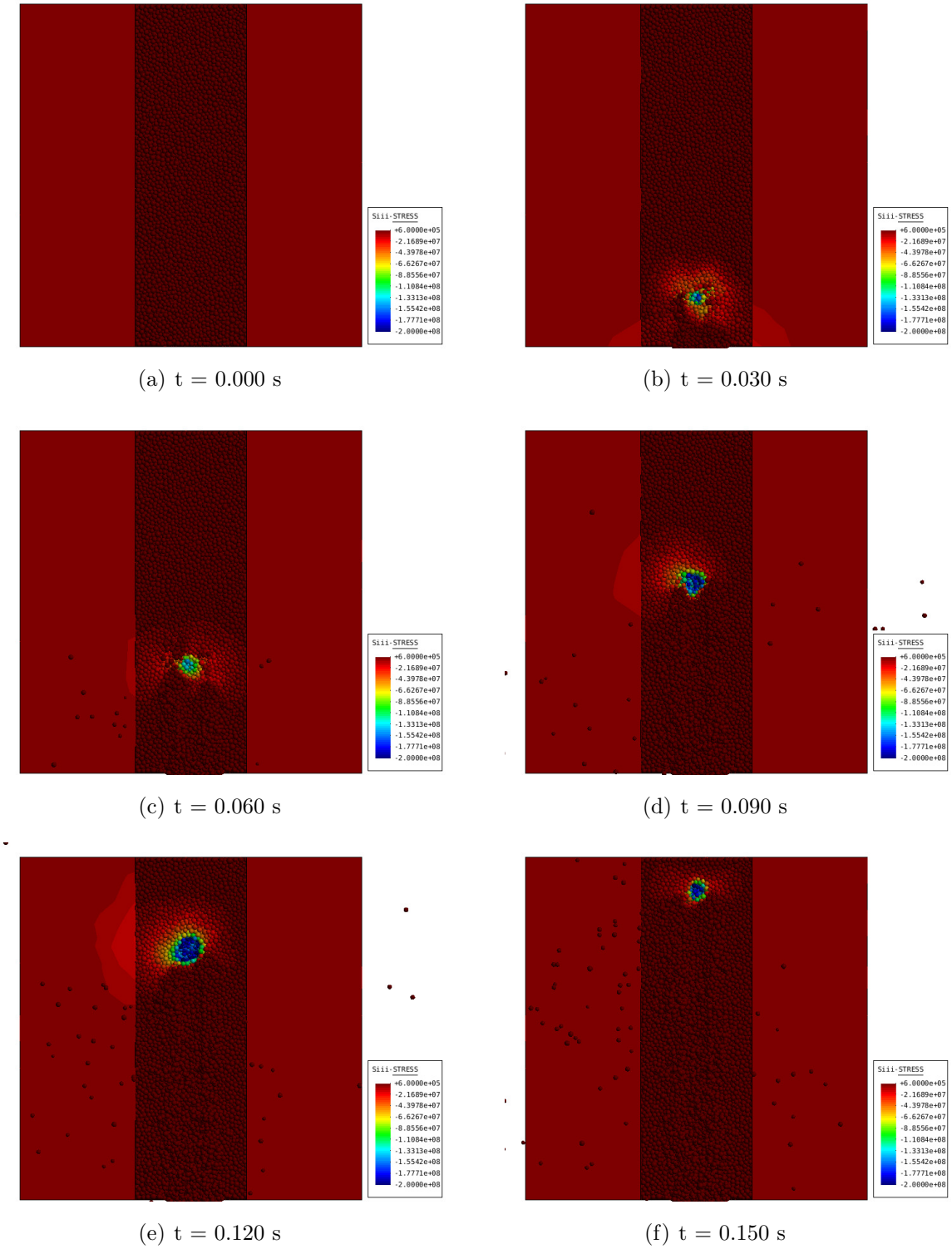

(a) t = 0.000 s (b) t = 0.030 s

(c) t = 0.060 s (d) t = 0.090 s

(e) t = 0.120 s (f) t = 0.150 s

Figure 6.13. Upper view of principal stress distribution (σ_3) in the LCM test with unrelieved material 1 and ring of 19".

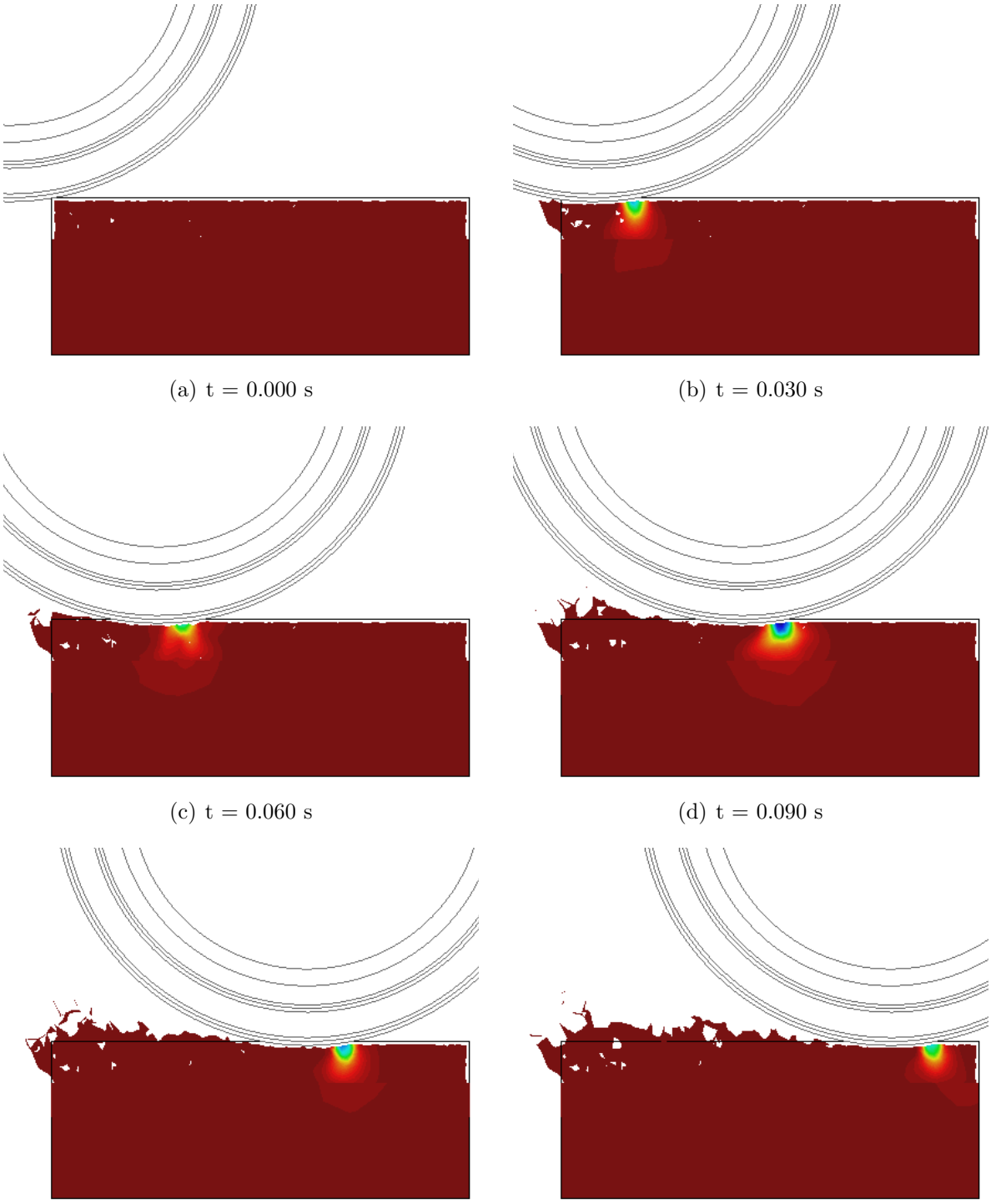

(a) t = 0.000 s

(b) t = 0.030 s

(c) t = 0.060 s

(d) t = 0.090 s

(e) t = 0.120 s

(f) t = 0.150 s

Figure 6.14. Lateral view of principal stress distribution (σ_3) in the LCM test with unrelieved material 1 and ring of 19".

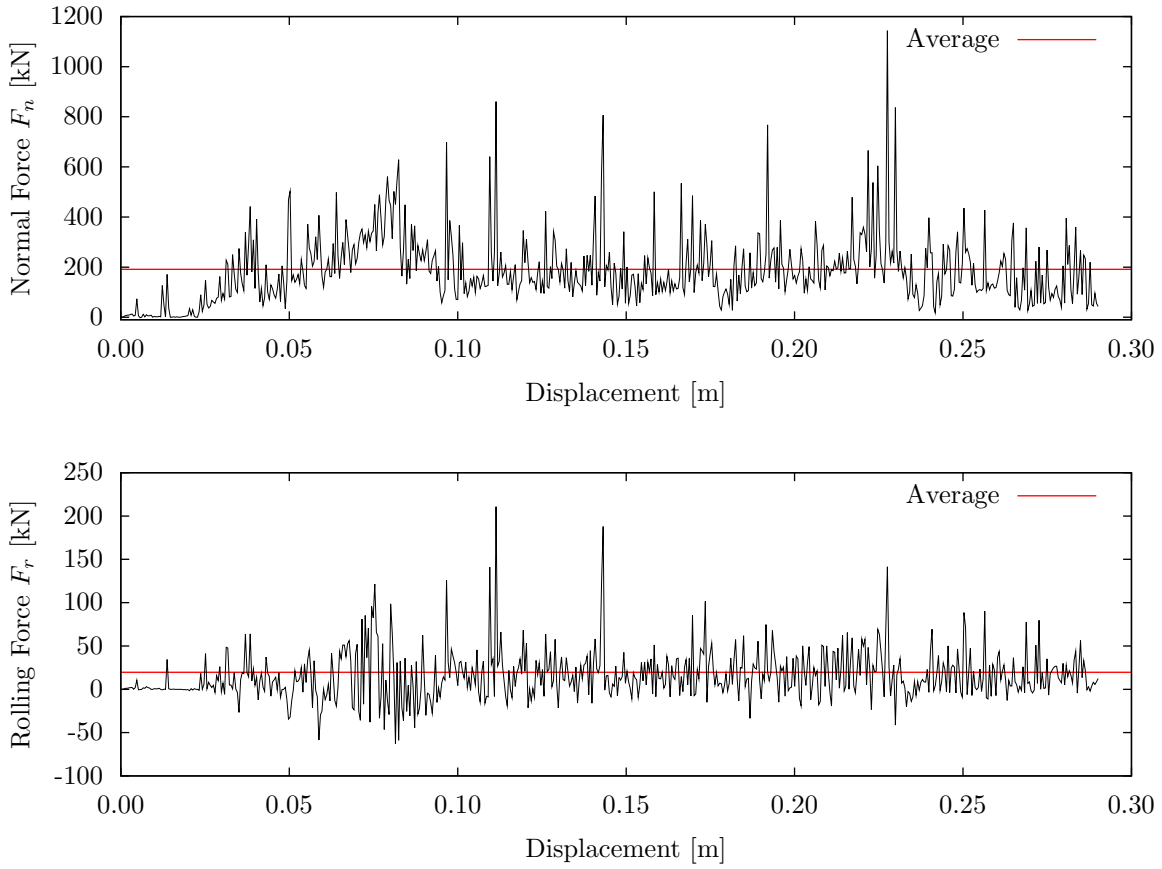

Figure 6.15. Cutting forces in LCM test with unrelieved material 1 and ring of 19".

which is not the case in the simulation. Nevertheless, for this material and disc profile an average normal force has been measured in-situ by a real TBM, with a normal force of 231.8 kN [71], which yield an error of 20% with the computed value. No information about the spacing is provided, but for the estimation of the TBMs performance it is common to consider a friction looses of 1.2. Considering this factor, a very close value to the experimental result can be obtained in the simulation.

For the evolution of the rolling force, depicted in Figure 6.15 (bottom), the average value is estimated in 19.608 kN. In this case experimental results are not available, however results can be considered to be good taken into account the range of values of the *cutting coefficients CC* found in the literature. Considering the CSM model, the angle ϕ for this case is 10.32°. Replacing this value in (6.5) and (6.6), the estimated rolling force is 17.25 kN, which has a difference of 13.7 % with the value obtained in the simulation.

The same simulation is performed now using the rock material 2, and the velocity of case 2. The evolution of the normal and rolling forces are shown in Figure 6.16. The estimated average value for the normal force is 159.40 kN. For this case, the actual average force measured in the TBM is 178.6 kN. Even considering the common coefficient for lost of performance, the value is still within the computed range, and hence, the numerical results can be considered acceptable.

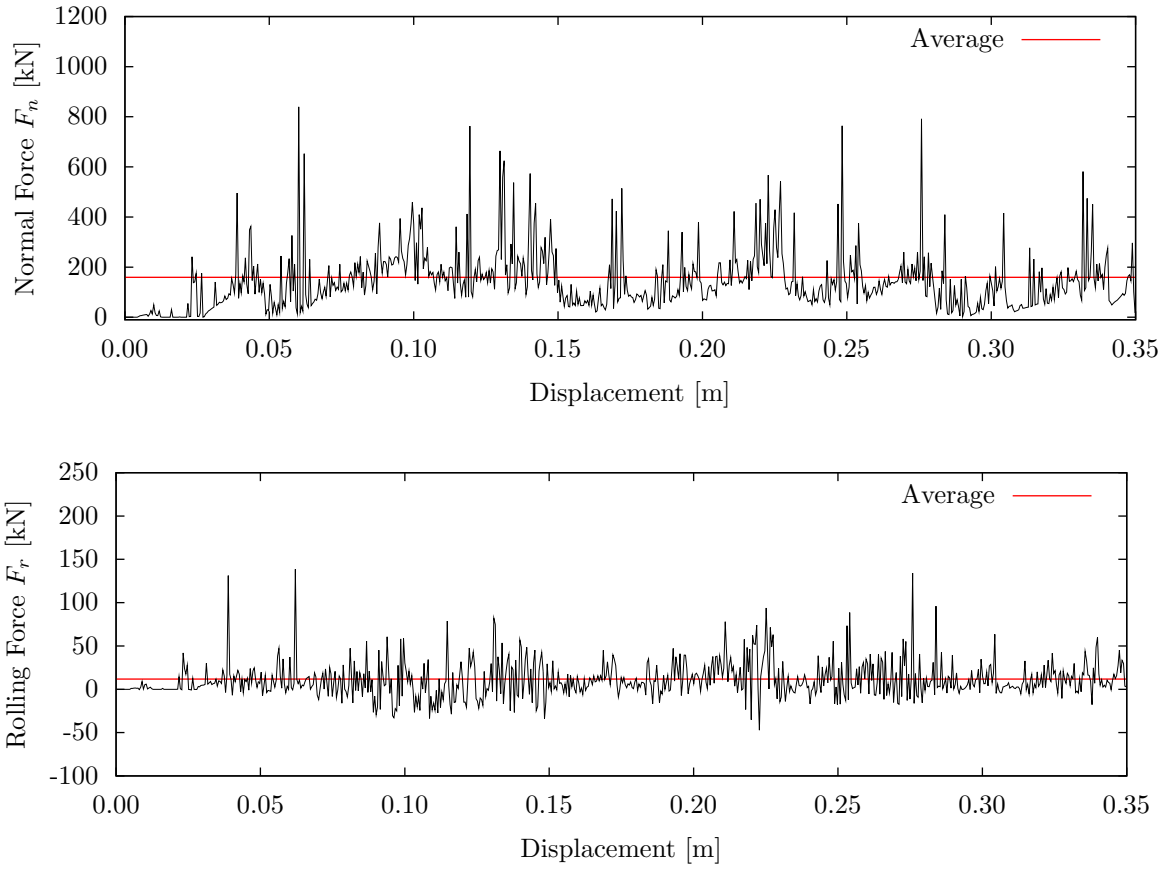

Figure 6.16. Cutting forces in LCM test with unrelieved material 2 and ring of 19".

The rolling force computed in this case presents an average value of 12.00 kN. Taken the same value of CC considered before for the CSM model, the value for the rolling force is 14.39 kN. Differently than in the previous case, now the computed rolling force is lower than the estimated by the CSM model in 17%.

In both cases, the stress in the contact area between the disc and rock specimens present a distribution different than the proposed by the CSM model. In the simulations, the stress presents a distribution similar to a Gaussian distribution. In order to verify

the stress results in the crushed zone, a zoom of the principal stress distribution in the contact area, for the rock specimen 1, is presented in Figure 6.17. The concentrated stress in a small region close to the attack point can be appreciated, while in the region close to the top of the contact area, in the lowest part of the disc cutter, the stress is almost zero.

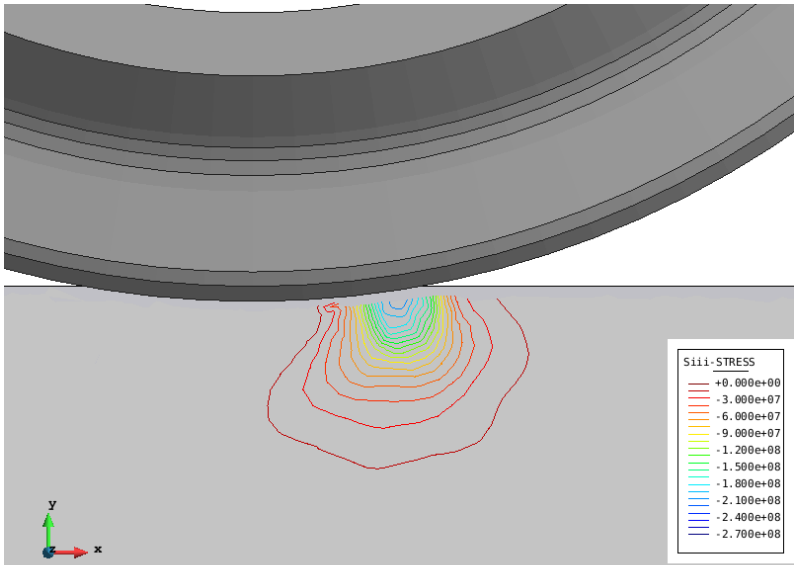

Figure 6.17. Detail of principal stress distribution in crushed zone for the LCM test with unrelieved material 1 and disc diameter 19" (t=0.09 s).

The simulation is now performed with the disc cutter of diameter 17", in order to show the influence of the ring shape in the interaction forces. The evolution of the normal and rolling forces for the rock material 1 are depicted in Figure 6.18.

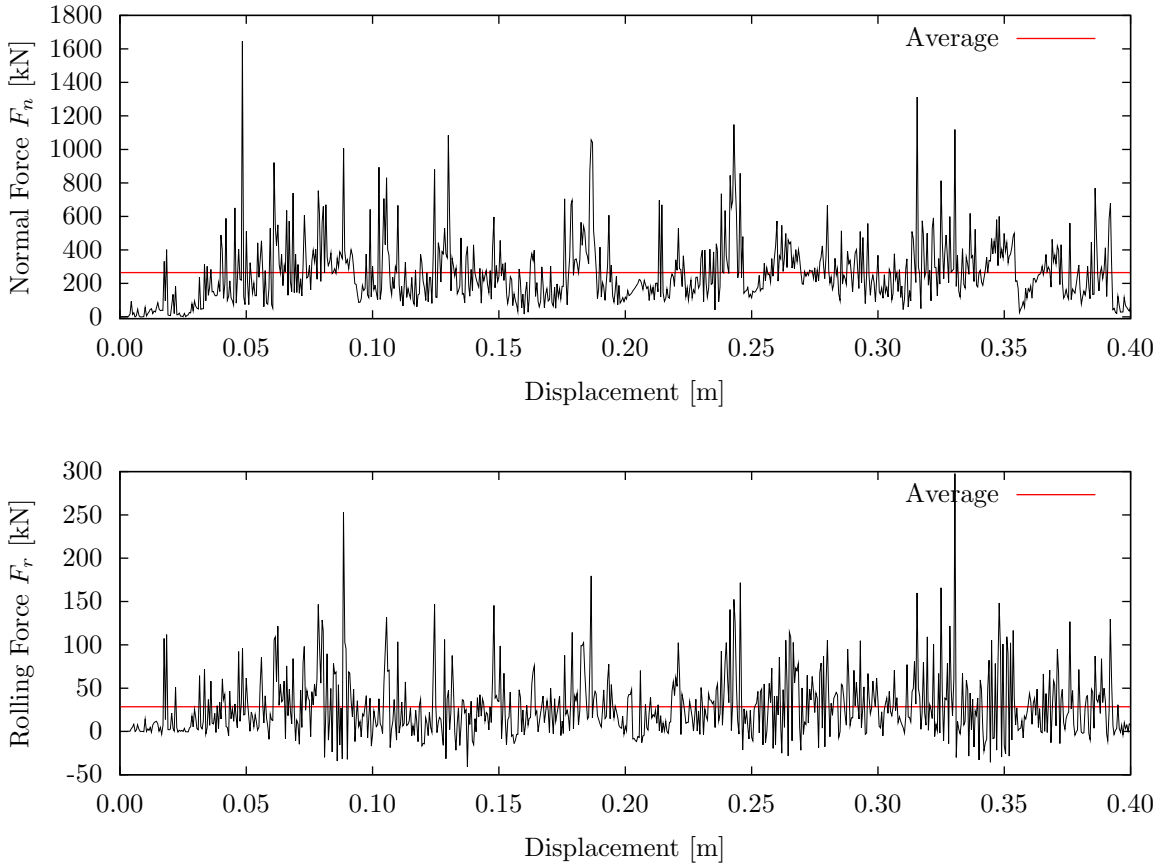

Figure 6.18. Cutting forces in LCM test with unrelieved material 1 and ring of 17".

The average normal force is estimated to be 264.40 kN. This is considerably higher than with the 19" disc cutter. As the material properties and the penetration are the same, the increase of the force is strictly related to the geometry. Following the CSM model, if the disc diameter and tip in the 19" disc cutter are higher, the area of the contact surface is higher, which yield a higher value of the total contact force.

This can be explained considering a different geometric aspect, which is related with the volume of material cut. Even if the area of the contact surface is higher in the 19" disc cutter, the transversal area of the disc (based in its profile) immersed in the rock is higher in the 17" disc. This is due to the trimmed area in the profile of the 19" disc, of 120 deg (see Figure 6.6). Taken into account the penetration of p = 3.9 mm, the transversal area of the 17" disc is around 75% higher than in the 19" disc.

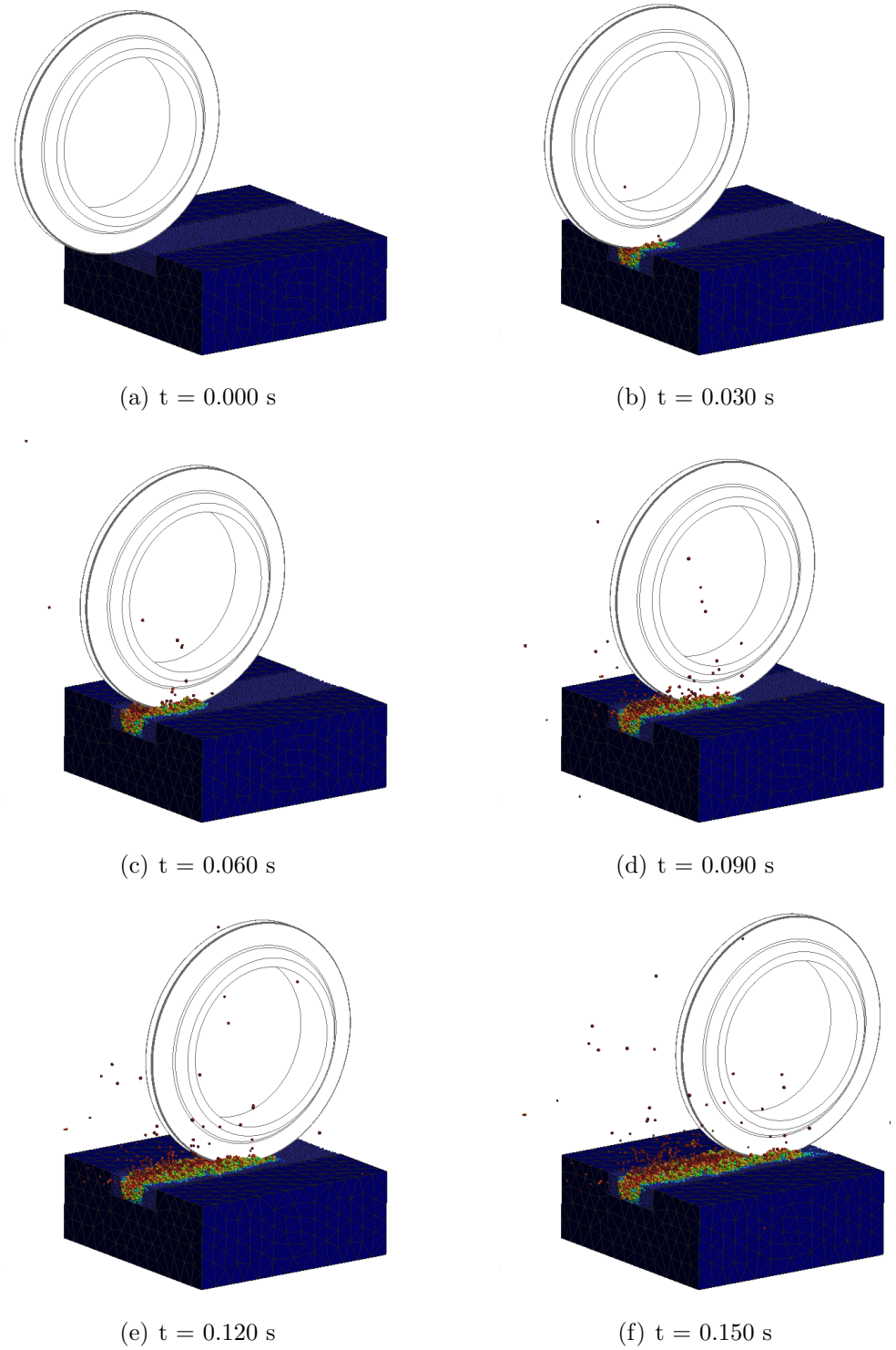

(a) t = 0.000 s

(b) t = 0.030 s

(c) t = 0.060 s

(d) t = 0.090 s

(e) t = 0.120 s

(f) t = 0.150 s

Figure 6.19. Evolution of damage in the LCM test with unrelieved material 1 and ring of 17".

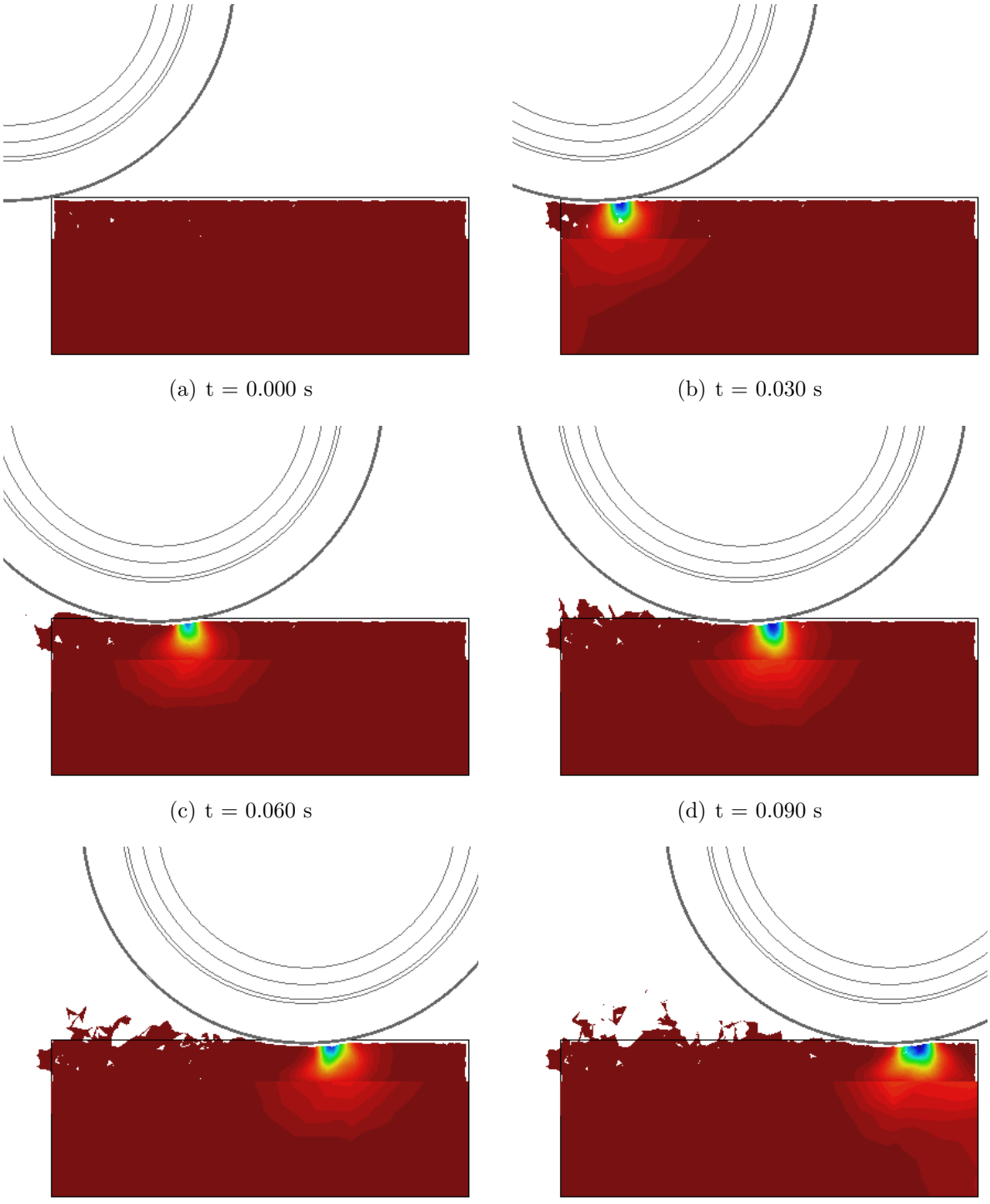

(a) t = 0.000 s

(b) t = 0.030 s

(c) t = 0.060 s

(d) t = 0.090 s

(e) t = 0.120 s

(f) t = 0.150 s

Figure 6.20. Lateral view of principal stress distribution (σ_3) in the LCM test with unrelieved material 1 and ring of 17".

Figure 6.18 shows the evolution of the rolling force, with an average value of 28.55 kN. This value is close to the estimated by the CC with the CSM model, with an angle $\phi = 10.91°$, which yield a value for the rolling force of 25.24 kN.

The evolution of the cutting process and the damage in the rock specimen is depicted in Figure 6.19, while the distribution of stress in the rock, around the contact area, is presented in Figure 6.20, in a longitudinal cut over the equivalent FEM mesh.

Similarly to the disc cutter of 19" diameter, the stress presents a non-uniform distribution, different to the proposed by Rostami in [97]. This phenomena is particularly interesting and should be analyzed in more the detail.

As mentioned before, the stress distribution around the contact area with both disc cutters presents a non-uniform distribution, which is different to the uniform pressure distribution proposed by Rostami [95, 97]. In order to have a better idea about this phenomenon, the average force distributions over the disc cutters are shown in Figure 6.21. The average force in both simulations presents a quasi-gaussian distribution. In the attack point, where the disc cutter start the contact with the rock the force is small in comparison with the pick force. The same occurs in the final part of the contact surface, where the force disappear almost completely. The pick force is not localized in the intermediate region, as proposed in the CSM model for the estimation of angle β [54, 96].

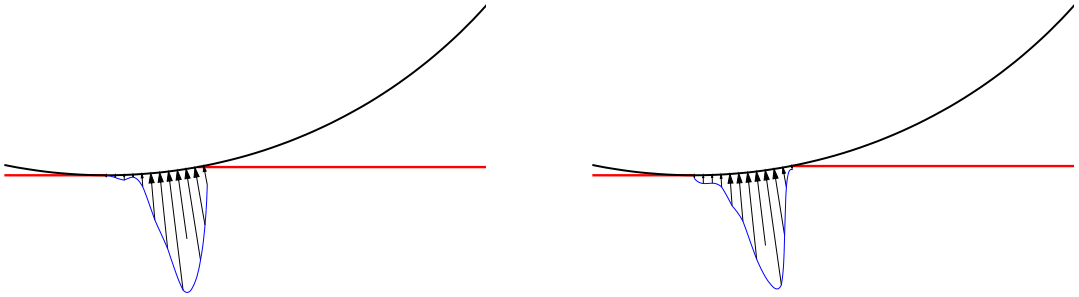

(a) Disc of 19" (b) Disc of 17"

Figure 6.21. Average distribution of normalized forces over disc cutters in LCM test with unrelieved material 1.

Taking the average of the normalized force distribution by the pick value in both cases, the estimated distribution obtained in the simulation is depicted in Figure 6.22. It is a gaussian distribution displaced to the right. This means that angle β is higher

than $\phi/2$.

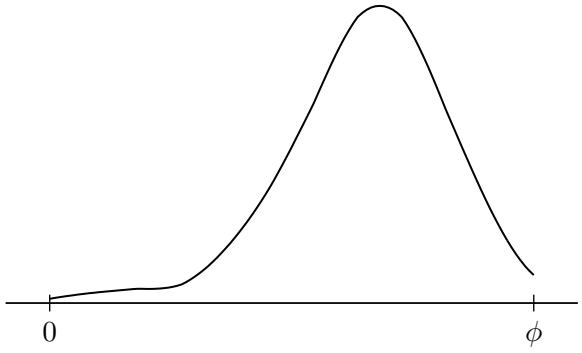

Figure 6.22. Estimated force distribution over disc cutter.

The β angle and cutting coefficient (CC) obtained in the simulation and predicted by the CSM model are summarized in Table 6.5. It can be noted that in both disc cutter geometries the angles β obtained in the simulations are higher than those estimated by the CSM model. This confirm the results obtained previously.

	CSM model		Simulation	
	19”	17”	19”	17”
β (deg)	5.158	5.453	5.859	6.163
CC	0.09027	0.09546	0.10262	0.10798

Table 6.5. Comparison of angle β in the LCM test with unrelieved material 1.

Most of the studies on the rock cutting with disc cutters found in the literature just consider the measurement of the interaction forces. However, the distribution of the forces over the disc seems not have been studied in detail. This point that can be crucial to understand the process resulting in an interesting example of the capabilities of the simulation technology proposed in that field.

In the next section, the comparison of the results obtained for both disc cutter geometries is presented, considering the different parameters related to the process. The simulations are performed considering the unrelieved rock specimen. Then relieved rock specimens are considered for the analysis of the disc spacing and the specific energy involved in the cutting process.

6.4.1.1 Sensitivity analysis of the cutting parameters

This section presents the analysis of influence for the different parameters involved in the rock cutting process. Most of the parameters are analyzed in an unrelieved rock specimen. However, for the spacing between disc cutters relieved rock specimens with different penetrations are considered.

Two different categories can be established for the different parameters involved in the rock cutting process, The first category is related to the mechanical properties of the rock specimen. Most of the studies reveal that the relevant mechanical properties of the rock are the compressive and tensile strengths. The elastic constants of the rock are not considered important for the estimation of the cutting forces, and are not analyzed in this section.

The second category involves the geometric settings of the cutting process. Here we can found the profile of the disc cutter, the spacing between discs and penetration.
All these relevant parameters, which are considered in the empirical/theoretical model, are analyzed in order to verify its influence on the interaction forces.

In order to obtain a most accurate measurement of the average values of the interaction forces, a range of the evolution of the forces is considered in order to avoid the boundary effect on the resulting forces. For the analysis presented below, a range between 0.1 and 0.3 m of the disc cutter displacement is considered.

Uniaxial compressive strength

One of the most significant mechanical parameters is the limit of compressive strength of the rock material, which is represented by the uniaxial compressive strength (UCS). This value represents the uniaxial compressive stress reached when the material fails completely.

Figure 6.23 shows the relationship between the average normal and rolling forces obtained in the simulation and the value of UCS estimated by changing the DEM parameter R_t. The relationship between UCS and R_t is obtained from the methodology for estimation of the DEM model parameters presented in Chapter 4.

The trend line shows the linear increasing of the forces in terms of the compressive strength. The different values of the UCS are estimated with the dimensionless scale function. As the macro strength ratio is constant due to the micro strength ratio is constant, the linear change it is expected as shown 6.3 for the CSM model. As the macro

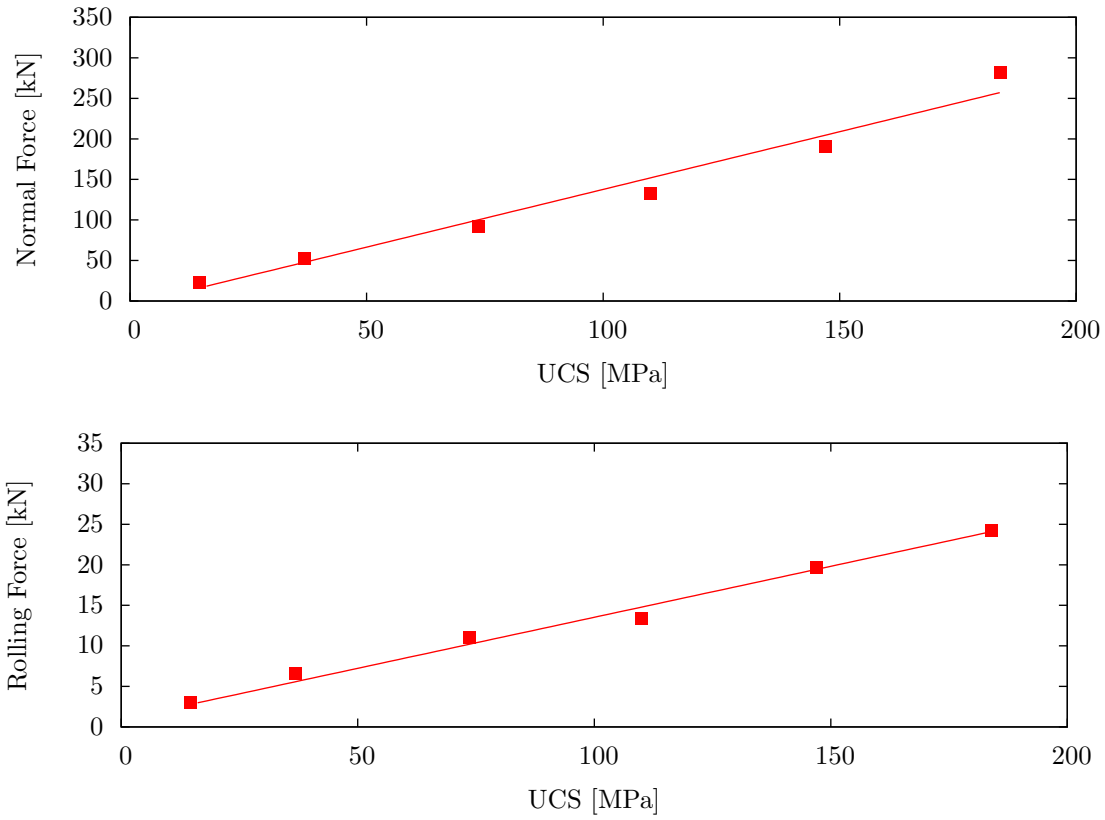

Figure 6.23. Normal and rolling forces with different values of UCS in LCM test, with unrelieved material 1 and ring of 19".

strength ratio is constant, the tensile strength in the equation can be replaced by the compressive strength times the strength ratio This allows us to take out the compressive strength of the root and obtain a linear equation of the pressure as a function of the compressive strength.

Even if the CSM model, and other theoretical models in the literature, relate the cutting coefficient with a poorly geometric considerations, as penetration and disc cutter radius, Figure 6.24 shows a linear relationship between the compressive strength and the cutting coefficient.

Even if the influence does not seem to be important, it would be interesting to verify this relationship with experimental results.

Cutting velocity

During the excavation process with a TBM, the disc cutters present different advancing velocities due to its position in the TBM cutterhead. As the normal force is distributed

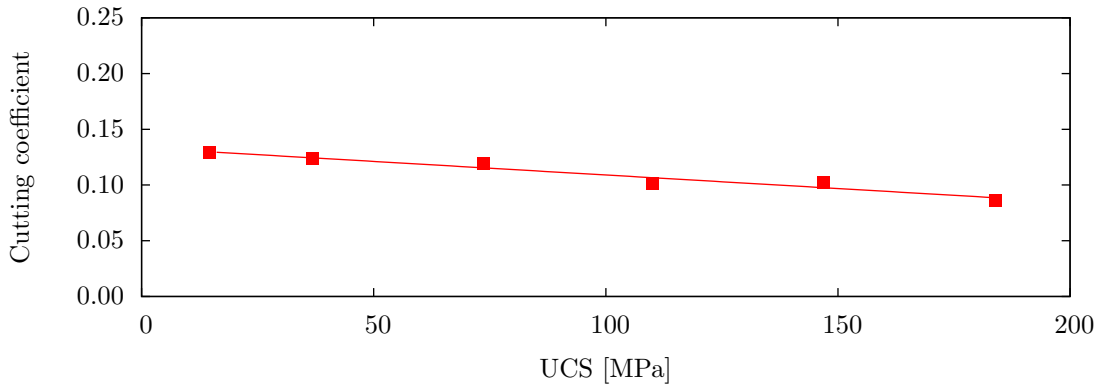

Figure 6.24. Cutting coefficient for different values of UCS in LCM test, with unrelieved material 1 and ring of 19".

through the cutterhead, it should be uniform in all the disc cutters.

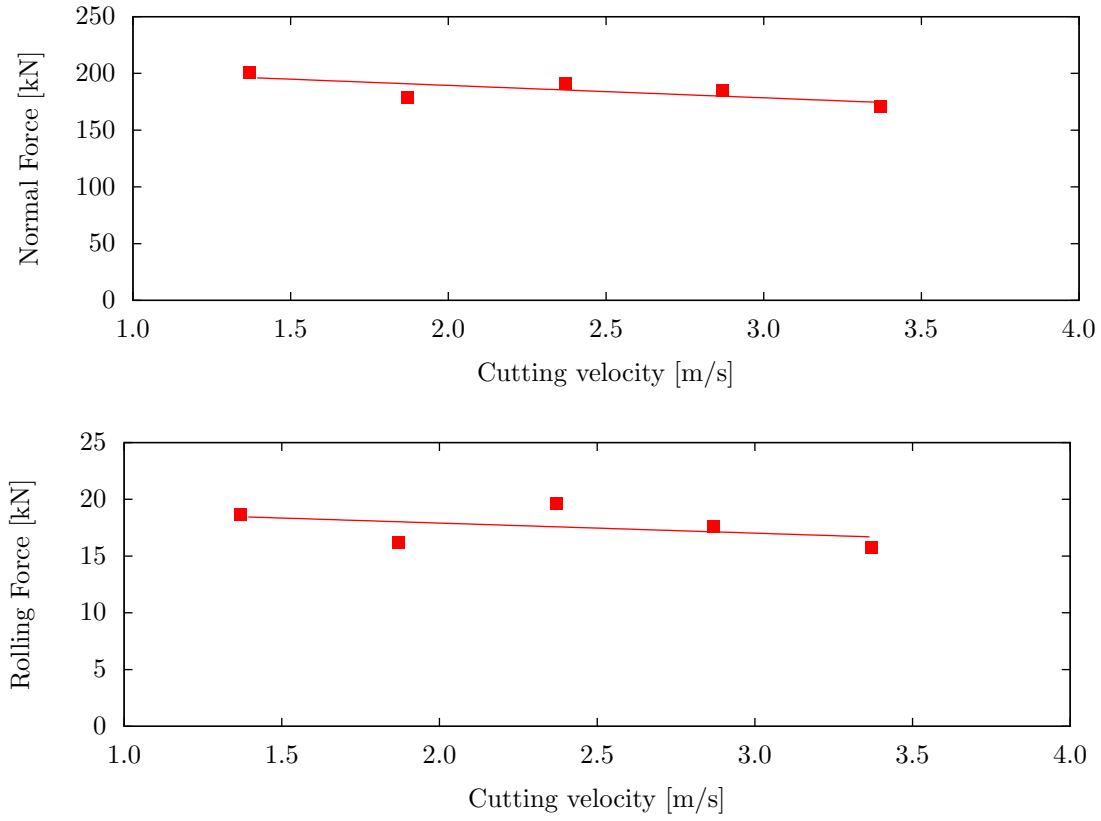

Figure 6.25. Normal and rolling forces for different values of cutting velocity in LCM test, with unrelieved material 1 and ring of 19".

Figure 6.25 shows the normal and rolling forces for different cutting velocities. The normal force decreases its value when the velocity increases, but the change rate is not significant. The same occurs with the rolling forces, but the rate is even lower than for the normal forces. Similar results were obtained by Cho et al. [29], via a FEM simulation of V-shape profile disc cutters.

Most of the theoretical/empirical models not include this parameters, assuming that this can be negligible. Even if the influence is small, this should be take into account for a more detailed analysis.

These values can be affected by different aspects related to the simulation process, as damping, time step or the moment of inertia selected for the rotation degrees of freedom in the disc cutter axis. The possible influence of those parameters should be studied in more detail. Nevertheless, this is considered out of the focus of the present work.

Penetration depth

The penetration depth, or penetration rate, is considered one of the most important geometric parameters, together with the disc spacing, that affect the performance of the TBM, as it indicates the advance rate of the TBM cutterhead.

All theoretical models assign an important role to this parameter, relating it with the volume of rock material excavated. This is linked with the energy required for the excavation process.

In Figure 6.26, the normal forces and rolling forces for different penetration depths are presented for the disc cutter of diameter 19" in both unrelieved rock specimens.

When the penetration depth increases, the normal force and the rolling force also increases. The influence of the penetration depth can be appreciated mainly in the rolling force, that is directly related with the energy required in the cutting process.

The CSM model bases the estimation of the cutting coefficient on these parameters, assuming a purely geometric criteria (see Equation (6.5)). Figure 6.27 shows the comparison of the resulting cutting coefficient in the simulations and the theoretical coefficient as estimated by the CSM model.

It can be noted that the resulting cutting coefficient for the rock material 2 presents a higher value than that obtained with the rock material 1 and the CSM model. This

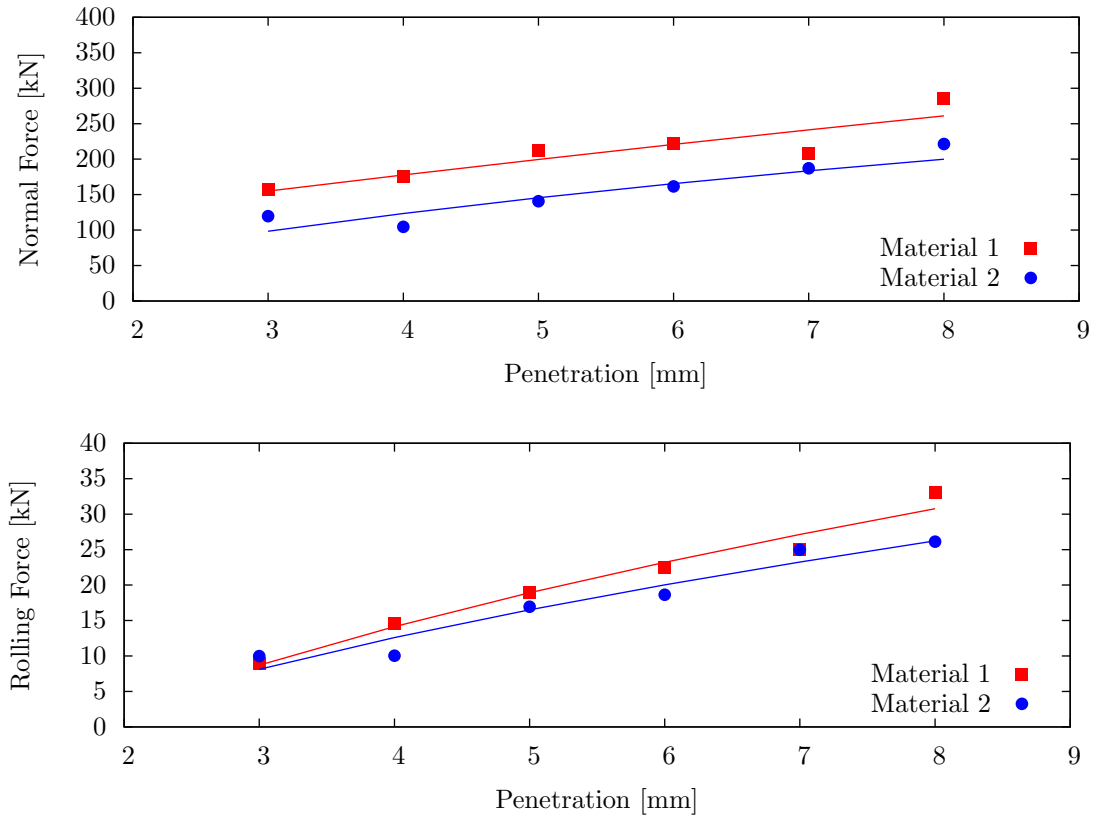

Figure 6.26. Normal and rolling forces for different penetration depths in LCM test, with ring of 19" and both unrelieved rock materials.

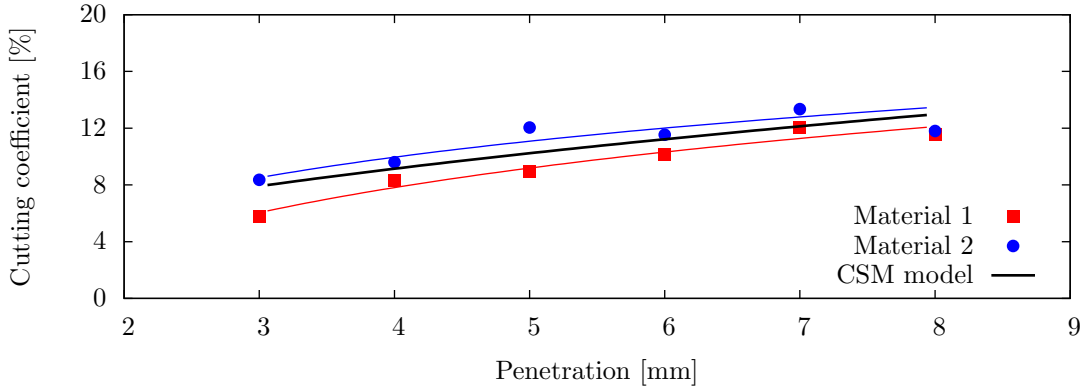

Figure 6.27. Comparison of simulated and theoretical cutting coefficient for different penetration depths in LCM test, with ring of 19" and both rock materials.

confirms the results of Figure 6.24, where it is shown that the cutting coefficient decreases while the compressive strength increase. As the only difference between both cases are the mechanical properties of the rock specimens, we can conclude that the cutting coefficient is also influenced by the mechanical properties, and not just for the penetration and radius of the disc cutter, as assumed in the CSM model.

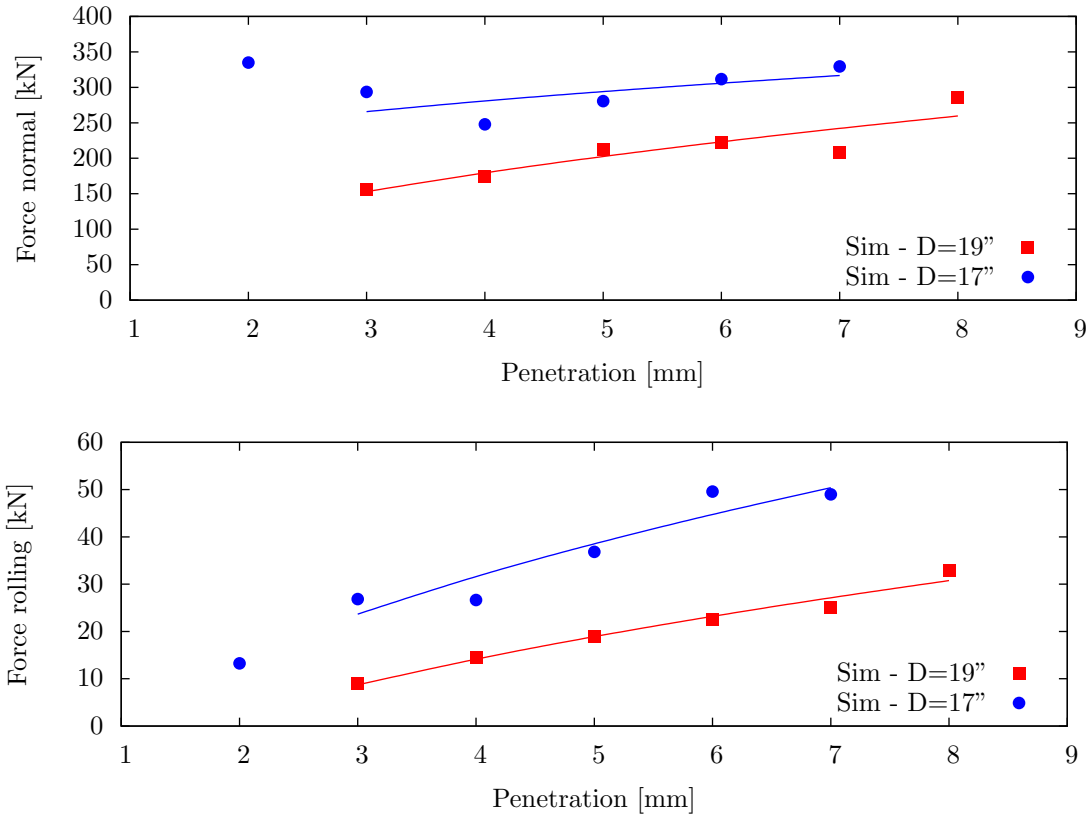

Figure 6.28. Comparison of normal and rolling forces for different penetration depths in LCM test, with rock material 1 and both disc cutters.

Together with the penetration, the disc cutter geometry is used in the theoretical model for the estimation of the contact forces and the cutting coefficient. In order to verify its influence the simulation is performed with both disc cutters for different penetration depths. The comparison of the normal and rolling forces for both disc cutters is presented in Figure 6.28.

The disc cutter of diameter 17” presents higher values for the interaction forces in both directions. This has been explained before, considering that the excavated volume is higher for this disc cutter geometry. Even taking into account that the disc cutter of

19” have a higher tip length, the profile shows that this value is projected and the tip of the disc presents a small angle, and have not a completely a constant cross section.

In the case of the normal forces, random results for lower penetration depth has been founded for the disc cutter of 17”. For penetration depths between 2-3 mm, the normal force seems to increase when the penetration decrease. This is not consistent with the rest of the values and the force for a penetration of 2 mm is not considered for the trend line. These phenomena can be related to the particle size distribution, as the penetration is lower than the average particle radius.

Figure 6.29 shows the comparison of the cutting coefficient resultant in the simulations with that estimated by the CSM model. The figure shows that the theoretical model underestimates the CC value for the disc cutter of 17”. Results are closer on the case of the disc cutter of 19”. The influence of different disc profile geometry parameters, as the contact surface area, should be investigated to verify the results and study in more detail its influence on the cutting coefficient.

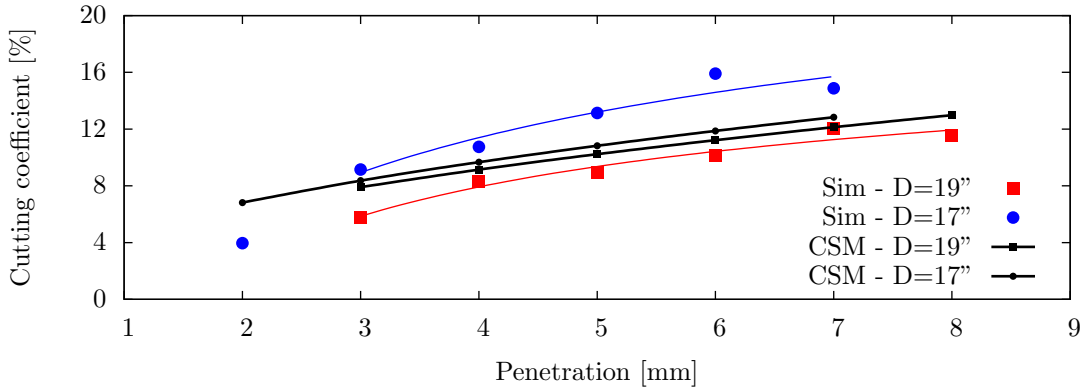

Figure 6.29. Comparison of simulated and theoretical cutting coefficient for different penetration depths in LCM test, with rock material 1 and both disc cutters.

6.4.2 Relieved rock specimen

All the results presented previously on this chapter has been obtained in unrelieved rock samples. In a real cutting process, as well as in LCM tests, the rock cutting analysis considers the influence of the previous passes of disc cutters, and the interaction of adjacent cutting paths.

The optimum spacing between disc cutters is one of the most important parameters in the design of TBMs for hard rock conditions. The spacing, and its relationship with the cutter penetration, have a direct effect in the chip formation and machine performance. The chips are formed by fracture propagation to an adjacent groove, as depicted in Figure 6.30.

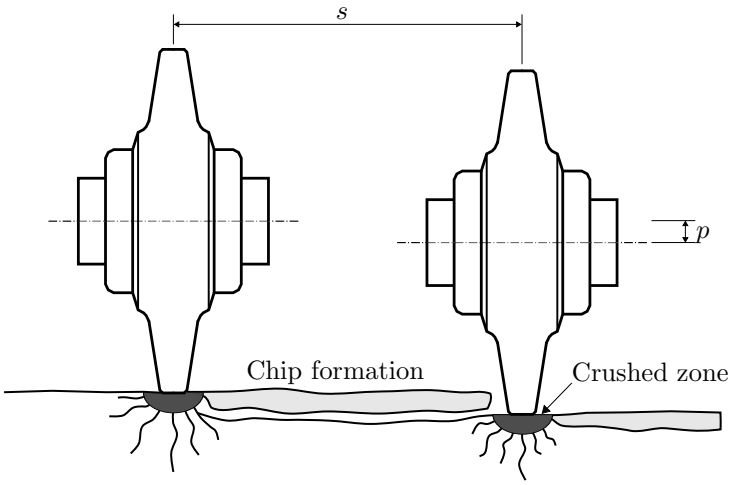

Figure 6.30. Influence of cutters spacing in fracture path.

The LCM test has been developed for the study and optimization of these parameters, considering the rock material properties and the disc cutter geometry. The optimum spacing between adjacent cutting for a given penetration of cutters is defined for the minimum energy required for the chip formation.

Figure 6.31 shows different cutting situations depending on the spacing selected. In the first case (Figure 6.31(a)), with a large spacing between cuttings, the generated crack length is not enough to meet with cracks already developed from the adjacent cut, and hence chips are not formed. This generates ridges between the adjacent grooves and the material can not be take out. In the second case (Figure 6.31(b)), the small spacing between cuttings generate an excessive loading on the rock, producing longer cracks and an over brake of the rock.

In the last case (Figure 6.31(c)), an optimum spacing between cuttings generates the formation of chips with an optimum size, where the cracks generated meet the crack

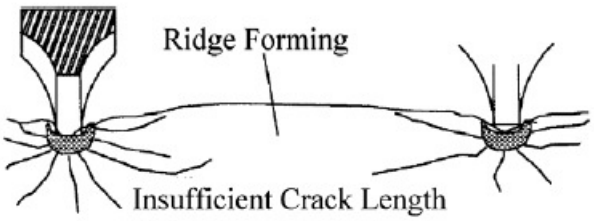

(a) Ridge formation do to lack of pressure and length of cracks

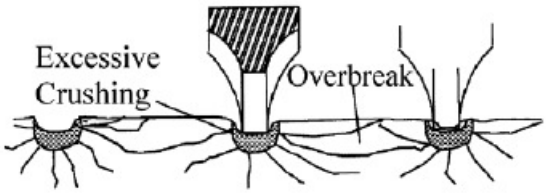

(b) Over break due to excessive loading and longer cracks

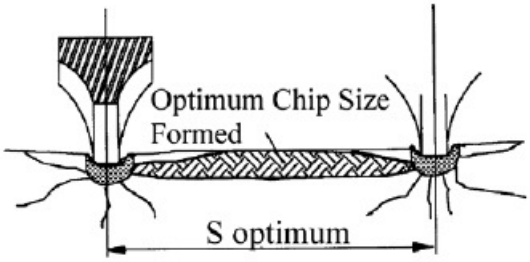

(c) Normal cutting with optimum crack length and direction

Figure 6.31. Chip formation for different cutting situations [1, 97].

previously formed in the adjacent cut. The generation of theses optimum-size chips increases the effectiveness of the cutting process, and consequently the efficiency of the full TBM.

The analysis of the influence of spacing and spacing/penetration parameters requires a modification of the original model for the rock specimen. In Figure 6.32, a new geometry for the rock sample is presented, where the influence of a previous cutting groove is considered.

For the new rock specimen geometry, the total size considered is the same that for the original one. Nevertheless, the with of the DEM domain is increased due to the maximum

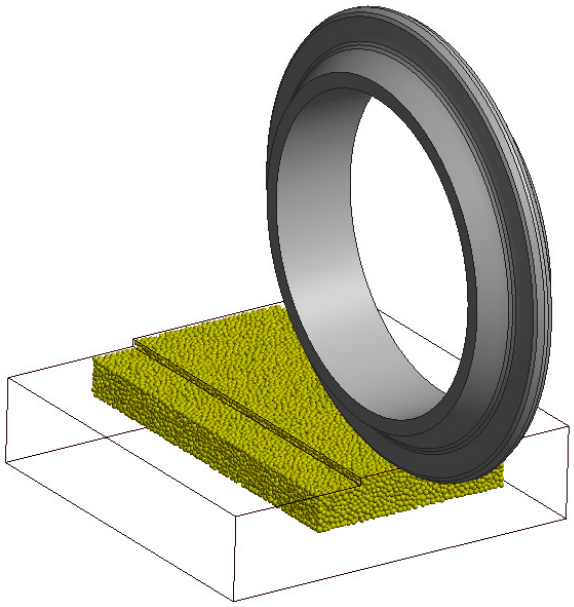

Figure 6.32. Numerical model of the LCM test, with spacing and penetration.

spacing that we want to reproduce. The maximum spacing considered is 130 mm, so the width of the new DEM domain is 0.23 m, as depicted in Figure 6.33.

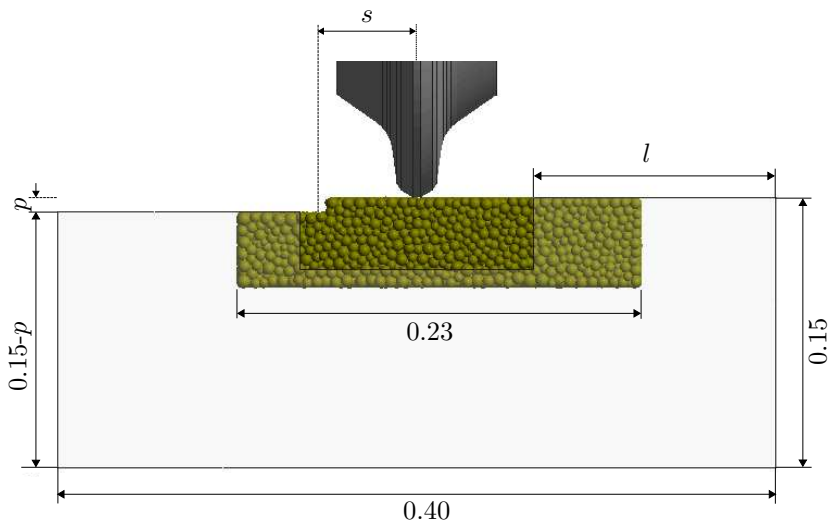

Figure 6.33. Geometric description of the DEM and FEM subdomains in relieved rock specimens for the LCM test (m).

The parameter l in Figure 6.33 varying depending on the spacing between the disc

cutter and the previous pass, in order to maintain the length from the disc cutter to the DEM/FEM coupling interface.

Two different specimens are generated, for 4 mm and 8 mm of the penetration. The subdomain discretized with DEM have 51668 and 50714 particles, respectively. The particles assembly characterization parameters are summarized in Table 6.6.

		Penetration	
Parameter	Description	4 mm	8 mm
N_p	Number of particles	51668	50714
$\bar{r}$	Average radius (mm)	2.5621	2.5593
$\widetilde{r}$	Characteristic radius (mm)	3.0039	2.9992
n_c	Coordination number	9.0635	9.1028
e	Porosity (%)	22.6470	22.8205

Table 6.6. Characterization of the particles assembly for LCM test with relieved rock specimens.

Using the methodology developed in Chapter 4, the DEM model parameters are estimated for the rock specimen 1. The model parameters for the new rock specimens are summarized in Table 6.7.

Since the CSM model consider the spacing between disc cutters, now is possible to compare the estimated forces by the CSM model and those obtained in the simulations. Figure 6.34 shows the normal forces and the rolling forces.

Parameter	Description	Penetration 4 mm	Penetration 8 mm
K_n	Stiffness in normal direction (MN/m)	160.79	160.79
K_t	Stiffness in tangential direction (MN/m)	16.325	16.325
K_t/K_n	Stiffness ratio	0.1015	0.1015
R_n	Strength of cohesive bonds in the normal direction (kN)	0.8482	0.5908
R_t	Strength of cohesive bonds in the tangential direction (kN)	4.1759	2.9087
ρ	Density (kg/m^3)	3085	3085

Table 6.7. DEM model parameters for LCM test with relieved rock specimens.

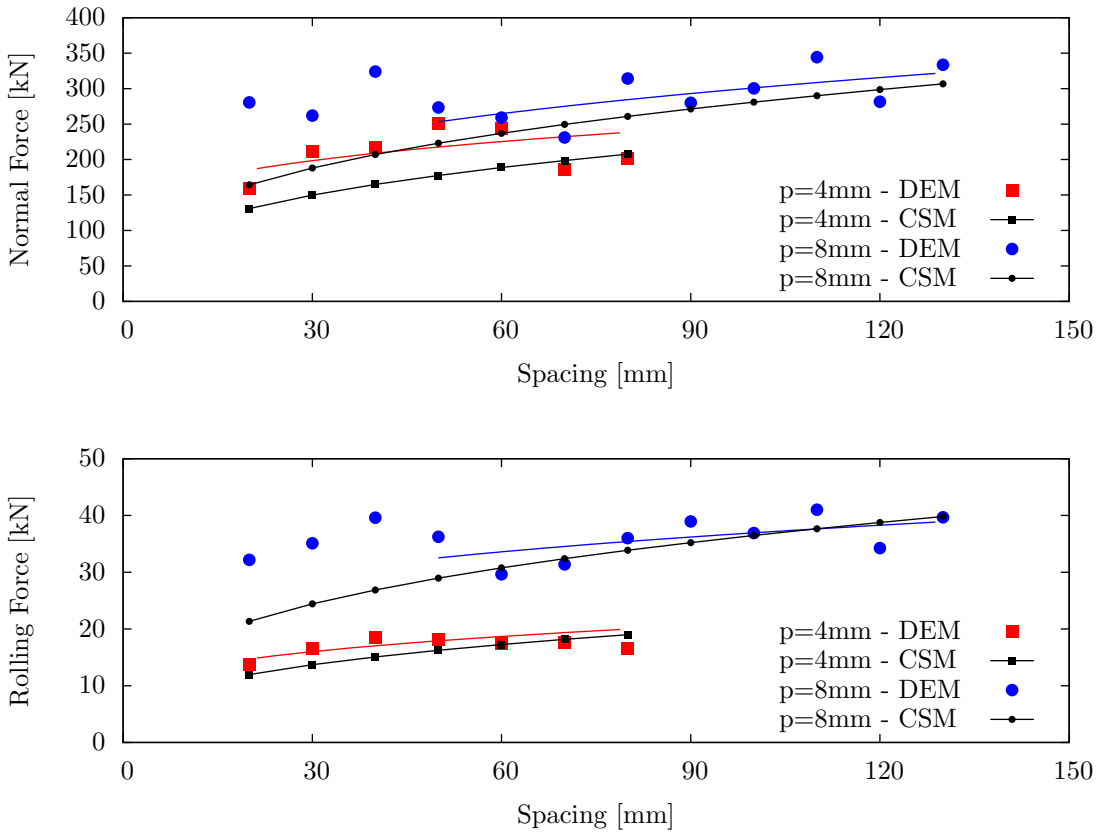

Figure 6.34. Normal and rolling force for different spacings in LCM test with relieved material 1 and ring 19" and both penetration depths.

In the case of the normal force, the curve shows that the forces obtained in the simulation are higher that those estimated with the CSM model for both cases.

For the rolling forces, again the estimated forces are lower than those obtained in the simulations. In this case, the difference is lower than for the normal forces.

The difference between the obtained forces and those estimated within the CSM model shows the same behaviour that for the unrelieved rock specimens. The hypothesis for the estimation of the cutting coefficient CC seems to be related with these differences.

In Figure 6.35 the cutting coefficients for different spacings between disc cutters, for 4 mm and 8 mm of penetration, are presented. In both cases the curve shows a completely independence of the spacing, as proposed by the CSM model. Nevertheless, the cutting coefficients estimated with the CSM model are higher than those computed in the simulations. These higher values of CC are reflected as lower values of the normal forces in comparison with those obtained in the simulations.

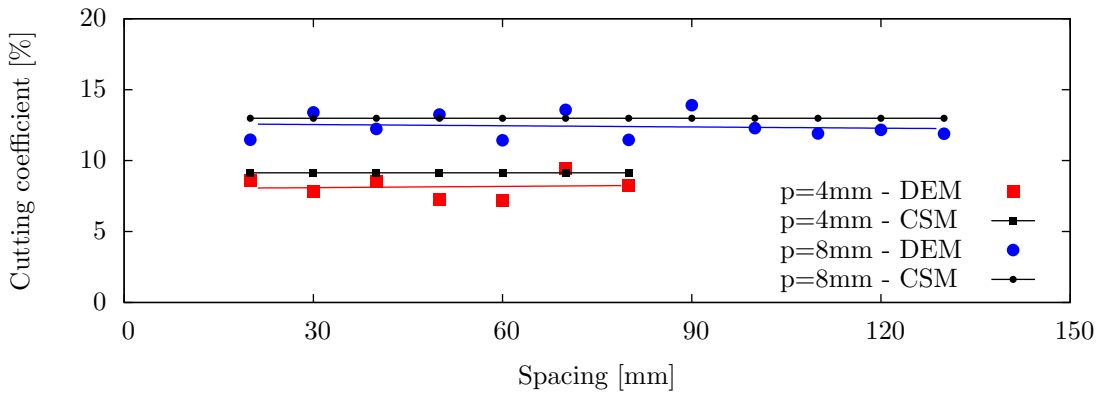

Figure 6.35. Cutting coefficient for different spacing and penetration values in LCM test with material 1 and ring of 19".

Comparing both cases, it can be seen that for a lower penetration depth results present a higher difference with the values estimated with the CSM model. The same occurs with the β angle. The estimated and calculated values of the cutting coefficient and angle β are summarized in Table 6.8.

The difference between the CSM model and the simulations can be explained by the definition of the pressure distribution in the disc cutters. Similar with was found in the analysis of the unrelieved rock specimens, the distribution of pressure over the disc cutter differs from that assumed in the CSM model, for which a uniform distribution of pressure over the disc cutter is proposed. The average distribution of the forces over the disc cutters for both penetration cases are presented in Figure 6.36, for a spacing p of 80 mm.

As for the unrelieved rock specimens, the pressure over the disc cutter presents a

	CSM model		Simulation	
	4 mm	8 mm	4 mm	8 mm
β (deg)	5.224	7.397	5.240	6.826
CC	0.0914	0.1298	0.0917	0.1197

Table 6.8. Comparison of angle β and cutting coefficient in LCM test with relieved material 1 and spacing of 80 mm.

distribution similar to a Guassian distribution.

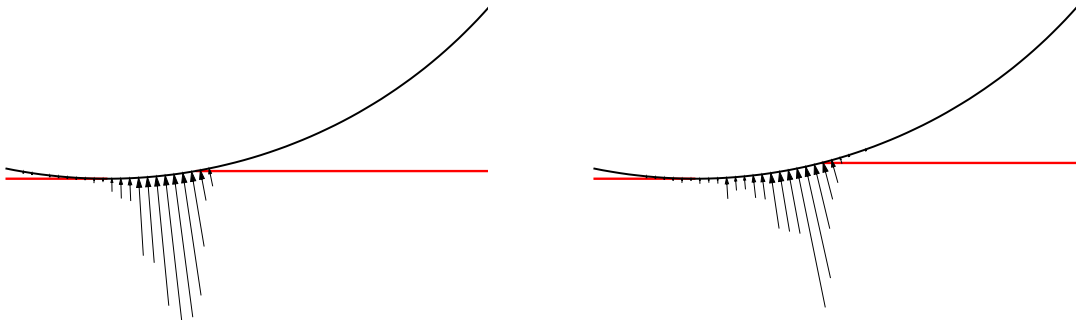

(a) $p = 4$ mm (b) $p = 8$ mm

Figure 6.36. Average distribution of normalized forces over disc cutters in LCM test with relieved material 1 and spacing of 80 mm.

For the definition of the optimum spacing/penetration ratio, an energy-based criteria is commonly used in the literature [95, 96, 103]. This ratio is used as one of the main design parameters in the TBMs, as it is required to define the configuration of the TBM shield.

The specific energy SE is defined as the amount of energy required to excavate a unit volume of rock, computed in units of kilowatt-hour per cubic meter (kWh/m^3). The SE for a single disc cutter is defined as the work done to excavate a volume V by

$$SE = \frac{F_R\, L}{V} \tag{6.9}$$

where L is the cutting distance (m) and V the cutting volume (m^3).

Taken into account that for the optimum conditions (see Figure 6.31), the excavated volume can be defined by the spacing s between the disc cutters and its penetration p,

the volume can be written as

$$V = A\,L = s\,p\,L \tag{6.10}$$

replacing the volume into (6.9), the specific energy is re-written as

$$SE = \frac{F_R}{p\,s} \tag{6.11}$$

Considering the definition of the specific energy and the simulation of the rock cutting in the relieved rock specimens for different values of penetration and spacing, the specific energy for the different cases is compared in Figure 6.37. The comparison of the specific energy computed for the relieved rock specimen and the estimated by the CSM model, for different values of penetration and spacing, are shown in Figure 6.37.

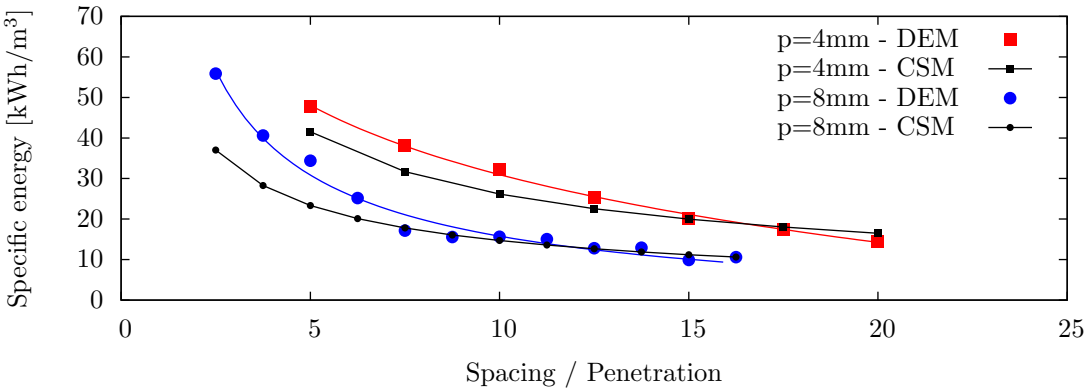

Figure 6.37. Specific energy for different spacing and penetration depths in LCM test with material 1 and ring of 19".

In Figure 6.37, the computed results are compared with the CSM model results. A good correlation of both results is obtained. This means that the simulation using the DEM allows reproducing the values obtained with the most popular theoretical/empirical model, and therefore, can be used for the analysis of the disc cutter on real conditions. Furthermore, this modelling technique allows analysing in a more simple way the influence of the disc cutter shape and, eventually, the change of the TBM performance due to wear in the disc cutters.

As a final comment, it is interesting to consider the differences obtained with the CSM model for the distribution for pressure over the disc cutters. The CSM model proposes a uniform distribution with the angle β calculated as the simple average of the contact area. However, the simulation shows a more complex situation with a Gaussian distribution.

Hence, the angle β seems to be related not just to the geometrical parameters proposed by the CSM model. But rather to the mechanical properties of the rock specimens.

Chapter 7

Summary and conclusions

This work has presented the development of different aspects related with the modelling of the rock cutting processes using the discrete element method. A summary of the results of this work are presented along with the main contributions of this work.

In Chapter 2, the implemented model using cylindrical (2D) and spherical (3D) particles has been summarized. The implementation assumes a linear perfectly-brittle model, in which the stiffnesses and strengths are global parameters in the whole particle assembly. A Velocity-Verlet algorithm has been used for the time integration scheme.

In Chapter 3, a new particle generation scheme has been introduced, in which the main goal is to achieve high density assemblies. This new particle packing algorithm presents a good level of isotropy and high coordination numbers. One of the interesting characteristics of the method is that it can be used to generate particles in 2D or 3D problems, taking as starting point a standard triangular or tetrahedral finite element mesh. This allows the generation of particle assemblies with complex geometries.

One of the most important results of this work, presented in Chapter 4, is the development of a methodology thats allow the estimation of the DEM contact parameters via a combination of dimensional analysis and micromechanics. Most of the dimensional analysis found in the literature do not correctly consider the characteristics of the particle assembly, such as the porosity or the particle size distribution. In the proposed methodology the dimensional analysis is corrected via the consideration of micromechanical equations. Characteristic parameters of the particle assembly, such as the coordination number or a characteristic radius are considered in the dimensionless number, that take into account the distribution of the particle size and the contact branch lengths.

The sensitivity analysis of the different parameters of the DEM model implemented allows the establishment of the influence of each of them in the modelling of rock materials. It can be concluded that for the strength ratio of the rock materials considered in this work, most of the bonds are broken by the tensile forces, no matter what failure model is selected. This fact has a direct relationship to the failure envelope involved in the constitutive model used, and should be studied with more detail in future work, to analyse possible changes in the breakage model considered.

A coupling scheme that allows the use of DEM and the FEM in the same domain has been presented in Chapter 5. The DEM/FEM coupling scheme introduced decreases the computational time with a negligible influence in the accuracy of the results, and permits the consideration of higher domains. By increasing the domain, the possible boundary effects in the simulation are avoided. This is very important for the analysis of real size excavation problems.

Also, a new adaptive algorithm that permits a change from FEM elements into DEM elements as been introduced. With a criteria based on the stress, the algorithm allows a progressive change from the FEM to the DEM discretization. This means that the DEM domains are only used where a concentration of stress is obtained and failure could occur. The FEM methodology used considers simple linear elastic behaviour, decreasing even further the computational time required for the simulations.

The only problem found in this adaptive coupling is the necessity to introduce equilibrium in the new particles after the projection of the kinematic variables, as the rotation of the particles can not be projected. A simple study shows that with few iterations the equilibrium in the new DEM domain can be achieved.

The study of different projection schemes for the kinematic variables, from the FEM to the DEM elements, could be performed in the future, considering different stress localization techniques.

All the developments presented in the previous chapters has been applied to the study of the rock cutting process with disc cutters, presented in Chapter 7. The linear cutting machine test is modeled considering different materials and disc cutter geometries, in order to analyze the possibilities of the simulation technology developed for this important industrial application. In this type of excavation process, the continuum-based simulation technology has been historically experienced problems due to the fragmentation of the rock, that can not be modeled in a simple way. The discrete-based methods allows the fragmentation process to be simulated in a more natural way, but the complexity of the parameter estimation and the computational cost involved has made its application

impossible for real-scale problems.

The results obtained with the DEM and DEM/FEM simulation models have been compared with a theoretical/empirical model developed by the Colorado School of Mines in the last decade, which has been used extensively by industry for the design of tunnel boring machines.

The simulations have been performed considering relieved and unrelieved rock specimens, in order to analyze the influence of the different geometrical and mechanical parameters involved in the cutting process. The results have shown a good correlation between the forces obtained in the simulations and those estimated by the CSM model.

The specific energy estimated with the CSM model and obtained in the simulations presents a good correlation. This means that the simulations using the DEM allows the values obtained with the most popular theoretical/empirical model to be reproduced, and can therefore be used for the analysis of disc cutters in real excavation conditions. Furthermore, this modelling technique allows the influence of the disc cutter shape and, eventually, the change of the TBM performance due to the wear in the disc cutters to be analyzed in a more simplistic manner.
An important difference has been found in the distribution of pressure over the disc cutters. While the CSM model proposes a uniform distribution of pressure, the simulation shows a more complex situation with a Gaussian distribution. The cutting coefficient, defined as a function of the angle β, is proposed by the CSM model as a function of the contact area of the disc cutter. In the simulation, an influence of the mechanical properties of the rock in the angle β has been found. Future simulations of the LCM test with disc cutters should provide a more detailed analysis of the pressure distribution, as well as the comparison with experimental results.

Summary of contribution of this work

The main contributions of the work are summarized bellow:

- A new particle packing algorithm for the particle assembly has been developed. The algorithm allows the generation of high density isotropic assemblies.

- A methodology for the estimation of the DEM model parameters, based on the dimensional analysis and taking into account the characterization parameters of the particle assembly has been proposed.

- We have defined a characteristic radius that represents in a better way the particle size distribution, and also considering the distribution of contacts through the branch length.

- A novel DEM/FEM adaptive coupling algorithm has been developed. It allows the use of larger domains and decrease the computational cost involved in the simulations.

- We have studied the rock cutting tests with disc cutter. Numerical results have been compared with the most popular prediction model for the estimation of the cutting forces and performance of the excavation machinery. Possible inconsistencies in the prediction model were noted.

Recommendations for future work

Based in the results obtained in the present work, some topics for future work that can allow the improvement of the DEM model used and a its application to the rock cutting processes are suggested:

- A possible improvement of the constitutive model used, considering different failure envelopes to reproduce, with more accuracy, the rock material behaviour. In particular, for the reproduction of the real strength ratio of the rock material.

- The particle packing algorithm can be extended to non-spherical particles. Elliptical particles can be implemented using the distance optimization algorithm. As the contact detection is more complex and expensive for non-spherical particle, some simplifications such as the consideration of a predefined aspect ratio or a fixed rotational angle (changing position and size) can be taken into account.

- The projection of the stress state and the kinematic variables from the FEM to the DEM elements, in the adaptive DEM/FEM coupling technique, can be improved considering different localization techniques.

- For the modelling of the rock cutting test with disc cutters, a more detailed analysis of the pressure distribution over the disc can be performed. This is the most relevant aspect due to the discrepancies obtained with the theoretical/empirical model.

Appendix A

Micromechanical stress tensor

The definition of the average stress tensor is widely discussed in literature [33, 68]. Normally its defined in terms of the force acting in the contact between particles and the geometry of the assembly. Bellow, the formulation derivated by Kruyt and Rothemburg in [33, 68] is presented.

The expression of the average stress tensor can be considered in two steps. First is related with the forces exerted on the particles by the boundary that encloses the assembly. The second step equates these quantities involving external forces to quantities involving internal forces. Finally, the micromechanical expression for the average stress tensor is obtained.

A.1 Stress tensor in terms of external forces

Considering the condition of quasi-static equilibrium and the absence of body forces, the equilibrium conditions (continuum) are

$$\frac{\partial \sigma_{ij}}{\partial x_j} = 0 \tag{A.1}$$

The average stress tensor in the volume V and surface S is defined by the Hill's lemma [61], based in the *representative volume element* (RVE), as

$$\bar{\sigma}_{ij} = \frac{1}{V} \int_V \sigma_{ij} dV \tag{A.2}$$

and rewritten

$$\bar{\sigma}_{ij} = \frac{1}{V} \int_V \frac{\partial (x_i \sigma_{kj})}{\partial x_k} dV - \frac{1}{V} \int_V x_i \frac{\partial \sigma_{kj}}{\partial x_k} dV \tag{A.3}$$

Considering the equilibrium condition, the second term it is zero. By the Gauss's theorem, the first term in (A.3) results in

$$\bar{\sigma}_{ij} = \frac{1}{V} \int_S n_k \sigma_{ik} x_j dV \tag{A.4}$$

where n_i is the normal to the surface S. Considering the loads to be point loads on the surface S we have

$$\bar{\sigma}_{ij} = \frac{1}{V} \sum_{c \in S} f_i^c \, x_j^c \tag{A.5}$$

where f_i is the surface force exerted on the surface of the particle c, and x_j^c its position. This gives us the expression for the average stress tensor in terms of external forces.

A.2 Stress tensor in terms of internal forces

The position of the contact point x_j^c can be written in terms of the particle p by

$$x_j^c = x_j^p + r_j^{pc} \tag{A.6}$$

where r_j^{pc} is the so-called *contact vector*, connecting the center of mass of particle p with the contact point c. Now, (A.5) can be rewritten for the particle q as

$$\bar{\sigma}_{ij}^p = \frac{1}{V_p} \sum_{c \in S_p} f_i^c (x_j^p + r_j^{pc}) = \frac{1}{V_p} \left(x_j^p \sum_{c \in S_p} f_i^c + \sum_{c \in S_p} f_i^c r_j^{pc} \right) \tag{A.7}$$

Considering the equilibrium condition (internal forces) for particle p in the absence of body forces is defined as

$$\sum_q f_i^{pq} = 0 \tag{A.8}$$

where the summation is over the particles q, in contact with p, and f_i^{pq} is the force exerted by particle q on the particle p.

The first term of the sum in (A.7) can be avoided, considering the equilibrium condition, and the average stress tensor for the particle p is obtained as

$$\bar{\sigma}_{ij}^p = \frac{1}{V_p} \sum_{c \in S_p} f_i^c r_j^{pc} \tag{A.9}$$

A.3 Average stress tensor

Considering the average function

$$Q = \langle Q \rangle = \frac{1}{V} \sum_{p \in V} V^p Q^p \tag{A.10}$$

where Q is the quantity to be averaged, V the volume of the cell used for the average procedure and V^p is the volume fraction of the particle who intersect with V, i.e. the subscript $p \in V$ denotes the particle-in-volume averaging procedure. The volume fraction is obtained from either $Q^p = 1$.

Considering the average function defined in (A.10), the average stress tensor over a control volume V is defined as

$$\bar{\sigma}_{ij} = \frac{1}{V} \sum_{p} V_p \bar{\sigma}_{ij}^p \tag{A.11}$$

Replacing the definition of the stress tensor for a particle q, defined in (A.9)

$$\bar{\sigma}_{ij} = \frac{1}{V} \sum_{p} V_p \left(\frac{1}{V_p} \sum_{c} f_i^c r_j^{pc} \right) = \frac{1}{V} \sum_{p} \sum_{c} f_i^c r_j^{pc} \tag{A.12}$$

As the contact force f_i^c it is the same for both particles p and q, then

$$f_i^{pc} = -f_i^{qc} \tag{A.13}$$

The averaged stress tensor can be written as

$$\bar{\sigma}_{ij} = \frac{1}{V} \sum_{c} f_i^c l_j^c \tag{A.14}$$

where l_j^c is the called *branch vector*, which joints the center of the particles in contact $(x_q - x_p)$.

Appendix B

Micromechanical strain tensor

This section summarizes the definition of the micro-mechanical strain tensor by Bagi [7], and compared with other formation in [9, 41]. The formulation describes accurated the micro-mechanical deformation of granular systems, allowing to reproduce the macroscopic strain through the averaging procedure.

B.1 Geometrical micro-variables

The granular system is divided in space cells defined by a Delaunay tesellation, consisting in triangles in the two-dimensional case and tetrahedra in the three-dimensional case. The cell is a simplex so it as D+1 nodes, with D as the dimension. The Delaunay tesellation connect the center of the particle centers, and their edges correspond to the shortest path beween them. In Figure B.1, it is shown that the edges can be physical contact between the particles, called *real* contacts, as the edge $\overline{po}$ or *virtual* contacts, as the edge $\overline{pq}$. All of them are geometrically characterized by the *branch vector*, defined previously.

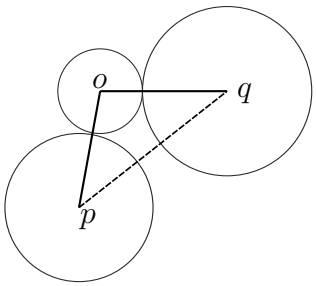

Figure B.1. Delaunay tesellation of three particles in 2D.

Considering the face k of the cell, opposite to the node k, the *area-vector* $\mathbf{b}^k$ it is defined in the following way:

- The magnitude of $\mathbf{b}^k$ is equal to the area of the face (length in 2D).
- The direction of $\mathbf{b}^k$ is normal to the face, pointing outwards.

It is easy to probe that

$$\sum_{k=1}^{D+1} \mathbf{b}^k = 0 \tag{B.1}$$

The vector it is illustrated in Figure B.2.

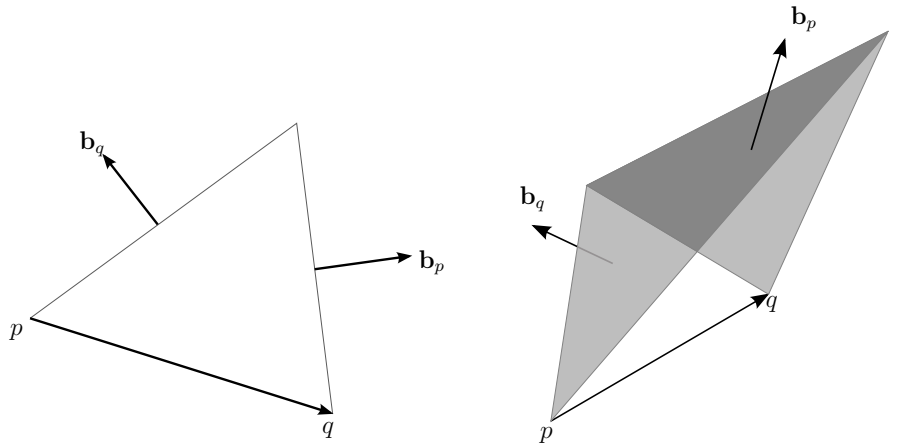

(a) Space cell in 2D: Triangle (b) Space cell in 3D: Tetrahedron

Figure B.2. Sketch of the quantities related with the space cell containing the edge $\overline{pq}$, with the area vectors $\mathbf{b}_q$ and $\mathbf{b}_q$.

Based in the previous definition, the vector $\mathbf{a}^k$ it is defined as

$$\mathbf{a}^k = -\frac{1}{D}\mathbf{b}^k \tag{B.2}$$

Finally, the most important geometrical micro-variable of the space cell system, called *complementary area vector*, can be defined. Vector $\mathbf{d}^{pq}$ is defined considering the summation in all the cells t that contain the edge pq, of the difference $\mathbf{a}_t^p$ and $\mathbf{a}_t^q$ as follows

$$\mathbf{d}^{pq} = \frac{1}{D+1}\sum_{t=1}^{T}(\mathbf{a}_t^p - \mathbf{a}_t^q) \tag{B.3}$$

This vector characterizes the neighborhood of the edge pq. It is interesting note that for all the Delaunay tesellation, the complementary area vector $\mathbf{d}^e$ and the generalized branch vector $\mathbf{l}^e$ satisfy the geometrical relationship

$$V\delta_{ij} = \sum_e l_i^e d_j^e \tag{B.4}$$

where δ_{ij} is the Kronecker delta function.

B.2 Strain tensor

Considering the strain tensor ε_{ij} as the displacement gradient

$$\varepsilon_{ij} = \frac{\partial u_i}{\partial x_j} \tag{B.5}$$

According with the Gauss theorem, the average of ε_{ij} in the Volume V is expressed as the surface integral

$$\bar{\varepsilon}_{ij} = \frac{1}{V} \iiint_V \varepsilon_{ij} \mathrm{d}V = \frac{1}{V} \iint_S u_i n_j \mathrm{d}S \tag{B.6}$$

If the domain is divided into sub-domains, the average displacement gradient tensor can be calculated separately for each sub-domain L as

$$\bar{\varepsilon}_{ij}^L = \frac{1}{V^L} \iint_{S^L} u_i n_j \mathrm{d}S \tag{B.7}$$

If the domain and the displacement gradient are continuous, the volume-weighted average it is

$$\bar{\varepsilon}_{ij} = \frac{1}{V} \sum_L V^L \bar{\varepsilon}_{ij}^L = \frac{1}{V} \iint_S u_i n_j \mathrm{d}S \tag{B.8}$$

Considering that the domain can be represented with the *space cell system* defined by the Delaunay tesellation, the sub-domain are considered as the triangles or tetrahedra. Considering that the displacement field $\mathbf{u}$ is linear along the boundary of the cells, the displacement gradient can be written in the form

$$\bar{\varepsilon}_{ij}^L = \frac{1}{V^L} \sum_k^{D+1} u_i^k a_j^k \tag{B.9}$$

where V^L is the volume of the cell, k run over its nodes, $\mathbf{u}^k$ is the translation of the node k, and $\mathbf{a}$ is the vector defined in the previous section. Since the sum of $\mathbf{a}^k$ in the cell is zero, the equation B.9 can be modified by subtracting the same $\mathbf{u}^0$ vector from each nodal displacement of the cell

$$\bar{\varepsilon}_{ij}^L = \frac{1}{V^L} \sum_k^{D+1} (u_i^k - u_i^0) a_j^k \tag{B.10}$$

This physically means that the rigid body translation does not change the deformation of the cell. If $\mathbf{u}^0$ is chosen as the average translation of the nodes

$$\mathbf{u}^0 = \frac{1}{D+1}\sum_{k}^{D+1}\mathbf{u}^k \tag{B.11}$$

Equation (B.10) can be re-written as

$$\bar{\varepsilon}_{ij}^{L} = \frac{1}{D+1}\frac{1}{V^L}\sum_{p<q}(u_i^p - u_i^q)(a_j^p - a_j^q) \tag{B.12}$$

Considering the notation $\nabla\mathbf{u}^{pq} = \mathbf{u}^p - \mathbf{u}^q$, and the definition of the complementary area vector defined in (B.3), the volume-weighted average displacement gradient tensor can be written as

$$\bar{\varepsilon}_{ij} = \frac{1}{V}\sum_{pq}\Delta u_i^{pq} d_j^{pq} \tag{B.13}$$

where pq are the edges that run over all the space cell system.

Note that the expression contains only discrete micro-variables, as the relative displacement of the neighboring nodes and the corresponding complementary area vectors. The skew-symmetric part of the tensor represents the average rigid-body rotation of the space cells, and the symmetric part (similarly to the continuum mechanical variable) expresses the deformations of the cells, been the strain tensor.

References

[1] O. Acaroglu, L. Ozdemir, and B. Asbury. A fuzzy logic model to predict specific energy requirement for tbm performance prediction. *Tunnelling and Underground Space Technology*, 23(5):600–608, 2008.

[2] I. Agnolin and N. Kruyt. On the elastic moduli of two-dimensional assemblies of disks: Relevance and modeling of fluctuations in particle displacements and rotations. *Int. J. Computers and Mathematics with Applications*, 55(2):245–256, 2008.

[3] I. Agnolin and J.-N. Roux. On the elastic moduli of three-dimensional assemblies of spheres: Characterization and modeling of fluctuations in the particle displacement and rotation. *Int. J. of Solids and Structures*, 45:1101–1123, 2008.

[4] B. J. Alder and T. E. Wainwright. Studies in molecular dynamics. I. General method. *The Journal of Chemical Physics*, 31(2):459–466, 1959.

[5] J. Argyris. An excursion into large rotations. *Comput. Meth. Appl. Mech. Eng.*, 32:85–155, 1982.

[6] K. Bagi. A quasi-static numerical model for micro-level analysis of granular assemblies. *Mechanics of Materials*, 16(1-2):101–110, 1993.

[7] K. Bagi. Stress and strain in granular assemblies. *Mechanics of Materials*, 22(3):165–177, 1996.

[8] K. Bagi. An algorithm to generate random dense arrangements for discrete element simulations of granular assemblies. *Granular Matter*, 7:31–43, 2005.

[9] K. Bagi. Analysis of microstructural strain tensors for granular assemblies. *Int. J. Solids and Structures*, 43:3166–3184, 2006.

[10] C. Balci and N. Bilgin. Correlative study of linear small and full-scale rock cutting tests to select mechanized excavation machines. *International Journal of Rock Mechanics and Mining Sciences*, 44:468–476, 2007.

[11] M. Bargiel. Geometrical properties of simulated packings of spherocylinders. In *Computational Science – ICCS 2008*, volume 5102 of *Lecture Notes in Computer Science*, pages 126–135. Springer Berlin / Heidelberg, 2008.

[12] K. Bathe and E. Wilson. *Numerical Methods in Finite Element Analysis*. Prentice Hall, 1976.

[13] R. Bathurst and L. Rothenburg. Micromechanical aspects of isotropic granular assemblies with linear contact interactions. *Journal of Applied Mechanics, ASME*, 55(1):17–23, 1988.

[14] T. Belytschko, P. Smolinski, and W. Liu. Stability of multi-time step partitioned integrators for the first order finite element systems. *Comput. Meth. Appl. Mech. Eng.*, 49:281–297, 1985.

[15] D. Benson and J. Hallquist. A simple rigid body algorithm for structural dynamics programs. *Int. J. Num. Meth. Eng.*, 12:723–749, 1986.

[16] H. Brandt. A study of the speed of sound in porous granular media. *Journal of Applied Mechanics, ASME*, 22:479–486, 1955.

[17] B. Cambou. Micromechanical approach in granular materials. In *Behaviour of Granular Materials*, volume 385, pages 170–216. Springer Wien, 1998.

[18] B. Cambou, M. Chaze, and F. Dedecker. Change of scale in granular materials. *Eur. J. Mech. A/Solids*, 19:999–1014, 2000.

[19] J. M. Carbonell. *Modeling of ground excavation with the particle finite element method*. PhD thesis, Escola Técnica Superior d'Enginers de Camins Canals i Ports, Universitat Politécnica de Catalunya, 2009.

[20] M. Cervera and M. Chiumenti. Mesh objective tensile cracking via a local continuum damage model and crack tracking technique. *Computer Methods in Applied Mechanics and Engineering*, 196(1-3):304–320, 2006.

[21] M. Cervera, M. Chiumenti, Q. Valverde, and C. A. de Saracibar. Mixed linear/linear simplicial elements for incompressible elasticity and plasticity. *Computer Methods in Applied Mechanics and Engineering*, 192(49-50):5249–5263, 2003.

[22] M. Cervera, L. Pelá, R. Clemente, and P. Roca. A crack-tracking technique for localized damage in quasi-brittle materials. *Engineering Fracture Mechanics*, 77(13):2431–2450, 2010.

[23] C. Chang and A. Misra. Theoretical and experimental study of regular packing of granules. *Journal of Engineering Mechanics, ASCE*, 115(4):704–720, 1989.

[24] C. Chang and A. Misra. Packing structure and mechanical properties of granulates. *Journal of Engineering Mechanics*, 116(5):1077–1093, 1990.

[25] C. Chang, Q. Shi, and C. Liao. Elastic constants for granular materials modeled as first-order strain-gradient continua. *Int. J. Solids and Structures*, 40:5565–5582, 2003.

[26] C. S. Chang and J. Gao. Second-gradient constitutive theory for granular material with random packing structure. *Int. J. Solids Structures*, 32(16):2279–2293, 1995.

[27] M. Chiumenti, Q. Valverde, C. Agelet de Saracibar, and M. Cervera. A stabilized formulation for incompressible elasticity using linear displacement and pressure interpolations. *Comput. Meth. Appl. Mech. Eng.*, 191:5253–5264, 2002.

[28] M. Chiumenti, Q. Valverde, C. A. de Saracibar, and M. Cervera. A stabilized formulation for incompressible plasticity using linear triangles and tetrahedra. *International Journal of Plasticity*, 20(8–9):1487–1504, 2004.

[29] J.-W. Cho, S. Jeon, S.-H. Yu, and S.-H. Chang. Optimum spacing of tbm disc cutters: A numerical simulation using the three-dimensional dynamic fracturing method. *Tunnelling and Underground Space Technology*, 25(3):230–244, 2010.

[30] R. Codina. Stabilization of incompressibility and convection through orthogonal sub-scales in finite element methods. *Comput. Meth. Appl. Mech. Eng.*, 190:1579–1599, 2000.

[31] R. Codina and J. Blasco. Stabilized finite element method for transient Navier-Stokes equations based on pressure gradient projection. *Comput. Meth. Appl. Mech. Eng.*, 182:287–300, 2000.

[32] L. Cui and C. O'Sullivan. Analysis of a triangulation based approach for specimen generation for discrete element simulations. *Granular Matter*, 5:135–145, 2003.

[33] P. Cundall and O. Strack. A discrete numerical method for granular assemblies. *Geotechnique*, 29:47–65, 1979.

[34] P. A. Cundall. A computer model for simulating progressive, large-scale movements in blocky rock systems. In *Symp. Int. Soc. Rock Mech.*, volume 2, pages 132–150, Nancy, 1971.

[35] P. A. Cundall. A computer model for rock-mass behaviour using interactive graphics for the input and output of geometrical data. Technical report, Report for the Missouri River Division, U.S. Army Corps of Engineers, University of Minnesota, 1974.

[36] P. A. Cundall and R. D. Hart. Numerical modeling of discontinua. *Engineering Computations*, 9:101–113, 1992.

[37] P. G. de Gennes. Granular matter: A tentative view. *Rev. Mod. Phys.*, 71(2):S374–S382, 1999.

[38] H. Deresiewicz. Mechanics of granular matter. In *Advances in Applied Mechanics*, volume 5, pages 233–306. Elsevier, 1958.

[39] P. Digby. The effective elastic moduli of porous granular rocks. *Journal of Applied Mechanics*, 48:803–808, 1981.

[40] F. Donzé, P. Mora, and S.-A. Magnier. Numerical simulation of faults and shear zones. *Geophysical Journal International*, 116:46–52, 1994.

[41] O. Durán, N. Kruyt, and S. Luding. Analysis of three-dimensional micro-mechanical strain formulations for granular materials: Evaluation of accuracy. *International Journal of Solids and Structures*, 47(2):251–260, 2010.

[42] R. N. Elias, M. A. Martins, and A. L. Coutinho. Simple finite element-based computation of distance functions in unstructured grids. *International Journal for Numerical Methods in Engineering*, 72(9):1095–1110, 2007.

[43] EMI. Excavation Engineering and Earth Mechanics Institute. Colorado School of Mines. *http://mining.mines.edu/emi*.

[44] EN1926. *Natural stone test methods - Determination of compressive strength*. European committee for standarization. Brussels, 1999.

[45] J. Evans. Random and cooperative sequential adsorption. *Reviews of Modern Physics*, 65(4):1281–1304, 1993.

[46] G. Exadaktylos, M. Stavropoulou, G. Xiroudakis, M. de Broissia, and H. Schwarz. A spatial estimation model for continuous rock mass characterization from the specific energy of a TBM. *Rock Mechanics and Rock Engineering*, 41:797–834, 2008.

[47] A. Fakhimi and T. Villegas. Application of dimensional analysis in calibration of a discrete element model for rock deformation and fracture. *Rock Mech. Rock Engng.*, 40(2):193–211, 2007.

[48] E. Farrokh, J. Rostami, and C. Laughton. Study of various models for estimation of penetration rate of hard rock TBMs. *Tunnelling and Underground Space Technology*, 30:110–123, 2012.

[49] Y. T. Feng, K. Han, and D. R. J. Owen. Filling domains with disks: an advancing front approach. *Int. J. Numer. Meth. Engng.*, 56:699–713, 2003.

[50] J.-A. Ferrez. *Dynamic triangulations for efficient 3D simulation of granular materials*. PhD thesis, École Polytechnique Fédérale De Lausanne, 2001.

[51] J.-A. Ferrez and T. Liebling. Robust 3D dynamic triangulations for collision detection in DEM simulations of granular materials. *EPFL Supercomputing Review*, 13:41–48, 2002.

[52] E. Forest and R. Ruth. Fourth-order symplectic integration. *Physica D*, 43:105–117, 1990.

[53] J. Gálvez, M. Elices, G. Guinea, and J. Planas. Mixed mode fracture of concrete under proportional and nonproportional loading. *International Journal of Fracture*, 94:267–284, 1998.

[54] R. Gertsch, L. Gertsch, and J. Rostami. Disc cutting tests in Colorado Red Granite: Implications for TBM performance prediction. *International Journal of Rock Mechanics and Mining Sciences*, 44(2):238–246, 2007.

[55] O. Häggström and R. Meester. Nearest neighbour and hard sphere models in continuum percolation. *Random Structures and Algorithms*, 9:295–315, 1996.

[56] J. Haile. *Molecular dynamics simulation: Elementary methods*. Wiley-Interscience, 1997.

[57] K. Han, Y. Feng, and D. Owen. Sphere packing with a geometric based compression algorithm. *Powder Technology*, 155(1):33–41, 2005.

[58] S. Hentz, L. Daudeville, and F. V. Donzé. Identification and validation of a discrete element model for concrete. *Journal of Engineering Mechanics*, 130(6):709–719, 2004.

[59] S. Hentz, F. V. Donzé, and L. Daudeville. Discrete element modelling of concrete submitted to dynamic loading at high strain rates. *Computers and Structures*, 82(29-30):2509–2524, 2004.

[60] H. Hertz. Über die berührung fester elasticher körper (On the contact of elastic solids). *Journal für die reine und angewandte Mathematik*, 92:156–171, 1882.

[61] R. Hill. Elastic properties of reinforced solids: Some theoretical principles. *Journal of Mechanics and Physics of Solids*, 11:357–372, 1963.

[62] H. Huang. *Discrete element modeling of tool-rock interaction*. PhD thesis, University of Minnesota, December 1999.

[63] H. Huang and E. Detournay. Intrinsic length scales in tool-rock interaction. *International Journal of Geomechanics*, 8(1):39–44, 2008.

[64] Itasca. *PDF2D 2.0 Particule flow code in two dimensions*. Minneapolis, MN, 1998.

[65] S. Ji and H. H. Shen. Effect of contact force models on granular flow dynamics. *J. Engrg. Mech.*, 132(11):1252–1259, 2006.

[66] H. Kruggel-Emden, M. Sturma, S. Wirtza, and V. Scherera. Selection of an appropriate time integration scheme for the discrete element method (DEM). *Computers & Chemical Engineering*, 32(10):2263–2279, 2008.

[67] N. Kruyt and L. Rothenburg. Statistics of the elastic behaviour of granular materials. *Int. J. Solids and Structures*, 38(28-29):4879–4899, 2001.

[68] N. P. Kruyt and L. Rothenburg. Micromechanical definition of the strain tensor for granular materials. *Journal of Applied Mechanics*, 118:706–711, 1996.

[69] N. P. Kruyt and L. Rothenburg. Micromechanical bounds for the effective elastic moduli of granular materials. *International Journal of Solids and Structures*, 39(2):311–324, 2002.

[70] M. R. Kuhn. Structured deformation in granular materials. *Mechanics of Materials*, 31:407–429, 1999.

[71] C. Labra, J. Rojek, E. Oñate, and F. Köppl. Tunconstruct D2.1.3.3: Report of numerical modeling of disc cutter wear. Technical report, CIMNE, 2008.

[72] C. Labra, J. Rojek, E. Oñate, and F. Zarate. Advances in discrete element modelling of underground excavations. *Acta Geotechnica*, 3(4):317–322, 2008.

[73] H. Langhaar. *Dimensional Analysis and Theory of Models*. Wiley, 1951.

[74] K. Levenberg. A method for the solution of certain problems in least squares. *Quart. Appl. Math.*, 2:164–168, 1944.

[75] C.-L. Liao, T.-P. Chang, and D.-H. Young. Stress-strain relationship for granular materials based on the hypothesis of best fit. *International Journal in Solids and Structures*, 34(31-32):4087–4100, 1997.

[76] X. Lin and T.-T. Ng. A three-dimensional discrete element model using arrays of ellipsoids. *Geotechnique*, 47(2):319–329, 1997.

[77] R. Löhner and E. Oñate. A general advancing front technique for filling space with arbitrary objects. *International Journal for Numerical Methods in Engineering*, 61(12):1977–1991, 2004.

[78] B. Lubachevsky and F. Stillinger. Geometrik properties of random disk packings. *J. Stat. Phys.*, 60:561–583, 1990.

[79] S. Luding. Micro-macro transition for anisotropic, frictional granular packings. *International Journal of Solids and Structures*, 41(21):5821–5836, 2004.

[80] D. Marquardt. An algorithm for least square estimation on nonlinear parameters. *SIAM J. Appl. Math.*, 11:431–441, 1963.

[81] R. D. Mindlin and H. Deresiewicz. Elastic spheres in contact under varying oblique forces. *J. Appl. Mech.*, 20:327–344, 1953.

[82] B. Nilsen and L. Ozdemir. Hard rock tunnel boring prediction and field performance. In *Rapid Excavation and Tunneling Conference RETC*, 1993.

[83] I. Omelyan, I. Mryglod, and R. Folk. Symplectic analytically integrable decomposition algorithms: classification, derivation, and application to molecular dynamics, quantum and celestial mechanics simulations. *Computer Physics Communications*, 151:272–314, 2003.

[84] E. Oñate and J. Rojek. Combination of discrete element and finite element methods for dynamic analysis of geomechanics problems. *Computer Methods in Applied Mechanics and Engineering*, 193(27-29):3087–3128, 2004.

[85] E. Oñate, J. Rojek, R. Taylor, and O. Zienkiewicz. Finite calculus form for incompresible solids using linear triangles and tetrahedra. *Int. J. Numer. Meth. Engng.*, 59:1473–1500, 2004.

[86] C. O'Sullivan and J. D. Bray. Selecting a suitable time step for discrete element simulations that use the central difference time integration scheme. *Engineering Computations*, 21(2/3/4):278–303, 2004.

[87] L. Ozdemir. *Development of theoretical equations for predicting tunnel borability.* PhD thesis, Colorado School of Mines, Golden, Colorado, USA, 1977.

[88] D. Potyondy and P. Cundall. A bonded-particle model for rock. *International Journal of Rock Mechanics and Mining Sciences*, 41(8):1329–1364, 2004. Rock Mechanics Results from the Underground Research Laboratory, Canada.

[89] D. Potyondy, P. Cundall, and C. Lee. Modelling rock using bonded assemblies of circular particles. In M. Aubertin, F. Hassani, and H. Mitri, editors, *2nd NARMS, Rock Mechanics Tools and Techniques*, pages 1937–1944, Montreal, June 1996.

[90] A. Rahman. Correlations in the motion of atoms in liquid argon. *Phys. Rev.*, 136(2A):A405–A411, 1964.

[91] A. Ramezanzadeh, J. Rostami, and R. Kastner. Performance prediction models for hard rock tunnel boring machines. In *Proceedings of Sixth Iranian Tunneling Conference*, Tehran, Iran, 2004.

[92] J. Rojek and E. Oñate. Multiscale analysis using a coupled discrete/finite element model. *Interaction and Multiscale Mechanics*, 1(1):1–31, 2007.

[93] J. Rojek, E. Oñate, F. Zarate, and J. Miquel. Modelling of rock, soil and granular materials using spherical elements. In *2nd European Conference on Computational Mechanics ECCM-2001*, Cracow, Poland, June 2001.

[94] J. Rojek, E. Oñate, F. Zárate, and J. Miquel Canet. Thermomechanical discrete element formulation for wear analysis of rock cutting tools. Technical report, CIMNE, Barcelona, 2004.

[95] J. Rostami. *Development of a force estimation model for rock fragmentation with disc cutters through theoretical modelling and physical measurement of crushed zone pressure.* PhD thesis, Colorado School of Mines, 1997.

[96] J. Rostami. Hard rock TBM cutterhead modeling for design and performance prediction. *Geomechanik und Tunnelbau*, 1:18–28, 2008.

[97] J. Rostami and L. Ozdemir. A new model for performance prediction of hard rock TBMs. In *Rapid Excavation and Tunneling Conference RETC*. Boston, USA, 1993.

[98] J. Rostami, L. Ozdemir, and B. Nilsen. Comparison between CMS and NTH hard rock TBM performance prediction models. In *Annual Technical Meeting of the Institute of Shaft Drilling and Technology (ISDT)*, pages 1–11, 1996.

[99] E. Rougier, A. Munjiza, and N. W. M. John. Numerical comparison of some explicit time integration schemes used in DEM, FEM/DEM and molecular dynamics. *Int. J. Numer. Meth. Engng.*, 61(6):856–879, 2004.

[100] F. Roxborough and H. Phillips. Rock excavation by disc cutter. *Int. J. Rock. Mech. Min. Sci. Geomech. Abstr.*, 12:361–366, 1975.

[101] H. Sanio. Prediction of the performance of disc cutters in anisotropic rock. *International Journal of Rock Mechanics and Mining Sciences & Geomechanics*, 22(3):153–161, 1985.

[102] M. Satake. Tensorial form definitions of discrete-mechanical quantities for granular assemblies. *International Journal of Solids and Structures*, 41(21):5775–5791, 2004.

[103] K. Sato, G. F., and K. Itakura. Prediction of disc cutter performance using a circular rock cutting ring. In *Proceedings 1st International Mine Mechanization and Automation Symposium*, Golden Colorado, USA, 1991.

[104] T. G. Sitharam and M. Nimbkar. Numerical modelling of the micromechanical behaviour of granular media by discrete element. *Geotechnical Engineering Bulletin*, 6(4):261–283, 1997.

[105] D. Stoyan. Random set: Models and statistics. *International Statistical Review*, 66:1–27, 1998.

[106] O. Su and N. A. Akcin. Numerical simulation of rock cutting using the discrete element method. *International Journal of Rock Mechanics and Mining Sciences*, 48(3):434–442, 2011.

[107] L. Taylor and D. Preece. Simulation of blasting induced rock motion. *Eng. Comput.*, 9(2):243–252, 1992.

[108] M. Tuckerman, B. Berne, and G. Martyna. Reply to comment on: Reversible multiple time scale molecular dynamics. *Journal of Chemical Physics*, 99:2278–2279, 1993.

[109] K. Walton. The effective elastic moduli of a random packing of spheres. *J. Mech. Phys. Solids*, 35(2):213–226, 1987.

[110] S. Xiao and T. Belytschko. A bridging domain method for coupling continua with molecular dynamics. *Computer Methods in Applied Mechanics and Engineering*, 193:1645–1669, 2004.

[111] S. Yagiz, J. Rostami, T. Kim, L. Ozdemir, and C. Merguerian. *Factors influencing performance of hard rock tunnel boring machines. In Rock Engineering in Difficult Ground Conditions – Soft Rocks and Karst.* Taylor & Francis Group, 2010.

[112] B. Yang, Y. Jiao, and S. Lei. A study on the effects of microparameters on macroproperties for specimens created by bonded particles. *Engineering Computations: International Journal for Computer-Aided Engineering and Software*, 23(6):607–631, 2006.

[113] Y. Yua, J. Yinb, and Z. Zhong. Shape effects in the brazilian tensile strength test and a 3D FEM correction. *International Journal of Rock Mechanics and Mining Sciences 2006*, 43:623–627, 2006.

[114] O. Zienkiewicz and R. Taylor. *The Finite Element Method (5th Ed.)*. Butterworth-Hienemann, 2000.